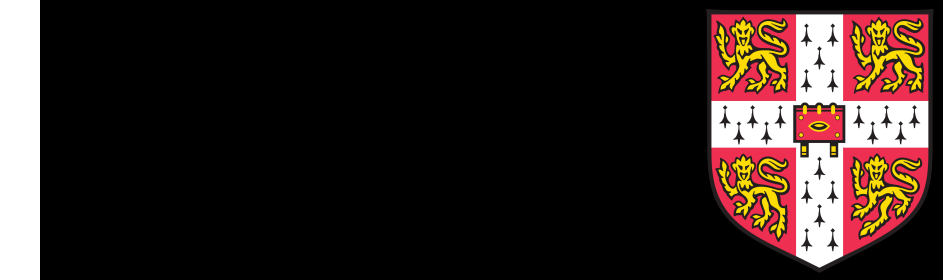

Black Hole Feedback in New Regimes: Modelling Dwarf Galaxies with Active Galactic Nuclei

Sophie Koudmani

Supervisors: Dr Debora Sijacki & Prof. Martin Haehnelt

Institute of Astronomy
University of Cambridge

This thesis is submitted for the degree of
Doctor of Philosophy

Churchill College, April 2021

DECLARATION

I hereby declare that this thesis is the result of my own work and includes nothing which is the outcome of work done in collaboration except as declared in the preface and specified in the text. The use of 'we' instead of 'I' throughout various parts of this thesis merely reflects a stylistic choice.

- Chapter 2 is based on work completed in collaboration with D. Sijacki, M. A. Bourne and M. C. Smith, published as: Koudmani S., Sijacki D., Bourne M. A., Smith M. C., 2019, 'Fast and energetic AGN-driven outflows in simulated dwarf galaxies', MNRAS, 484, 2047.

- Chapter 3 is based on work completed in collaboration with N. A. Henden and D. Sijacki, published as: Koudmani S., Henden N. A. and Sijacki D., 2021, 'A little FABLE: exploring AGN feedback in dwarf galaxies with cosmological simulations', MNRAS, 503, 3568.

Chapter 1 does not present any original research, though note that Section 1.4.3 is based on the introduction of Koudmani et al. (2021). Chapters 4 and 5 are based on work currently being prepared for publication.
I confirm that this thesis is not substantially the same as any that I have submitted, or, is being concurrently submitted for a degree or diploma or other qualification at the University of Cambridge or any other University or similar institution except as declared in the Preface and specified in the text. The length of this thesis does not exceed the prescribed word limit for the Degree Committee of Physics and Chemistry of 60,000 words.

Sophie Koudmani
Churchill College, April 2021

ABSTRACT

Black Hole Feedback in New Regimes:
Modelling Dwarf Galaxies with Active Galactic Nuclei

Sophie Koudmani

Contrary to the standard lore, there is mounting observational evidence that feedback from active galactic nuclei (AGN) may also play a role at the low-mass end of the galaxy population. In this thesis, I explore that possibility employing both isolated and cosmological simulations of dwarf galaxies.

Firstly, I perform high-resolution simulations of isolated dwarf galaxies. In these simulations, the AGN has only a limited direct effect on star formation rates. There is, however, a significant effect on outflows, which are notably enhanced by the AGN to much higher temperatures and velocities. This indicates that AGN may play an indirect role in quenching dwarf galaxies by hindering cosmic gas inflows.

I further investigate this quenching scenario using the cosmological simulation suite FABLE. While in the local Universe the majority of AGN in dwarfs are much dimmer than the stellar component, for $z \geq 2$ there is a significant population of AGN that outshine their hosts. These high-redshift overmassive black holes contribute to the quenching of dwarfs, whereas at late cosmic times supernova (SN) feedback is more efficient. However, the lack of high-luminosity X-ray AGN in FABLE at low redshifts highlights an interesting possibility that SN feedback could be too strong in FABLE's dwarfs, curtailing AGN growth and feedback.

To examine the interplay between SNe and AGN accretion in more detail, I run a series of cosmological zoom-in simulations. I find that AGN feedback in tandem with more realistic SN feedback can be a successful alternative quenching mechanism to strong SN feedback in dwarfs, provided that the AGN is able to enter the high-accretion regime for at least part of its history. However, the Bondi rate generally prevents low-mass black holes from accreting efficiently, even though sufficient amounts of gas are available in these dwarfs.

Finally, I present a more robust AGN accretion model based on a unified accretion disc, which combines the ADIOS flow and standard thin disc schemes. This model will allow for the self-consistent exploration of the high-accretion regime in dwarf galaxies and detailed modelling of multimessenger signatures, in preparation for the next-generation electromagnetic and gravitational-wave observatories.

Für meine kleine Schwester Paula

ACKNOWLEDGEMENTS

First and foremost, I would like to express my gratitude to my supervisor Debora Sijacki for her invaluable guidance and support throughout the past four years, always encouraging me to believe in myself and take on new challenges. I feel very lucky to have had such an inspiring mentor and role model.

I would also like to thank my secondary supervisor Martin Haehnelt for his kind encouragement and sound advice throughout my time at the Institute, always having an open ear for any kinds of concerns from paper writing and debugging issues to postdoc applications and negotiations.

The Science and Technology Facilities Council provided the funding for this PhD project for which I am very grateful. Furthermore, I would like to thank Churchill College for their support, including the great accommodation provision and for assisting with the travel funding for two international conferences, with special thanks to the graduate student administrator Rebecca Sawalmeh.

I would also like to thank Paul Hewett and Debbie Peterson for running an excellent graduate student programme at the Institute of Astronomy and for helping me out with all manner of administrative issues during the PhD (including getting stuck in Denver during a snowstorm)!

Moreover, I would like to thank my examiners, Carlos Frenk and Roberto Maiolino, for an interesting viva with great discussions and valuable feedback. Similarly, I would like to thank the assessors of the end-of-year progress reports, Cathie Clarke, Ewald Puchwein, Matt Auger, and George Efstathiou, for their helpful advice both on the PhD project and academic careers planning. Furthermore, I would like to thank Sylvain Veilleux for useful discussions about AGN-driven outflows.

Useful insights (and consolation) were also obtained during the weekly ‘Sims Group Meeting’ and I would like to thank all the group members for their support – special mentions go to the fellow DiRAC hackathon participants Lewis, Nick, Aneesh, Rosie, Jake and Martin. Go Team AREGPU!

O15, also known as the ‘Best Office’, has served as my happy place throughout the PhD. Jasleen and Nick, thanks for making me feel so welcome and for all of the hilarious bants and shenanigans! Aoife and Sam, I still cannot believe that we ended up only spending a few months in O15 together, but the virtual edition of the Best Office kept going strong despite the pandemic chaos surrounding us.

I would also like to thank my other PhD colleagues for the great times that we have spent together, including fancy formals, punting adventures, and, of course, lunch at Greenwich; in particular Amy Rankine, fellow AGN enthusiast as well as a fabulous friend, and the rest of the TBD crew, especially Fruzsi, Luis, Anjali and Matthew. I would also like to acknowledge the board games group which provided the perfect antidote to PhD life: Nick, Jasleen, Douglas, Matteo, Lukas, and Laura.

I would be amiss if I did not also mention the various educators and mentors that helped me along the path towards starting a PhD in the first place. I would like to thank my teachers at Lessing-Gymnasium Norderstedt who supported me in the crucial early stages of that journey, in particular Frau Eileck and Herr Sterner, as well as my tutors and supervisors during undergrad, Adrianne Slyz, Joseph Conlon, Laura Lauro-Taroni, Jonathan Pritchard and Julien Devriendt, who always encouraged and supported me to pursue a career in academia.

A big thank you is also owed to my amazing friends Lucy, Leander, Joe, Will, Pauline, Haengeun, Sveti, Mareike and Melanie (a necessarily incomplete list!), as well as to my wonderful family. I would like to thank Mama and Papa for instilling a growth mindset in me and for always encouraging me to pursue my ambitions. I would also like to thank my Omas and Opa for their warm support. A special mention must go to my little sister Paula. Her strength, top-notch humour and selfless commitment to social justice inspire me every single day.

Finally, I would like to thank Rob for his unwavering support and for bringing so much happiness into my life. The PhD journey can be ‘a bit of’ a rollercoaster, and I am incredibly grateful to him for helping me through the tough times and for celebrating the good times. Everything about you – I like!

Zwei Dinge erfüllen das Gemüt mit immer neuer und zunehmender Bewunderung und Ehrfurcht, je öfter und anhaltender sich das Nachdenken damit beschäftigt: Der bestirnte Himmel über mir und das moralische Gesetz in mir.

Two things fill the soul with ever new and increasing wonder and awe, the more often and persistently the mind concerns itself with them: The starry sky above me and the moral law within me.

Immanuel Kant, 1788, Kritik der praktischen Vernunft

TABLE OF CONTENTS

LIST OF FIGURES

List of tables

CHAPTER 1

INTRODUCTION

1.1 Island universes and dark stars

Early ideas about both galaxies and black holes were already developed in the eighteenth century, building on Newton's theory of gravity (Newton, 1687). Nowadays, the presence of central black holes in most massive galaxies is firmly established and observational evidence as well as theoretical arguments point towards a co-evolution of these two components, driven by black hole feedback. However, the exact modus operandi of this feedback process as well as its role in low-mass galaxies are still open questions in astrophysics. In this thesis, I explore the impact of active black holes on the formation and evolution of dwarf galaxies using numerical simulations.

This introductory chapter provides the necessary theoretical and observational background for the subsequent investigations. Firstly, I give a brief historical overview of research into galaxies (see Section 1.1.1) and black holes (see Section 1.1.2), respectively, before describing the current theory of structure formation, and its challenges, in Section 1.2. I continue with an overview of the relevant numerical techniques in Section 1.3 and a summary of feedback mechanisms in galaxy formation in Section 1.4. Finally, I outline the set-up of the thesis in Section 1.5.

1.1.1 Galaxies: a historical overview

The concept of galaxies traces back to the eighteenth century, spurred on by the debate on the origin of nebulae observed in the night sky. At the time, the only galaxy whose existence was known was the Milky Way (indeed the etymology of *galaxy* derives from the Greek term for the Milky Way, *galaxías kúklos*, literally 'milky circle').

In addition to the diffuse band of the Milky Way, astronomers had observed other diffuse objects in the night sky, the nebulae. Proponents of the 'island universe' hypothesis argued that these nebulae were systems of stars outside our own Galaxy and in fact should be thought of as galaxies in their own right. One famous advocate of this theory was Immanuel Kant who argued that "all this is in perfect agreement with the view that these elliptical figures are just universes and, so to speak, Milky Ways"[1] based on his Newtonian analysis of the Milky Way as a disc and its consequent appearance to an external observer, building on the work by Wright (1750).

In the twentieth century, this intuitively developed picture would finally be put on a firm observational basis. Edwin Hubble was able to measure the distances to the nebulae NGC 6822, M33 and M31 with the aid of the period-luminosity relation found by Leavitt and Pickering (1912) for Cepheid variable stars – the first 'standard candles' in astronomy. This allowed him to demonstrate that these nebulae's distances were indeed much larger than the size of the Milky Way, as estimated by Shapley (1918), confirming the 'island universe' hypothesis (Hubble, 1925, 1926, 1929b).

In the next decades, the new field of extragalactic astronomy advanced hugely. Radio observations enabled astronomers to detect not only stars but also gas in galaxies. Optical and radio measurements of galaxy rotation curves showed approximately flat profiles which suggested that there must be a radially increasing amount of undetected additional matter present in the outskirts of galaxies (Rubin and Ford, 1970; Rogstad and Shostak, 1972; Roberts and Rots, 1973; Rubin et al., 1978, 1980). Ostriker et al. (1974) and Einasto et al. (1974) used the hints provided by the rotation curves as well as other observational evidence, such as the dynamics of satellite galaxies, to argue that the mass-to-light ratio of massive galaxies was of order ~ 200, requiring the presence of 'hidden matter'. Together with cosmological modelling of the large-scale structure of the Universe, this established a paradigm where non-luminous dark matter dominates the mass budget of galaxies and of the Universe as a whole.

Note that Zwicky (1933) had already postulated the existence of dark matter forty years earlier based on the measurements of galaxy velocities in the Coma cluster. However, this hypothesis only gained popularity when additional evidence from galaxy samples and other cosmological probes became available. Indeed, the interplay between extragalactic astronomy and cosmology paved the way for the theory of galaxy formation within an expanding universe, which is laid out in Section 1.2.

[1] "[...] alles stimmt vollkommen überein, diese elliptische Figuren für eben dergleichen Weltordnungen und, so zu reden, Milchstraßen zu halten" (Kant, 1755, 255:6–8).

Galaxies are now known to form hierarchically (White and Rees, 1978) with the least massive galaxies, so-called dwarf galaxies, the smallest building blocks in this structure formation process. Dwarf galaxies are very dark matter dominated systems and extremely susceptible to the effects of energetic astrophysical phenomena, such as supernovae (SNe), due to their shallow potential wells. This makes them interesting testbeds both for dark matter physics and for astrophysics, though at the same time this also means that dwarf galaxies are rather difficult to model and several apparent discrepancies between observations and theoretical predictions remain (see Section 1.2.7.2).

This could point to a need for new fundamental physics, e.g. a different form of dark matter. On the other hand, this mismatch could also mean that we need to include additional astrophysical phenomena that have so far been ignored by theorists. Recently, it has been suggested the apparent discrepancies between theory and observations could be explained by the presence of black holes in dwarf galaxies (e.g. Silk, 2017).

1.1.2 Point of no return: theory and observations of black holes

A black hole is a dense object with an extremely strong gravitational field, entrapping both matter and light within its event horizon. The idea of black holes first appeared in the late eighteenth century. Michell (1784) and Laplace (1796) independently developed the theory of 'dark stars'. They noted that massive, dense stars would have a Newtonian escape velocity greater than the speed of light, which would render them invisible. This analysis was founded on a particle-based (corpuscular) theory of light, assuming that corpuscles were attracted by the star in the same way as matter. Dark stars were then a natural consequence of Newtonian gravity. However, the theory of dark stars fell out of fashion when the massless wave-like nature of light was discovered which suggested that light would be unaffected by gravity.

This was all changed by the development of General Relativity (GR, Einstein, 1915), which outlines how the action of gravity is communicated via the curvature of spacetime, i.e. even a light ray traversing the spacetime close to a strongly gravitating object would have its path bent and may even be entrapped by a black hole.

Schwarzschild found the solution to the GR field equations for a spherically symmetric metric describing a time-steady non-rotating black hole, then known as a Schwarzschild singularity[2] (Schwarzschild, 1916). However, whether these singularities were physical was still very much in doubt.

Chandrasekhar (1931) introduced the idea of black holes as stellar remnants, finding the maximum mass for white dwarfs, above which these objects would gravitationally collapse.

[2]Note that the term *black hole* was not used until the 1960s when it was popularised by John Wheeler.

This idea was further developed by Oppenheimer and Snyder (1939), who presented the solutions of the field equations which describe the process of a star's gravitational collapse.

The first hint of the existence of supermassive black holes (SMBHs), many orders of magnitude more massive than stellar remnants, came from the discovery of the first quasar QSO 3C 273 (Schmidt, 1963), which was also shown to be a highly variable source (Smith and Hoffleit, 1963). In the same year, the axially symmetric Kerr metric of a rotating black hole was developed (Kerr, 1963).

Motivated by the renewed interest in gravitational collapse due to the quasar discovery, Penrose (1965) set out to demonstrate that gravitational collapse into a singularity was a natural consequence of GR – even without the assumptions of symmetry by Schwarzschild (1916) and Kerr (1963), which had raised suspicions that these solutions would not occur in reality. The 2020 Nobel Prize in Physics was recently awarded to Roger Penrose "for the discovery that black hole formation is a robust prediction of the theory of general relativity" together with the observational astronomers Reinhard Genzel and Andrea Ghez (see below).

At the same time, there was sustained theoretical effort to explain the inferred high quasar luminosities. This led to the paradigm of quasars being powered by the accretion onto SMBHs (Hoyle and Fowler, 1963; Salpeter, 1964; Zel'dovich, 1964; Lynden-Bell, 1969; Lynden-Bell and Rees, 1971). However, there was no dynamical evidence for the existence of these SMBHs until the 1980s when digital imaging enabled astronomers to resolve the gravitational sphere of influence of SMBHs. The *Hubble Space Telescope* discovered a multitude of additional objects owing to its high spatial resolution, so that demographic studies became possible. Further recent progress in the mapping of the black hole population has been driven by adaptive optics, maser black hole searches and reverberation mapping (see Kormendy and Ho, 2013, for a summary of the history of dynamical SMBH detections).

The strongest evidence of the existence of a SMBH to date comes from our own Galaxy, which was established by the independent observing programmes led by Reinhard Genzel and Andrea Ghez (see Eckart and Genzel, 1997; Ghez et al., 1998, and follow-up papers). Their work was awarded the other half of the 2020 Nobel Prize in Physics "for the discovery of a supermassive object at the centre of our galaxy".

Whilst most massive galaxies are inferred to host SMBHs (see Kormendy and Ho, 2013, and references therein), for dwarf galaxies the black hole occupation fraction is still unclear (e.g Greene et al., 2020) since their black holes fall into the intermediate-mass black hole (IMBH) regime and are therefore much more difficult to detect.

However, gravitational wave interferometers have opened a new window into the Universe by picking up signals from black hole mergers. In 2017, Rainer Weiss, Barry Barish and Kip Thorne were awarded the Nobel Prize in Physics "for decisive contributions to the

LIGO detector and the observation of gravitational waves". Note that whilst LIGO can only detect stellar-mass black holes, the next-generation spaceborne interferometer LISA and pulsar timing arrays will push into the IMBH and SMBH regime. Moreover, atom interferometer observatories, such as the proposed experimental programme AION, will map gravitational waves in the mid-frequency range between LIGO and LISA. Furthermore, future deep electromagnetic surveys with *JWST*, *RST*, *Athena*, *Lynx* and SKA will be able to provide complementary constraints on the black hole growth via accretion. These upcoming observational facilities are set to revolutionise our picture of black holes in galaxy evolution and will push observational constraints to much lower black hole masses.

1.2 Cosmic structure formation

Modern cosmology has made huge progress in modelling the evolution of our Universe and the formation of structures, within the framework of GR. In the generally accepted picture, the Universe has expanded for the past 13.8 billion years starting off from a highly compressed state (the 'Big Bang Theory'), and has formed the diversity of galaxies we observe today in the process. This general model is rooted in the discovery by Georges Lemaître and Edwin Hubble that distant galaxies are receding from us with a speed proportional to their distance (Lemaître, 1927; Hubble, 1929a).

1.2.1 Cosmic expansion

The expansion of the Universe can be parametrized via the scale factor a, which gives the growth of the spatial extent of the Universe and is usually defined such that $a(t_0) = 1$ at the present time. The redshift, which is observationally defined as the wavelength displacement and can be measured directly from astrophysical spectra of objects of interest, is given by the ratio of the present-day scale factor to the scale factor at a previous time for a homogeneous and isotropic Universe:

$$z = \frac{\lambda_{\rm obs} - \lambda_{\rm em}}{\lambda_{\rm em}} = \frac{a(t_0)}{a(t)} - 1, \tag{1.1}$$

where $\lambda_{\rm obs}$ is the observed wavelength and $\lambda_{\rm em}$ is the emitted wavelength measured in the object's restframe. Due to the light travel time effect, the redshift is then both a measure of the object's distance as well as of the object's observed epoch in the Universe's history. The scale factor also allows us to define comoving units based on a coordinate system that follows the expansion of the Universe, which are related to the proper (physical) coordinates as: $\Delta x = \frac{\Delta r}{a(t)}$, where x is the comoving coordinate and r is the proper coordinate.

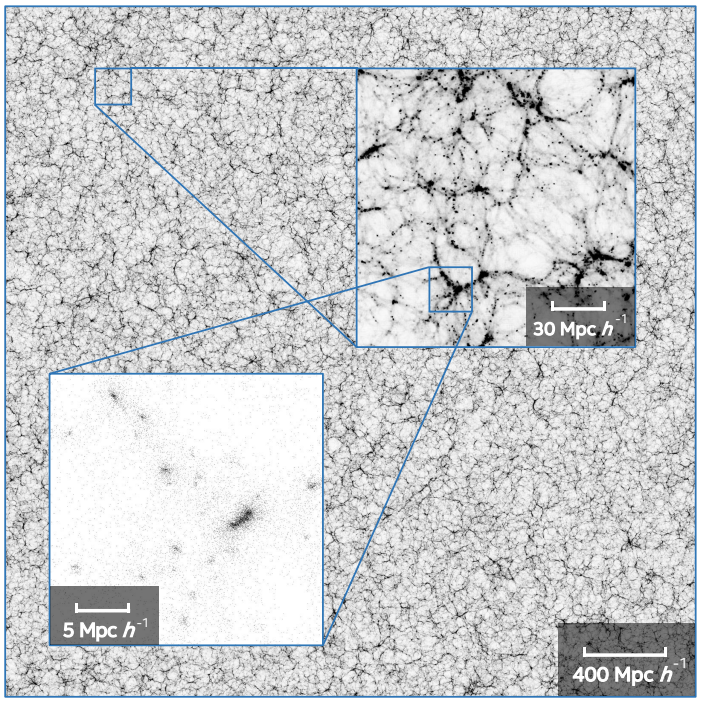

Fig. 1.1 A slice of the simulation box from the Cosmo-π simulation (box size $= 3200$ Mpc$\,h^{-1}$, slice width $= 20$ Mpc$\,h^{-1}$). In the main panel the dark matter column densities are rendered on a grey scale, whilst the subpanels show the direct projection of CDM N-body particles. The homogeneous and isotropic dark matter distribution in the main panel is a reflection of the Cosmological Principle. As we move to smaller scales the Cosmological Principle is no longer valid, with the filamentary structure distinguishable on intermediate scales and individual dark matter halos clearly identifiable on small scales. This figure is reproduced from Cheng et al. (2020). © 2020 IEEE. Reprinted with permission.

1.2.2 The ΛCDM model

The evolution of the scale factor across cosmic time can principally be obtained from the GR field equations, which link the Universe's geometry with its energy contents. The currently most popular cosmological model is based on a universe, which is dominated by dark energy (~ 70 per cent of the energy density) and dark matter (~ 26 per cent of energy density). Dark energy is modelled as the cosmological constant, Λ, in the GR field equations, which represents a 'vacuum energy' driving the accelerated expansion of the Universe. Dark matter is taken to be non-relativistic, so-called 'cold' dark matter (CDM). The CDM component is weakly interacting, effectively collisionless, and, in particular, CDM does not interact electromagnetically. These two dominating dark components have given the concordance model of cosmology its name – the ΛCDM model. Note that the ordinary matter (so-called 'baryonic' matter) only represents ~ 4 per cent of the energy density in the ΛCDM universe.

Table 1.1 Cosmological parameter values and 68% confidence limits derived by the Planck Collaboration XIII (2016) based on the Planck power spectra (including polarisation measurements) in combination with Planck lensing reconstruction and external data of baryon acoustic oscillations, type Ia SNe and the Hubble constant. From left to right the parameters are: dark energy density parameter, matter density parameter, baryon density parameter, root-mean-square matter fluctuations in linear theory (averaged over a sphere of radius 8 Mpch^{-1}), Hubble constant, and age of the Universe. Note that all parameter values correspond to today's values at t_0 and that the densities are fractional densities normalised by (today's) critical density for a flat universe. Parameter values were fitted using the base ΛCDM model, which is specified by six parameters.

Ω_Λ	Ω_m	$\Omega_\mathrm{b}h^2$	σ_8	H_0 [km s^{-1} Mpc^{-1}]	t_0 [Gyr]
0.6935	0.3065	0.02227	0.8154	67.9	13.796
±0.0072	±0.0072	±0.00020	±0.0090	±0.55	±0.029

On large scales, the Cosmological Principle states that the spatial distribution of matter in the Universe is isotropic and homogeneous. This principle is beautifully confirmed by the large-scale distribution of galaxies (e.g. the BOSS survey, see Dawson et al., 2013) and the cosmic microwave background (CMB, Penzias and Wilson, 1965; Smoot et al., 1992; Bennett et al., 2003; Spergel et al., 2003; Planck Collaboration XIII, 2016). Figure 1.1 shows projections from a large-scale structure simulation of the ΛCDM universe, which nicely reflects the Cosmological Principle at large scales whilst the zoomed-in subpanels show cosmic structures on smaller scales where the Cosmological Principle is no longer obeyed.

1.2.3 The cosmic microwave background

The CMB originates from the surface of last scattering during the epoch of recombination when the Universe turned transparent and was merely 380,000 years old. During this epoch, temperatures had dropped due to the cosmic expansion and protons could capture free electrons to recombine into hydrogen atoms (e.g. Peebles, 1968; Zel'dovich et al., 1969). The photons released during this epoch can be observed today (redshifted into the microwave range) as the CMB. The CMB follows the spectrum of a black body with a temperature of $T = 2.726$ K. The temperature fluctuations in the CMB are limited to about 1 part in 10^5, providing an upper limit on the magnitude of the anisotropies in the early Universe. Furthermore, the analysis of the power spectrum of these anisotropies can provide tight constraints on cosmological parameters, including the energy contents of the Universe. Table 1.1 shows the cosmological parameters obtained from the CMB by the Planck Collaboration.

1.2.4 Inflationary epoch

As we move to smaller scales ($\lesssim 100$ Mpc), the Cosmological Principle is clearly no longer valid, with the distribution of galaxies and galaxy clusters no longer homogeneous and isotropic on these scales. In the ΛCDM model, these cosmic structures originate from tiny primordial density perturbations, which are hypothesised to have developed during an inflationary epoch of exponential expansion driven by the vacuum energy of one or more quantum fields in the very early Universe. Quantum fluctuations in these fields could provide the seeds for the primordial density fluctuations, however, the exact origin is still uncertain. Instead, the properties of these perturbations can be estimated phenomenologically from observations, e.g. the CMB can provide us with insights into the wavelengths and magnitudes of the density perturbations present at recombination.

1.2.5 Linear regime: the growth of gravitational instabilities

In this section, I explore the evolution of the perturbations in the linear regime, using Newtonian gravity for the treatment of fluid dynamics (also see Bonnor, 1957). Though of course to be fully consistent, these derivations would need to be carried out using GR (see Lifshitz, 1946, for an equivalent GR derivation). However, for massive, non-relativistic particles (and far away from a black hole), the Newtonian treatment provides useful qualitative and quantitative insights, provided that matter is the dominant component in the Universe[3]. It also needs to be emphasised that the Newtonian treatment is only valid for scales smaller than the particle horizon $r_{\rm h}$, which is defined as the maximum distance that a particle could have travelled since the Big Bang:

$$r_{\rm h}(t) = \int_0^t \frac{{\rm c}\,{\rm d}t'}{a(t')}. \tag{1.2}$$

With these caveats in mind, the evolution of the density perturbations can then be modelled using the equations governing an ideal, non-relativistic, self-gravitating fluid. Conservation of mass gives the continuity equation:

$$\frac{\partial \rho}{\partial t} + \nabla \cdot (\rho \mathbf{u}) = 0, \tag{1.3}$$

where $\rho = \rho(\mathbf{r},t)$ and $\mathbf{u} = \mathbf{u}(\mathbf{r},t)$ are the density and velocity fields, respectively, in proper units.

[3] According to the ΛCDM model, matter is the dominant component from matter radiation equality at $z \sim 3400$ to the time when the cosmological constant takes over at $z \sim 0.3$, spanning approximately 10.2 Gyr, so this approximation is valid for the majority of the Universe's history.

And from conservation of momentum, the Euler equation is obtained:

$$\frac{\partial \mathbf{u}}{\partial t} + (\mathbf{u}\cdot\nabla)\,\mathbf{u} + \frac{1}{\rho}\nabla P + \nabla\phi = 0, \tag{1.4}$$

where $P = P(\mathbf{r},t)$ and $\phi = \phi(\mathbf{r},t)$ are the fluid pressure and gravitational potential in proper units. The latter can be calculated from the Poisson equation:

$$\nabla^2\phi = 4\pi \mathrm{G}\rho, \tag{1.5}$$

where G is the gravitational constant.

Note that these are five equations for six variables, so an additional relation is needed to close the set. This relation is given by the energy equation. Though for isentropic evolution (i.e. adiabatic and reversible), we can bypass the energy equation and instead use a barotropic equation of state $P = P(\rho)$ to close the fluid equations.

These equations can be more conveniently expressed in a comoving coordinate system $\mathbf{x} = \mathbf{r}/a$. These comoving fluid equations can then be used to study the evolution of the density fluctuations in the early Universe. Firstly, define the overdensity field as:

$$\delta(\mathbf{x},t) = \frac{\rho(\mathbf{x},t) - \bar{\rho}(t)}{\bar{\rho}(t)}, \tag{1.6}$$

where $\bar{\rho}$ is the homogeneous background average density.

One can then rewrite the fluid velocity as $\mathbf{u} = \dot{a}\mathbf{x} + \mathbf{v}$, where $\dot{a}\mathbf{x}$ is the Hubble flow, i.e. the velocity due to the expansion of the Universe, and $\mathbf{v} = \mathbf{v}(\mathbf{x},t)$ is the so-called peculiar velocity associated with the perturbation. Furthermore, a new potential may be defined as $\Phi = \phi + \frac{1}{2}a\ddot{a}\mathbf{x}^2$, which corresponds to the potential sourced by the perturbations.

Perturbations are small at recombination from the CMB data ($\delta \sim 10^{-5}$), so perturbation theory can be used to linearise equations 1.3 - 1.5 with $\delta \ll 1$ and $\mathbf{v} \ll \dot{a}\mathbf{x}$, $|\Phi| \ll \left|\frac{1}{2}a\ddot{a}\mathbf{x}^2\right|$ as the small density, velocity and potential perturbations, respectively. Furthermore, assuming that the perturbations are adiabatic, the pressure can be written as $P(\mathbf{x},t) = \bar{P}(t) + \delta P(\mathbf{x},t) = \bar{P}(t) + (\partial P/\partial\rho)_S\,\delta\rho(\mathbf{x},t) = \bar{P}(t) + c_\mathrm{s}^2\bar{\rho}\delta(\mathbf{x},t)$, where c_s is the adiabatic sound speed.

Substituting these expressions into equations 1.3 - 1.5, neglecting all higher order terms and using the Friedmann-Lemaître equations of the homogeneous Universe (Friedmann, 1922; Lemaître, 1927) to eliminate the 0^{th} order terms, yields:

$$\frac{\partial\delta}{\partial t} + \frac{1}{a}(\nabla\cdot\mathbf{v}) = 0 \tag{1.7}$$

$$\frac{\partial\mathbf{v}}{\partial t} + \frac{\dot{a}}{a}\mathbf{v} + \frac{1}{a}\nabla\Phi + \frac{c_\mathrm{s}^2}{a}\nabla\delta = 0 \tag{1.8}$$

$$\nabla^2\Phi = 4\pi G\bar{\rho}a^2\delta \tag{1.9}$$

Then take the gradient of equation 1.8 and substitute in equations 1.7 and 1.9 to obtain a second order differential equation for the density perturbation. Transforming this equation to Fourier space, with $\delta(\mathbf{x},t) = \sum_{\mathbf{k}} \delta_{\mathbf{k}}(t)e^{i\mathbf{k}\cdot\mathbf{x}}$, gives

$$\ddot{\delta}_{\mathbf{k}} + 2H\dot{\delta}_{\mathbf{k}} + \left(\frac{c_s^2}{a^2}k^2 - 4\pi G\bar{\rho}\right)\delta_{\mathbf{k}} = 0, \tag{1.10}$$

where $H = \dot{a}/a$ is the Hubble parameter. This is the equation of a damped harmonic oscillator, with the damping term stemming from the Hubble flow and the oscillation frequency ω given by $\omega^2 = \left(\frac{c_s^2}{a^2}k^2 - 4\pi G\bar{\rho}\right)$. This system has two different types of solutions depending on the sign of ω^2. If $\omega^2 > 0$, the system exhibits oscillatory behaviour in the form of acoustic waves. If $\omega^2 < 0$, the solution represents a non-propagating stationary wave of either increasing or decreasing amplitude. The former is referred to as the Jeans instability, a gravitational instability which depends on the balance between gravity and pressure forces (Jeans, 1902). The changeover between these two regimes then occurs at a characteristic wavenumber $k_{\mathrm{J,comoving}}$ defined by $\omega^2 = 0$, which corresponds to the (proper) Jeans length, λ_{J}:

$$\lambda_{\mathrm{J}} = a\lambda_{\mathrm{J,comoving}} = a\frac{2\pi}{k_{\mathrm{J,comoving}}} = c_s\sqrt{\frac{\pi}{G\bar{\rho}}}. \tag{1.11}$$

Intuitively, this wavelength can be interpreted by noting that if the gravitational free-fall time $t_{\mathrm{ff}} \sim 1/\sqrt{G\rho}$ is much smaller than the sound crossing time $t_{\mathrm{h}} \sim \lambda/c_s$, then $\lambda \gg \lambda_{\mathrm{J}}$ and gravity dominates over pressure, so perturbations will grow. If $\lambda \ll \lambda_{\mathrm{J}}$, pressure is stronger than gravity resulting in acoustic waves. The Jeans length can also be used to obtain a characteristic Jeans mass, $M_{\mathrm{J}} = \frac{4}{3}\bar{\rho}\lambda_{\mathrm{J}}^3$.

The top panel of Figure 1.2 shows the evolution of the Jeans length as a function of scale factor. The times of matter-radiation equality, t_{eq}, and recombination (photon decoupling), t_{dec}, are also indicated for reference. In the radiation-dominated universe, prior to t_{eq}, the photon energy density declines rapidly whilst the speed of sound is constant, set by radiation pressure. Therefore, the Jeans length increases. For $t_{\mathrm{eq}} < t < t_{\mathrm{dec}}$, the decrease in sound speed is compensated by the decrease in density leading to a constant (comoving) Jeans length. However, after recombination, the gas pressure becomes dominant and the overall pressure drops significantly. This dramatically decreases the Jeans mass by about nine orders of magnitude to the scale of a globular cluster with $M_{\mathrm{J}} \sim 10^6\ \mathrm{M}_\odot$ (e.g. Mo et al., 2010).

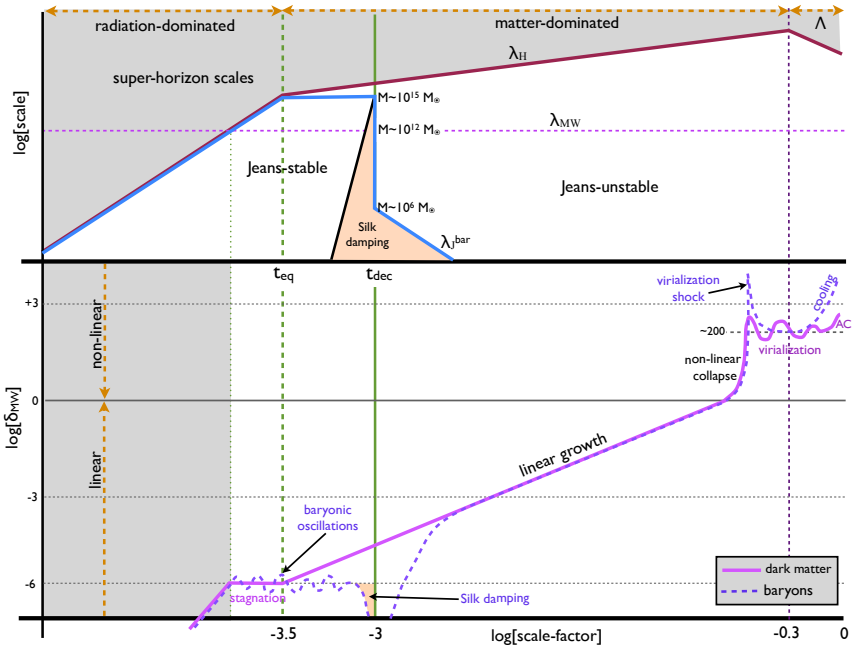

Fig. 1.2 Cosmic evolution of the length scales governing structure formation (horizon scale, $\lambda_{\rm H}$, Jeans length of the baryons, $\lambda_{\rm Jbar}$, Silk scale, $\lambda_{\rm S}$) with the Milky Way perturbation length, $\lambda_{\rm MW}$, indicated for reference (upper panel) and of a Milky-Way scale perturbation, $\delta_{\rm MW}$, for the baryonic and the dark matter component (lower panel) as a function of scale factor. The scale factors corresponding to matter-radiation equality, $t_{\rm eq}$, and recombination (photon decoupling), $t_{\rm dec}$, are indicated by dashed and solid green lines, respectively. This figure is reproduced from the 'Theory of Galaxy Formation' lecture notes[4] by Frank van den Bosch. © Frank van den Bosch, Yale University. Reprinted with permission.

However, there are several processes which dampen and/or limit the growth of perturbations. For example, the Hubble drag of the expanding Universe will resist the perturbation growth and super-horizon perturbations (where the perturbation length λ exceeds the scale of the particle horizon) are frozen. Furthermore, Silk damping and free streaming both act to erase small-scale perturbations and are therefore important processes to consider for unravelling the galaxy formation process.

1.2.5.1 Silk damping

Before recombination, baryons and radiation are tightly coupled, so that the photon mean free path is negligible, whilst after recombination, photons can propagate freely (forming the CMB), with the mean free path being infinite. During recombination, there is a short

[4] See http://campuspress.yale.edu/astro610/ for the 'ASTR 610: Theory of Galaxy Formation' lectures by Frank van den Bosch at Yale University. The figure is taken from Lecture 1 (see http://www.astro.yale.edu/vdbosch/astro610_lecture1.pdf for the slides).

transition period ($\Delta z \sim 80$), when the photon path becomes finite. This results in the photons random-walking out of the overdense regions (where photons are overabundant), damping the small-scale fluctuations. Note that the acoustic oscillations in the baryonic component are damped as well since these are driven by the radiation pressure during this epoch. This process is called Silk damping (Silk, 1968).

During a time t, a photon takes on average $N = ct/\lambda_{\rm mfp}$ steps, where $\lambda_{\rm mfp}$ is the mean free path. Kinetic theory can then be used to calculate the Silk scale, $\lambda_{\rm S}$, below which perturbations will be damped:

$$\lambda_{\rm S} = \left(\frac{N}{3}\right)^{\frac{1}{2}} \lambda_{\rm mfp} = \left(\frac{ct}{3\sigma_{\rm T} n_{\rm e}}\right)^{\frac{1}{2}}, \tag{1.12}$$

where $\sigma_{\rm T}$ is the Thomson cross section and $n_{\rm e}$ is the electron number density. Depending on the expansion rate of the Universe and the matter density, the Silk scale is associated with masses in the range 10^{12}–10^{14} $M_\odot$, i.e. perturbations on galaxy mass scales are erased by Silk damping (see Figure 1.2, upper panel, for the cosmic evolution of the Silk scale).

This would suggest that galaxy formation must proceed in a top-down manner with more massive structures forming first and then fragmenting. To allow sufficient time for this fragmentation process, the large-scale perturbations would need to have large amplitudes with anisotropies of the order of 1 part in 10^3 (e.g. Mo et al., 2010). However, anisotropies on this scale were already ruled out in the 1980s by CMB observations (Uson and Wilkinson, 1984).

All these issues disappear when considering the CDM component, which does not interact with electromagnetic radiation and is therefore not affected by Silk damping. Since dark matter is the dominant matter component, the baryons fall into the potential wells created by dark matter perturbations at the end of recombination, reversing the effects of Silk damping. Hence the Silk scale does not present an issue for galaxy formation in the ΛCDM model. This point is illustrated in the lower panel of Figure 1.2 which shows the evolution of a Milky-Way scale perturbation for both the baryonic and the dark matter component. However, Silk damping still has an impact on the CMB with photon diffusion damping making the CMB more uniform.

It should also be noted that some baryons will advect out of the potential wells created by the dark matter due to the supersonic relative velocities between baryons and CDM (Tseliakhovich and Hirata, 2010). These bulk relative motions stem from the standing acoustic waves and are supersonic due to the drop in sound speed after recombination. In regions with high relative velocities, this will suppress the condensation of gas into haloes at high redshifts, also affecting the formation of the first stars (Bromm, 2013).

1.2.5.2 Free streaming

CDM is collisionless and therefore does not generate acoustic waves, though an analogous Jeans wavelength may still be defined by replacing the sound speed with the velocity dispersion. Formally, this replacement can be made since the continuity and momentum equations for a collisionless fluid with isotropic and homogeneous velocity dispersion are exactly the same as for a collisional fluid, replacing the sound speed c_s by the velocity dispersion σ. This yields the dark matter analogue of the Jeans wavelength, $\lambda_{J,DM}$:

$$\lambda_{J,DM} = \sigma \sqrt{\frac{\pi}{G\bar{\rho}}}. \tag{1.13}$$

Intuitively, perturbations smaller than $\lambda_{J,DM}$ are washed out in a collisionless fluid since particles disperse in random directions. If the dispersion timescale is shorter than the Hubble time, the perturbations will be damped. This process is called free streaming.

Free streaming then sets the low-mass end for structure formation in a dark-matter dominated Universe. Note that if the random motions are relativistic, free-streaming damping will once again eliminate substructures on galaxy scales, e.g. for 'hot' dark matter in the form of neutrinos with masses $30m_{30}$ eV, all structures below a mass scale of $4 \times 10^{15} m_{30}^{-2}$ $M_\odot$ are damped by free streaming (Bond et al., 1980). A neutrino-dominated universe would therefore follow top-down structure formation. Numerical simulations have shown that the resulting clustering in a neutrino-dominated universe is inconsistent with the observed clustering scale of galaxies (White et al., 1983; Hut and White, 1984; White et al., 1984), ruling out this hot dark matter model.

CDM, on the other hand, is non-relativistic at the time of decoupling and therefore the impact of free streaming is negligible in this model. For estimating the proper free-streaming length and corresponding free-streaming mass, one needs to take into account both the production mechanism and the particle mass. Current particles considered for CDM result in free-streaming masses from 10^{-6} $M_\odot$ for canonical weakly interacting massive particles (WIMPs) (Green et al., 2004) to 10^{-15} $M_\odot$ for the QCD axion (Nambu and Sasaki, 1990), i.e. for CDM one would expect a plethora of substructures.

It should be noted that there are several alternative viable dark matter models, which also match the constraints set by large-scale structure behaving in a similar way to CDM, whilst deviating from CDM on dwarf galaxy scales. Dwarf galaxy observations then become strong discriminators for these models, and indeed, many of these models have been motivated by the apparent failure of CDM to match observed dwarf properties. The small-scale challenges and some of the alternative dark matter models are discussed in Sections 1.2.7.2 and 1.2.8, respectively.

1.2.6 Non-linear regime: the formation of haloes and galaxies

The final stage of structure formation, when density perturbations are of order unity or higher, occurs in the non-linear regime. The different perturbation modes couple to one another and the dark matter collapses into virialised haloes, decoupling from the Hubble expansion.

There is no longer an analytical solution in this regime, however, simplified models can give insights such as spherical collapse models (e.g. Gunn and Gott, 1972), but second order effects can also be included analytically such as elliptical collapse (e.g. Zel'dovich, 1970; Icke, 1973; White and Silk, 1979).

1.2.6.1 Abundances and density profiles of haloes

Following the spherical collapse model, dark matter haloes are a factor $\Delta_{\rm vir} \sim 18\pi^2 \sim 178$ denser than the background Universe after virialisation (e.g. Peebles, 1980), though see Bryan and Norman (1998) for a more rigorous time-dependent estimate of $\Delta_{\rm vir}$. The resulting values are generally around 200, so the virial quantities of a dark matter halo are derived assuming $\Delta_{\rm vir} = 200$ in the community. The virial radius $R_{\rm vir}$ can then be defined as the radius which encloses a mean density of 200 times higher than the critical density for a flat Universe, $\rho_{\rm crit}$, and the virial mass, $M_{\rm vir}$, as the halo mass enclosed within $R_{\rm vir}$.

Press and Schechter (1974) developed an analytical model to derive the halo mass function assuming an initially Gaussian random perturbation field. The key assumption in their derivation was that the probability for perturbations δ_M to exceed a critical density for collapse at time t would be the same as the mass fraction that is contained within halos with mass greater than M at time t. This yielded a halo mass function following a power-law at the low-mass end and exponentially suppressed at the high-mass end, with the transition mass growing with cosmic time. They also tested their analytical model with N-body simulations (though with a mere 1000 particles, the resolutions were too low to draw firm conclusions). Indeed N-body simulations would become a crucial tool for studying dark matter halo abundances and structures (see Section 1.3.1 for an overview of N-body schemes).

Early N-body simulations of the CDM universe were carried out by Davis et al. (1985) and Frenk et al. (1985) and found good agreement with the observed galaxy distribution under the assumption that galaxies only form at high peaks of the initial density field (and for a flat CDM universe). Further work revealed that CDM haloes in N-body simulations were in good agreement with the predictions from Press and Schechter (1974), following a power law with index close to -2 and a high-mass cut-off rapidly increasing with cosmic time (Frenk et al., 1988).

Though note that modern high-resolution N-body simulations, such as the Millennium Simulation (Springel et al., 2005b) and its successors Millennium-II (Boylan-Kolchin et al., 2009) and Millennium-XXL (Angulo et al., 2012), find a clear departure from the Press-Schechter mass function which underpredicts the high-mass end of the simulated mass function by up to an order of magnitude. This is partly related to the assumption of spherical collapse as halo mass functions derived using the ellipsoidal excursion set formalism are found to give a better fit (e.g. Sheth et al., 2001).

The increasing resolution of N-body simulations, due to increasing computational power and optimisations (see Section 1.3.1), also allowed for the investigation of halo density profiles. These simulations showed that haloes formed by (dissipationless) hierarchical clustering can be described by a universal density profile following a double power law, the NFW profile (Navarro et al., 1996b, 1997):

$$\rho_{\rm NFW}(r) = \frac{\rho_{\rm c}\delta_{\rm c}}{(r/r_{\rm s})(1+r/r_{\rm s})^2}, \tag{1.14}$$

where $\rho_{\rm c}$ is the critical density, $\delta_{\rm c}$ is the characteristic halo density and $r_{\rm s}$ is a scale radius.

Note that for $r \ll r_{\rm s}$, we obtain $\rho_{\rm NFW}(r) \propto r^{-1}$, i.e. a cuspy profile. It was found that there is a tight correlation between $M_{\rm vir}$ and $\delta_{\rm c}$ so that the NFW profile can be characterised by a single parameter, the concentration parameter $c = R_{\rm vir}/r_{\rm s}$, albeit with large scatter (e.g. Bullock et al., 2001; Eke et al., 2001; Neto et al., 2007; Macciò et al., 2008; Zhao et al., 2009).

High-resolution simulations of the CDM universe also started to be able to resolve substructure: within the radius of the dark matter halo there are distinct virialised clumps of dark matter, so-called subhaloes, which host satellite galaxies or cluster galaxies (e.g. Ghigna et al., 1998; Moore et al., 1999; Springel et al., 2008).

1.2.6.2 Galaxy formation

Since dark matter dominates over baryonic matter, the gas collapses within these haloes, being pulled inwards by the dark matter. This led White and Rees (1978) to propose a two-stage theory of galaxy formation, where the large-scale distribution of matter is determined by gravitational clustering and galaxy formation is determined by gas-dynamical dissipative processes.

The gas is shock-heated by the collapsing dark matter and then cools radiatively, condensing at the centre of the halo. As the emission of photons is isotropic, the gas conserves its angular momentum whilst cooling. The contraction of the gas sphere therefore leads to a

spin-up as well as flattening of the gas distribution. The increased surface density triggers star formation in the newly-formed gas disc and a proto-galaxy is formed.

Note that the initial angular momentum stems from tidal torques due to the asymmetry in the matter distribution (Hoyle, 1949; Fall and Efstathiou, 1980) and stored angular momentum from relative orbits prior to halo mergers (White et al., 1984; Porciani et al., 2002).

The dark and baryonic components then build up together by accreting and merging with other structures containing a mixture of dark and baryonic materials (Lacey and Cole, 1993).

However, subsequent work revealed that in the absence of any form of energy input, an unacceptably large fraction of baryons cool and condense in low-mass haloes at high redshifts so that some sort of feedback mechanism is needed (Larson, 1974; Cole, 1991; White and Frenk, 1991) to avoid a 'cooling catastrophe' (see Balogh et al., 2001, for a review). See Section 1.4 for an overview of feedback mechanisms in galaxy formation.

1.2.7 Comparison with observations

1.2.7.1 Large-scale structure

Comparisons with astronomical observations have been crucial for the development of the ΛCDM model. At large scales, this model has been extremely successful in matching observations, in particular with regards to the CMB (Planck Collaboration XIII, 2016) and the clustering of galaxies (Colless et al., 2001; Zehavi et al., 2002; Hawkins et al., 2003; Tegmark et al., 2004; Cole et al., 2005; Eisenstein et al., 2005). The Millennium simulation (Springel et al., 2005b) beautifully reproduced the structures observed by large-scale astronomical surveys. Since then box sizes and particle numbers in N-body simulations have been steadily increasing (see Figure 1.4), making ever more accurate predictions for large-scale structure which will be tested with the next-generation of galaxy surveys with LSST, *Euclid* and *RST*.

1.2.7.2 Small-scale challenges

Whilst the ΛCDM model is in excellent agreement with large-scale observations, there are a number of apparent discrepancies when comparing observations of dwarf galaxies with predictions of dark matter only simulations. For a recent review of the small-scale challenges to the ΛCDM paradigm see Bullock and Boylan-Kolchin (2017).

These apparent discrepancies concern, for example, a large disparity in the number of observed dwarf satellite galaxies with respect to the number of dark matter subhaloes that may be hosting these systems – the so-called missing satellites problem (e.g. Kauffmann et al., 1993; Klypin et al., 1999; Moore et al., 1999). This discrepancy is now attributed to the suppression of star formation in these low-mass systems, in particular by reionization (e.g.

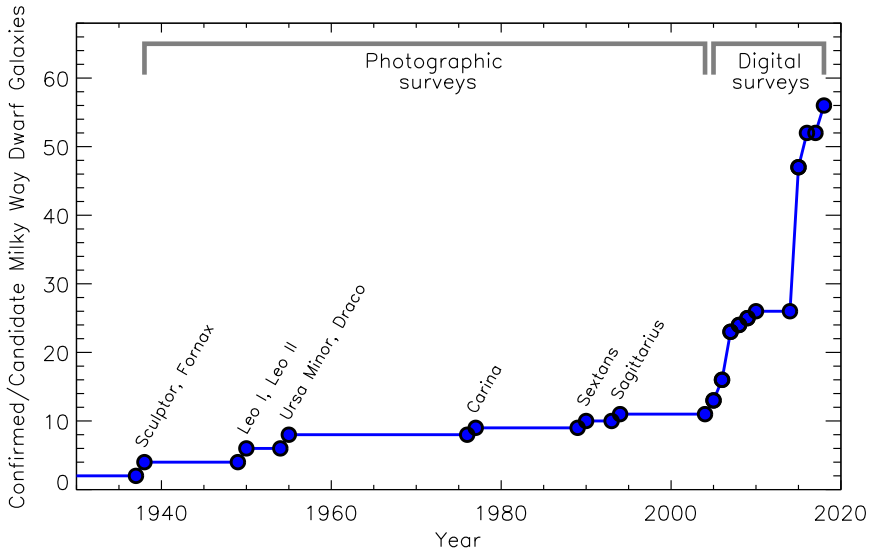

Fig. 1.3 Number of confirmed/candidate Milky Way satellite galaxies as a function of time. The objects shown here include all spectroscopically confirmed dwarf galaxies as well as those suspected to be dwarfs based on less conclusive spectroscopic and photometric measurements. This figure is reproduced from Simon (2019). © 2019 Annual Reviews. Reprinted with permission conveyed through Copyright Clearance Center, Inc.

Efstathiou, 1992, see Section 1.4.1), so that these so-called ultra-faint dwarfs are extremely difficult to detect. This is supported by the rapidly increasing number of confirmed/candidate Milky Way satellites which have been identified by the large-area digital surveys (see Figure 1.3). Currently there are about 60 known Milky Way satellites and future surveys could increase this to the hundreds (e.g. Tollerud et al., 2008; Newton et al., 2018).

There is also an apparent lack of observed massive satellites, the too-big-to-fail problem (Boylan-Kolchin et al., 2011), as the inferred central masses of the most massive observed satellites do not match the central masses of the most massive simulated subhaloes.

Another apparent discrepancy concerns the inferred dark matter halo profiles of observed dwarfs, which do not seem to agree with the cuspy dark matter profile predicted by the ΛCDM model – the cusp versus core problem (e.g. Flores and Primack, 1994; Moore, 1994).

Finally, the observed diversity of rotation curves of dwarf galaxies with the same maximum circular velocity (Oman et al., 2015) is seemingly in contradiction with the prediction by the ΛCDM model that structure formation should be a self-similar process (see Section 1.2.6.1).

All of the above small-scale discrepancies are usually explained with ‘baryonic physics’ (e.g. Sawala et al., 2016) and observational uncertainties. Indeed, powerful feedback processes may fundamentally affect the gravitational potential and dark matter distribution (see

e.g. Navarro et al., 1996a; Pontzen and Governato, 2014). Though some issues, such as the observed diversity of rotation curves, are difficult to account for completely (see e.g. Santos-Santos et al., 2020, for a recent systematic investigation).

1.2.8 Alternative dark matter models

The apparent discrepancies between the CDM predictions for dark matter substructure and dwarf galaxy observations has also prompted investigations into alternative dark matter models such as warm dark matter (WDM, Blumenthal et al., 1982). For simulations in the WDM universe, see e.g. Lovell et al. (2012). WDM is an intermediate model between hot dark matter and CDM, with a free-streaming cut-off at the dwarf galaxy scale. WDM therefore erases small-scale structure, solving the missing satellites problem. Furthermore, due to the absence of the smallest structures, haloes of a given mass will have later formation times and therefore also lower central densities which helps with the too-big-to-fail problem. Nevertheless, WDM cannot resolve the cusp versus core problem as the cores formed in this model are not large enough (e.g. Shao et al., 2013). A lower limit on the WDM particle mass can be inferred from Milky Way satellites as well as small-scale structure in the Lyman-α forest (see e.g. Polisensky and Ricotti, 2011; Lovell et al., 2014; Bose et al., 2016; Iršič et al., 2017; Brooks, 2019).

Others have suggested relaxing the collisionless assumption in the CDM model, proposing self-interacting dark matter (SIDM, Spergel and Steinhardt, 2000), which can reproduce the cores inferred from dwarf galaxy rotation curves (e.g. Vogelsberger et al., 2014a). SIDM particles scatter elastically with each other, producing cored density profiles and reducing the ellipticity of the halo (see Tulin and Yu, 2018, for a recent review on the impact of SIDM on small-scale structure). The predictions on ellipticity and density profiles can provide strong constraints on the scattering cross section, most notably from strong lensing measurements of galaxy clusters (e.g. see Meneghetti et al., 2001; Miralda-Escudé, 2002; Randall et al., 2008), which have suggested much lower cross sections than would be required for producing cores in dwarfs. This has led to a preference for SIDM models with a velocity-dependent cross section which decreases from the dwarf to the cluster scale (e.g. Vogelsberger et al., 2012b).

Finally, fuzzy dark matter (FDM, Hu et al., 2000; Peebles, 2000; Marsh and Silk, 2014) models offer another possible modification to the fiducial dark matter model. In the FDM model, dark matter is made up of extremely low-mass particles, such as ultralight axions, which have long de Broglie wavelengths ($\sim$ kpc scale) resulting in a 'fuzziness' in the particle positions and a corresponding zero-point momentum (see Niemeyer, 2020, for a recent review). This heats up the central region of the halo, inducing a cored profile, and suppresses small-scale structure in the dwarf regime (where the de Broglie wavelength is of

the same order as the virial radius). Similarly to WDM this also means that tight constraints can be obtained on the FDM mass from the Milky Way satellites and from the Lyman-α forest (e.g. Hui et al., 2017). For scales much larger than the de Broglie wavelength, FDM behaves similarly to CDM.

However, large uncertainties about the severity of the small-scale challenges remain, mainly due to uncertainties in baryonic physics (see Section 1.4) but observational uncertainties also remain. The accurate modelling of low-mass galaxies is therefore crucial to determine whether a departure from the CDM model is necessary.

This emphasises the need to model both the gravitational clustering with N-body techniques as well as the evolution of the baryonic component. In the next section, I present a range of numerical techniques that have been developed to model galaxy formation in a cosmological context.

1.3 Numerical simulations

As mentioned in Section 1.2.6, once perturbations leave the linear regime, analytical solutions only exist for special cases and therefore numerical methods are required to model structure formation. Furthermore, the numerical approach is particularly crucial when modelling galaxy formation as this requires solving the equations of hydrodynamics.

1.3.1 N-body schemes

Since CDM dominates the mass budget in the ΛCDM model, it is important to develop accurate methods for numerically modelling collisionless fluids. This can be achieved by discretising the fluid into N particles and calculating gravitational forces between these particles – an N-body problem. Note that in practice, this discretisation step also means that the gravitational forces will have to be 'softened' below a certain particle separation to avoid two-body interactions that are caused by the finite resolution of these simulations rather than being physical. This is usually achieved via the introduction of a softening length based on the mean particle separation (see e.g. Power et al., 2003, for a convergence study on choosing the optimal softening length value).

Various different methods have been developed for numerically solving N-body problems, balancing speed, resolution and accuracy. The simplest and most accurate technique is direct summation of the forces, the so-called particle-particle (PP) method. However, with this method, the computational cost grows as the square of the number of particle pairs so that the PP method becomes prohibitively expensive as the resolution is increased. Though recently,

significant speed-ups have been obtained by porting direct N-body codes to GPUs (e.g. Wang et al., 2015).

The particle-mesh (PM) method (e.g. Klypin and Shandarin, 1983) reduces computational cost by interpolating the density distribution of dark matter onto a regular grid with periodic boundary conditions. A Fast Fourier Transform can then be used to compute the gravitational forces via the Poisson equation. Though note that, with this method, the force resolution is limited by the size of the grid and this algorithm performs rather poorly at small scales.

The P^3M method (Efstathiou et al., 1985; Couchman, 1991) combines the advantages of the two aforementioned methods, computing the short-range forces with direct summation and the long-range forces using a grid. An alternative solution to circumventing the resolution issues of the PM method is to use a hierarchy of grids, with the finest grids placed in regions where the highest force resolution is required – the adaptive mesh refinement (AMR) method (Norman and Bryan, 1999). The Poisson equation can then be solved using iterative multigrid methods.

Finally, there are also so-called Tree methods (Barnes and Hut, 1986) for evaluating the gravitational forces. These introduce a hierarchy of cells such that each cell containing more than one particle is subdivided into smaller cells until each cell contains at most one particle. At large distances, this Tree structure can then be used to calculate the gravitational forces based on a multipole expansion, grouping particles at similar distances together. At short distances the PP method is used to evaluate the gravitational forces. The Tree method then allows for the resolution of the gravitational forces down to the softening length. This method is also often combined with the PM approach (the TreePM method), which allows simulators to increase the dynamic range with the PM method whilst maintaining high accuracy at small scales with the tree method.

For simulations that are focused on obtaining statistical measures of large-scale structure rather than accurate trajectories of individual particles, the PMPM method, nesting two PM grids, can deliver significant performance boosts due to memory consumption reduction. Cheng et al. (2020) took advantage of this to run a simulation with ~ 4.4 trillion particles to $z = 0$, the largest completed cosmological N-body simulation to date. Projections of the simulation output are shown in Figure 1.1.

Potter et al. (2017) have demonstrated the feasibility of even more extreme particle counts with their 8 trillion particle benchmark runs. Their code takes advantage of the fast multipole method (Greengard and Rokhlin, 1987), which achieves a linear scaling with particle number for Tree codes, combined with GPU acceleration.

Figure 1.4 shows the number of particles used in N-body simulations as a function of year of publication. For reference, the increase expected due to Moore's law is also

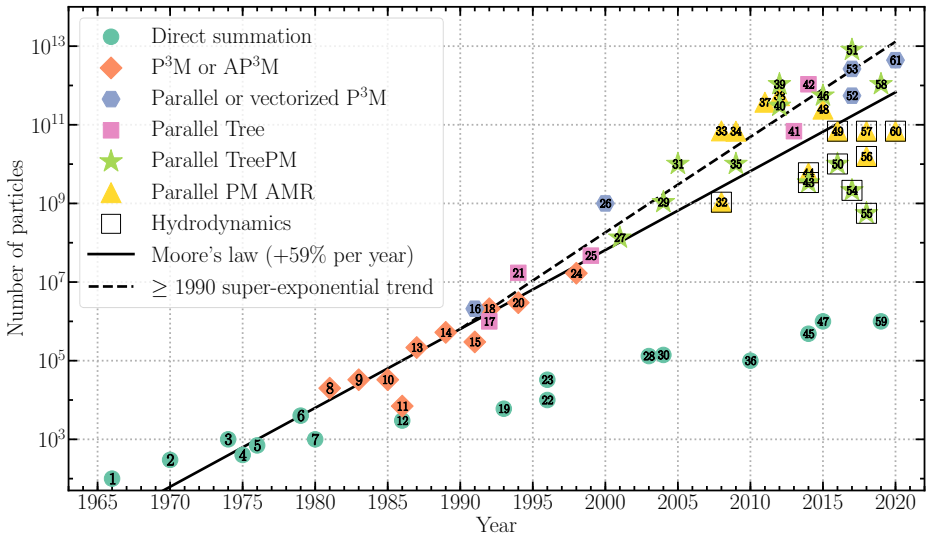

Fig. 1.4 Evolution of the number of particles used in N-body simulations as a function of year of publication including the Millennium simulation (reference number 31, Springel et al., 2005b), the eight trillion particle benchmark run (reference number 51) by Potter et al. (2017) and the Cosmo-π simulation (reference number 61) by Cheng et al. (2020), which is also shown in Figure 1.1. The symbols and colours indicate the technique used for the gravity calculations: particle-particle-particle-mesh (P^3M) and adaptive P^3M (AP^3M); parallel or vectorized P^3M; Tree; TreePM; and particle-mesh with adaptive mesh refinement (PM AMR). Hydrodynamical simulations are represented in a black square. This figure is reproduced from a blog post[5] by Florent Leclercq which also provides a full list of the reference numbers.

shown. As direct summation methods scale with the square of the particle number these simulations lie below Moore's law. On the other hand, for (gravity-only) simulations based on variants and/or hybrids of the PM method and/or Tree method, a super-exponential trend can be inferred since the 1990s, reflecting the continuous optimisation of the algorithms. Novel codes designed for heterogeneous accelerated architectures will play a crucial role in continuing this trend.

1.3.2 Connecting haloes with galaxies

To compare the predictions from N-body simulations with astronomical observations, it is crucial to also model the baryonic component and in particular the formation of galaxies.

There are several different approaches to connecting dark matter haloes with galaxies (see Wechsler and Tinker, 2018, for a recent review), both for simulated and observed galaxy

[5] See https://florent-leclercq.eu/blog.php?page=2 for the blog post and https://github.com/florent-leclercq/Moore_law_cosmosims for the companion Github repository.

data. I provide just a brief summary below before focusing on the main tool used in this thesis: hydrodynamical simulations.

Most straightforwardly, observed galaxy distributions can be linked to dark matter haloes via the abundance matching technique, where galaxies are assigned to haloes in order of mass (Frenk et al., 1988; Colín et al., 1999; Kravtsov and Klypin, 1999). This scheme was further refined with the development of the subhalo abundance matching (SHAM), as higher-resolution N-body simulations could also resolve the substructure within the dark matter haloes (e.g. Tasitsiomi et al., 2004; Conroy et al., 2006; Springel et al., 2008; Behroozi et al., 2010; Moster et al., 2010).

Alternatively, halo occupation distribution (HOD) modelling may be used to link dark matter haloes with simulated galaxies. With the HOD approach, one calculates the probability for a halo to host a number of galaxies with a certain set of properties, such as luminosity or stellar mass (e.g. Benson et al., 2000; Berlind and Weinberg, 2002; Bullock et al., 2002). Usually the bias of a population is defined as a conditional probability for a given halo mass in HOD models.

A similar approach is used for the conditional luminosity function (CLF) modelling, which gives the number of galaxies within a given luminosity range that reside within a halo of a given mass (e.g. Yang et al., 2003; van den Bosch et al., 2007).

Semi-analytical models (SAMs) have also played an important role in inferring galaxy properties from N-body simulations. These models trace galaxy formation history through halo merger trees[6] and approximate the relevant astrophysical processes with various parametrized models (e.g. White and Frenk, 1991; Kauffmann et al., 1993; Somerville and Primack, 1999; Cole et al., 2000; Bower et al., 2006; Croton, 2006; Guo et al., 2013). This allows SAMs to cover a huge parameter space relatively cheaply. MCMC techniques (Henriques et al., 2009; Lu et al., 2011) or Bayesian emulator approaches (Bower et al., 2010) can then be used to explore parameter degeneracies and assess goodness of fit for various models.

Finally, the baryonic component can also be modelled directly with the aid of hydrodynamical simulations. This is described in more detail in the following Section 1.3.3. Also see Somerville and Davé (2015) for a review of both SAMs and hydrodynamical simulations for modelling galaxy formation in a cosmological context.

[6]Usually, the merger trees are extracted from N-body simulations, but they can also be constructed analytically (e.g. Lacey and Cole, 1993).

1.3.3 Hydrodynamical simulations

Traditionally, there have been two main approaches for discretising the gas to solve the equations of hydrodynamics: particle-based methods and grid-based methods.

The most common particle-based method is the Smoothed Particle Hydrodynamics (SPH) scheme (Gingold and Monaghan, 1977; Lucy, 1977), where the density at any given point is calculated as a sum of the surrounding (smoothed) particles weighted by the particle mass and the smoothing kernel function. This kernel function is taken to be zero outside the smoothing length, which is usually defined as the radius of a sphere containing a certain number of neighbours. One of the disadvantages of this method is that the development of fluid instabilities can be numerically suppressed (Agertz et al., 2007), which also inhibits entropy generation due to less efficient mixing (Mitchell et al., 2009). On the plus side, the Lagrangian nature of this method means that the resolution naturally follows the density of the fluid flow. However, there have been various improvements in the modern SPH methods such as corrected/optimised SPH codes (e.g. Read et al., 2010), density-independent (pressure-based) SPH (Saitoh and Makino, 2013) and generalised volume elements (Hopkins, 2013). Well-known codes that have implemented the SPH method and are used for galaxy formation simulations include GADGET (Springel et al., 2001b) and GASOLINE (Wadsley et al., 2004). ANARCHY is an updated pressure-based version of GADGET and was used for the EAGLE project (see appendix A of Schaye et al., 2015). Furthermore, the SWIFT code has implemented several SPH schemes (including 'traditional' SPH and pressure-based SPH) as well as a meshless finite-mass (MFM) scheme similar to the GIZMO code by Hopkins (2015).

The equations of hydrodynamics can also be solved with an AMR method, which improves on the treatment of discontinuities and, in particular, shocks. However, one needs to be careful that the root grid resolution is high enough, or otherwise the formation of low-mass haloes may be suppressed (O'Shea et al., 2005; Heitmann et al., 2008). Furthermore, if a Cartesian grid is used, preferred directions are introduced with the AMR method. Again several codes have implemented the AMR method for astrophysical applications, including RAMSES (Teyssier, 2002) and ENZO (O'Shea et al., 2004).

There are also hydro solvers based on hybrid schemes which combine the advantages of the above methods, such as the MFM and meshless finite-volume (MFV) methods, which are implemented in the GIZMO code (Hopkins, 2015). Another class of hydro solvers are the moving mesh codes, such as the AREPO code (Springel, 2010) which is used for all of the simulations presented in this thesis. AREPO models the gas with an unstructured mesh determined by the Voronoi tessellation and moving with the local flow velocity (with minor corrections to avoid the distortion of gas cells). Due to the quasi-Lagrangian nature of the code, AREPO retains Galilean invariance, which is not strictly conserved in the grid-

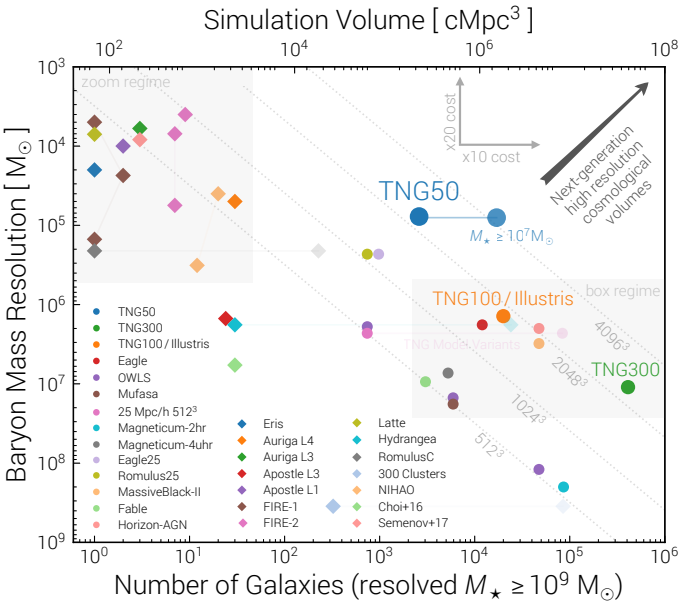

Fig. 1.5 Comparison of recent cosmological hydrodynamical simulations showing baryon mass resolution against number of resolved galaxies, both for cosmological box simulations (circles) and for zoom-in simulation suites (diamonds). The next-generation cosmological box simulations will push towards the upper right corner of this parameter space. This figure is reproduced from Nelson et al. (2019).

based codes, and naturally follows the fluid flow, with the resolution adapting to the local density. At the same time, the mesh structure allows for better resolution of shocks, contact discontinuities and fluid instabilities (Bauer and Springel, 2012; Kereš et al., 2012; Sijacki et al., 2012; Torrey et al., 2012; Vogelsberger et al., 2012a).

It should also be noted that whilst Newtonian gravity offers a good approximation for structure formation in the matter-dominated Universe, this assumption may start to break down as additional astrophysical processes are included and the resolution is increased. In particular for the subparsec modelling of SMBHs in galaxy formation simulations, post-Newtonian corrections are required and these have recently been implemented into astrophysical codes such as GADGET (Rantala et al., 2017), taking advantage of algorithmic chain regularization.

It was known early on that different code implementations could lead to significantly different results for astrophysical applications. In particular, the hydro solvers used to yield different results whilst there was good agreement for dark matter properties (Frenk et al., 1999). This situation has significantly improved now and the main uncertainties lie within the unresolved subgrid physics (e.g. Scannapieco et al., 2012).

1.3.4 Subgrid physics

In the ideal scenario, galaxy formation would be treated as an ab initio problem, specified by the initial conditions and relevant physical processes and laws. However, this is currently impossible to achieve due to two main issues: limited dynamic range and uncertainties in the physics governing important astrophysical processes, such as star formation or black hole formation and evolution.

1.3.4.1 The issue of limited dynamic range

With the current computational capabilities we cannot achieve sufficient dynamic range to model both the cosmological environment and small-scale processes; for a statistical sample of galaxies, we require a simulation scale of ~ 100 Mpc due to cosmic variance stemming from the Cosmological Principle (see Section 1.2.2) whilst the Schwarzschild radius of a SMBH with mass 10^6 $M_\odot$ is $\sim 10^{-7}$ pc, i.e. in principle a dynamic range spanning 15 orders of magnitude would be needed. This means that one has to include these processes via so-called subgrid prescriptions which are used to include the effects of important astrophysical processes below the resolution scale.

However, modelling these processes is highly non-trivial and crucially depends on the available resolution, with more physically motivated models becoming feasible as smaller spatial and temporal scales are resolved (see Section 1.4). There is further uncertainty on which unresolved phenomena (such as turbulence or cosmic rays) may need to additionally be included in the modelling to obtain realistic galaxies.

Isolated simulations of individual galaxies are therefore important testbeds for developing and testing novel subgrid models at high resolutions. However, since these simulations do not include the cosmological environment or any evolutionary aspects due to cosmological mergers, they cannot assess whether feedback mechanisms may be able to disrupt cosmic inflows and regulate star formation in a maintenance-mode fashion.

Cosmological zoom-in simulations can get around these issues by achieving both high-resolution and including the cosmic environment. This is achieved by selecting a region of interest from a large-volume N-body simulation and resimulating this region at higher resolution, whilst the remaining simulation volume stays at the coarse resolution (see Katz and White, 1993, for one of the first papers exploring this technique). Zoom-in simulations can be particularly useful for studying rare objects, such as galaxy clusters, since large boxes would be required to include these, and several simulation projects, such as C-EAGLE (Bahé et al., 2017; Barnes et al., 2017), FABLE (Henden et al., 2018), and ROMULUSC (Tremmel et al., 2019), take advantage of the zoom-in technique to model the evolution of clusters.

On the other hand, zoom-in simulations can study low-mass to intermediate-mass galaxies at increasingly high resolution. In particular, the Eris (Guedes et al., 2011) and Auriga (Grand et al., 2017) projects both used zoom-in simulations to investigate Milky-Way type galaxies, whilst the APOSTLE simulations (Sawala et al., 2016) simulated a dozen Local Group regions using zoom-in techniques, providing a useful laboratory for studying the small-scale challenges discussed in Section 1.2.7.2. Furthermore, the FIRE-1 (Hopkins et al., 2014) and FIRE-2 (Hopkins et al., 2018a) projects have used zoom-ins to study galaxy formation across a variety of stellar masses.

However, whilst zoom-in simulations allow for the detailed investigation of astrophysical processes in a cosmological context, they lack the statistical power of large-volume cosmological box simulations. This dichotomy can be seen in Figure 1.5, which shows the distribution of recent hydrodynamical simulations of galaxy formation in the number of galaxies – mass resolution space. Zoom-simulations occupy the upper left-hand corner of this plot with high resolutions but low numbers of galaxies simulated, whilst current large-volume cosmological simulations, such as EAGLE (Schaye et al., 2015), Horizon-AGN (Dubois et al., 2014a) or Illustris (Vogelsberger et al., 2014b), are found in the lower right-hand corner, with a large number of galaxies at the cost of low resolution. The aim of the next-generation cosmological boxes is to push towards the upper right-hand corner of the plot combining high resolution with large simulation volumes. High-resolution cosmological boxes such as TNG50 (Nelson et al., 2019; Pillepich et al., 2019) are starting to push towards this regime (see also NewHorizon, Dubois et al., 2020). Note that with dwarf galaxy zoom-in simulations the resolution can be pushed even further than shown in this diagram to $\sim$ tens $M_{\odot}$, resolving the multiphase ISM and SN remnants (Smith et al., 2019; Wheeler et al., 2019; Agertz et al., 2020; Gutcke et al., 2021).

1.3.4.2 Including additional physics

To obtain realistic galaxies, one must go beyond gravity and simple hydrodynamics. Radiative processes play an important role in astrophysics and are crucial for accurately modelling the thermal evolution of the gas. In hydrodynamical simulations, radiative cooling is usually included based on tabulated cooling rates for the primordial gas (Katz et al., 1996) and metal-line emission assuming collisional ionization equilibrium (Sutherland and Dopita, 1993). The effect of the metagalactic UV background (e.g. Faucher-Giguère et al., 2009; Haardt and Madau, 2012; Puchwein et al., 2019; Faucher-Giguère, 2020) on radiative cooling can similarly be included via interpolation from a cooling table (e.g. Wiersma et al., 2009a). Note that to obtain the correct cooling rates, the chemical enrichment from stellar evolution needs to be included as well (Wiersma et al., 2009b). It is also worth emphasising that

there are more advanced cooling curves which include non-equilibrium as well as molecular cooling (e.g. Smith et al., 2017), however running with these cooling modules is rather expensive and therefore these are not (yet) commonly adopted.

If the gas is allowed to cool, it will condense and reach the necessary densities to form stars. Gravitational instabilities drive the formation of giant molecular clouds (GMCs), which are the primary reservoirs of cold star-forming gas (see Dobbs et al., 2014, for a review). Star formation in simulations is therefore usually implemented based on a Schmidt law (Schmidt, 1959) with a simple density threshold and fixed efficiency per free-fall time, but more complex recipes exist based on virialised regions and convergence flows (e.g. Hopkins et al., 2014; Kimm et al., 2016; Hopkins et al., 2018a; Smith et al., 2020).

To avoid excessive star formation, feedback physics then also needs to be included in the simulations. Usually it is assumed that stellar feedback (in particular SN feedback from massive stars) and black hole feedback are the most important processes for star formation suppression. These feedback processes and their implementation into simulations are discussed in more detail in the following Section 1.4.

Next-generation simulations will also need to determine which other physical processes may need to be included in the subgrid prescriptions to work towards a comprehensive model of galaxy formation. Some significant progress has already been made in this direction, in particular with regards to the inclusion of radiation from stars and active galactic nuclei (AGN) (e.g. Choi et al., 2012; Kannan et al., 2014a; Rosdahl and Teyssier, 2015; Bieri et al., 2017; Costa et al., 2018b; Rosdahl et al., 2018; Kannan et al., 2020) and the modelling of important nonthermal components of the ISM, such as magnetic fields and cosmic rays (Uhlig et al., 2012; Booth et al., 2013; Hanasz et al., 2013; Salem and Bryan, 2014; Pakmor et al., 2016; Farber et al., 2018; Holguin et al., 2019; Dashyan and Dubois, 2020; Hopkins et al., 2021). See Naab and Ostriker (2017) for a review of the remaining challenges in galaxy formation.

1.4 The role of feedback

Feedback processes play a crucial role in galaxy formation, regulating star formation both in the low-mass and in the high-mass regimes (White and Frenk, 1991; Kauffmann et al., 1993). This can most easily be seen by comparing the average conversion efficiency from baryons into stars across different halo masses (see Figure 1.6): whilst Milky-Way type galaxies with halo masses of $\sim 10^{12}$ $M_\odot$ are very efficient at forming stars, this efficiency declines towards higher masses and falls even more rapidly towards the low-mass end. In the common theoretical model, the low-mass end is thought to be suppressed by stellar feedback

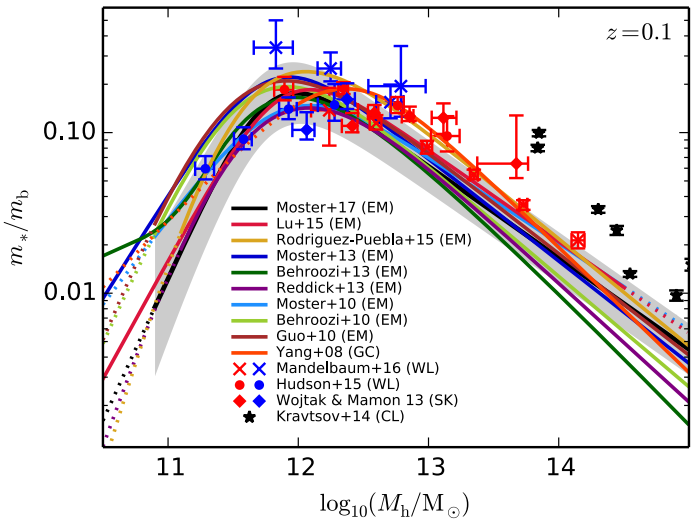

Fig. 1.6 Comparison of the average conversion efficiency of baryon mass (m_b) into stellar mass (m_*) as a function of halo mass M_h including data from empirical models (EM), a galaxy group catalogue (GC), X-ray observations of clusters (CL), and results for active and passive galaxies (blue and red symbols) from weak lensing (WL) and satellite kinematics (SK) with the respective references indicated by the figure legend. The shaded region corresponds to the 1σ credibility level by Moster et al. (2018). This figure is reproduced from Moster et al. (2018).

whilst the high-mass is hypothesised to be regulated by black hole feedback. In this section, I will summarise how these feedback processes have been incorporated into cosmological simulations – and how the fiducial models have been challenged by recent observations of active black holes in dwarf galaxies.

1.4.1 Star formation regulation in low-mass galaxies

At the low-mass end, environmental processes play a crucial role in the suppression of star formation. Ram pressure stripping, tidal forces, and mergers can all contribute to removing or heating the gas in dwarf galaxies (e.g. Peng et al., 2010; Smith et al., 2012; Wetzel et al., 2013). This is also supported by the observational finding that dwarfs in medium- and high-density environments have ceased star formation (Geha et al., 2012). Furthermore, large numbers of dwarfs are quenched by photoheating from the metagalactic UV background (e.g. Efstathiou, 1992; Okamoto et al., 2008; Fitts et al., 2016; Katz et al., 2020) below a characteristic halo mass of $M_c \sim 10^{10}$ $M_\odot$ at $z = 0$.

For field dwarfs above this threshold, internal processes are important for regulating star formation. Traditionally this 'self-quenching' at the low-mass end has been assumed to stem from stellar feedback with SNe considered to be a particularly promising process

energetically (see Larson, 1974; McKee and Ostriker, 1977; White and Rees, 1978; Dekel and Silk, 1986, for some of the first papers on this topic).

However, implementing this process into hydrodynamical simulations turned out to be rather difficult due to the overcooling problem, with the thermal energy released by the SNe promptly being radiated away. This is not necessarily physical as cooling rates may not be reliable at low resolutions. Furthermore, the cold dense phase of the interstellar medium (ISM) could not be resolved in cosmological simulations so that the gravitational instabilities governing star formation could not be modelled explicitly. To overcome these issues, Springel and Hernquist (2003) developed a subgrid prescription which is activated once the Jeans mass falls below the particle mass (translating into a density threshold of approximately 0.1 cm^{-3} for typical resolutions employed at the time). Below this value, an effective polytropic equation of state is used which represents both the hot phase due to SN feedback and the cold phase (also see Agertz et al., 2011; Dalla Vecchia and Schaye, 2012). However, it was found that the thermal SN heating incorporated into the model was not sufficient to avoid the overcooling problem (Springel and Hernquist, 2003), necessitating the introduction of an additional model for galactic winds and outflows. Others suggested delayed cooling (e.g. Stinson et al., 2006) or probabilistic heating schemes (e.g. Dalla Vecchia and Schaye, 2012) to tackle the overcooling problem. Note that the parameters driving SN feedback in these models are still very uncertain and must therefore be calibrated to observables such as the abundance of low-mass galaxies (e.g. Vogelsberger et al., 2013; Schaye et al., 2015; Pillepich et al., 2018), necessarily limiting the predictive power of simulations in terms of the strength of the stellar feedback[7].

Large-volume cosmological simulations have not yet reached the required resolution to resolve the multi-phase ISM and model star formation and stellar feedback more explicitly. However, in cosmological zoom-in simulations (e.g. Hopkins et al., 2018b; Smith et al., 2019; Wheeler et al., 2019; Agertz et al., 2020; Dubois et al., 2020) and in small uniform cosmological volumes (e.g. Rosdahl et al., 2018), resolutions are now high enough to allow for a more faithful treatment of star formation and stellar feedback, including cooling to low temperatures and resolving individual SN events. Many of these simulations now also include additional stellar feedback channels such as photoionization or stellar winds. Though even with these more explicit models, and in many cases with extra feedback channels included, it is found that either high star formation efficiencies (Hopkins et al., 2018b; Smith et al., 2018; Wheeler et al., 2019; Agertz et al., 2020), higher SN rates (Rosdahl et al., 2018) or higher SN energetics (Dubois et al., 2020) are required to match observed stellar properties.

[7]Though note that even within the freedom provided by these models, massive galaxies cannot be brought into agreement with observations only by the means of stellar feedback (e.g. Crain et al., 2009; Kannan et al., 2014b; Beckmann et al., 2017).

This could point to a need to further improve the ISM model and indeed several groups are working on this by explicitly sampling from the IMF to better reproduce the effects of clustering and also by further improving the feedback prescriptions, in particular with regards to radiation, chemistry and dust physics (e.g. Hu et al., 2017; Emerick et al., 2018, 2019; Hu, 2019; Emerick et al., 2020; Kannan et al., 2020; Smith et al., 2020; Gutcke et al., 2021; Smith, 2021). On the other hand, the failure to regulate star formation in dwarfs with stellar feedback alone in a cosmological setting may suggest that a completely new process would need to be included in dwarf simulations.

1.4.2 Black hole feedback in massive galaxies

In parallel to the development of stellar feedback processes for low-mass galaxies, black hole feedback from AGN has established itself as a successful mechanism for the suppression of cooling and star formation in massive galaxies. This was originally motivated by the discovery of the ubiquity of black holes in massive galaxies and the scaling relations: since the late 1990s, there has been strong dynamical evidence that most massive galaxies host a SMBH, with masses $\sim 10^6$–10^9 $M_\odot$, (Kormendy and Richstone, 1995; Magorrian et al., 1998). These dynamical samples also exhibit tight scaling relations between SMBH masses and the stellar properties of the host galaxy, both with respect to the central velocity dispersion (e.g. Ferrarese and Merritt, 2000; Gebhardt et al., 2000; Tremaine et al., 2002; Gültekin et al., 2009) and the spheroidal mass (e.g. McLure and Dunlop, 2002; Marconi and Hunt, 2003; Häring and Rix, 2004; Kormendy and Ho, 2013).

This discovery spurred on a variety of theoretical activities investigating the role of quasars and other AGN. Several theoretical models, based on SAMs and/or post-processing of hydrodynamical simulations to include AGN, demonstrated that the scaling relations could be explained by a *co-evolution* of black holes and their hosts (Haehnelt and Kauffmann, 2000; Kauffmann and Haehnelt, 2000; Di Matteo et al., 2003; Volonteri et al., 2003; Wyithe and Loeb, 2003; Di Matteo et al., 2004). In particular, it was shown that quasars could impact their hosts by producing high-velocity winds (e.g. Silk and Rees, 1998; King, 2003) and that AGN jets could prevent the cooling catastrophe in massive elliptical galaxies (Binney and Tabor, 1995). It should be noted that even in the early 2000s only two examples of AGN in dwarf galaxies were known, Pox 52 (Kunth et al., 1987) and NGC 4395 (Filippenko and Sargent, 1989), so not much thought was given to modelling these phenomena in low-mass galaxies at this point. To investigate the black hole – galaxy connection self-consistently in hydrodynamical simulations, Di Matteo et al. (2005) and Springel et al. (2005a) developed a subgrid model for AGN growth and feedback, which founded the basis for subsequent implementations of AGN physics in cosmological simulations.

In this model, the accretion rate is estimated using the Bondi-Hoyle-Lyttleton model (Hoyle and Lyttleton, 1939; Bondi and Hoyle, 1944; Bondi, 1952), which is based on steady, spherically symmetric accretion with the gas being at rest at infinity. The black hole accretion rate is then given by (Bondi, 1952):

$$\dot{M}_{\rm Bondi} = \frac{4\pi {\rm G}^2 M_{\rm BH}^2 \rho_\infty}{(c_\infty^2 + v_{\rm rel}^2)^{3/2}}, \tag{1.15}$$

where $M_{\rm BH}$ is the black hole mass, ρ_∞ is the density at infinity, c_∞ is the sound speed at infinity and $v_{\rm rel}$ is the relative velocity between the black hole and the gas at infinity. In practice, the relevant quantities are usually estimated as a weighted average of gas resolution elements in the vicinity of the black hole. Also note that often the $v_{\rm rel}$ is neglected, in particular when repositioning schemes are used which force black holes to stay at the potential minimum of the halo (e.g. Sijacki et al., 2015; Pillepich et al., 2018).

The Bondi formula is technically only valid for spherically symmetric accretion at the Bondi radius, $r_{\rm Bondi} = \frac{GM_{\rm BH}}{c_\infty^2 + v_{\rm rel}^2}$. This resolution is typically not achieved by cosmological simulations and therefore a boost parameter α is included which accounts for the unresolved multiphase nature of the ISM, typically $\alpha \sim 100$ (also see Booth and Schaye, 2009; Johansson et al., 2009; Sijacki et al., 2011). However, note that Schaye et al. (2015) abandoned the boost factor in favour of scaling the Bondi rate by the ratio of the Bondi time (sound crossing time at the Bondi radius) and viscous timescale (Rosas-Guevara et al., 2015).

It is further assumed that the accretion rate is limited by the Eddington rate, $\dot{M}_{\rm Edd}$, the maximum luminosity for spherically symmetric accretion. For the accretion of fully ionized hydrogen this limit is given by:

$$\dot{M}_{\rm Edd} = \frac{4\pi {\rm G} M_{\rm BH} {\rm m_p}}{\varepsilon_{\rm r} \sigma_{\rm T} {\rm c}}, \tag{1.16}$$

where $\rm m_p$ is the proton mass and $\varepsilon_{\rm r}$ is the radiative efficiency.

The black hole luminosity can also be obtained from the radiative efficiency, which is set by the binding energy at the innermost stable radius. The radiative efficiency can vary significantly depending on the black hole spin and accretion flow physics. In Di Matteo et al. (2005) and Springel et al. (2005a), the radiative efficiency is taken to have a constant value of $\varepsilon_{\rm r} = 0.1$, representing an average radiative efficiency for a Schwarzschild black hole with a radiatively efficient accretion flow.

It is then further assumed that a fixed fraction $\varepsilon_{\rm f}$ of the luminosity can couple thermally and isotropically as AGN feedback to the gas. This value is taken to be $\varepsilon_{\rm f} \sim 0.05$, which leads to good agreement with the observed scaling relation (Di Matteo et al., 2005, 2008). Sijacki et al. (2007) extended this model to include 'radio mode' feedback which would be

expected to occur once the accretion flow becomes radiatively inefficient at low accretion rates, with the thermal, isotropic 'quasar mode' only activated at high accretion rates. This implementation was also used in the Illustris simulation (Sijacki et al., 2015) and similar two-channel models have been used for other simulation projects, such as Horizon-AGN (Dubois et al., 2014a) or IllustrisTNG (Pillepich et al., 2018). Yet other simulation projects such as OWLS (Schaye et al., 2010) or EAGLE (Schaye et al., 2015) have concentrated on modifying the quasar mode itself by introducing a duty cycle, which significantly enhances the effectiveness of the quasar mode. Later simulation projects, such as FABLE (Henden et al., 2018), combined both approaches and found that a quasar duty cycle together with strong radio mode feedback was needed to reproduce both the high-mass end of the galaxy stellar mass function (GSMF) and the gas mass fractions of massive haloes. Furthermore, two-channel feedback models were also included into SAMs and used to investigate the impact of AGN feedback on massive galaxies (e.g. Bower et al., 2006; Croton, 2006; Somerville et al., 2008; Fanidakis et al., 2011).

These theoretical efforts demonstrated that AGN feedback can suppress the high-mass end of the GSMF, in agreement with observations (Puchwein and Springel, 2012; Dubois et al., 2014a; Vogelsberger et al., 2014b; Khandai et al., 2015; Schaye et al., 2015; Henden et al., 2018; Pillepich et al., 2018). However, the implementation of the AGN feedback precluded investigating AGN in dwarfs in physically interesting regimes due to two main factors.

Firstly, the Bondi rate (see equation 1.15) is proportional to the square of the black hole mass so that the accretion onto low-mass black holes is suppressed. In particular, since cosmological simulations typically employ massive seeds with $M_{\mathrm{BH,seed}} \sim 10^5$–$10^6$ $\mathrm{M}_\odot$, the slow growth phase will correspond to the dwarf regime by construction. However, the Bondi model is overly simplistic and based on several assumptions on the gas conditions that likely do not apply in the AGN setting, e.g. spherical symmetry and negligible angular momentum. Other implementations which take the angular momentum of the gas into account, such as the torque-driven black hole growth model (Anglés-Alcázar et al., 2015, 2017a) or modified Bondi models (e.g. Curtis and Sijacki, 2016), find significantly different rates from the fiducial Bondi model.

Secondly, the strong SN feedback that is employed by cosmological simulations to regulate the low-mass end (see Section 1.4.1) evacuates the gas from the central region of dwarf galaxies, suppressing the black hole growth by construction (see e.g. Dubois et al., 2015; Anglés-Alcázar et al., 2017b; Habouzit et al., 2017; Trebitsch et al., 2018).

1.4.3 Black hole feedback in dwarf galaxies?

Recently, it has been suggested by Silk (2017) that dwarf galaxy abundances and other small-scale challenges (see Section 1.2.7.2) may be explained by including AGN feedback in dwarf galaxy models. Dashyan et al. (2018) explore this using an analytical model and find that AGN feedback could be an alternative and more successful source of negative feedback than SNe in dwarf galaxies.

This demonstrates that AGN feedback in dwarfs could be an energetically viable mechanism. Furthermore, recent observations of AGN in dwarf galaxies have revolutionised our picture of low-mass galaxy formation, with growing observational evidence for AGN, and even AGN feedback, in dwarf galaxies.

Some of the first systematic searches for AGN in dwarf galaxies were carried out by searching SDSS dwarf galaxies for optical AGN signatures (see e.g. Greene and Ho, 2004, 2007; Reines et al., 2013; Chilingarian et al., 2018). These studies use the BPT (Baldwin et al., 1981) diagram to confirm the AGN nature of these sources and broad optical emission lines to estimate the black hole mass, where available, measuring black hole masses down to $M_{\rm BH} \sim 3 \times 10^4$ M$_\odot$. Note that Cann et al. (2019) find that standard optical spectral classification schemes used to identify higher mass black holes do not apply when the black hole mass falls below $M_{\rm BH} \sim 10^4$ M$_\odot$, so BPT diagnostics may become less useful for exploring AGN activity in the low-mass regime. Moreover, low-mass AGN can easily be outshone by star formation in the optical band. Therefore, only bright AGN are recovered resulting in low occupation fractions, e.g. Reines et al. (2013) obtain an AGN occupation fraction of ~ 0.5 per cent for their optically-selected sample of AGN in dwarf galaxies.

These two issues underline the importance of multi-wavelength studies. For example, X-ray observations have the advantage that they are less biased towards type 1 AGN (especially at higher redshifts) and that they suffer less from contamination from star formation. Follow-up X-ray observations can then be used to confirm optically-selected AGN (Baldassare et al., 2015, 2017; Chilingarian et al., 2018). Furthermore, wide-field X-ray surveys have identified large samples of AGN in dwarf galaxies via their X-ray emission (e.g. Schramm and Silverman, 2013; Lemons et al., 2015; Miller et al., 2015; Mezcua et al., 2016; Pardo et al., 2016; Aird et al., 2018; Mezcua et al., 2018; Birchall et al., 2020). These X-ray surveys also include AGN in dwarf galaxies that would have been missed by the BPT diagnostics due to the optical AGN contribution being less than that from galaxy emission (see e.g. Birchall et al., 2020), resulting in higher AGN occupation fractions than for the optically-selected samples. For example, Pardo et al. (2016) find an overall AGN occupation fraction of 0.6–3 per cent, whilst the occupation for high X-ray luminosities ($\log(L_{\rm X}\ [{\rm erg\,s^{-1}}]) \geq 41.5$) is estimated to be ~ 0.2–0.4 per cent (Aird et al., 2018; Mezcua et al., 2018; Birchall et al.,

2020), more akin to the optically-selected samples which are likely dominated by bright sources.

Furthermore, infrared (IR) surveys have been able to identify 'optically-hidden' AGN in dwarf galaxies (e.g. Satyapal et al., 2014; Sartori et al., 2015; Marleau et al., 2017; Kaviraj et al., 2019), resulting in significantly higher AGN fractions than from optical samples, e.g. Kaviraj et al. (2019) find AGN occupation fractions for dwarf galaxies in the range $\sim$ 10–30 per cent. However see Lupi et al. (2020) who caution that resolution effects and source overlapping may contaminate IR-selected AGN samples in the low-mass regime.

Radio observations have also been employed to search for AGN in dwarf galaxies, yielding a sample of AGN with radio jets in the low-mass regime (e.g. Greene et al., 2006; Wrobel and Ho, 2006; Wrobel et al., 2008; Nyland et al., 2012; Reines and Deller, 2012; Reines et al., 2014; Nyland et al., 2017; Mezcua et al., 2018, 2019; Reines et al., 2020).

Resolved observations are another promising tool for revealing moderate-luminosity AGN in dwarf galaxies, which would be missed using integrated emission line diagnostics (e.g. Dickey et al., 2019; Mezcua and Domínguez Sánchez, 2020).

Finally, there are several future facilities that are expected to find large samples of black holes in dwarf galaxies. Long-term optical variability searches will be instrumental for identifying AGN missed by other selection techniques, especially in the era of LSST (e.g. Baldassare et al., 2020). The gravitational wave observatory LISA will be aimed at detecting gravitational waves from the coalescence of black holes with masses $M_{\rm BH} \sim 10^4$–$10^7 {\rm M}_\odot$ and is therefore optimally placed to study the black hole population in the low-mass regime. Recent simulation studies have highlighted the multimessenger signatures of black holes in dwarfs (Bellovary et al., 2019; Volonteri et al., 2020). *JWST* will also provide important insights into AGN in dwarf galaxies and alleviate the above-mentioned resolution issues of current IR studies (e.g. Cann et al., 2018). The combination of *JWST* with future X-ray missions (*Athena*, *Lynx*) will be a powerful tool for mapping the AGN population in dwarf galaxies at higher redshifts (e.g. Civano et al., 2019; Haiman et al., 2019) and lower luminosities (e.g. Schirra et al., 2020). The ngVLA will map the weakly-accreting AGN in dwarf galaxies and provide insights into the jet-driven feedback mechanisms in the low-mass regime as well as black hole seeding mechanisms (e.g. Nyland and Alatalo, 2018; Plotkin and Reines, 2018).

Beyond constraining the AGN demographics at the low-mass end, recent observations have started investigating whether AGN in dwarf galaxies could have a significant impact on their hosts – with a particular focus on quenching and outflows. Penny et al. (2018) study quiescent dwarf galaxies in the MaNGA survey and find that six out of 69 quiescent MaNGA dwarfs have optical AGN signatures. Interestingly, five out of six of these dwarfs have an

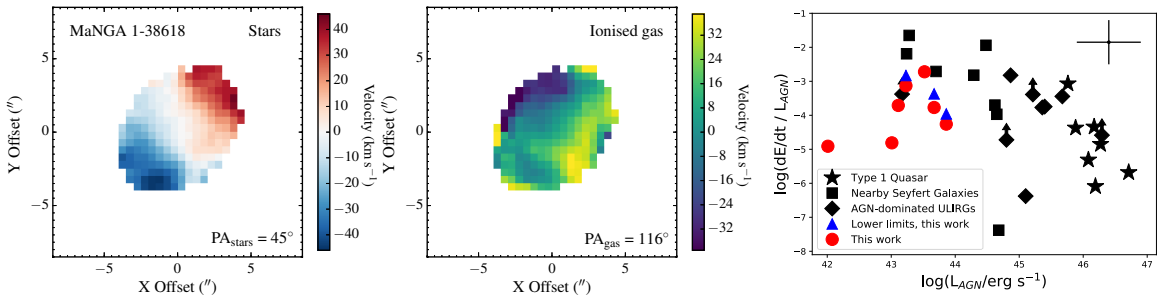

Fig. 1.7 *Left-hand and middle panels:* MaNGA line-of-sight velocity maps for the stars and the ionized gas of a dwarf galaxy with optical AGN signatures. The ionized gas component is clearly kinematically offset from the stellar component which may indicate the presence of an AGN-driven outflow. This figure is reproduced from Penny et al. (2018). *Right-hand panel:* Ratios of the kinetic energy outflow rates to the AGN bolometric luminosities as a function of the AGN bolometric luminosities based on the integral-field spectroscopy data of AGN-driven outflows in dwarfs obtained by Liu et al. (2020) with KCWI. Outflow detections are shown as red circles and lower limits as blue triangles. For comparison, data for type 1 quasars and nearby Seyfert galaxies (Rupke et al., 2017) as well as AGN-dominated ULIRGs (Rose et al., 2018) are also shown. The estimated typical errors of the data points are noted as black crosses in the upper-right corners of both panels. This figure is reproduced from Liu et al. (2020)[8]. © AAS. Reprinted with permission.

ionized gas component that is kinematically offset from the stellar component which could be a sign of AGN-driven outflows (see Figure 1.7, left and middle panels). Manzano-King et al. (2019) find direct evidence of spatially extended high-velocity ionized gas outflows in nine dwarf galaxies hosting AGN, for six of these the emission-line ratios of the outflow itself are consistent with AGN ionization. Liu et al. (2020) present an integral field spectroscopy follow-up study of a subsample of these dwarf galaxies, investigating the gas outflows in more detail. They find that the ratios of kinetic energy outflow rates to AGN luminosities are in agreement with ratios obtained for more massive galaxies, suggesting that AGN are indeed capable of driving the observed outflows (see Figure 1.7, right panel). Liu et al. (2020) also outline how this adds support to the idea that these outflows are scaled-down versions of the outflows in more luminous AGN, driven by the same fundamental AGN processes. Dickey et al. (2019) study quiescent dwarfs in isolated environments and find that 16 out of 20 quiescent isolated dwarfs have AGN-like line ratios.

These tantalising observational hints at AGN activity in dwarfs, including AGN-driven outflows and star formation suppression, call for a renewed theoretical effort to investigate AGN in dwarfs from scratch, relaxing the constraints given by previous modelling efforts.

[8] https://doi.org/10.3847/1538-4357/abc269

1.5 Thesis set-up

The aim of this thesis is to investigate AGN feedback in new regimes using hydrodynamical simulations of dwarf galaxies and to assess the impact that AGN may have on these low-mass systems in the context of both recent observations and galaxy formation theory. For this purpose, I carried out isolated simulations as well as cosmological zoom-in simulations of dwarf galaxies. Furthermore, I analysed the role of AGN at the low-mass end of the galaxy population using the large-volume simulation FABLE. Finally, I also developed a new model for AGN accretion through an adiabatic inflow-outflow solution (ADIOS, Blandford and Begelman, 1999) flow. Brief summaries of the different chapters are provided below:

- In Chapter 2, I investigate different models of AGN activity, ranging from isotropic, thermal winds to collimated, mass-loaded, bipolar outflows in high-resolution isolated simulations of dwarf galaxies using the moving mesh code AREPO. The AGN luminosity is set to a fixed fraction of the Eddington luminosity $L_{\rm Edd}$ based on the initial black hole mass so that the maximum direct impact of AGN activity on dwarf galaxies (within an isolated set-up) may be explored. This chapter is based on Koudmani et al. (2019).

- In Chapter 3, I use the cosmological simulation suite FABLE to further explore AGN-driven outflows in dwarfs. Note that, like most large-scale cosmological simulations, FABLE employs (artificially) strong SN feedback to regulate star formation in dwarfs, stunting black hole accretion rates and luminosities. Notwithstanding this, I investigate the impact of AGN at the low-mass end by making relative comparisons between low-mass galaxies with minimal growth and those that have had significant black hole growth (as indicated by the offset from the mean scaling relations). This chapter is based on Koudmani et al. (2021).

- In Chapter 4, I perform a series of high-resolution zoom-in simulations of dwarf galaxies, varying the AGN prescription and SN energetics. I test both self-regulated accretion based on the Bondi prescription and fixed high Eddington accretion bursts to assess whether AGN feedback could be a successful regulator of star formation in dwarfs in lieu of strong SN feedback. This chapter is based on work that is currently being prepared for publication.

- In Chapter 5, I present a new unified black hole accretion disc model that proceeds via the standard thin disc (Shakura and Sunyaev, 1973) at high Eddington ratios and via the ADIOS model at low Eddington ratios, with the intermediate stage modelled

as a truncated disc. This model covers all radiative regimes and could therefore become a replacement for the simplistic Bondi accretion prescription in next-generation cosmological simulations. This chapter is based on work that is currently being prepared for publication.

- In Chapter 6, I summarise the main conclusions of the thesis and give an outlook on future research avenues, with a particular focus on applications and further extensions of the novel accretion disc model.

CHAPTER 2

MODELLING AGN-DRIVEN OUTFLOWS WITH ISOLATED DWARF GALAXY SIMULATIONS

2.1 Background

As outlined in Section 1.2.7.2, dwarf galaxies are interesting cosmological probes due to a number of apparent discrepancies when comparing dwarf observations with the predictions of the ΛCDM model, including the missing satellites problem (e.g. Kauffmann et al., 1993; Klypin et al., 1999; Moore et al., 1999), too-big-to-fail problem (Boylan-Kolchin et al., 2011) and cusp versus core problem (for one of the first papers on this subject, see Moore, 1994). Whilst this has prompted some to question the validity of the CDM model (see Section 1.2.8), others have identified a number of important baryonic processes that may fundamentally affect dwarf properties and largely alleviate the aforementioned discrepancies (see Section 1.4.1). Reionization suppression (e.g. Efstathiou, 1992; Okamoto et al., 2008; Fitts et al., 2016) and supernova (SN) feedback (e.g. Larson, 1974; Dekel and Silk, 1986; Mori et al., 2002) are the most commonly invoked mechanisms in theoretical models. However, the importance of other feedback channels (e.g. photoionization, radiation pressure, or stellar winds) in dwarf galaxies is still controversial.

Recently, it has been suggested by Silk (2017) that feedback from intermediate mass black holes (IMBHs) in dwarf galaxies could solve many of the above issues including abundances, baryon fraction, and the cusp versus core problem. These ideas have been motivated by the growing observational evidence for active galactic nuclei (AGN) in dwarf galaxies. Below we highlight some of the studies that are of particular relevance to this investigation (see Section 1.4.3 for a more comprehensive overview of the observational evidence).

Chilingarian et al. (2018) carried out an automated search for IMBHs in dwarf galaxies analysing one million SDSS galaxy spectra. They only keep objects with $M_{\rm BH} < 2 \times 10^5$ $M_\odot$

and the BPT (Baldwin et al., 1981) classification has to be "AGN" or "composite", among other criteria. This yields a sample of 305 IMBH candidates including all previously known AGN in the IMBH mass regime. 18 of those have sufficiently deep X-ray observations to rule out or confirm an AGN. This results in a sample of 10 'bona fide' intermediate mass AGN, five of which were previously known.

More direct evidence for AGN feedback comes from the SDSS-IV (Blanton et al., 2017) MaNGA (Bundy et al., 2014) survey where 6 out of 69 quenched low-mass ($M_* < 5 \times 10^9$ M$_\odot$) galaxies appear to have an active AGN that is preventing on-going star formation (Penny et al., 2018). Five of these six galaxies have kinematic signatures consistent with outflows. This discovery challenges the canonical picture of quenching mechanisms where it is assumed that stellar feedback channels are solely responsible for regulating star formation in low-mass galaxies. Might AGN also play a role in the evolution of dwarf galaxies?

This question has been addressed by a number of theoretical studies – with varied results (see Section 1.4.3 for details). Whilst analytical models look promising (Dashyan et al., 2018), most numerical simulations (e.g. Habouzit et al., 2017; Trebitsch et al., 2018; Bellovary et al., 2019) find inefficient black hole growth in dwarfs (though see Barai and De Gouveia Dal Pino, 2019, who find in their high-redshift simulations that Eddington fractions increase with time to $0.2-0.8$ at redshift $z = 4$). For most of these simulations, the Bondi-Hoyle-Lyttleton (BHL) accretion rate (Hoyle and Lyttleton, 1939; Bondi and Hoyle, 1944) is used as the AGN accretion prescription which, due to its quadratic dependency on the black hole mass, makes it difficult for IMBHs to accrete significant amounts of gas. As feedback is directly coupled to accretion, this will then also result in low AGN luminosities. Note that whilst this approach allows simulators to model accretion self-consistently, there is no observational evidence for central black holes accreting at the BHL rate. Moreover, observations of intermediate mass AGN consistently find high Eddington fractions so there must be a scenario which allows IMBHs to accrete efficiently.

Here we therefore decide to take a phenomenological, but more adaptable approach and let the AGN in our simulations accrete at a fixed fraction of the Eddington rate $\dot{M}_{\rm Edd}$ based on the initial black hole mass. This allows us to explore a wide parameter space to determine which AGN luminosity would be required for AGN feedback to affect dwarf galaxies and then compare back to observations to assess whether such luminosities would be realistic[1]. The aim is to assess the maximum possible impact of AGN feedback, without worrying

[1]Note that Trebitsch et al. (2018) also have one run in their simulation suite where they let the BH accrete as much gas 'as possible' limited by the Eddington rate. However, in practice their accretion algorithm does not allow for significant accretion once the central region gets depleted by SN feedback and therefore the accretion ends up being sub-Eddington for the majority of the simulation.

how the gas would get accreted, and investigate the effect on the baryonic content of dwarf galaxies, including the gas content, star formation and outflow properties.

The outline of the chapter is as follows. We describe our numerical methods in Section 2.2, including a summary of the SN and AGN models. In Section 2.3, we describe the different set-ups for our isolated dwarf galaxy simulations, in particular the initial conditions and the 'switched-on' physics modules for each simulation run. We then present our simulation results in Section 2.4 where we analyse the star formation and outflow properties, and compare our results to observations from MaNGA. We discuss these results and compare them to other studies in Section 2.5, and finally conclude in Section 2.6.

2.2 Methodology

All simulations presented in this work are carried out with the massively-parallel AREPO code (Springel, 2010), where fluids are modelled as a moving mesh using a quasi-Lagrangian finite volume technique. The unstructured mesh is based on the Voronoi tessellation of a set of discrete points that cover the whole computational domain. These mesh-generating points are allowed to move with the local flow velocity, with minor corrections to avoid excessive distortion of the gas cells.

Gravitational interactions are modelled using the TreePM approach, with star particles as collisionless particles representing whole stellar populations. For our isolated set-ups we simply model dark matter as a static gravitational potential. The sub-grid models for SN and AGN feedback physics are extensively described in Smith et al. (2018) and Curtis and Sijacki (2015) and only a brief summary is given below (see Sections 2.2.1 and 2.2.2). In addition to these, we include primordial and metal line cooling (cf. Vogelsberger et al., 2013) and we do not include a UV background. Note that we impose a non-thermal pressure floor to ensure that the Jeans length is resolved by a minimum number of cells, $N_{J,min} = 14$, to avoid artificial fragmentation (see Smith et al., 2018, for details).

2.2.1 Star formation & ISM model

2.2.1.1 Star formation

If a gas cell's density is above a certain threshold n_{SF}, it is marked as star-forming and its SFR is calculated using a simple Schmidt law:

$$\dot{\rho}_* = \varepsilon_{SF} \frac{\rho}{t_{ff}}, \tag{2.1}$$

where $\varepsilon_{\rm SF}$ is the instantaneous star formation efficiency, ρ is the gas density and $t_{\rm ff} = \sqrt{3\pi/32G\rho}$ is the dynamical free-fall time. For the density threshold we take a fiducial value of $n_{\rm SF} = 10$ cm^{-3}. There is indication of a wide range of star formation efficiencies in molecular clouds ranging from less than 1 to 40 per cent (see e.g. Krumholz and Tan, 2007), so we test two different values for the instantaneous star formation efficiency: $\varepsilon_{\rm SF} = 1.5$ per cent and $\varepsilon_{\rm SF} = 15$ per cent (see Section 2.3.2 for a more detailed discussion of the choice of the $\varepsilon_{\rm SF}$ parameter).

2.2.1.2 SN feedback

With this feedback scheme, individual SNe are resolved in time and at each time-step for each star particle SN rates, $\dot{N}_{\rm SN}$, are tabulated as a function of age and metallicity from STARBURST99 (Leitherer et al., 1999) assuming a Kroupa (2002) initial mass function. The number of SNe of a given particle in a given time-step then gets drawn from a Poisson distribution with mean $\bar{N}_{\rm SN} = \dot{N}_{\rm SN}\Delta t$, where Δt is the time-step. Note that we also introduce a time step limiter so that $\bar{N}_{\rm SN} \ll 1$.

For each SN, mass, metals, energy and momentum are distributed into the gas cell hosting the star particle as well as all neighbouring gas cells that share a face with the host cell. To achieve an isotropic distribution of these quantities, we use the weighting scheme from Hopkins et al. (2018a,b) assigning a vector weight $\bar{\mathbf{w}}_\mathbf{i}$ to each neighbour (see also Smith et al., 2018). The host cell receives a set fraction $f_{\rm host} = 0.05$ of the ejecta mass $m_{\rm ej}$ and the SN energy $E_{\rm SN}$. Here we adopt $m_{\rm ej} = 10$ M$_\odot$, 2 M$_\odot$ in metals, and $E_{\rm SN} = 10^{51}$ erg. The total momentum imparted to the neighbouring cells is $p_{\rm tot} = \sqrt{2m_{\rm ej}E_{\rm SN}}$.

In the 'no feedback' simulations, host cells and neighbours receive mass and metals as described above but their energy and momentum are not altered. For other simulations, we use the 'mechanical feedback' mode which aims to account for the PdV work done during the Sedov-Taylor phase of the SN remnant (SNR) evolution in the event that it is unresolved. During this adiabatic phase, the momentum of the SNR can be boosted by around an order of magnitude. By comparing the initial momentum of the SNR to its momentum after it has swept up some ambient material, this boost factor can be parametrized in terms of the weighted ejecta mass $\Delta m_i = |\bar{\mathbf{w}}_\mathbf{i}| m_{\rm ej}$ and the swept-up cell mass m_i:

$$f_{\rm boost} = {\rm MIN}\left[\sqrt{1 + \frac{m_i}{\Delta m_i}}, \frac{p_{\rm fin}}{p_{\rm tot}}\right], \tag{2.2}$$

where $p_{\rm fin}$ is the momentum of the SNR as it exits the energy conserving Sedov-Taylor phase and transitions to the momentum conserving snowplough phase. From fits to simulations of individual SNe (see Blondin et al., 1998; Thornton et al., 1998; Geen et al., 2015; Kim and

Ostriker, 2015; Kimm et al., 2015; Martizzi et al., 2015), we take the asymptotic momentum as:

$$p_{\rm fin} = 3 \times 10^5 {\rm km\ s^{-1}\ M_\odot} E_{51}^{16/17} n_{\rm H}^{-2/17} Z'^{-0.14}, \tag{2.3}$$

where $E_{51} = (E_{\rm SN}/10^{51}{\rm erg}) = N_{\rm SN}$ is the number of SNe, $Z' = {\rm MAX}(Z/{\rm Z}_\odot, 0.01)$ is the metallicity in solar units, and $n_{\rm H}$ is the hydrogen number density in ${\rm cm}^{-3}$. Note that this boost factor is calculated for each neighbouring cell individually.

2.2.2 AGN model

2.2.2.1 Refinement strategy

AREPO is a quasi-Lagrangian code, i.e. it aims to keep cell masses constant within a factor two of the target mass $m_{\rm target}$. However, alternative refinement criteria can be implemented allowing for regions of interest to be refined to much lower masses and higher spatial resolution. The AGN model by Curtis and Sijacki (2015) uses a super-Lagrangian refinement criterion for the region around the black hole with the aim of resolving gas flows, and therefore AGN feedback mechanisms, more accurately. The size of the refinement region is set equal to the black hole smoothing length $h_{\rm BH}$ which is defined as the radius of the sphere containing a total mass of $32 \times m_{\rm target}$. This ensures that the refinement region contains a constant amount of mass. Cells within the refinement region then get (de-)refined so that their cell radius $R_{\rm cell}$ is within

$$0.5 l_{\rm ref} < R_{\rm cell} < l_{\rm ref}, \tag{2.4}$$

$$l_{\rm ref} = \frac{d}{h_{\rm BH}} (R_{\rm cell,max} - R_{\rm cell,min}) + R_{\rm cell,min}, \tag{2.5}$$

where d is the gas cell's distance from the black hole, $R_{\rm cell,min}$ is the minimum cell radius (set to the Bondi radius $r_{\rm B}$), and $R_{\rm cell,max}$ is the maximum cell radius (set to $0.1 h_{\rm BH}$). Note that in the original implementation $R_{\rm cell,max}$ is set to $0.5 h_{\rm BH}$ though we find that in our simulations we need a lower value to obtain a relatively smooth cell size distribution (see Appendix 2.B). We also set a minimum gas cell mass $m_{\rm min} = 2 \times 10^{-1}\ {\rm M_\odot} = 10^{-3} m_{\rm target}$. Note that this means that for the majority of the simulation, the Bondi radius is not resolved. However, this is not a significant concern as we have constant accretion rates, and therefore only need outflow properties to be converged. Note that we tested both higher and lower values for the minimum mass and found that for resolving energy and mass injection, the above minimum mass value is sufficient (see Appendix 2.A).

For feedback injection, we use both an isotropic scheme with simple energy-driven spherical winds and a non-isotropic scheme with collimated, mass-loaded, bipolar outflows. The latter is motivated by unresolved dynamics, e.g. magnetic fields close to the black hole, which lead to the observed bipolar outflows from AGN (Rupke and Veilleux, 2011; Maiolino et al., 2012). Note that we fix the bipolar cone's orientation to be aligned with the z-axis.

The two AGN models are depicted in Figure 2.1. The main panels show edge-on projections of the Voronoi mesh with the colour coding indicating the temperature of the gas cells. Each panel also has two insets zooming in on the central region with colour coding representing the gas velocity and the gas density, respectively. We notice much stronger and more collimated outflows for the bipolar injection model with high gas velocities. With the bipolar model, we retain a warm, medium-density component in the central region, whereas with the isotropic model all the gas in the central region is dispersed and heated to high temperatures. The figure also shows the wide range of cell sizes in the simulation from ~ 50 pc in the central region to ~ 500 pc in the outflows entering the circumgalactic medium (CGM).

2.2.2.2 Accretion model

Our primary aim in this work is to explore how energetic the AGN feedback would need to be to significantly affect the host galaxy's evolution. To this end, we let the black hole accrete at a fixed fraction $f_{\rm Edd}$ of the Eddington rate $\dot{M}_{\rm Edd}$ based on the initial black hole mass $M_{\rm BH,initial}$. The black hole accretion rate $\dot{M}_{\rm BH}$ then becomes

$$\dot{M}_{\rm BH} = f_{\rm Edd} \times \dot{M}_{\rm Edd}, \tag{2.6}$$

where

$$\dot{M}_{\rm Edd} = \frac{4\pi {\rm G} M_{\rm BH} {\rm m_p}}{\varepsilon_{\rm r} \sigma_{\rm T} {\rm c}}, \tag{2.7}$$

where G is the gravitational constant, $\rm m_p$ is the mass of a proton, $\varepsilon_{\rm r} = 0.1$ is the assumed radiative efficiency, $\sigma_{\rm T}$ is the Thomson cross-section, and c is the speed of light.

At each time-step $\Delta M = \dot{M}_{\rm BH}(1-\varepsilon_{\rm r})\Delta t$ gets drained from the gas cells within $h_{\rm BH}$ using a top-hat weighting scheme so that each cell loses $\Delta m = \Delta M \times m_{\rm cell}/\Sigma m_{\rm cell}$. We apply a limit to the mass being drained from a given cell to 90 per cent of that cell's mass. In the case of the bipolar scheme, we only drain mass from the regions outside the bipolar feedback cone.

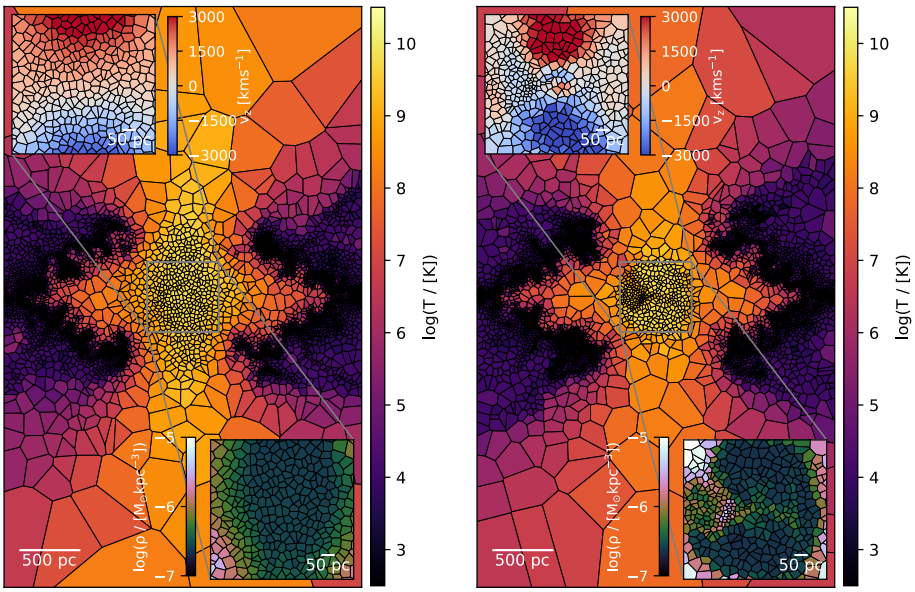

Fig. 2.1 Edge-on projections of the Voronoi mesh ($3.0 \times 5.0 \times 0.2$ kpc) for the two different AGN injection models at $t \sim 25$ Myr. The left panel shows the isotropic, thermal feedback scheme, and the right panel shows the bipolar, mass-loaded outflows. The colour coding in the main panels indicates the gas temperature, and the colour coding in the two insets indicates the vertical gas velocity and gas density, respectively.

2.2.2.3 Injection model

For isotropic feedback, the AGN luminosity is set to a fraction ε_r of the accreted rest-mass energy. In each time-step we then inject $\Delta E_\mathrm{feed} = \varepsilon_\mathrm{f}\varepsilon_\mathrm{r}\dot{M}_\mathrm{BH}\Delta t\mathrm{c}^2$ where $\varepsilon_\mathrm{f} = 0.05$ is the feedback efficiency. The energy is distributed over all cells within h_BH in an isotropic manner using a cubic spline kernel weighting.

For non-isotropic feedback, we inject the feedback energy into a bipolar cone of opening angle $\theta_\mathrm{out} = \pi/3$. In addition, we include the entrainment of mass into this feedback scheme by defining an efficiency parameter ε_out which represents the fraction of gas that is swept up into the outflow. Here we set $\varepsilon_\mathrm{out} = 0.5$ following Curtis and Sijacki (2015). The luminosity then gets reduced to $\varepsilon_\mathrm{r}(1-\varepsilon_\mathrm{out})\dot{M}_\mathrm{BH}c^2$. Both mass and energy get injected into the cells that are within the bipolar cone and h_BH according to the cubic spline kernel weighting. Note that if we want to compare the two injection schemes at fixed luminosity, we need to double the accretion rate for the bipolar feedback.

2.2.3 Adjustments

We do not want stars to form in the refinement region as having star particles of significantly lower mass colliding with more massive particles would lead to spurious N-body heating effects. Curtis and Sijacki (2015) take care of that issue by setting the SFRs of all gas cells in the refinement region to zero. Since a central aspect of our project is to address the question of whether an AGN would be able to quench star formation, we still record the theoretical SFRs for gas cells in the refinement region but do not allow star particles to form there.

Different from the modified equation of state models, the Smith et al. (2018) model resolves individual SN events in time and directly relates them to star particles rather than modelling SN feedback non-locally. We therefore need to include an extra mechanism to prevent SN events in the refinement region: if the mass of the gas host cell is less than 20 per cent of the target gas mass we discard the SN. This ensures that the ejecta mass will never be on the same order or larger than the host cell mass. Also since we are using the aggressive refinement, a cell's shape might not be regular for a certain fraction of time which could cause issues for the isotropic weighting scheme in the SN feedback scheme. We keep track of the fraction of discarded SN events to ensure that we are not losing a significant amount of stellar feedback (see Appendix 2.B).

2.3 Simulations

2.3.1 Initial conditions

The initial conditions comprise an isolated galaxy consisting of a stellar and gas disc, and a stellar bulge surrounded by hot (10^6 K), low-density (10^{-6} cm^{-3}) gas representing the CGM. The dark matter component is modelled by a static background potential in the form of an NFW profile (Navarro et al., 1997) with concentration parameter $c = 10$ and spin parameter $\lambda = 0.04$. The baryonic component of the initial conditions was originally generated with the MAKEDISK code (Springel et al., 2005a). Note that the star particles from the initial disc and bulge component do not contribute to the stellar feedback.

Here we focus on a system of total mass 10^{11} M$_\odot$, with 3.5 per cent of the mass in the disc and 0.35 per cent of the mass in bulge component. The disc is gas-rich with a gas fraction $f_{\rm gas} = 0.5$. This allows SNe and AGN to be effective in our simulations as both require a substantial gas reservoir. Also note that our isolated galaxy is not necessarily a local dwarf, indeed with our high gas fraction, this system is more of a high-redshift analogue. The total stellar mass of our galaxy is 2.1×10^9 M$_\odot$ which is a typical mass for observed dwarf

galaxies hosting AGN (see e.g. Reines and Volonteri, 2015; Penny et al., 2018). The initial temperature of the gas disc is set to 4.6×10^4 K and the initial disc metallicity to 0.1 $Z_\odot$. The virial radius of the halo is $R_{\rm vir} = 75.5$ kpc and we choose the size of the simulated box to be $4 \times R_{\rm vir} = 302$ kpc so that the entire halo is encapsulated. The gas cells and star particles are set to have the same target mass $m_{\rm target} = 200$ $M_\odot$. The minimum gravitational softening length for the gas cells and the fixed gravitational softening length for the star particles are set to the same value $\varepsilon_{\rm grav} = 3.8$ pc. Note that this is the same system as the 'large galaxy' in Smith et al. (2018). The only modification we make to this set-up is to add a central black hole with mass $M_{\rm BH} = 10^5$ $M_\odot$.

We choose this black hole mass, since on the one hand it is comparable to black hole masses for systems with similar bulge masses in the literature (see e.g. Chilingarian et al., 2018) and on the other hand it allows us to test AGN feedback in the intermediate-mass black hole (IMBH) range, 10^2 $M_\odot < M_{\rm IMBH} < 10^5$ $M_\odot$. Note however that this black hole mass represents a conservative choice and using the $M_{\rm BH} - M_*$ relation from Reines and Volonteri (2015), we obtain a black hole mass of approximately 5×10^5 $M_\odot$.

2.3.2 Simulation details

We would like to identify the set-up where AGN activity has the most significant impact on dwarf galaxies. We start off with what we consider to be the most promising configuration and then investigate different variants of this fiducial run to assess which conditions are required for suppressing star formation.

Observations of intermediate mass AGN consistently find high Eddington fractions. Whilst this is obviously influenced by an observational bias, it does demonstrate that there is a non-negligible population of dwarf galaxies with AGN accreting efficiently. Figure 2.2 shows the observed X-ray luminosities and IMBH masses of ten confirmed intermediate mass AGN (Chilingarian et al., 2018). For comparison, we also show the regions corresponding to different Eddington fractions on the diagram. There is a lot of uncertainty associated with converting between X-ray and bolometric luminosities. Some argue that the bolometric correction, κ, should increase with luminosity (see e.g. Hopkins et al., 2007), whilst others find that Eddington fraction is a stronger discriminator between the high and low κ populations (Vasudevan and Fabian, 2007). In our context this difference is crucial as the AGN considered here have low luminosities, due to the low black hole mass, but high Eddington fractions. We therefore show our inferred X-ray luminosities for different Eddington fractions as shaded regions with the lower bounds calculated using the Vasudevan and Fabian (2007) correction and the upper bounds are obtained using the bolometric correction from Hopkins et al. (2007). Note that two out of ten observed AGN luminosities lie above 100 per cent

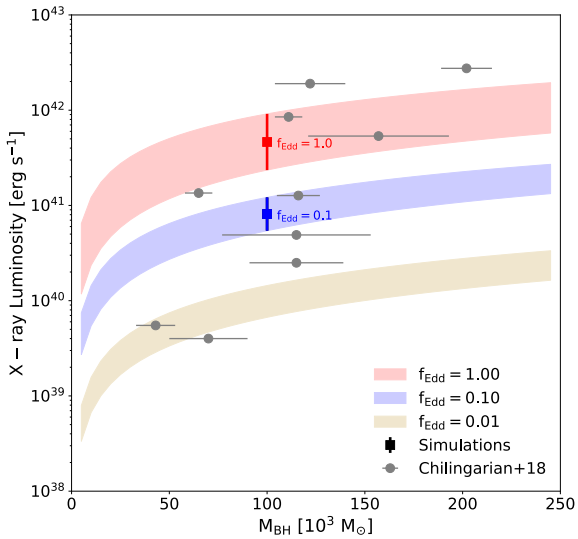

Fig. 2.2 X-ray luminosity against black hole mass. Observational data of active IMBHs from Chilingarian et al. (2018) are shown in grey. The shaded regions show Eddington fractions $f_{\rm Edd} = 0.01, 0.1, 1.0$, where the lower boundary is given by an Eddington fraction dependent (Vasudevan and Fabian, 2007) and the upper boundary by a luminosity dependent (Hopkins et al., 2007) bolometric correction. Our two simulation set-ups are indicated as squares.

of the inferred Eddington rate. However these IMBHs might have been observed at the peak of a duty cycle, and in that case using the maximum observed luminosity constantly in our simulations would likely overestimate the impact of the AGN. We therefore choose the more conservative Eddington fractions of 10 or 100 per cent for our runs (indicated as coloured squares in Figure 2.2). Furthermore, we set our fiducial instantaneous star formation efficiency to $\varepsilon_{\rm SF} = 0.15$ to obtain high SN efficiency.

We hypothesise that the isotropic thermal feedback would be most effective in influencing star formation, as it drives energy directly into the disc. We therefore choose the run with an AGN emitting thermal energy isotropically at 100 per cent of the Eddington rate as our fiducial set-up (SN+AGNTh100). We also repeat the same run with the AGN shining at 10 per cent of the Eddington luminosity (SN+AGNTh10), and with the AGN shining at 100 per cent of the Eddington luminosity, but with the energy input being restricted to a bipolar cone and additional mass loading (SN+AGNBi100). Note that we expect the latter to be less efficient at regulating star formation as most of the thermal energy will simply escape from the galaxy. Finally, we also test a set-up with a lower star formation efficiency of $\varepsilon_{\rm SF} = 0.015$ (SN+AGNTh100Low).

For comparison we also carried out SN only runs as well as runs without any feedback at both star formation efficiencies (SN, SNLow, NoFeedback, and NoFeedbackLow). All simulation runs and their properties are listed in Table 2.1.

Table 2.1 Overview of the isolated simulation runs, where we list star formation efficiencies ($\varepsilon_{\rm SF}$), AGN luminosities, and "switched-on" feedback mechanisms.

Name	$\varepsilon_{\rm SF}$	$\frac{L_{\rm AGN}}{L_{\rm Edd}}$	Feedback Physics
NoFeedback	0.15	0.0	no energetic feedback
NoFeedbackLow	0.015	0.0	no energetic feedback
SN	0.15	0.0	SNe
SNLow	0.015	0.0	SNe
SN+AGNTh100	0.15	1.0	SNe, AGN (thermal)
SN + AGNTh100Low	0.015	1.0	SNe, AGN (thermal)
SN+AGNTh10	0.15	0.1	SNe, AGN (thermal)
SN+AGNBi100	0.15	1.0	SNe, AGN (bipolar)

2.4 Results

2.4.1 Gas properties

We start our analysis by inspecting the visuals of the simulation suite which are shown in Figure 2.3. Here, $50 \times 100 \times 10$ kpc edge-on projections of surface density, temperature, vertical velocity and metallicity at $t = 300$ Myr are plotted. As expected, both of the runs without energetic feedback ('NoFeedbackLow' and 'NoFeedback') overcool resulting in a massive overproduction of stars. The high $\varepsilon_{\rm SF}$ run has slightly more metals as even more stars are formed with this set-up. None of the two no feedback runs have outflows.

Adding SN feedback to this set-up triggers large-scale outflows. However at low $\varepsilon_{\rm SF}$, the outflows are much weaker consisting of mainly slow-moving, relatively dense gas and only reaching heights of $z \sim 35$ kpc. The high $\varepsilon_{\rm SF}$ run drives much stronger outflows which reach heights $z > 50$ kpc. The outflows have a significant warm component ($T \sim 10^5$ K), but are still relatively slow ($v_{\rm z} \sim 10^2$ kms^{-1}). Close to the disc, both SN runs have small-scale hot outflows, reaching temperatures $T \sim 10^6$ K. We also observe a significant galactic fountain effect close to the disc which is even stronger for the high $\varepsilon_{\rm SF}$ run due to a recent quenching episode which weakened the SN feedback.

With additional AGN activity outflows are significantly enhanced. At low $\varepsilon_{\rm SF}$, the outflows reach extremely high velocities of several thousands kms^{-1}. The bulk component of the outflowing material is hot ($T \sim 10^7$ K), low-density, and high-metallicity ($Z \gtrsim {\rm Z}_\odot$). While in the 'SNLow' run, the propagation of metals into the CGM is limited, the outflows in the 'SN+AGNTh100Low' run are powerful enough to increase the metallicity in the whole surrounding region.

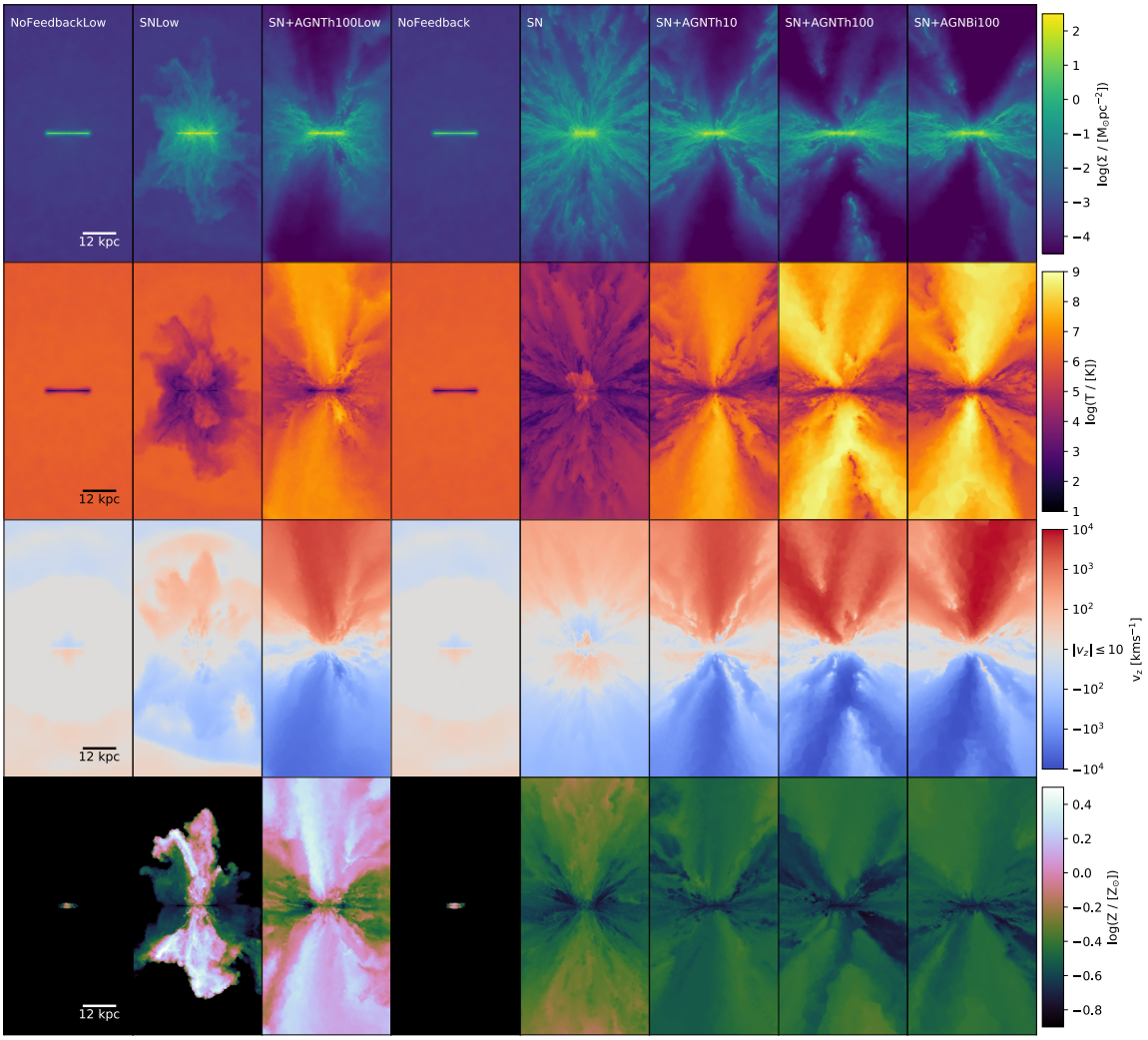

Fig. 2.3 $50 \times 100 \times 10$ kpc edge-on projections of all the simulation runs at $t = 300$ Myr. The first row shows surface densities, the second row shows temperatures, the third row shows vertical velocities, and the fourth row shows metallicities. The low $\varepsilon_{\rm SF}$ runs are depicted on the left hand side, and the high $\varepsilon_{\rm SF}$ runs on the right hand side. With only SN feedback, the outflows are slow, warm, and high-density. With additional AGN feedback, the outflows have an additional hot, low-density component moving at high velocities. The differences in outflow metallicities at $t = 300$ Myr are largely driven by differences in outflow histories rather than star formation.

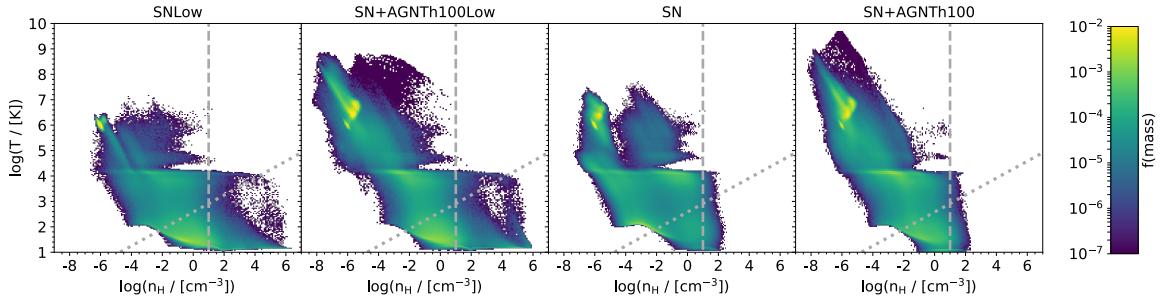

Fig. 2.4 Comparison of the phase diagrams for the two star formation efficiencies at $t = 300$ Myr. The models used are labelled on the panels. Colour coding corresponds to the fraction of gas mass within a given pixel. The dashed line indicates the star formation threshold and the dotted line indicates the non-thermal pressure floor. For the runs where feedback is efficient ('SN+AGNTh100Low', 'SN' and 'SN+AGNTh100'), a significant amount of mass is located in the low-density, high-temperature region of the phase diagram, representing hot outflows. For the AGN runs, these outflows reach extremely high temperatures up to $T \sim 10^9$ K. The gas above the star formation density threshold is barely affected by the addition of AGN feedback.

At high $\varepsilon_{\rm SF}$, the AGN runs have lower metallicity than the 'SN' run within the extent of the projections shown. Though this difference is not driven by SN activity, but by different outflow properties[2]. Suppression of central SFRs by the AGN is a secondary effect, the overall metal mass between 'SN' and 'SN+AGNTh100' differs by only three per cent.

The AGN runs at high $\varepsilon_{\rm SF}$ are significantly more multi-phase than the other set-ups. Outflow velocities range from tens to thousands kms^{-1} and outflow temperatures from $\sim 10^4$ K to $\gtrsim 10^9$ K. As the simulation evolves the hot gas fraction increases due to the constant input of thermal energy.

We can compare the effect of different energy injection schemes and different $\varepsilon_{\rm SF}$ in more detail by looking at the phase diagrams. Figure 2.4 shows the phase diagrams of the gas for the SN and high luminosity thermal wind runs at $t = 300$ Myr. Colour coding represents the fraction of mass in a given pixel. For all runs, the CGM gas is visible at $T \sim 10^6$ K and $n_{\rm H} \sim 10^{-6}$ cm^{-3} and the ISM gas at $T \lesssim 4.5 \times 10^4$ K. The connection between those two regions represents gas cooling from the CGM onto the disc. The dotted line indicates the non-thermal pressure floor and the star formation density threshold is shown as a vertical dashed grey line.

The low $\varepsilon_{\rm SF}$ runs all have significant amounts of dense, cool gas above this threshold (~ 5 per cent of gas is star-forming in both cases). The gas has short cooling times and mostly

[2]In the AGN runs, the metals from the initial starburst get ejected earlier as the AGN triggers outflows from the very beginning, different from the SN feedback which takes ~ 40 Myr to develop its full effect. Furthermore, the AGN runs eject material at a higher rate, so at $t = 300$ Myr, the high metallicity material has reached heights $z > 50$ kpc.

occupies the high-density, low-temperature region of the phase diagram. Nevertheless, some of the gas manages to get to higher temperatures, where cooling times are longer. We obtain small-scale outflows for the 'SNLow' run, with some gas ($M_{\rm hot} \sim 9 \times 10^2$ M$_\odot$) reaching temperatures above 10^7 K. The 'SN+AGNTh100Low' run produces large outflows with significant amount of gas in the hot phase ($M_{\rm hot} \sim 7 \times 10^7$ M$_\odot$). For the $\varepsilon_{\rm SF} = 15$ per cent runs, we have strong outflows both with and without an AGN. The SN feedback drives powerful outflows ($M_{\rm hot} \sim 3 \times 10^6$ M$_\odot$) and efficiently regulates star formation. The AGN activity increases the hot mass by approximately two orders of magnitude to $M_{\rm hot} \sim 1 \times 10^8$ M$_\odot$, and the outflows are more multiphase also containing warm components (cf. Figure 2.3). As with the low $\varepsilon_{\rm SF}$ case, the gas above the star formation density threshold is barely affected by the AGN and for both high $\varepsilon_{\rm SF}$ runs, we have a star-forming gas mass fraction of less than one percent.

For the runs where feedback is efficient, 'SN+AGNTh100Low', 'SN+AGNTh100' and 'SN', a significant amount of mass is located in the low-density, high-temperature region of the phase diagram at 10^{-6} cm$^{-3} \lesssim$ n$_{\rm H} \lesssim 10^{-5}$ cm^{-3} and 10^6 K $\lesssim$ T $\lesssim 10^7$ K. This feature represents the hot outflows, which carry a significant amount of gas mass away from the galaxy (see Section 2.4.3). For the two AGN runs, we also have a second high-temperature feature. As can be seen from the colour coding, these cells are super-refined gas cells within the black hole smoothing length. This feature is then explained as a by-product of the super-Lagrangian refinement scheme together with a minimum mass constraint[3].

2.4.2 Star formation

Before we delve into the details of outflows in section 2.4.3, we want to assess the impact of AGN activity on star formation which is one of the most fundamental quantities of galaxy formation. Figure 2.5 shows the SFRs for $\varepsilon_{\rm SF} = 1.5$ per cent and $\varepsilon_{\rm SF} = 15$ per cent. For the $\varepsilon_{\rm SF} = 1.5$ per cent case, the no feedback run has a starburst between ~ 30 and 150 Myr using up most of the gas and then follows the SFRs of the two feedback runs. The 'SN+AGNTh100Low' run forms slightly more stars than the 'SNLow' run early on[4] and then has roughly similar, albeit systematically lower, SFRs. This can be seen more clearly in the inset which shows the ratio between the AGN and the SN only run.

For the $\varepsilon_{\rm SF} = 15$ per cent runs, there is an early peak in the SFR at $t \sim 25$ Myr. Afterwards, the SFR of the 'NoFeedback' run slightly decreases, with the majority of the high-density

[3] As discussed in Appendix 2.B, a significant number of cells will reach the minimum mass which is set to 2×10^{-1} M$_\odot$. This leads to the strip in the phase diagram of the 'SN+AGNTh100' run. In the low $\varepsilon_{\rm SF}$ case, higher central surface densities mean that fewer cells will reach the minimum mass and therefore the distribution of the gas phases in the refinement region is broadened.

[4] This a positive feedback effect from gas being compressed on the expanding AGN bubble.

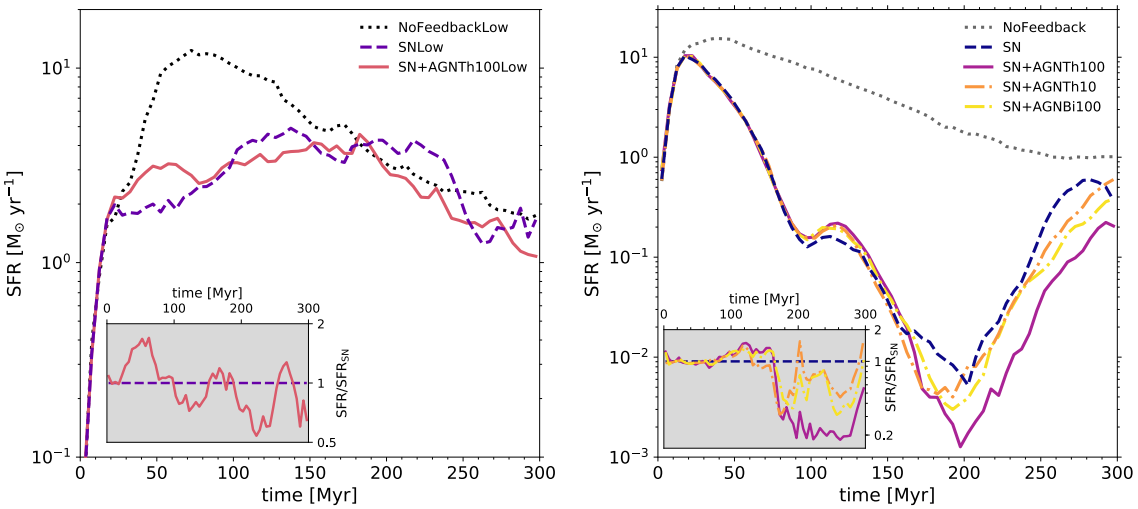

Fig. 2.5 *Left panel:* SFRs for the $\epsilon_{SF} = 1.5$ per cent runs. The inset shows the ratio between the AGN and SN only runs. Adding AGN outflows does not have a significant effect on SFRs in this set-up. *Right panel:* SFRs for the $\epsilon_{SF} = 15$ per cent runs. The inset shows the ratio between the AGN and SN only runs. All AGN outflow models affect SFRs at late times. The high-luminosity, thermal run ('SN+AGNTh100') is the most effective, suppressing the SFR by approximately a factor of five for $t \gtrsim 200$ Myr.

gas having been consumed, while the SFRs of the runs including SN feedback decrease rapidly. This makes sense as a burst of star formation will be followed by a burst of SN activity. At around $t \sim 90$ Myr, the SFR of the 'SN' run' drops slightly below the SFR of the AGN runs. Finally, at around $t \sim 160$ Myr, the AGN outflows start taking effect. The SFRs of all three AGN runs start falling below the 'SN' run. The 'SN+AGNTh100' run has the most significant effect, decreasing SFRs by approximately a factor of five for $t \gtrsim 200$ Myr. The other two AGN runs have qualitatively similar effects, though the offset is less significant here. Since the bipolar mode only injects energy into a double cone perpendicular to the disc, we would not expect it to have a large effect on the cold disc gas – the isotropic thermal winds can have a much more significant impact here. Also note that towards the end of the simulation at $t \sim 300$ Myr, the SFRs start decreasing again. We followed the 'SN' and 'SN+AGNTh100' slightly longer and found that the pattern of SFR peak followed by SFR trough (due to high SN activity) keeps repeating, as one would expect with a strong stellar feedback loop.

From the temporal evolution of star formation properties, one could conclude that AGN outflows do not significantly affect star formation in dwarf galaxies. However, looking at the spatial distribution instead, we see a small but systematic offset with star formation being suppressed in the central region for different AGN models, luminosities and star formation efficiencies. Figure 2.6 shows the SFR within a given radius R for $\epsilon_{SF} = 1.5$ per cent and

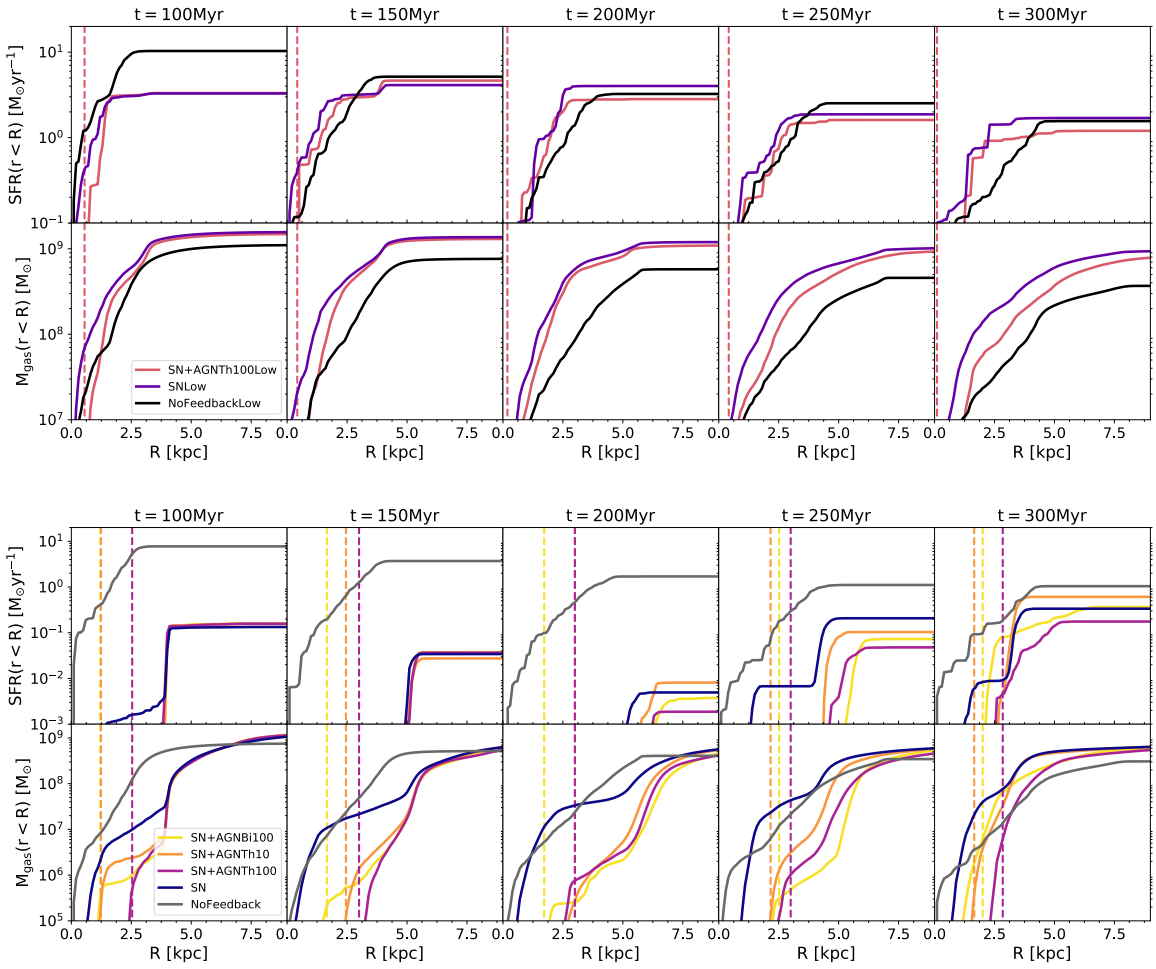

Fig. 2.6 Cumulative SFRs as a function of distance from the galaxy centre for $\varepsilon_{\rm SF} = 1.5$ per cent (top panel) and $\varepsilon_{\rm SF} = 15$ per cent (bottom panel) runs. For comparison cumulative gas masses are also shown in each case. The black hole smoothing lengths (equal to the size of the refinement region) are indicated as vertical dashed lines. For the runs with AGN feedback, central SFRs are systematically suppressed, in particular at high $\varepsilon_{\rm SF}$.

$\varepsilon_{\rm SF} = 15$ per cent. For reference, the enclosed gas mass is also shown in the lower panels. The black hole smoothing lengths are indicated as vertical dashed lines.

For the low $\varepsilon_{\rm SF}$ runs, central SFRs are slightly suppressed when including AGN outflows on top of SNe at $t = 100$, 250, 300 Myr. For the high $\varepsilon_{\rm SF}$ runs, this effect is more pronounced. Here the AGN runs have lower central SFRs for the majority of the simulation times. In all cases, the AGN activity has significantly depleted the central region, though note that at fixed luminosity the bipolar run has a much smaller effect on the gas distribution than the isotropic thermal run. This is largely due to energy injection rather than mass accretion effects, as the accreted mass over $t = 300$ Myr amounts to merely $M_{\rm acc,tot} = f_{\rm Edd} \times 6.7 \times 10^5$ M$_\odot$, whilst the offsets observed are at least on the order of $10^6 - 10^7$ M$_\odot$.

Overall, we find that, even with an AGN shining at 100 per cent of the Eddington luminosity, we cannot suppress star formation globally, though we do observe significant effects locally. Partly this is due to the SN feedback being very efficient so that the majority of the quenching work has already been done. Another reason that AGN activity does not affect star formation is that most of the AGN feedback energy escapes along the path of least resistance, i.e. in this case perpendicular to the disc (see e.g. Wagner et al., 2013; Bourne et al., 2014; Costa et al., 2014; Gabor and Bournaud, 2014; Bieri et al., 2017).

In addition there are some caveats with our isolated model, the most important one being that we do not have gas inflows. If we had gas inflows these would likely be hindered by an AGN, as we see significant global effects of AGN activity on galactic outflows (cf. Figure 2.3). These effects will be analysed in more detail in the next section.

2.4.3 Outflow properties

We further investigate the outflows visible in Figure 2.3 by plotting the mass outflow rate $\dot{M}_{\rm out}$, the mass loading factor (ratio of mass outflow rate to SFR), the thermal energy outflow rate $\dot{U}_{\rm out}$ and the mass-weighted average outflow velocity $< v_{\rm out} >$ at three target heights ($H = 2$ kpc, $H = 20$ kpc, and $H = 75.5$ kpc $= R_{\rm vir}$) for a slice of thickness d$z = 200$ pc in Figure 2.7. The virial velocity is indicated as a dashed grey line in the panels showing the average outflow velocities. Outflow velocities are taken vertically away from the disc plane, and we only include gas flowing away from the disc by requiring $\mathrm{sgn}(v_z) = \mathrm{sgn}(z)$.

At low $\varepsilon_{\rm SF}$, we can see clear differences between the 'SNLow' and 'SN+AGNTh100Low' runs for all quantities considered. The AGN runs have large-scale outflows from the beginning of the simulation run. The SN only runs have small-scale outflows from $t \sim 50$ Myr. This is because it takes some time for stars to form and explode as SNe, whilst the AGN is active from the beginning of the simulation. The SN-driven outflows at $H = 2$ kpc reach mass outflow rates similar to the 'SN+AGNTh100Low' run. The outflows at $H = 20$ kpc, however, are about one order of magnitude weaker and only reach significant outflow rates from $t = 250$ Myr onwards. For 'SNLow', no outflows reach the virial radius, within the simulation time. This shows that the outflows at $H = 2$ kpc mainly originate from a warm fountain, which does not propagate into the CGM.

Due to the similar SFRs, the mass loading factors follow the same pattern. Note that from observations and theory, we would expect mass loading factors between one and ten, whilst we get a mass loading factor of order 0.1 for both runs at $H = 2$ kpc. Remarkably, even with a sustained high-luminosity AGN, we do not obtain high mass loading.

We also consider the outflow rate of thermal energy per unit mass. At $H = 2$ kpc, there is some thermal energy outflow for the 'SNLow' run. This is mainly associated with the warm

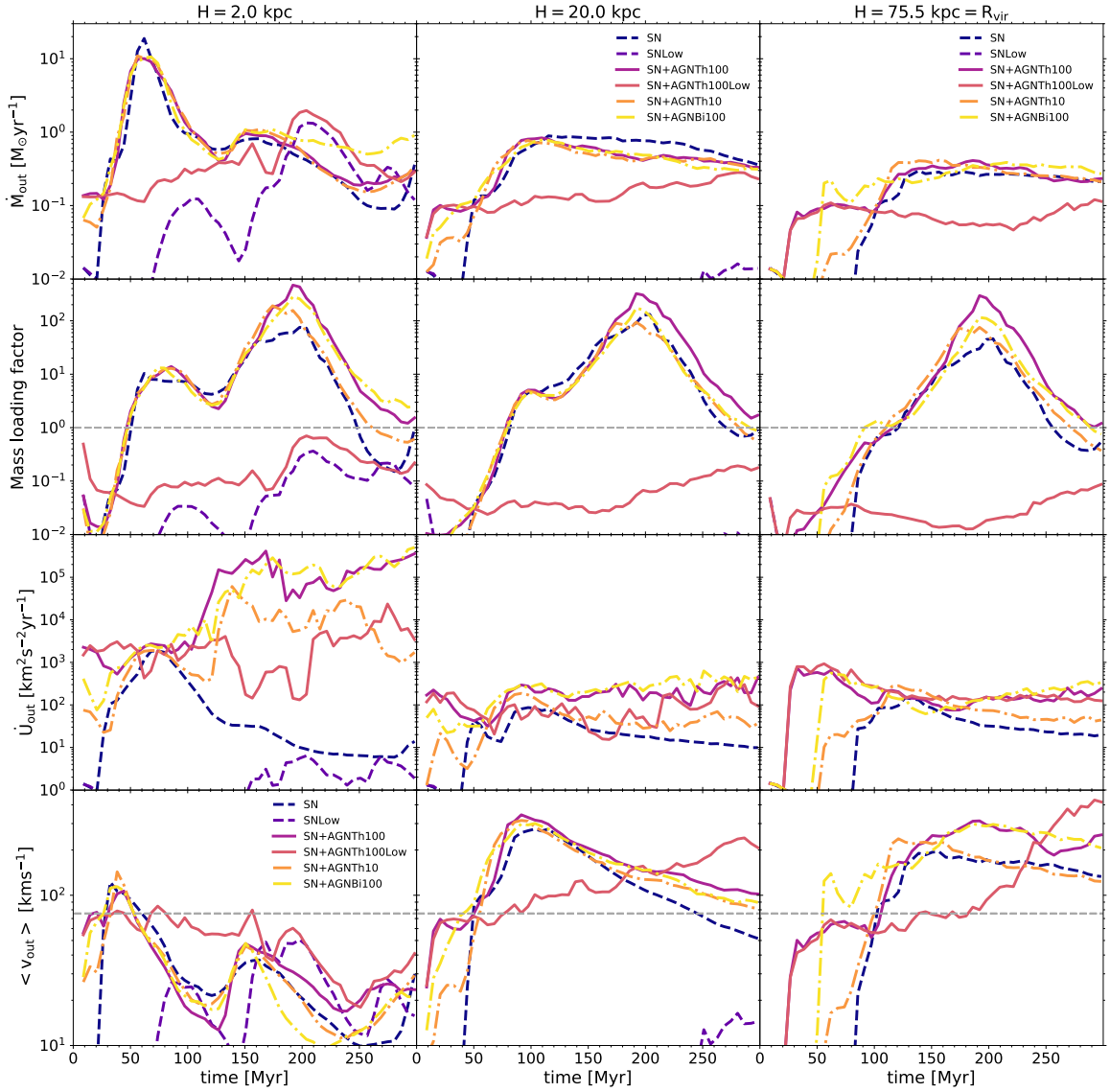

Fig. 2.7 Outflow properties against time for the $\epsilon_{\rm SF} = 1.5$ per cent and the $\epsilon_{\rm SF} = 15$ per cent runs calculated at target heights H = 2 kpc (left column), H = 20 kpc (middle column), and H = 75.5 kpc = $R_{\rm vir}$ (right column). The first row shows the mass outflow rates $\dot{M}_{\rm out}$, the second row shows the mass loading factor, the third row shows the thermal energy outflow rates $\dot{U}_{\rm out}$, and the fourth row shows the average outflow velocities $< v_{\rm out} >$ (the virial velocity is indicated as a dashed grey line). The different models used are given by the figure legend. The 'SNLow' run, in general, does not have powerful enough feedback to drive significant outflows, and even by adding an AGN shining at 100 per cent of the Eddington luminosity, we do not obtain significant mass loading factors. When SN feedback is efficient (high $\epsilon_{\rm SF}$ runs), the most striking difference are the thermal outflow rates, with the AGN expelling up to five orders of magnitude more thermal energy from the galaxy.

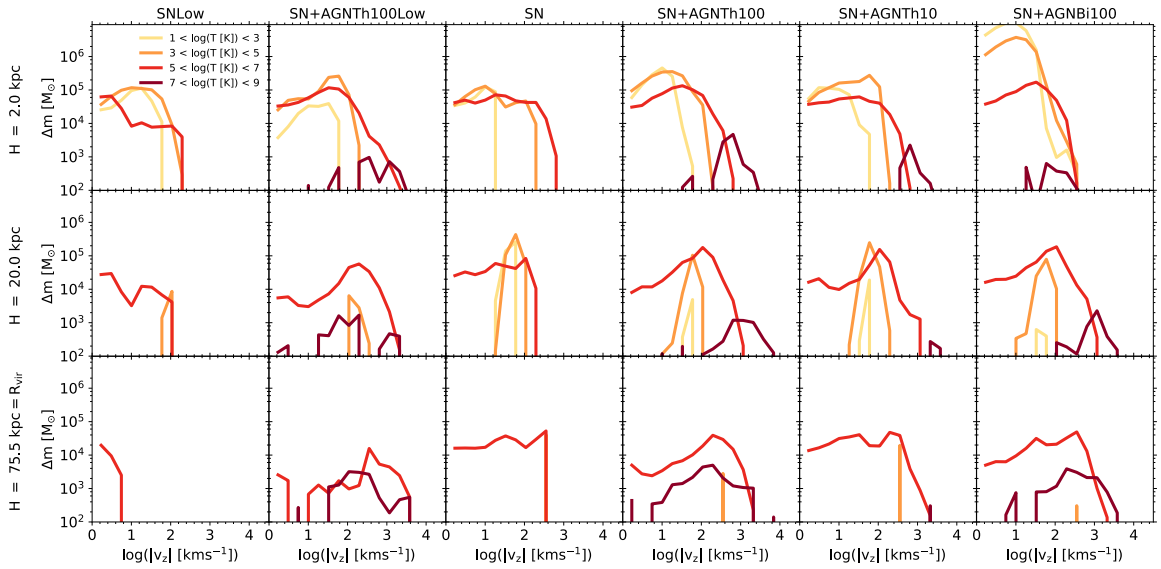

Fig. 2.8 Mass histogram of outflow velocities split by temperatures at three target heights H = 2 kpc (top row), H = 20 kpc (middle row), and H = 75.5 kpc = R_{vir} (bottom row) at $t = 300$ Myr. The thermal and kinematic properties of the AGN feedback runs are significantly different from their SN only equivalents even with a more conservative luminosity of ten per cent L_{Edd}. Only the AGN-driven outflows carry a 'very hot' outflow component with temperatures above 10^7 K, and these outflows are much faster reaching several thousands kms^{-1}.

fountain, as this component is not present at larger heights. The 'SN+AGNTh100Low' run has significant thermal energy outflow rates, comparable with the high ε_{SF} AGN runs.

Finally, we compare the mass-weighted average outflow velocities. Note that these will be biased towards lower velocities, as we also capture the slow-moving CGM gas which happens to have its (extremely small) velocity orientated away from the disc. Close to the disc, at $H = 2$ kpc, the 'SN+AGNTh100Low' outflow velocities are initially quite high at $60 - 80$ kms^{-1}, but then decrease at later times as the additional slow-moving SN-driven outflow lowers the average velocity. At the virial radius there is a sharp increase in outflow velocities from $t \sim 200$ Myr onwards as there is no more SN-driven component, and all of the material is hot. Also note that further away from the disc, at $H = 20, 75.5$ kpc, the average outflow velocity is consistently above the virial velocity at late times, suggesting that outflows might become unbound. The 'SNLow' outflow velocities fluctuate between 20 and 50 kms^{-1} at $H = 2$ kpc (in accordance with the timings of SN bursts). There are no outflows with significant velocities further away from the disc.

For the high ε_{SF} runs, we also have AGN-driven outflows from the very beginning of the simulations, whilst there is a time delay of $t \sim 25$ Myr for the 'SN' run, again set by the time it takes for stars to form and explode as SNe. The time delay is shorter here as the star

formation is more efficient. For all runs, there is a high amount of mass outflow at $H = 2$ kpc at $t \sim 60$ Myr. This is caused by the extreme SN activity following the starburst at $t \sim 25$ Myr (cf. Figure 2.5).

Overall, the outflow rates are roughly similar for the different feedback models with slightly higher mass outflow rates for the 'SN+AGNBi100' run, which makes sense as these outflows have additional mass-loading from the AGN. At large scales the outflow rates are much steadier and there is not a significant difference between the models, once SN feedback starts driving outflows. As SFRs do not differ too much between the different set-ups, the time evolution of the mass loading factors follows a similar pattern, spanning values from 10^{-2} to several hundreds. The first maximum at $H = 2$ kpc is largely due to the initial starburst, and is absent at the other two target heights, again suggesting that the initial burst ends up as a warm fountain and the outflow does not manage to fully escape.

Note that close to the disc, the average outflow velocity stays below the virial velocity for all times except the initial starburst. Similarly, the peak at $H = 20$ kpc is also associated with the peak in SN activity. However, at the virial radius this peak vanishes, and from $t = 100$ Myr onwards, all high $\varepsilon_{\rm SF}$ runs have outflows steadily above the virial velocity, as only the most energetic gas manages to escape to this height. Note that with AGN activity the outflows at the virial radius are much faster at late times. This can be explained by noting that AGN-driven outflows are mainly low-density and hot, while the SN-driven outflows carry significant amounts of warm and relatively dense material, moving at significantly lower velocities (cf. vertical velocity projections in Figure 2.3).

This point is strengthened by the significant differences in the thermal energy outflow rates. At small scales the difference reaches more than five orders of magnitudes at $t \sim 300$ Myr when SN activity is significantly suppressed due to the minimum in star formation at $t \sim 200$ Myr. At large scales, we also observe significant offsets up to almost two orders of magnitude. The difference between the thermal properties decrease as the cold and warm component of the SN outflows do not make it to large disc heights so that the thermal properties far away from the disc are relatively similar.

We further investigate the kinematic and thermal properties of the different runs by inspecting the velocity distribution of the different gas phases. Figure 2.8 shows the mass in different velocity bins split by temperatures (cold: $10 - 10^3$ K, warm: $10^3 - 10^5$ K, hot: $10^5 - 10^7$ K, very hot: $10^7 - 10^9$ K) at the three target heights $H = 2$ kpc, $H = 20$ kpc, and $H = 75.5$ kpc at $t = 300$ Myr. We also include inflows here as we are mainly interested in whether the gas is slow or fast moving rather than the direction. The CGM is clearly identifiable as the hot, slow-moving component.

The first interesting point to note is that neither the 'SNLow' nor the 'SN' run has a very hot component. Close to the disc, both runs have a warm and a hot component with velocities up to several hundreds kms^{-1}, and a slow-moving cold outflow component. The 'SN' run also has a significant cold component at intermediate heights ($H = 20$ kpc), whilst the outflow 'SNLow' run is mainly just in the hot phase. At the virial radius, the 'SN' outflow has all its gas mass in the hot phase, whilst for the 'SNLow' run, we are left with only the CGM component, since the outflows do not propagate far enough.

All of the AGN models result in outflows with a very hot component, and also have broader velocity distributions with outflow speeds reaching thousands of kms^{-1}. Another interesting thing to note is that while all AGN outflows have a significant cold component at small scales, this is mostly lost at large scales due to lower outflow velocities in the cold phase and mixing with the very hot component. At the virial radius, all outflows are almost exclusively hot or very hot.

In the whole simulation volume, the 'SN' run and the runs with AGN outflows have similar amounts of fast-moving gas ($|v_z| > 10^2$ kms^{-1}) with $M_{\rm fast} \sim 10^8$ M$_\odot$, but while for the AGN runs 10 per cent of that fast-moving gas is very hot, for the 'SN' run it is only 1 per cent. For 'SNLow', we only have $M_{\rm fast} \sim 10^6$ M$_\odot$, of which just 0.01 per cent is hot. Note that the thermal outflow properties may be resolution dependent (see e.g. Hu, 2019; Smith et al., 2019), though this would be a relative effect, with both SNe and AGN becoming more effective in heating the gas at higher resolution.

Overall, we conclude that the thermal and kinematic properties of the AGN runs are significantly different from their SN only equivalents even with a more conservative luminosity of ten per cent $L_{\rm Edd}$. These distinct differences between the kinematic properties of the simulations are promising as they carry specific observational signatures. In the next section, we discuss these possible signatures in more detail and how the results from our simulations compare to observations from MaNGA.

2.4.4 Comparison to MaNGA

There is some first evidence of AGN feedback in dwarf galaxies from the SDSS-IV MaNGA survey. Penny et al. (2018) analyse the MaNGA MPL-5 sample to find AGN candidates in the dwarf galaxy population[5]. In particular they aim to find red geyser candidates, which typically have kinematically offset ionized gas, either the result of accretion or outflows of material generated by AGN-driven winds. They identify five dwarf galaxies with little or no star formation and an ionized gas component which is offset from the stars. All of these

[5]Here dwarf galaxies are defined as having absolute magnitude fainter than $M_{\rm V} = -19$, central stellar velocity dispersion $\sigma_* < 100$ kms^{-1} and stellar mass $M_* < 5 \times 10^9$ M$_\odot$.

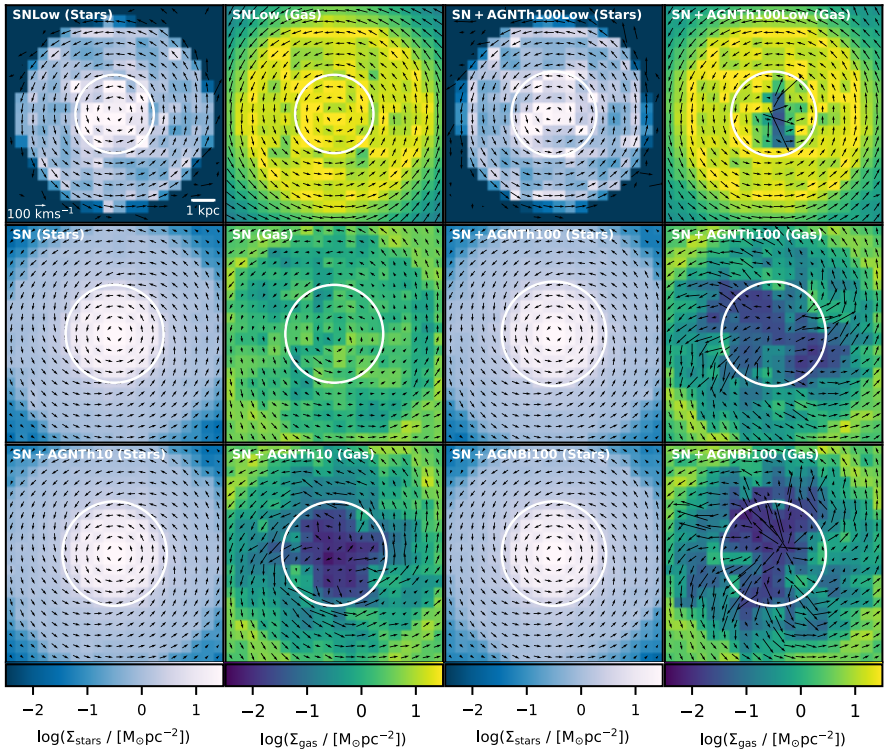

Fig. 2.9 Comparison between the 2D velocity maps of the stars and gas in the simulations at $t = 150$ Myr. The colour coding of the pixels indicates the surface density. The spatial coverage of the primary MaNGA sample of $1.5R_{\rm eff}$ is indicated by a white circle. With added AGN feedback, the central circular motion is significantly altered by the outflows so that the gas would be seen as kinematically offset. With SN feedback alone, the circular motion remains dominant and we do not observe this feature.

five galaxies have central spectral signatures indicating AGN activity, providing tentative evidence for maintenance mode AGN feedback.

We would like to test whether a similar kinematic offset would be observed for our simulated dwarf galaxies with AGN-driven outflows and how the probability of observing such an offset compares to the runs with only SNe. For an observable effect on the line-of-sight velocity, the outflow component has to be larger than the rotational component. In Figure 2.9, we show some representative two-dimensional maps of the mass-weighted velocity components in the disc plane for gas and newly-formed stars (i.e. excluding the stars from the initial conditions) at $t = 150$ Myr. The colour coding of the pixels indicates the surface density allowing us to relate the velocities to the matter distribution. In addition, the region covered by $1.5R_{\rm eff}$, where $R_{\rm eff}$ is the effective radius, corresponding to the spatial coverage of the primary MaNGA sample, is indicated by a white circle. For all runs, the rotational pattern of the stellar component is undisturbed, suggesting that the large-scale

kinematics of the newly-formed stars are not affected by feedback or outflows. The gas velocities are not affected by SN feedback either. However, adding an AGN makes a significant difference, with the central velocity patterns being visibly altered by the AGN-driven outflows. As only the central region is taken into account when inferring line-of-sight velocities, the gas component will then be significantly offset from the stellar component.

To have a fair comparison between our simulation and the MaNGA results, we create mock line-of-sight velocity maps for both stars and ionized gas[6]. Here we define a gas cell as ionized if the neutral hydrogen abundance is less than 0.1 per cent. We have checked a range of values from 10^{-3} to one per cent and find that our results do not depend on this cut-off. When creating the velocity maps, we only use gas cells and stars within $1.5R_{\rm eff}$, in analogy to MaNGA. We also match the resolution of our velocity maps to the MaNGA resolution at the median redshift of the primary sample ($\sim$ 304 pc). In each pixel, we weight the velocities by the luminosity, i.e. by the mass for the stars and by the square of the density for the gas, as the latter is proportional to the emissivity. As the galaxies in the MaNGA sample have no preference for a particular orientation, we create velocity maps at three different inclination angles $\alpha_{\rm tilt}$: 0° (edge-on), 45°, and 75° (nearly face-on). We do not create velocity maps for the face-on case as the contribution of the rotational velocity to the line-of-sight velocity virtually vanishes.

We then carry out the same analysis that was done with the MaNGA maps in Penny et al. (2018). Firstly, we convolve the velocity maps with a Gaussian filter of filter size two pixels. We then use these maps to measure the global kinematic position angle[7] (PA) of the ionized gas and the stellar component using the method described in Krajnović et al. (2006). Figure 2.10 shows example mock velocity maps for $\alpha_{\rm tilt} = 45°$ at $t = 150$ Myr. The PAs are also given. As we have chosen the axes so that the angular momentum vector of the disc is aligned with the z axis, we would expect the PA to be 90°. For the stellar component this gets recovered within $\pm 10°$. Yet for the gas component, we obtain significant offsets when AGN activity is included, as could have been expected from Figure 2.9. Also note that these non-rotational velocity components have much higher magnitudes than the rotational velocities. This effect is even more significant than in the observed MaNGA maps. However, the low-mass AGN host galaxies in MaNGA have a typical bolometric luminosity of $L_{\rm bol} = 3.7 \times 10^{41}$ ergs^{-1} so with a BH mass of 10^5 M$_\odot$, this would be approximately three per cent of the Eddington luminosity rather than the 10 or 100 per cent that we employ in our simulations.

[6]Note that in our simulations ionized gas is the result of AGN heating while we do not consider the effect of AGN radiation and how this may lead to additional ionized gas.

[7]The kinematic position angle describes the orientation of the velocity map, and is related to the projection of the angular momentum vector.

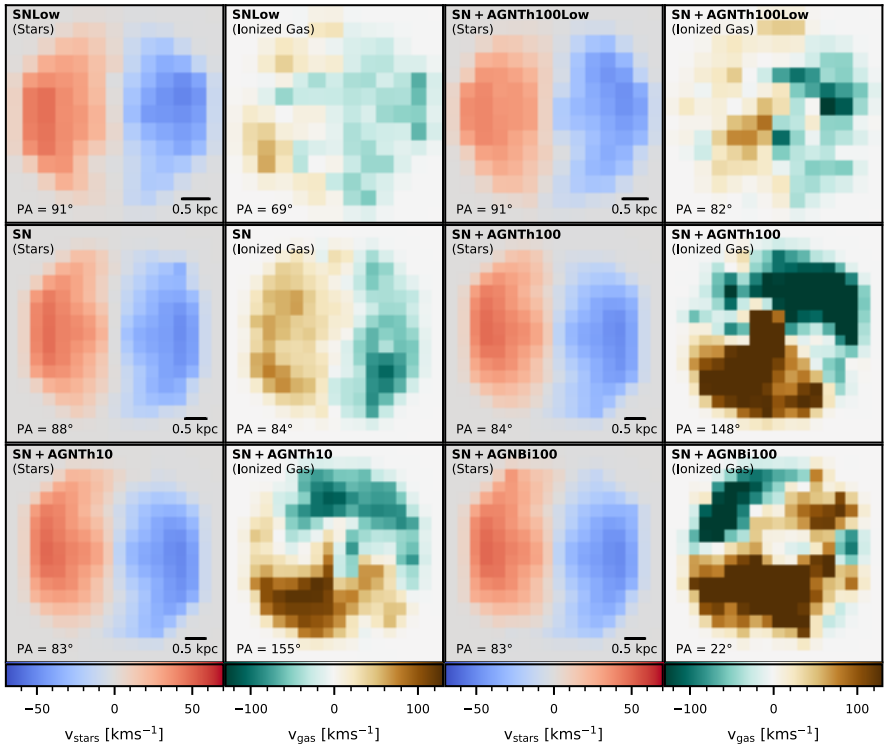

Fig. 2.10 Comparison between the line-of-sight velocity maps for stars and ionized gas at $t = 150$ Myr. Only gas and stars within $1.5R_{\rm eff}$ are included (in analogy to MaNGA), and the spatial resolution is matched to the MaNGA resolution at the mean redshift of the primary sample. For the AGN runs, the ionized gas is visibly offset from the stellar component.

We go on to construct velocity maps and measure the kinematic offsets for simulation outputs every 2 Myr between $t = 40$ Myr and $t = 300$ Myr (we choose 40 Myr as a starting time to allow the initial conditions to settle and the SN feedback to develop fully). We then use all of these values to calculate the probability for the offset to be at least a given angle θ for the three different inclination angles. These probability distributions are shown in the first three panels of Figure 2.11. The minimum angle for the gas to be categorised as 'kinematically offset' using the Penny et al. (2018) scheme, $\theta = 30°$, is shown as a grey dashed line. For all three inclination angles, galaxies with AGN are significantly more likely to be categorised as offset, and this difference increases with increasing inclination angle.

In the rightmost panel we show the probability distribution inferred from the thirteen quenched MaNGA galaxies which have both a detectable ionized gas and stellar component[8]. We separate out the seven galaxies which have been identified as star-forming (SF) or

[8]We adjust the kinematic offsets given by Penny et al. (2018) to be within $0° < \Delta{\rm PA} < 90°$ to facilitate comparison with our simulations which are always co-rotating.

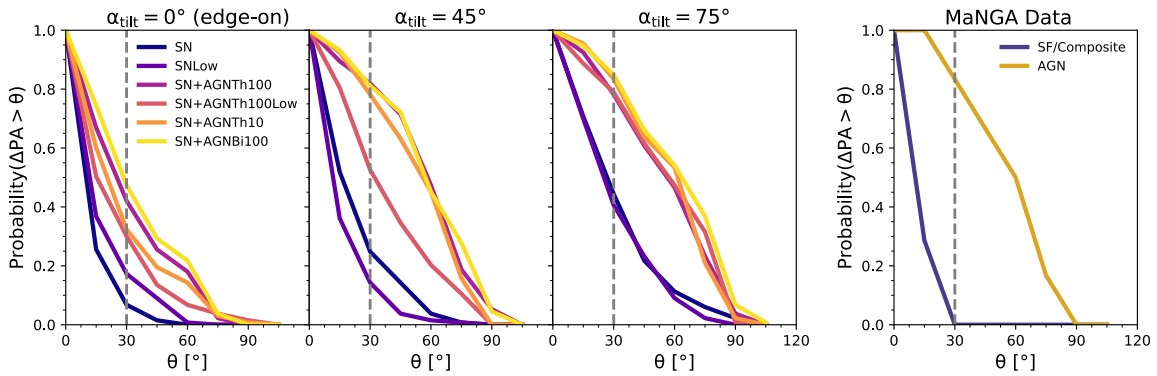

Fig. 2.11 Probability distribution for the kinematic offset between gas and stars to be at least an angle θ for different inclination angles of the disc from edge-on (0°) to nearly face-on (75°). These 'probabilities' are calculated as normalised frequencies of how often a certain offset is observed for $t > 40$ Myr. For the observed data, we use the thirteen quenched MaNGA galaxies from Penny et al. (2018), which also have a detectable ionized gas component. The minimum angle for the gas to be categorised as 'kinematically offset' using the Penny et al. (2018) scheme, $\theta = 30°$, is shown as a grey dashed line. For all three inclination angles galaxies with AGN activity are significantly more likely to be categorised as offset.

composite and the six galaxies which have been identified as AGN in the BPT diagram. As with our simulated galaxies, the probability to obtain significant offsets is much higher, and the frequency for different angles for the galaxies with an AGN is very similar to the distribution in our simulations. Though these probabilities should be treated with caution due to the small sample size. Also note that for MaNGA there is not a single galaxy without AGN activity which has been categorised as offset, while from our models we would expect between 10 and 30 per cent of SF galaxies to fall into that category. However, note that Penny et al. (2018) only select galaxies which have little or no star formation so by construction there should not be strong stellar feedback present in this sample. If we impose an arbitrary SFR cut on our simulated data points, e.g. SFR < 0.5 $M_{\odot}yr^{-1}$, the probability to obtain significant kinematic offsets with the SN only runs is significantly lower, while the probability distribution of the AGN runs is barely affected.

2.5 Discussion

We considered AGN-driven outflows in tandem with SN feedback to assess whether AGN activity affects dwarf galaxy properties. For this investigation, we made use of novel feedback models and a super-Lagrangian refinement scheme which allowed us to increase resolving power by up to three orders of magnitude in mass resolution around the black hole. We found that AGN feedback on its own only has a small effect on global SFRs. This is in line

with findings from other numerical simulations, e.g. Sijacki et al. (2007), Wadepuhl and Springel (2011), and Schaye et al. (2015) find that including AGN feedback in addition to SN feedback only has a negligible effect on SFRs for low-mass systems. The analytical findings from Dashyan et al. (2018), however, would suggest that AGN feedback should dominate over SN feedback for our set-up. While we do not obtain this, we find that AGN feedback has a significant effect on local quantities, e.g. the location of star formation and the driving of outflows. It seems that different from the distributed SN feedback, feedback from AGN is mainly local. The MaNGA survey (Penny et al., 2018) finds that dwarfs with observable signs of AGN activity have an ionized gas component that is kinematically offset from the stellar component suggesting that the AGN is causing outflows. We observe a similar effect in our simulations which further supports the supposition that this kinematic signature is AGN-driven.

However, note that we may be underestimating the effectiveness of SNe as we neither model other stellar feedback channels nor have a turbulent ISM model, which Hopkins et al. (2014) and Kimm et al. (2015) find to significantly enhance the ability of SNe to efficiently couple to the gas. This may reduce the gas supply to the central black hole or lead to hotter and faster outflows even with lower AGN luminosities. Further simulations are needed to explore these issues in detail.

Another shortcoming of our model is the isolated set-up meaning that we do not have gas inflows. The next step in this investigation would then be to run cosmological zoom-in simulations of AGN feedback in dwarf galaxies and investigate how the effectiveness of AGN feedback changes over cosmic time. Smith et al. (2019) find that in their SN only simulations of high-redshift dwarf galaxies, significant amounts of dense gas accumulate in the galaxy centre. This high-redshift behaviour is worth exploring as high central gas densities would facilitate the growth of IMBHs in the early Universe and also make it easier for AGN feedback to regulate the overall SFR. Furthermore, the more irregular and clumpy morphology of high-redshift dwarfs may facilitate AGN outflow leakage into the CGM. Preventive feedback in the form of CGM heating by the hot AGN-driven outflows might play a more important role than ejective feedback for AGN in dwarf galaxies (cf. Penny et al., 2018).

Other studies of AGN feedback in cosmological simulations of dwarf galaxies have found that SN feedback stunts accretion (see e.g. Habouzit et al., 2017; Trebitsch et al., 2018). However, we know that there are at least some AGN in dwarfs accreting efficiently from observations. To replicate this in numerical simulations we need a more elaborate accretion scheme than the currently widely adopted Bondi accretion model.

2.6 Conclusions

We have investigated the role of AGN-driven outflows in dwarf galaxies using isolated disc galaxy simulations. The disc contains the majority of the baryonic mass with $M_{\rm disc} = 3.5 \times 10^9$ M$_\odot$, and is gas-rich: 50 per cent of the initial disc mass is in gas akin to high-redshift analogues. We add a black hole of mass $M_{\rm BH} = 10^5$ M$_\odot$ allowing us to test AGN activity at the upper end of the IMBH range.

For this investigation, we made use of the star formation and SN feedback model by Smith et al. (2018) and the AGN model by Curtis and Sijacki (2015). We used different AGN outflow models, ranging from simple energy-driven spherical winds to collimated, mass-loaded, bipolar outflows, and employed a super-Lagrangian refinement scheme to accurately resolve the energy injection, increasing the gas resolution around the central black hole by three orders of magnitude. We tested two different star formation efficiencies, $\varepsilon_{\rm SF} = 0.015, 0.15$ and two different (constant) AGN luminosities $L_{\rm AGN} = 0.1 L_{\rm Edd}, 1.0 L_{\rm Edd}$. This way we could assess the maximum possible impact an AGN could have on this type of system. Our most important findings are the following:

1. There is a small but systematic effect of AGN outflows on central SFRs for all set-ups explored, while significant effects on the global SFR are only obtained with strong SN feedback and sustained high-luminosity isotropic AGN outflows ('SN+AGNTh100' run). This indicates that AGN feedback in dwarf galaxies is unlikely to directly regulate their global SFRs.

2. AGN activity in dwarf galaxies is however effective in enhancing outflows when there is also strong SN feedback present. If the SN feedback is inefficient, even adding an AGN shining at 100 per cent of the Eddington luminosity does not produce large mass loading factors.

3. With AGN feedback included, the outflows reach much higher velocities (up to 10^4 kms^{-1} compared to 10^2 kms^{-1} without an AGN) and much higher temperatures (up to 10^9 K instead of 10^7 K).

4. We find similar kinematic signatures as in observed dwarf galaxies hosting an AGN from the MaNGA survey. SN feedback alone does not drive strong enough outflows to significantly offset the rotational motion – even when the star formation efficiency is high and SN feedback is strong. This then strengthens the supposition by Penny et al. (2018) that these kinematic offsets are caused by an AGN-driven outflow.

Cosmological simulations are needed to fully answer the question of whether AGN feedback could affect star formation in dwarf galaxies. Our findings from the isolated galaxy set-up indicate that while AGN are unlikely to directly affect global dwarf SFRs, galactic outflows are significantly enhanced. In realistic cosmological environments inflows are known to be important especially for high-redshift dwarfs. It is hence possible that AGN-boosted outflows may prevent some of this cosmic 'pristine' gas reaching the dwarfs in the first place, providing a mechanism for indirect star formation regulation.

2.A Minimum mass parameter

Since we have a constant accretion rate, only the energy injection scheme needs to be converged, which does not necessarily require resolving the Bondi radius. The smallest mass scale of the super-Lagrangian refinement is set via the minimum mass parameter $m_{\rm min}$. Before setting up our main simulation suite presented in this chapter, we ran simulations equivalent to the 'SN+AGNBi100' set-up at lower resolution ($m_{\rm cell} = 2000\ {\rm M}_\odot$) to test the convergence behaviour of $m_{\rm min}$. The bipolar AGN feedback is particularly reliant on gas flows being accurately resolved due to the more complex injection scheme.

Projections of the Voronoi mesh for the four different runs ($m_{\rm min} = 0.002, 0.2, 20, 2000\ {\rm M}_\odot$, where the last one is simply a run without super-Lagrangian refinement) at $t = 25$ Myr are shown in Figure 2.12. The colour coding indicates the gas cell temperature. The bipolar cone structure is clearly visible for the lowest minimum mass run, $m_{\rm min} = 0.002\ {\rm M}_\odot$, and also discernible for $m_{\rm min} = 0.2\ {\rm M}_\odot$. There is no clear cone structure for the other two cases.

These mesh visualisations illustrate one of the main issues with not accurately resolving energy injection for any type of feedback. Massive gas cells, in general, have a higher absolute energy content. If the amount of energy injected into the cell is small compared to that overall energy content, the temperature change will be small and the gas cell will not get moved to a smaller time-step. If the gas cell's time-step is longer than the cooling time, the thermal energy is lost immediately. For the bipolar feedback scheme, additional considerations need to be taken into account. In particular with sustained, powerful feedback, the conical energy injection region can get almost completely depleted so that only a few cells actually have their centres in the injection region. In extreme cases, there are no gas cells in the 'allowed' bipolar cone region so that the energy cannot get injected. At $t = 25$ Myr with $m_{\rm min} = 20\ {\rm M}_\odot$, two massive cells located in the cone region have received the majority of the energy, whilst the cells in the very centre of the galaxy have received no energy as they are not within the cone region. The $m_{\rm min} = 2000\ {\rm M}_\odot$ overcools with no cells

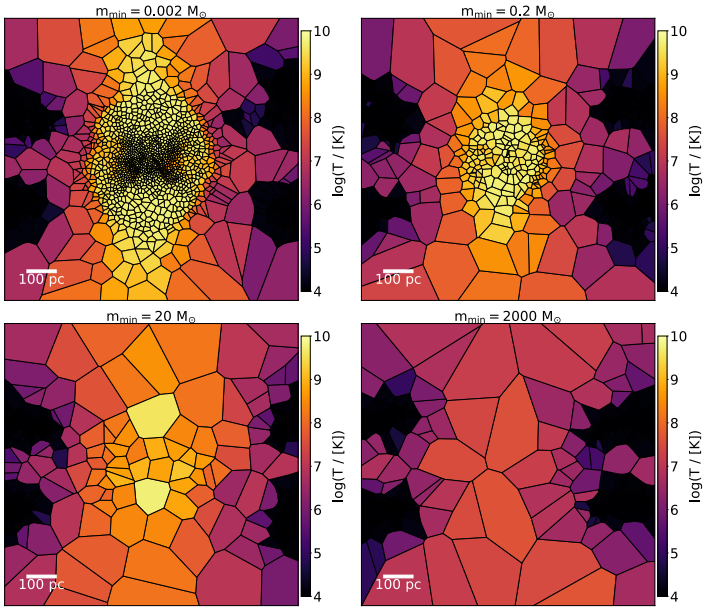

Fig. 2.12 $1.0 \times 1.0 \times 0.4$ kpc projections of the Voronoi mesh for the different convergence test runs ($m_{\rm min} = 0.002, 0.2, 20, 2000$ M$_\odot$, where the last one is simply a run without super-Lagrangian refinement) at $t = 25$ Myr. Colour coding indicates the temperature of the gas cells. Without the refinement scheme, the gas overcools. As the minimum mass is decreased, there is a sufficient number of cells within the bipolar cone region and cells retain high thermal energy content.

above 10^8 K in the inner region. This shows that to heat the ISM and CGM from the galaxy centre outwards with a conical geometry we require a minimum mass of at most 0.2 M$_\odot$.

Next, we gauge the effect of the minimum mass parameter more quantitatively, by assessing star formation and outflow convergence. Figure 2.13 shows the SFRs for the four bipolar feedback convergence runs. For comparison the SFR of the equivalent SN only run is also shown. Overall, the SFRs for the bipolar runs are in good agreement – within the expected fluctuations. From $t = 200$ Myr onwards, all of the bipolar runs are systematically offset from the SN only run though this offset is small, similarly to the equivalent high-resolution runs (cf. Figure 2.5).

Figure 2.14 shows the thermal energy outflow rate $\dot{U}_{\rm out}$ at three target heights, $H = 0.2$ kpc, $H = 2.0$ kpc, and $H = 20.0$ kpc, for a slice of thickness d$z = 200$ pc. There are two significant differences to note. Firstly, the driving of outflows on large scales is slightly delayed without extra refinement, suggesting that we need the super-Lagrangian refinement to efficiently drive outflows. Secondly, there are significant differences in the thermal energy outflow rates, especially at small scales. The lower the minimum mass, the more efficiently thermal energy is transported away from the black hole. Even at large scales, $H = 20.0$ kpc, there is still a factor five difference when the super-Lagrangian refinement scheme is

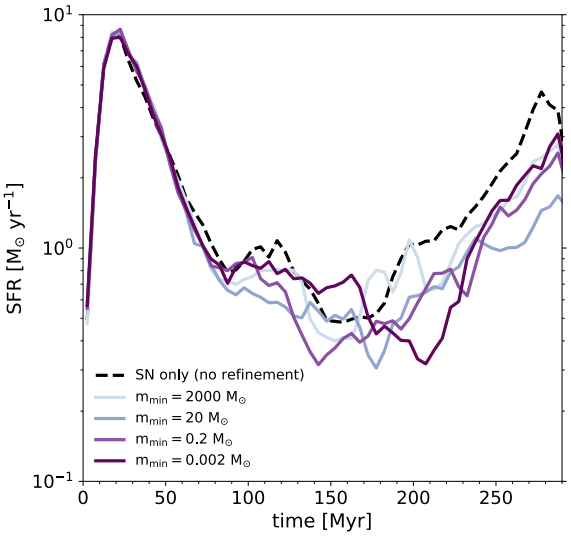

Fig. 2.13 SFRs as a function of time for the low resolution AGN convergence test runs. For comparison the SN only run is also shown. The SFRs of all AGN runs are in good agreement, within the expected fluctuations. From $t = 200$ Myr onwards, the SFRs of the AGN runs are systematically lower than the SFRs of the SN run.

employed. We also inspected velocity histograms split by temperature and found that there is more fast and very hot gas with additional refinement. For the overall mass outflow rate and average outflow velocity, there are no significant differences between the schemes, as these are dominated by the slower moving warm phase, present in all of the runs.

Overall, we conclude that for the thermal outflow properties to be converged, we need a minimum mass in the refinement region of at most 0.2 $M_\odot$, even though for getting SFRs converged this is not crucial, as the cold star-forming phase is not affected.

2.B Super-Lagrangian refinement scheme and feedback

The super-Lagrangian refinement scheme sets a range of allowed cell radii for the gas cells within the refinement radius $R_{\rm ref}$. Recall that the refinement radius is set equal to the black hole smoothing length so that we will have a larger refinement region for lower central densities (see Section 2.2.2). The maximum cell radius at the boundary of the refinement region is set proportional to the refinement region radius. Both radii are related to the target gas cell mass via the boundary cell density and the average refinement region density, respectively. However, these two radii will only be proportional to each other, if we assume the ratio of these two densities to be constant. For example, if we assume these two densities to be equal, the ratio should be approximately 0.3.

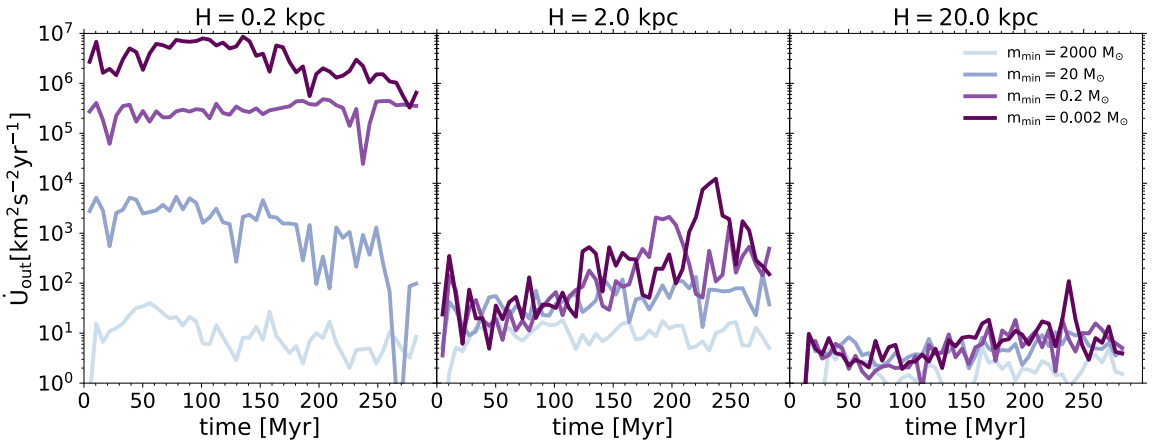

Fig. 2.14 Thermal energy outflow rates as a function of time for the low resolution AGN convergence test runs calculated at target heights H = 0.2 kpc (left panel), H = 2.0 kpc (middle panel), and H = 20.0 kpc (right panel). Thermal energy outflow rates are significantly higher with super-Lagrangian refinement and decreasing minimum mass. This effect is particularly significant at small scales.

We expect the average refinement region density to be lower than the value at the boundary, since the latter is less affected by feedback, and therefore choose a fiducial value of $r_{\rm cell,boundary} = 0.1R_{\rm ref}$. With strong feedback, this value might need to be even lower, and with weak feedback, leaving the refinement region with a relatively uniform density, this value would need to be higher. We do not want to overtune our simulations, so we use $r_{\rm cell,boundary} = 0.1R_{\rm ref}$ for all of our runs. Figure 2.15 shows the cell size distribution for the low and high star formation efficiency runs at $t = 25, 150, 300$ Myr. We plot average cell size against distance from the black hole to check whether the gas cells within the smoothing length have been properly refined. For comparison, we also show the cell sizes for a run with the same set-up as 'SN+AGNTh100' but without super-Lagrangian refinement around the black hole.

Firstly, we note that the cells in the refinement region, whilst much smaller in mass, are not necessarily smaller in volume. This is because in our simulations, the refinement scheme mainly counteracts the strong AGN feedback inflating the cells around the black hole, leading to relatively smooth cell sizes, rather than ultra refined ones. For both of the high-luminosity thermal runs, there are sharp transitions in cell size at the refinement region border. For 'SN+AGNTh100', these always go to larger cell sizes as the central region has very low densities due to the early, high SN activity and aggressive AGN feedback. For the 'SN+AGNTh100Low' run, there is a transition to smaller cell sizes. The transitions for the 'SN+AGNBi100' and 'SN+AGNTh10' run are more regularized, since the former does not inject energy directly into the disc, and the latter is at lower luminosity and less aggressive.

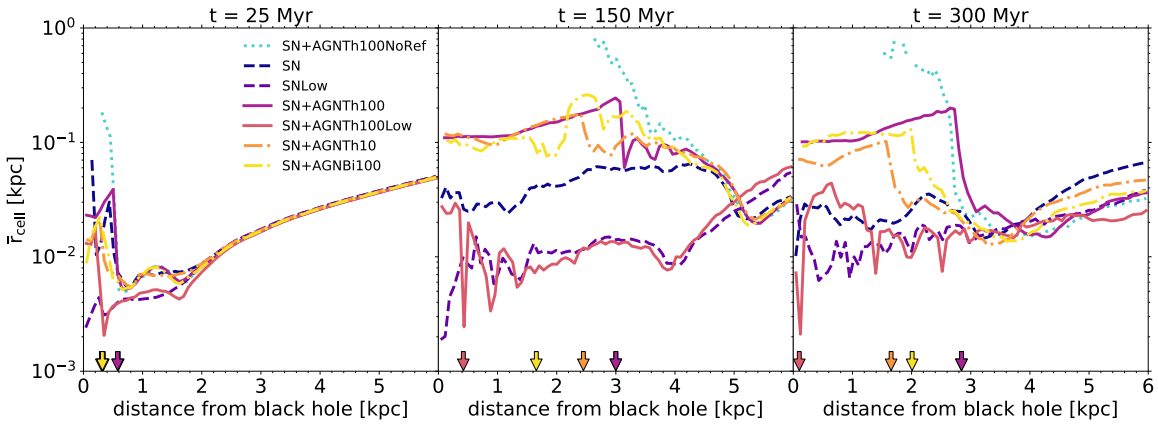

Fig. 2.15 Mean gas cell radii as a function of distance from the black hole for all feedback runs at $t = 25, 150, 300$ Myr. For comparison, we also show the cell sizes for a run with the same set-up as 'SN+AGNTh100' but without super-Lagrangian refinement around the black hole. The respective sizes of the refinement region are indicated by the coloured arrows. The AGN energy injection significantly lowers the density of the central region. Without additional refinement, central cell sizes reach ~ 1 kpc and we therefore do not have any gas cell centres near the black hole at late times. The super-Lagrangian refinement scheme counteracts this cell size inflation and the region around the black hole stays well-resolved.

However, note that without super-Lagrangian refinement, the cell size transition is even more extreme, sharply rising to ~ 1 kpc. Furthermore, due to the inflated cell sizes, there are no gas cell centres in the central kpc at late times.

Also note that there are similar spatial resolution issues with any kind of extreme feedback, e.g. the strong SN feedback in the 'SN' run also leads to larger cell sizes in the centre, in particular at early times. In addition, there are some small discontinuities simply from using up the central dense gas in star formation which introduces a bias towards larger cell sizes at the centre of the galaxy.

Curtis and Sijacki (2015) already noticed this issue with constant accretion schemes and found that if they go higher than ten per cent of the initial Eddington rate, the gas gets blown away on a short time-scale. As we only run our simulations for up to 300 Myr, we still have enough gas to feed the black hole, however this is an important caveat of the constant accretion scheme that needs to be kept in mind when testing extreme cases. Though this is beyond the scope of this chapter exploring the effects of additional regularisation mechanisms (e.g. setting a maximum volume ratio for neighbouring cells) would be desirable for a future study.

Figure 2.16 shows the volume-weighted distribution of cell masses in the central region at $t = 25$ Myr. The minimum allowed gas cell mass 10^{-1} $M_\odot$ (cells have to be within a factor two of the minimum mass 2×10^{-1} $M_\odot$) is indicated as a horizontal grey line. A significant

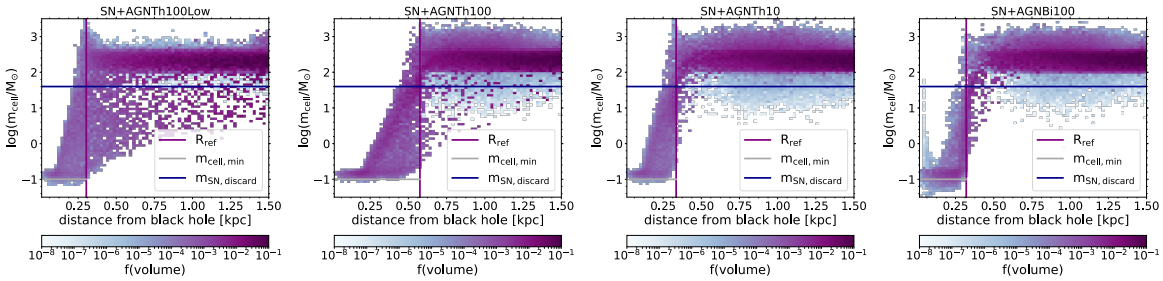

Fig. 2.16 Volume-weighted distribution of gas cell masses as a function of distance from the black hole for the runs with AGN feedback runs at $t = 25$ Myr. The border of the refinement region is indicated in purple, the minimum gas mass in grey, and the minimum mass for hosting a SN in blue.

fraction of gas cells in the refinement region reach the minimum mass, which we will have to keep in mind for the interpretation of our results. For the bipolar injection scheme we also have some cells close to the black hole with much higher masses, these are the cells outside the cone region which are unaffected by feedback and therefore have a much higher density. This figure also shows how many gas cells fall below the cut-off mass for hosting SNe $m_{\rm SN,discard}$ (indicated as a blue horizontal line). Outside of the refinement region only a negligible amount of gas cells is below the SN threshold mass suggesting that SN rates should not be severely affected by this criterion.

To make this claim more quantitative, we show the number of discarded SNe as well as the ratio between discarded and total number of SNe for all AGN runs in Figure 2.17. For comparison, we also show the SFRs of the high-luminosity thermal AGN runs, including the high $\varepsilon_{\rm SF}$ run without additional refinement, and the SN only runs. Most of the SNe are discarded at early times, however, as can be seen from the SFRs, this does not affect global star formation. For the first ~ 25 Myr, there is a rapid gas collapse from the initial conditions and SNe are not effective. Therefore losing SNe at early times will have a small effect. Overall, the discarded fraction is approximately 2 per cent for 'SN+AGNTh100Low', 6 per cent for 'SN+AGNTh10', 7 per cent for 'SN+AGNBi100', and 18 per cent for 'SN+AGNTh100'. For the first three, the discarded fraction is not significant but nevertheless non-negligible and could have a small effect on total feedback energetics. The high discarded fraction for the 'SN+AGNTh100' run is largely due to the aggressive constant isotropic feedback, heating up and dispersing the gas around the black hole. However, this aggressive feedback also means that the inner region, where we discard the SNe, is significantly heated up anyway so additional SNe would not make much of a difference here, as can be seen from the negligible difference in SFRs between 'SN+AGNTh100' and 'SN+AGNTh100NoRef'. Also note that the same SN event might get discarded repeatedly so our discarded SNe fractions represent an upper limit.

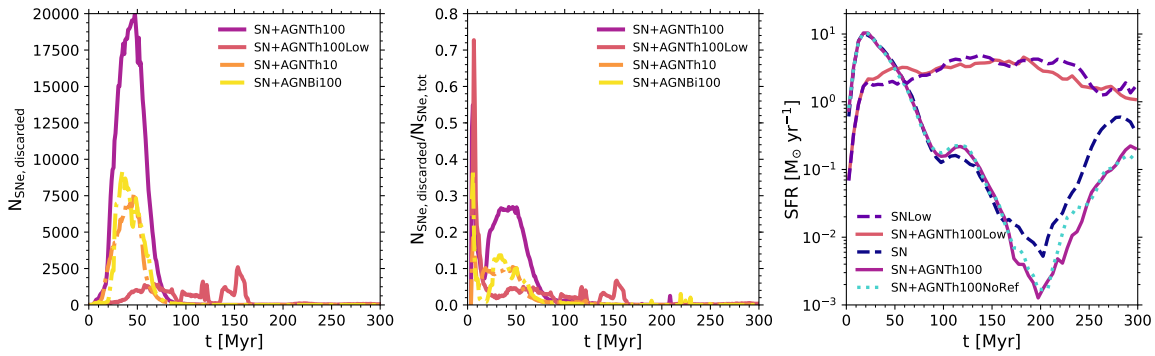

Fig. 2.17 The impact of discarding SNe in super-refined cells ($m_{\rm cell} < 0.2 m_{\rm target}$). *Left panel*: number of discarded SNe against time. *Middle panel*: fraction of discarded SNe against time for the AGN feedback runs. *Right panel*: SFRs for the most aggressive AGN feedback models (thermal feedback at the Eddington luminosity) and the SN only runs as well as the thermal AGN feedback run without additional refinement ('SN+AGNTh100NoRef'), for the latter two virtually no SNe are discarded as we do not use the super-Lagrangian refinement scheme. Note that even though a significant number of SNe get discarded at early times (between 6 and 28 per cent), the SFRs are not affected. This is because the inner region, where we discard the SNe, is already heated up by the AGN activity so additional SNe would not make much of a difference here.

CHAPTER 3

EXPLORING AGN FEEDBACK IN DWARF GALAXIES WITH COSMOLOGICAL SIMULATIONS

3.1 Background

At the high-mass end of the galaxy population, simulations have shown that feedback from active galactic nuclei (AGN) can bring stellar properties into agreement with observations (Puchwein and Springel, 2012; Dubois et al., 2014a; Vogelsberger et al., 2014b; Khandai et al., 2015; Schaye et al., 2015; Weinberger et al., 2017; Henden et al., 2018). However, whether reionization and supernova (SN) feedback are sufficient to regulate the low-mass end of the galaxy stellar mass function (GSMF) is still unclear (see Sections 1.4.1 and 1.4.2 for an overview of feedback mechanisms in low-mass and high-mass galaxies, respectively). Recently, it has been speculated that AGN may also contribute to regulating star formation at the low-mass end (see e.g. Silk, 2017). This idea has been motivated by several observational studies which have identified a population of dwarf galaxies hosting AGN (see Section 1.4.3 for a detailed summary of the observational evidence for AGN in dwarfs).

So far theoretical investigations have yielded mixed results. On the one hand, analytical models of AGN feedback in dwarf galaxies look promising, suggesting that AGN could provide an alternative and more successful source of negative feedback than SNe (Silk, 2017; Dashyan et al., 2018). On the other hand, in numerical simulations, strong SN feedback can hinder the growth of black holes (BHs) in low-mass galaxies rendering AGN feedback ineffective (see e.g. Dubois et al., 2015; Anglés-Alcázar et al., 2017b; Habouzit et al., 2017; Trebitsch et al., 2018). However, if BHs in simulations are able to grow efficiently, they can have a significant impact on their hosts (Barai and De Gouveia Dal Pino, 2019; Sharma et al., 2020).

In Chapter 2, we systematically tested the effect of AGN activity in a series of isolated simulations of dwarf galaxies. We found that the outflows reach significantly higher velocities and temperatures with added AGN feedback. However, AGN activity did not have a significant effect on the global star formation rate (SFR) in our isolated set-up.

The considerations above suggest an interesting possibility that AGN feedback may play an indirect role in regulating star formation at the low-mass end. For example, the AGN-boosted outflows might be able to hinder cosmic gas inflows. Cosmological simulations are needed to investigate these possibilities.

In this chapter, we use the FABLE (*Feedback Acting on Baryons in Large-scale Environments*) simulation suite (Henden et al., 2018, 2019, 2020) to explore the role of AGN feedback in the low-mass regime within a realistic cosmological environment. Keeping in mind that the FABLE parameters have been tuned so that SN feedback is strong to regulate the low-mass end of the GSMF, we investigate whether low-mass galaxies with efficient BH growth have significantly different physical properties than the ones without AGN activity - with a particular focus on outflow properties and SFRs. Though we note that any effect we find from AGN feedback in the low-mass regime is likely to be a lower limit. Furthermore, we aim to compare the FABLE galaxies to observations of dwarf galaxies with AGN and to make predictions for future observations.

The outline of this chapter is as follows. We describe the characteristics of the FABLE simulation suite and the sub-grid models in Sections 3.2.1 and 3.2.2, respectively. The methods for identifying haloes and galaxies in FABLE and the definition of the low-mass galaxy sample are given in Section 3.2.3 and we describe how we calculate the outflow properties of these galaxies in Section 3.2.4. Our methods for creating mock MaNGA observations and X-ray luminosities are outlined in Sections 3.2.5 and 3.2.6. In Section 3.3, we present our results on the AGN population (Section 3.3.1), the scaling relations (Section 3.3.2), the properties of low-mass galaxies with overmassive BHs (Section 3.3.3), mock MaNGA observations (Section 3.3.4), and mock X-ray observations (Section 3.3.5). We discuss our results in Section 3.4 and summarise our main findings in Section 3.5.

3.2 Methodology

3.2.1 Basic simulation properties

We use the cosmological simulation suite FABLE for our analysis of AGN feedback in low-mass galaxies. The FABLE simulation suite is extensively described in Henden et al. (2018), and only a brief summary is given below.

The FABLE simulations were carried out with the massively parallel AREPO code (Springel, 2010), where fluid dynamics is discretized on a moving mesh using a quasi-Lagrangian finite volume technique. The unstructured mesh is based on the Voronoi tessellation of a set of discrete points that cover the whole computational domain. These mesh-generating points are allowed to move with the local flow velocity, with minor corrections to avoid excessive distortion of the gas cells. Gravitational interactions are modelled using the TreePM approach, with stars and DM modelled as collisionless particles.

The FABLE suite consists of a large-volume cosmological box simulation as well as a series of zoom-in simulations of individual groups and clusters. As we are interested in low-mass galaxies in representative regions of the Universe, we focus only on the results from the cosmological box for this study.

The comoving 40 h^{-1} Mpc box was evolved using initial conditions for a uniformly-sampled cosmological volume based on a Planck cosmology (see Planck Collaboration XIII, 2016). The volume contains 512^3 DM particles with masses $m_{\rm DM} = 3.4 \times 10^7\ h^{-1}\,{\rm M}_\odot$ and initially 512^3 gas resolution elements with target mass $\overline{m}_{\rm gas} = 6.4 \times 10^6\ h^{-1}\,{\rm M}_\odot$. The gravitational softening length is set to 2.393 h^{-1} kpc in physical coordinates below $z = 5$ and fixed in comoving coordinates at higher redshift.

The FABLE sub-grid models are largely based on the Illustris galaxy formation model (Vogelsberger et al., 2013; Genel et al., 2014; Torrey et al., 2014; Vogelsberger et al., 2014b; Sijacki et al., 2015). Whilst the models for star formation (Springel and Hernquist, 2003), radiative cooling (Katz et al., 1996; Wiersma et al., 2009a), and chemical enrichment (Wiersma et al., 2009b) are unchanged from Illustris, the stellar feedback (Vogelsberger et al., 2013) and AGN feedback (Di Matteo et al., 2005; Springel et al., 2005a; Sijacki et al., 2007, 2015) models have been updated (see Section 3.2.2). Both the stellar and the AGN feedback models were calibrated to reproduce observations of the local GSMF and the gas mass fractions of observed massive haloes.

3.2.2 Feedback models

3.2.2.1 Stellar feedback

Stellar feedback is included as a sub-grid model for galactic winds and outflows (see Vogelsberger et al., 2013, for details). In the Illustris simulation, these winds are purely kinetic. In FABLE, this is modified so that one third of the wind energy is imparted as thermal energy, which slows down the cooling of the gas thereby increasing the overall effectiveness of the stellar feedback (see Marinacci et al., 2014; Henden et al., 2018).

3.2.2.2 BH seeding and growth

BHs are modelled as collisionless sink particles. BH seeds of mass $M_{\rm BH,seed} = 10^5\ h^{-1}\,{\rm M}_\odot$ are placed into every DM halo above $5 \times 10^{10}\ h^{-1}\,{\rm M}_\odot$. Subsequently, these seeds can grow via mergers with other BHs and via gas accretion (see Vogelsberger et al., 2013, for details). In brief, BH particles accrete at the Eddington-limited Bondi-Hoyle-Lyttleton-like rate boosted by a factor of $\alpha = 100$ (Hoyle and Lyttleton, 1939; Bondi and Hoyle, 1944; Springel et al., 2005a). The radiative efficiency is set to be a constant $\varepsilon_{\rm r} = 0.1$. A fraction of $(1 - \varepsilon_{\rm r})$ of the accreted mass is added to the BH mass, whilst the rest is available as feedback energy.

Following Illustris, FABLE uses a repositioning scheme to ensure that the BH particle stays at the gravitational minimum of its host halo. This prevents spurious BH movement due to two body scattering effects with massive DM or star particles (see Sijacki et al., 2015). Though we note that this also precludes us from investigating physical off-nuclear BH motion as has been found in some observations (e.g. Mezcua and Domínguez Sánchez, 2020; Reines et al., 2020) and simulations (e.g. Bellovary et al., 2019) of dwarf galaxies. However, there are currently only few firm observational indications of offset massive BHs (e.g. Komossa, 2012; Shen et al., 2019). Also see Tremmel et al. (2018) for a discussion of off-nuclear BHs in more massive objects.

3.2.2.3 AGN feedback

In analogy to Illustris, the AGN feedback operates in either one of two states depending on the Eddington fraction $f_{\rm Edd}$: the high accretion rate quasar mode (Di Matteo et al., 2005; Springel et al., 2005a) or the low accretion rate radio mode (Sijacki et al., 2007). The BH particles switch to the quasar mode once they exceed a critical Eddington fraction $f_{\rm Edd,QM}$. In the FABLE model, this threshold is set to $f_{\rm Edd,QM} = 0.01$.

This AGN feedback model has been modified in FABLE by introducing a duty cycle to the quasar mode. The feedback energy is accumulated over $\delta t = 25$ Myr, before being released in a single event, to reduce overcooling (see Booth and Schaye, 2009; Henden et al., 2018). The remainder of the feedback energy that is not coupled to the surrounding gas by the quasar or radio mode goes into radiative electromagnetic feedback, which is approximated as an additional radiation field around the BH superposed with the redshift-dependent ultraviolet background (Vogelsberger et al., 2013).

3.2.3 Galaxy identification

Haloes and subhaloes are identified via friends-of-friends (FoF) and SUBFIND algorithms (Davis et al., 1985; Springel et al., 2001a; Dolag et al., 2009). For the FoF search, we choose a linking length of 0.2 multiplied by the mean inter-particle separation. We then use SUBFIND to identify gravitationally self-bound subhaloes within each FoF halo. The 'central subhalo' is the subhalo at the minimum gravitational potential of the FoF halo. All other subhaloes in the FoF halo are categorised as satellite subhaloes.

We consider each subhalo with at least 100 star particles to be a resolved galaxy, yielding a minimum stellar mass of approximately 10^9 $M_\odot$. For this investigation, we only consider central subhaloes, as our focus is on intrinsic feedback processes rather than environmental effects.

At each redshift, our low-mass galaxy sample consists of all central subhaloes that host a BH and have a stellar mass in the range $9.0 \leq \log(M_{\rm stellar}\ [{\rm M}_\odot]) < 10.5$ at the given redshift. Stellar mass here is defined as the mass of all star particles within twice the stellar half-mass radius, $r_{\rm eff}$. The minimum mass is set by the above resolution requirements. In addition, we restrict our sample to galaxies with masses below the knee of the GSMF ($\mathscr{M}^* = 10^{10.5}$ $M_\odot$), where AGN feedback had previously been assumed to be ineffective.

To investigate the impact of AGN feedback as a function of stellar mass, we divide up the low-mass galaxy sample into three mass bins of equal widths in log space: dwarf galaxies ($9.0 \leq \log(M_{\rm stellar}\ [{\rm M}_\odot]) < 9.5$), massive dwarf galaxies ($9.5 \leq \log(M_{\rm stellar}\ [{\rm M}_\odot]) < 10.0$), and $\mathscr{M}^*$ galaxies ($10.0 \leq \log(M_{\rm stellar}\ [{\rm M}_\odot]) < 10.5$).

3.2.4 Outflow properties

We would like to assess whether AGN feedback can have an impact on the overall outflow properties of low-mass galaxies. To this end, we extract the outflow properties from the simulation data for the whole gas (i.e. not separating out the different gas phases). Though note that FABLE does not include cooling below 10^4 K, so these outflow properties mainly correspond to the warm and to the hot gas phase.

We obtain the outflow properties for each galaxy as follows: Firstly, we centre the gas coordinates on the potential minimum of the galaxy. Then we subtract the peculiar velocity (here defined as the mass-weighted mean velocity of all gas cells within twice the virial radius[1], $2R_{\rm vir}$) from the gas velocities. We then calculate the outflow properties at two

[1]Throughout this chapter, the virial quantities of a system are defined by a mean density of 200$\times$ the critical density of the Universe.

different target radii $r_t = 0.2R_{vir}, R_{vir}$ within shells of widths $\Delta r = 10, 20$ kpc, respectively[2]. We select all gas cells within the $r_t \pm \frac{\Delta r}{2}$ shell and calculate the radial velocities v_r for all of these cells. We then mark gas cells with $v_r < 0$ as inflowing and gas cells with $v_r > 0$ as outflowing. Note that we only calculate the outflow properties for galaxies that have at least ten gas cells (at least five inflowing and at least five outflowing) within the shell considered.

We then use the inflowing and outflowing gas cells to calculate the mass flow rates through the $r_t \pm \frac{\Delta r}{2}$ shell as follows:

$$\dot{M}_{out} = \sum_{\substack{|r-r_t|<\frac{\Delta r}{2} \\ v_r>0}} \frac{m_{cell} v_r}{\Delta r}, \tag{3.1}$$

$$\dot{M}_{in} = \sum_{\substack{|r-r_t|<\frac{\Delta r}{2} \\ v_r<0}} \frac{m_{cell} v_r}{\Delta r}, \tag{3.2}$$

$$\dot{M}_{tot} = \dot{M}_{out} + \dot{M}_{in}. \tag{3.3}$$

Here m_{cell} is the gas cell mass, $\dot{M}_{out}$ is the outflow rate, $\dot{M}_{in}$ is the inflow rate, and $\dot{M}_{tot}$ is the total mass flow rate.

We also calculate the outflow velocities and temperatures. We define the outflow velocity, v_{out}, as the mass-weighted mean velocity of all gas cells within the shell centred at r_t with $v_r > 0$. Similarly, we define the outflow temperature, T_{out}, as the mass-weighted mean temperature of all cells within the shell centred at r_t with $v_r > 0$.

Using the above quantities, we then also calculate the momentum outflow rate, $\dot{P}_{out}$, and the kinetic energy outflow rate, $\dot{E}_{kin,out}$, as:

$$\dot{P}_{out} = \sum_{\substack{|r-r_t|<\frac{\Delta r}{2} \\ v_r>0}} \frac{m_{cell} v_r}{\Delta r} v_r, \tag{3.4}$$

$$\dot{E}_{kin,out} = \frac{1}{2} \sum_{\substack{|r-r_t|<\frac{\Delta r}{2} \\ v_r>0}} \frac{m_{cell} v_r}{\Delta r} v_r^2. \tag{3.5}$$

Finally, we also calculate the mass loading factor, β, as

$$\beta = \frac{\dot{M}_{out}}{SFR(r \leq r_t)}, \tag{3.6}$$

[2]Note that in both cases we tested various shell widths and found that the results are well converged and do not depend on the exact choice of Δr, as long as the width is large enough to have a sufficient number of gas cells within the shell.

where SFR($r \leq r_t$) is the summed up SFR of all gas cells within r_t.

3.2.5 Mock MaNGA maps

The MaNGA survey found kinematically misaligned gas in quenched dwarf galaxies with AGN signatures hinting at AGN-driven outflows (see Penny et al., 2018). In Chapter 2, we created mock MaNGA maps of isolated simulations of dwarf galaxies to explore these kinematic offsets (see Section 2.4.4). Here we adapt this procedure to cosmological simulations, as described below.

3.2.5.1 Sample selection

To accurately determine the kinematic position angle (PA), the galaxies need to have clear rotational features. To automatically select galaxies that are rotationally supported, we only keep galaxies with $V_{max}/\sigma > 1.1$, where V_{max} is the maximum value of the respective subhalo's spherically averaged rotation curve and σ is the 3D velocity dispersion of the same subhalo. Visual inspection of our sample galaxies confirms that this is an efficient criterion for ensuring sufficient rotational support.

All star particles or ionized gas cells that belong to the galaxy's FoF group are included along the projection direction for the mock line-of-sight (l.o.s.) velocity maps. We require that there should be at least 50 star particles and 50 ionized gas cells within the $1.5r_{eff}$ 2D aperture (corresponding to the spatial coverage of the primary MaNGA sample). Here r_{eff} is the stellar half-mass radius. This ensures that the kinematics are well resolved by the simulation. Due to the weightings (see Section 3.2.5.2) the projected l.o.s. velocities are mostly sensitive to the kinematics of the central galaxy and are measured up to the scale of the virial radius, and therefore these measurements are only minimally affected by the (significantly smaller) gravitational softening.

3.2.5.2 Line-of-sight velocity maps

We match the resolution of our mock MaNGA maps to the pixel size of the MaNGA final reduced data cubes (0.5 arcsec). We analyse three different redshifts ($z = 0$, 0.2, 0.4). Note that for the local $z = 0$ sample, we calculate the spatial resolution assuming that these galaxies are observed at the mean redshift of the primary MaNGA sample, $\bar{z} = 0.03$. We do not consider higher redshifts than $z = 0.4$, as the resolution of the MaNGA survey would prohibit us from confidently identifying kinematic PAs.

We create separate l.o.s velocity maps for the star particles and the ionized gas cells. We keep all gas cells with neutral hydrogen abundance, fraction of the hydrogen cell mass (or density) in neutral hydrogen, $n_{\rm H,neutral} < 10^{-2}$ to isolate the ionized gas[3].

For each subhalo, we centre the velocity map on the minimum gravitational potential and subtract the systemic velocity, here taken as the mass-weighted mean velocity within $1.5r_{\rm eff}$.

To separate out the effect of the inclination angle on kinematic misalignments, we rotate all galaxies into the same orientation for our analysis. To this end, we calculate the stellar total angular momentum $\mathbf{J}_{\rm stellar}$ within $1.5r_{\rm eff}$ and rotate each galaxy (both stars and gas) so that $\mathbf{J}_{\rm stellar}$ is aligned with the z-axis. We then project the stellar / gas kinematics onto the y-z plane so that all galaxies are viewed edge-on. As an optional additional step, the disc can then be inclined by rotating about the y-axis to test the effect of the inclination angle.

We project the ionized gas / stellar velocity distribution onto a grid corresponding to the spatial extent and resolution of the MaNGA data. We define the stellar smoothing length as the radius enclosing the 64 nearest neighbours and the gas smoothing length as 2.5 times the cell radius. We set a maximum smoothing length as 50 times the pixel size, though in practice that limit is rarely reached.

We weight the velocity contributions to each pixel by the cubic spline smoothing kernel. In addition, we impose a luminosity-like weighting: the stars by their mass[4] and the gas cells by the square of their density. Note that when creating these smoothed maps we consider all resolution elements within a $2.5r_{\rm eff}$ 2D aperture as some might contribute to pixels within the $1.5r_{\rm eff}$ 2D aperture even though their centres lie outside that aperture.

Finally, we convolve the resulting velocity map with a Gaussian filter of FWHM $= 2.5$ arcsec to model the effect of the MaNGA PSF.

3.2.5.3 Kinematic position angles

The kinematic PA is related to the projected angular momentum vector and traces the position of the maximum change in velocity on the map (see e.g. Krajnović et al., 2006). Following Penny et al. (2018), we determine the kinematic PAs of both ionized gas and stars using the `fit_kinematic_pa` routine (see Krajnović et al., 2006, for a detailed description). Note that this routine only returns PAs in the range $0° \leq {\rm PA} < 180°$, which does not take the sense of

[3] We plotted the $n_{\rm H,neutral} - v_{\rm l.o.s.}$ distribution for a sample of galaxies across different mass bins and redshifts, and found that there was a clear break below that value.

[4] We repeated these measurements for a subset of our galaxy sample weighting the star particle contributions by the stellar bolometric luminosity instead of by the stellar mass. We found that the results regarding the kinematic PA are not affected but that the velocity maps look somewhat different because the rotationally supported stars enter with different weights.

the rotation into account. We identify the redshifted part of the velocity map to convert the PAs to the $0° \leq \mathrm{PA} < 360°$ range.

The kinematic offset between gas and stars is then defined as $\Delta\mathrm{PA} = |\mathrm{PA}_{\mathrm{stars}} - \mathrm{PA}_{\mathrm{gas}}|$. Gas and stars are considered to be in dynamical equilibrium if $\Delta\mathrm{PA} = 0°$or $180°$. As in the observational study by Penny et al. (2018), we then define the gas as kinematically misaligned if $30° \leq \Delta\mathrm{PA} < 150°$.

3.2.6 Mock X-ray luminosities

X-ray studies by *Chandra* and *XMM-Newton* have resulted in large samples of AGN candidates in low-mass galaxies. As X-ray surveys push to higher redshifts, it has become possible to start studying the redshift evolution of AGN activity in these galaxies. To compare the AGN population in FABLE to these observational findings, we calculate the X-ray properties of the FABLE galaxies.

We define the bolometric BH luminosity as $L_{\mathrm{BH}} = \varepsilon_{\mathrm{r}} \dot{M}_{\mathrm{BH}} \mathrm{c}^2$, where ε_r is the radiative efficiency, $\dot{M}_{\mathrm{BH}}$ is the BH accretion rate and c is the speed of light (see Section 3.2.2.3). To obtain the BH luminosities in the soft (0.5 - 2 keV) and hard (2 - 10 keV) X-ray band, we use the bolometric corrections from Shen et al. (2020). To assess the detectability of these low-luminosity AGN, we also estimate the X-ray luminosities of X-ray binaries (XRBs) and the hot gas in the galaxy.

To obtain an estimate for the contribution from XRBs, we use the redshift-dependent relation from Lehmer et al. (2016) which relates the total X-ray luminosity $L_{\mathrm{X,XRB}}$ to the SFR and stellar mass (M_{stellar}):

$$\left(\frac{L_{\mathrm{X,XRB}}}{\mathrm{erg\,s^{-1}}}\right) = \alpha_0 (1+z)^{\gamma} \left(\frac{M_{\mathrm{stellar}}}{\mathrm{M_\odot}}\right) + \beta_0 (1+z)^{\delta} \left(\frac{\mathrm{SFR}}{\mathrm{M_\odot\,yr^{-1}}}\right). \tag{3.7}$$

The parameter values in the soft X-ray band are $\log(\alpha_0) = 29.04$, $\log(\beta_0) = 39.38$, $\gamma = 3.78$, and $\delta = 0.99$. In the hard X-ray band, the parameter values are given by $\log(\alpha_0) = 29.37$, $\log(\beta_0) = 39.28$, $\gamma = 2.03$, and $\delta = 1.31$. To estimate the FABLE luminosities, we evaluate both the SFR and M_{stellar} within $2r_{\mathrm{eff}}$.

We calculate the hot gas contribution using the relationship between the X-ray luminosity of the diffuse ISM and the SFR from Mineo et al. (2012):

$$\left(\frac{L_{\mathrm{X,gas}}}{\mathrm{erg\,s^{-1}}}\right) = 8.3 \times 10^{38} \times \left(\frac{\mathrm{SFR}}{\mathrm{M_\odot\,yr^{-1}}}\right). \tag{3.8}$$

Again, we calculate the SFR within $2r_{\mathrm{eff}}$ here. Note that the above relation only applies to soft X-ray luminosities. To obtain the contribution in the hard X-ray band, we assume a

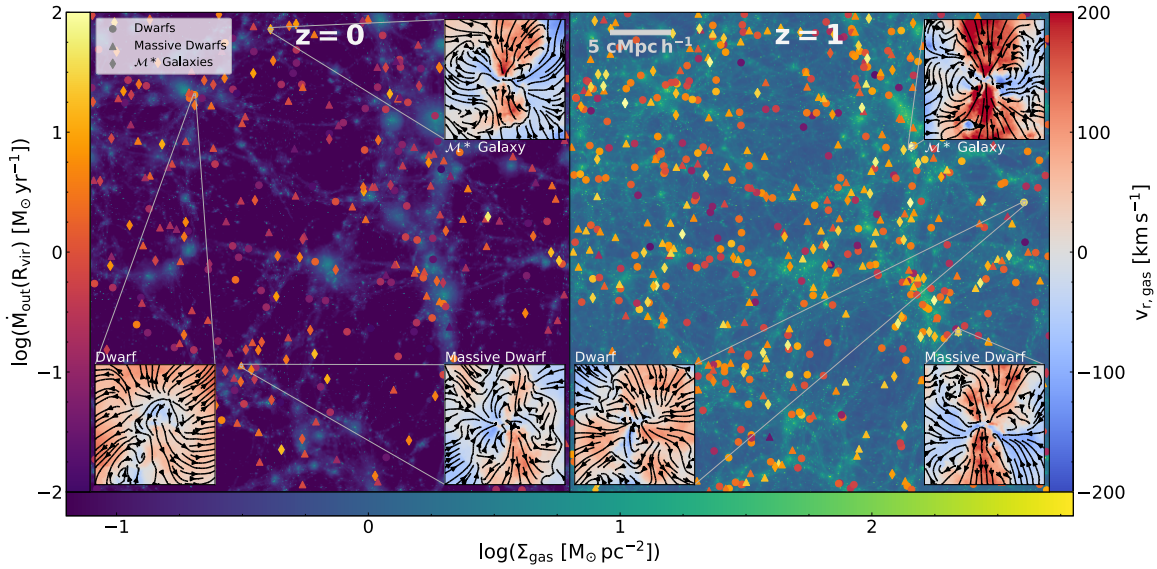

Fig. 3.1 Surface density projections of the total gas for the whole FABLE simulation box at redshifts $z = 0$ (left panel) and $z = 1$ (right panel). The markers show the locations of low-mass galaxies that host an actively accreting BH ($f_{\rm Edd} > 10^{-3}$). The marker style indicates the respective stellar mass bin with the sample divided up into dwarf galaxies ($9.0 \leq \log(M_{\rm stellar}\ [{\rm M}_\odot]) < 9.5$), massive dwarf galaxies ($9.5 \leq \log(M_{\rm stellar}\ [{\rm M}_\odot]) < 10.0$), and $\mathscr{M}^*$ galaxies ($10.0 \leq \log(M_{\rm stellar}\ [{\rm M}_\odot]) < 10.5$). The marker colour shows the mass outflow rate of the total gas at the virial radius, $R_{\rm vir}$. For each of the three mass bins at both redshifts, we select an example galaxy with a high outflow rate and show the projected outflow kinematics of the total gas in the zoomed-in insets (projection dimensions $2R_{\rm vir} \times 2R_{\rm vir} \times 2R_{\rm vir}$). The inset colour-coding indicates the radial velocity and the velocity streamlines are shown in black. Note that these insets have been rotated so that the galaxies are viewed edge-on.

photon index $\Gamma = 3$, which is a good representation of a thermal model with temperature 0.7 - 1 keV (see Mezcua et al., 2018).

3.3 Results

3.3.1 The AGN population

We start our analysis by inspecting the large-scale distribution of AGN in low-mass galaxies in our simulation. Figure 3.1 shows projections of the total gas surface density for the whole FABLE simulation box at $z = 0$ (left panel) and $z = 1$ (right panel). The markers show the locations of active low-mass galaxies (with Eddington fractions $f_{\rm Edd} > 10^{-3}$). The galaxies' stellar masses are indicated by the marker style with the sample split into dwarfs with $9.0 \leq \log(M_{\rm stellar}\ [{\rm M}_\odot]) < 9.5$, massive dwarfs with $9.5 \leq \log(M_{\rm stellar}\ [{\rm M}_\odot]) < 10.0$, and $\mathscr{M}^*$ galaxies with $10.0 \leq \log(M_{\rm stellar}\ [{\rm M}_\odot]) < 10.5$. Focusing on the spatial distribution,

there are low-mass galaxies with AGN in all types of cosmic environments: voids, filaments, and knots. This is in line with the observational findings from SDSS galaxies, which suggest that environment is not an important factor in triggering AGN activity in dwarf galaxies (Kristensen et al., 2020). There are significantly more active low-mass galaxies at redshift $z = 1$ than at $z = 0$.

The marker colour shows the galactic outflow rates at the virial radius, $R_{\rm vir}$ for the total gas (see Section 3.2.4). Across all mass bins (and at both redshifts), we find active galaxies with large-scale outflows at the virial radius ($\dot{M}_{\rm out} \gtrsim 10\ {\rm M}_{\odot}\,{\rm yr}^{-1}$). There are higher outflow rates and velocities at redshift $z = 1$ compared to $z = 0$. Unsurprisingly, more massive galaxies tend to be associated with stronger outflows, given the larger SFRs and BH masses in those systems. Though the more massive galaxies also have larger escape velocities than the low-mass objects.

For each of the three mass bins at both redshifts, we select a representative example galaxy with a high outflow rate and show $2R_{\rm vir} \times 2R_{\rm vir} \times 2R_{\rm vir}$ slices of the outflows in the zoomed-in insets. The inset colour-coding shows projections of the radial velocity of the total gas with the streamlines overlaid on the projection. Note that the galaxies shown in these projections have been rotated so that they are viewed edge-on. The more massive galaxies have collimated outflows, whilst the outflows for the example dwarf galaxies are more isotropic. For all of the example galaxies shown here, the outflows are able to propagate to the virial radius.

The outflow velocities of the total gas at $R_{\rm vir}$, as defined in Section 3.2.4, range from ~ 50 to $150\ {\rm km\,s}^{-1}$. In most cases the outflows decelerate between $0.2R_{\rm vir}$ and $R_{\rm vir}$. To estimate the escape velocity for these haloes we use the virial velocity, $V_{\rm vir}$, for simplicity, which ranges from ~ 80 to $210\ {\rm km\,s}^{-1}$. For most of these example galaxies, the mean outflow velocity at $R_{\rm vir}$ does not exceed the virial velocity, indicating galactic fountain nature of the outflows. The exception to this is the dwarf example galaxy at $z = 0$. For this galaxy, the outflows accelerate from $42\ {\rm km\,s}^{-1}$ at $0.2R_{\rm vir}$ to $94\ {\rm km\,s}^{-1}$ at $R_{\rm vir}$, exceeding $V_{\rm vir} = 81\ {\rm km\,s}^{-1}$. Note that this galaxy has an overmassive BH relative to its stellar mass with $M_{\rm BH} = 4 \times 10^5\ {\rm M}_{\odot}$ and $M_{\rm stellar} = 10^9\ {\rm M}_{\odot}$ (see FABLE scaling relations in Figure 3.3) and is in a crowded region with strong cosmic inflows.

Even though the outflow velocities of the total gas do not exceed $V_{\rm vir}$ in the other cases shown, the fast phase of the outflow is able to reach velocities higher than $V_{\rm vir}$ in all cases. The maximum velocities of the outflowing gas range from ~ 150 to $500\ {\rm km\,s}^{-1}$. We also checked the temperature distributions of these outflows and find that the outflows at $R_{\rm vir}$ are multiphase with temperatures ranging from 8×10^3 K to 3×10^6 K. The fast phase of the outflow corresponds to the hot phase, with temperatures between $\sim 10^5$ K and 10^6 K.

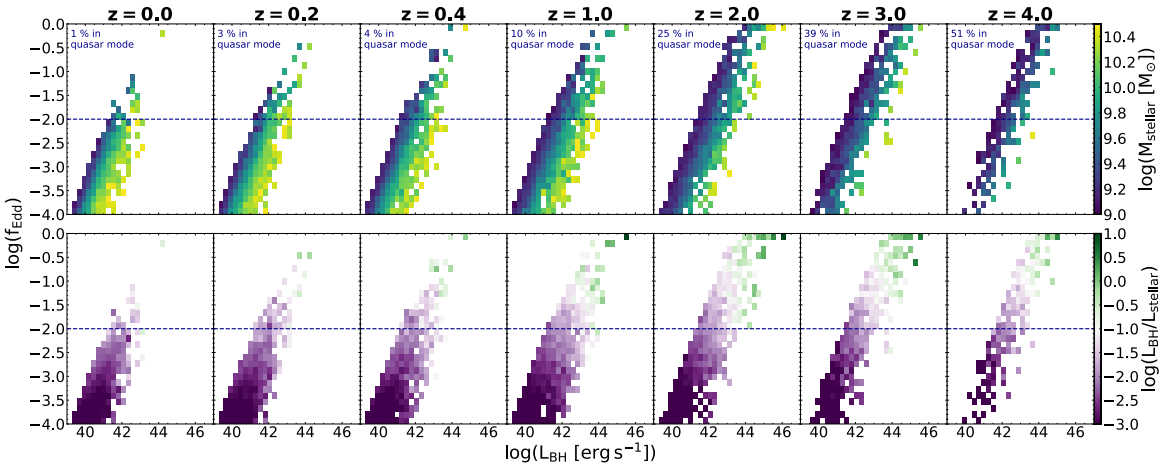

Fig. 3.2 The redshift evolution of the population of BHs hosted by low-mass galaxies ($9.0 \leq \log(M_{\rm stellar}\ [{\rm M}_\odot]) < 10.5$). At each redshift, the distribution of BHs in the $L_{\rm BH} - f_{\rm Edd}$ space is shown. The colour coding indicates the average $M_{\rm stellar}$ (top panel) and the average $L_{\rm BH}/L_{\rm stellar}$ ratio (bottom panel). The Eddington fraction where the BHs transition to quasar mode feedback ($f_{\rm Edd,QM} = 10^{-2}$) is shown by the blue dashed line. The percentage of BHs that are in the quasar mode (out of the whole low-mass galaxy population) is given in the upper left corner for each redshift. There are very few bright AGN in low-mass galaxies at low redshifts, rendering these AGN hard to detect. The high-redshift population is much more promising with $\sim 25-50$ per cent in the quasar mode. The bottom panel illustrates how in the majority of cases, the stars in the galaxy outshine the AGN, demonstrating the importance of multi-wavelength studies. Again this problem is alleviated for high Eddington fraction accretors at higher redshifts.

Having established that a significant number of low-mass galaxies with AGN in FABLE have appreciable outflows, we move on to investigate the radiative properties of this population. Figure 3.2 shows the distribution of the low-mass AGN population in $L_{\rm BH} - f_{\rm Edd}$ space, where $L_{\rm BH}$ is the bolometric BH luminosity. We show this distribution at a range of redshifts between $z = 0$ and $z = 4$, focusing on the high Eddington fraction end of this distribution ($f_{\rm Edd} \geq 10^{-4}$). The threshold Eddington fraction for transition to the quasar mode ($f_{\rm Edd,QM} = 10^{-2}$) is shown as a blue dashed line. Furthermore, the fraction of BHs in the quasar mode (out of all BHs hosted by low-mass galaxies) is given in the upper left corner for each redshift.

The colour-coding in the upper panel indicates the average stellar mass in each pixel. Dwarf galaxies (with $\log(M_{\rm stellar}\ [{\rm M}_\odot]) < 9.5$) dominate the galaxy sample at high redshifts and the high-z distribution is quite narrow. Moving to lower redshifts, the distribution broadens as we get a wider range of stellar masses.

There is a clear stellar mass gradient where at a fixed BH luminosity, BHs with higher Eddington fractions tend to be hosted by less massive galaxies. There are very few highly-

accreting BHs at low redshifts ($z < 1$) rendering these AGN difficult to detect. Though note that FABLE may underproduce high-luminosity sources at low redshifts (see Section 3.3.5).

At $z = 0$, only one per cent of BHs in low-mass galaxies are in the quasar mode. This increases to 10 per cent at $z = 1$, and goes up to 51 per cent at $z = 4$. Future facilities (such as *Athena*, *Lynx*, *JWST* or the *Roman Space Telescope*) will be able to probe this early phase of significant activity, as predicted by our simulations. Note that we have compared the evolution of the number density of AGN for different luminosity bins in FABLE with Hopkins et al. (2007). We found that this is in good agreement and reproduces the cosmic downsizing effect, so the overall evolution of AGN luminosities in FABLE appears to be realistic.

At low redshifts, observational searches according to our model are likely only uncovering the tip of the iceberg. This issue is explored in more detail in the lower panel where the colour coding shows the average ratio between the (bolometric) BH luminosity $L_{\rm BH}$, and the central (bolometric) stellar luminosity $L_{\rm stellar}$. Here we take the central stellar luminosity to be the luminosity generated by all of the star particles within the stellar half-mass radius. We estimate the luminosity of each star particle using the up-to-date Bruzual and Charlot (2003) stellar population synthesis models for a Chabrier (2003) IMF, and calculate the bolometric luminosity as a function of stellar age and metallicity.

The majority of AGN in low-mass galaxies are outshone by the stars in their host galaxies – even for highly accreting BHs. Therefore resolved studies as well as multi-wavelength surveys, such as probing the IR and the X-ray regime, are crucial tools for mapping this elusive population (see Section 1.4.3).

3.3.2 Scaling relations

We move on to investigate the relationship between the BHs and the stellar and gaseous components of their host galaxies. Figure 3.3 shows the scaling relations of BH mass, $M_{\rm BH}$, against stellar mass, $M_{\rm stellar}$, and BH mass against gas mass, $M_{\rm gas}$, at redshifts $z = 0$ and $z = 1$.

Both $M_{\rm stellar}$ and $M_{\rm gas}$ are calculated within twice the stellar half-mass radius, so these are scaling relations for a proxy for the total galaxy mass, rather than comparing just to the bulge component. We use the total galaxy mass since bulge decompositions are rather difficult for observations at the low-mass end (e.g. MacArthur et al., 2003; Reines and Volonteri, 2015; Greene et al., 2020) due to the high resolution requirements (although see Schutte et al., 2019).

To investigate whether there is a link between the scatter in the scaling relations and feedback activity in FABLE, we define 2D bins (bin dimensions: 0.1 dex $\times$ 0.2 dex) with at least ten objects and colour-code them by their mean outflow rate at $R_{\rm vir}$ (using the outflow

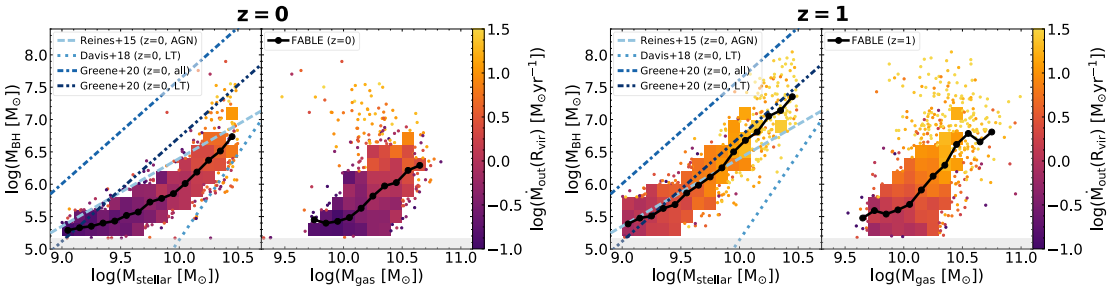

Fig. 3.3 Scaling relations of BH mass, $M_{\rm BH}$, against stellar mass, $M_{\rm stellar}$, and gas mass, $M_{\rm gas}$, at $z = 0$ (left panel) and $z = 1$ (right panel). The grey-shaded area indicates the seeding floor at $M_{\rm BH,seed} = 10^5\ h^{-1}\,{\rm M}_\odot$. The FABLE binned mean scaling relations (bin width 0.1 dex, at least ten objects per bin) are shown as solid black curves with the bin midpoints indicated by filled black circles. Some of the observed $M_{\rm BH} - M_{\rm stellar}$ scaling relations from the literature, as listed in the legend, are also shown for comparison. These are broadly in agreement with the results from FABLE, though the FABLE BHs are undermassive compared to most of the observed scaling relations. We also show the binned distribution of the whole FABLE low-mass galaxy sample with colour-coded histograms. 2D bins with at least ten objects are colour-coded by the mean outflow rate of the total gas at $R_{\rm vir}$, and otherwise we plot the individual objects colour-coded by their respective outflow rates to indicate the behaviour of outliers. Higher outflow rates are obtained for BHs with larger positive offsets from the $M_{\rm BH} - M_{\rm gas}$ relation. At $z = 1$, the $M_{\rm BH}/M_{\rm stellar}$ and $M_{\rm BH}/M_{\rm gas}$ ratios increase and higher outflow rates occur.

rate definition from Section 3.2.4 for the total gas). For more sparsely-populated bins, we plot the individual objects colour-coded by their respective outflow rates. This allows us to show the mean outflow properties of the low-mass galaxy population, whilst also indicating the behaviour of outliers.

The binned mean scaling relations (bin width 0.1 dex, at least ten objects per bin) for the FABLE galaxies are shown by the solid black lines with the filled black circles indicating the bin midpoint values. For comparison, we plot some of the observed $M_{\rm BH} - M_{\rm stellar}$ relations. Here, we mainly focus on relations derived for late-type galaxies (marked by 'LT'). These are most applicable to our low-mass galaxy sample as late-type (star-forming) galaxies dominate the local GSMF at the low-mass end (e.g. Muzzin et al., 2013; Vogelsberger et al., 2014b). This distinction is important as scaling relations obtained from late-type galaxies have a lower normalization than scaling relations derived from early-type galaxies (Greene et al., 2010; Reines and Volonteri, 2015; Greene et al., 2016; Läsker et al., 2016; Davis et al., 2018; Greene et al., 2020).

The relation shown from Reines and Volonteri (2015) is derived from a sample of local AGN (a significant number of which are spirals or discs), mostly containing broad-line AGN but also a subsample of dwarfs and reverberation-mapped AGN. This relation also has a significantly lower normalization than for early-type galaxies (see Reines and Volonteri, 2015,

for a detailed discussion). Moreover, we include the scaling relation derived by Davis et al. (2018) from a sample of 40 spiral galaxies with directly measured BH masses[5]. Finally, we show the relations obtained by Greene et al. (2020). These are based on the dynamical sample from Kormendy and Ho (2013) as well as additional dynamical measurements published since then (Greene et al., 2016; Saglia et al., 2016; Krajnović et al., 2018; Thater et al., 2019), particularly at low masses (Den Brok et al., 2015; Nguyen et al., 2018, 2019), as well as upper limits (Barth et al., 2009; Neumayer and Walcher, 2012; De Lorenzi et al., 2013). In addition to the relation derived from the late-type Greene et al. (2020) sample, we also show the relation derived from the whole Greene et al. (2020) sample, including both early-type and late-type galaxies. This relation has a greater than 0.7 dex higher normalization, demonstrating the significant effect of including early-type galaxies in the analysis.

It should be noted that there is a scarcity of dynamical BH mass measurements below $M_{\rm stellar} = 3 \times 10^{10}$ M$_\odot$, so care should be taken when comparing any of the above observed relations with simulated low-mass galaxies. Broad-line AGN can be used as an alternative means to establish a scaling relation for observed low-mass galaxies, however this comes with its own difficulties, as the virial factor $f_{\rm vir}$ still carries high uncertainties.

An additional complication is introduced by the different stellar mass-to-light ratios used in observational studies (see discussion in Reines and Volonteri, 2015; Davis et al., 2018, 2019). Note that this has no effect on the slope of the scaling relation, just on the normalization. Fully adjusting for this effect would be beyond the scope of this chapter, however, we reduce the stellar masses from Greene et al. (2020), which were obtained from the Bell et al. (2003) fitting functions, by -0.093 dex (Gallazzi et al., 2008; Zibetti et al., 2009), so that they are appropriate for a Chabrier IMF, as adopted in FABLE. For the Reines and Volonteri (2015) and Davis et al. (2018) relations, we make no adjustments, as these stellar masses were calculated assuming a Chabrier IMF and we do not attempt to harmonise the stellar mass measurements beyond a common IMF.

Keeping the above caveats in mind, we note that the local BH population in FABLE is undermassive compared to most of the observed scaling relations, with the exception of the Davis et al. (2018) relation. This relation has a significantly lower normalization than the other observed relations and brackets the lower end of the FABLE distribution. The closest agreement is reached with the Reines and Volonteri (2015) relation, though the FABLE mean relation lies consistently below this observed relation with discrepancies from $\sim 0.1 - 0.4$ dex. The late-type relation from Greene et al. (2020) brackets the upper end of the FABLE distribution, whilst the overall relation from Greene et al. (2020), including both early-type

[5] As in Graham et al. (2019), we use the relation obtained from the symmetric fit using the FITEXY routine to extrapolate the relation to lower masses.

and late-type galaxies, lies significantly above the mean relation derived from FABLE and has hardly any overlap with the simulation data.

We also caution that at the low-mass end of the BH mass distribution, where BH masses have not grown considerably from the seed mass of $M_{\rm BH,seed} = 10^5\ h^{-1}\,{\rm M}_\odot$, alternative seeding models could affect the simulated scaling relations.

Despite the uncertainties regarding the normalization of the observed relations, Figure 3.3 suggests that FABLE may underproduce the masses of AGN in low-mass galaxies at $z = 0$ and that any effect we find from AGN on low-mass galaxies in FABLE might constitute a lower limit of the possible effect of AGN feedback in that mass range. This is also supported by the absence of high-luminosity X-ray dwarfs from FABLE at low redshifts (see Section 3.3.5).

As we move to $z = 1$, we find a significantly higher $M_{\rm BH}/M_{\rm stellar}$ ratio, suggesting that the BHs grew faster than their host galaxies were assembled in the FABLE simulation, similarly to what has been found in Illustris (Sijacki et al., 2015). Whether the observed scaling relations evolve at higher redshifts is still controversial. While some studies find that the $M_{\rm BH}/M_{\rm stellar}$, or equivalently the $M_{\rm BH}/L_{\rm stellar}$, ratio increases towards higher redshifts (e.g. Kormendy and Ho, 2013; Bongiorno et al., 2014; Park et al., 2015; Yang et al., 2018; Ding et al., 2020), others find that there is no evolution up to $z \sim 1-2.5$ (e.g. Schramm and Silverman, 2013; Sun et al., 2015; Suh et al., 2020).

However note that, as with the local galaxies, these results are mainly just extrapolated from the high-mass end of the galaxy population. High-redshift studies of BHs in low-mass galaxies are only just at the beginning (see Sections 1.4.3 and 3.3.5). The next generation X-ray missions (*Athena*, *Lynx*) and deep spectroscopic surveys with the *Roman Space Telescope* and *JWST* will make it possible to obtain significant samples of AGN in low-mass galaxies at intermediate redshifts (see Greene et al., 2020). This will allow us to test our prediction that the $M_{\rm BH}/M_{\rm stellar}$ ratio should increase with redshift.

Focusing now on the relationship between $M_{\rm BH}$ and $M_{\rm gas}$, we note that the gas mass scaling relations have a similar slope to the stellar mass scaling relations. Furthermore, the $M_{\rm BH}/M_{\rm gas}$ ratio likewise increases from $z = 0$ to $z = 1$. However, the $M_{\rm BH}/M_{\rm gas}$ ratio has a significantly higher amount of scatter than the quite tightly correlated $M_{\rm BH} - M_{\rm stellar}$ relation. Interestingly, BHs with large positive offsets from the mean $M_{\rm BH} - M_{\rm gas}$ relation tend to have higher mass outflow rates, indicating that these overmassive AGN are able to drive more powerful outflows. For the stellar mass relation, the trend is weaker as the outflow activity also increases for higher stellar masses due to increased stellar feedback.

The increased outflow rates for overmassive BHs at a fixed gas mass provide an interesting hint that AGN can enhance galactic outflows once enough gas mass is available. The

relationship between overmassive BHs and host galaxy properties is investigated more closely in the next section.

3.3.3 Overmassive black holes and galaxy properties

Figure 3.4 shows various outflow quantities for the total gas at $R_{\rm vir}$ (mass outflow rate $\dot{M}_{\rm out}$, total mass flow rate $\dot{M}_{\rm tot}$, outflow velocity $v_{\rm out}$, outflow temperature $T_{\rm out}$, mass loading factor β) as well as integrated galaxy properties (gas mass to stellar mass ratio $f_{\rm gas}$, BH luminosity $L_{\rm BH}$, specific SFR (sSFR)) plotted against $M_{\rm gas}$, both at $z = 0$ and at $z = 1$. The outflow properties at $R_{\rm vir}$ are calculated within a spherical shell of width $\Delta r = 20$ kpc. For reference, we also checked the outflow properties at $0.2R_{\rm vir}$, where we used a shell of width $\Delta r = 10$ kpc. See Section 3.2.4 for more details on the calculation of the outflow properties for the total gas.

We include the whole low-mass galaxy sample and colour-code the distribution by the offset from the mean $M_{\rm BH} - M_{\rm gas}$ relation from Figure 3.3. Overmassive BHs, with BH masses above the mean BH mass $<M_{\rm BH}>$ for a given gas mass, are shown in red, whilst undermassive BHs are shown in blue. As in Figure 3.3, we show binned mean quantities where there are at least ten objects per bin, and otherwise the individual objects are plotted. In each case, we also show the binned mean relation, where there are at least ten objects per 0.15 dex gas mass bin, as a solid black line, with the bin midpoint values shown as filled black circles.

We plot the variation of outflow and galaxy properties with $M_{\rm BH}$ at fixed gas mass as the gas supply is a crucial quantity for the effectiveness of the AGN. On the one hand, the AGN needs a sufficient amount of gas to be able to accrete efficiently. On the other hand, AGN feedback can only drive large-scale outflows if there is a sufficient amount of gas to couple to in the host galaxy. To have a fair comparison, it is therefore important to keep $M_{\rm gas}$ constant. Figure 3.4 shows that there are strong correlations between the offset from the $M_{\rm BH} - M_{\rm gas}$ relation and all of the quantities considered at fixed gas mass. However, note that we would expect these correlations to be amplified by the tight relation between $M_{\rm BH}$ and $M_{\rm stellar}$ (see Figure 3.3), i.e. overmassive BHs at fixed gas mass will also tend to be associated with higher stellar masses. To ensure that the trends from Figure 3.4 are not just driven by increased stellar feedback activity, we show the same plot for overmassive BHs at fixed stellar mass (see Appendix 3.A). Broadly, the outflow trends are recovered at fixed stellar mass, though the separation of the sample into undermassive and overmassive BHs is less clear-cut. This is partly due to the small scatter in $M_{\rm BH}$ at fixed $M_{\rm stellar}$. In addition, as discussed above, the AGN's ability to influence its host galaxy is tightly correlated with gas availability. Therefore not keeping the gas mass fixed further blurs the correlation, as there will be a

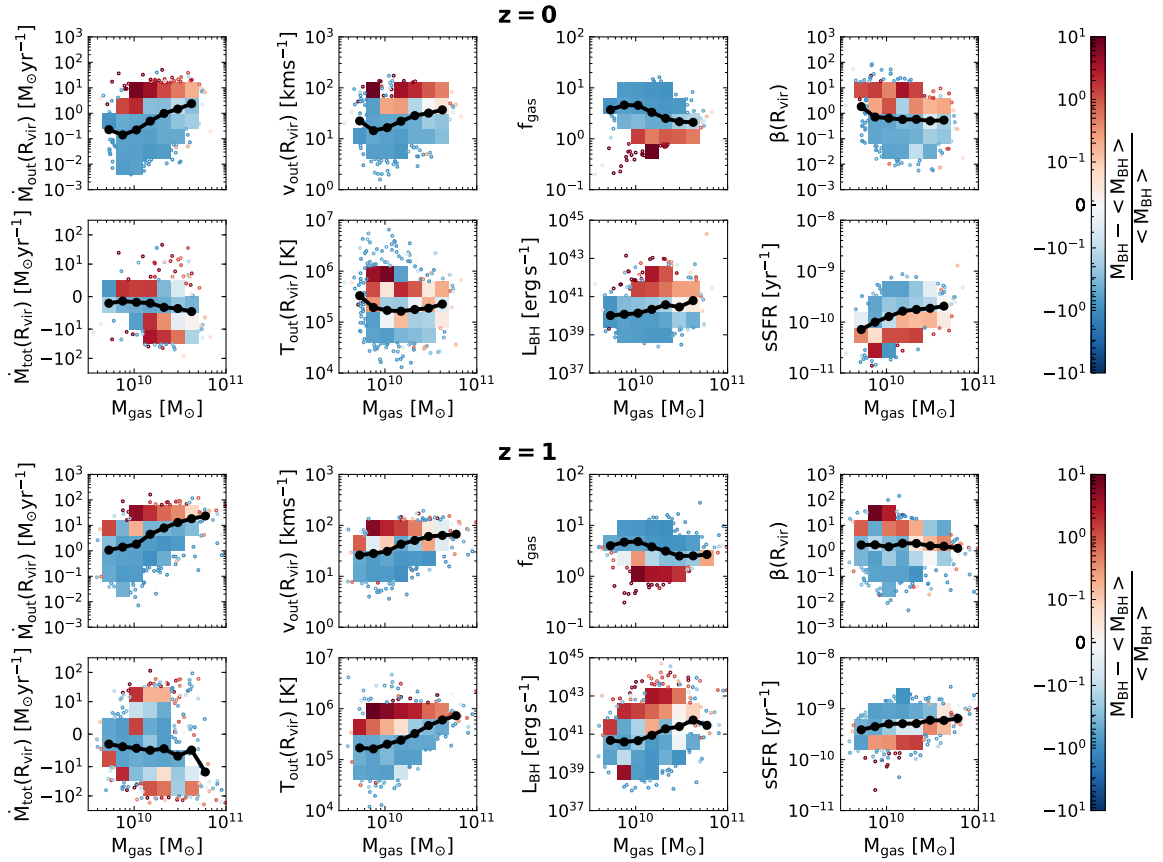

Fig. 3.4 Outflow characteristics of the total gas and galaxy properties against total gas mass at $z = 0$ (upper panel) and $z = 1$ (lower panel) for the FABLE low-mass galaxy sample. In each case the binned mean relation is shown as a solid black curve with the filled black circles indicating the bin midpoints. The colour coding of the distribution indicates the offset from the mean $M_{\rm BH} - M_{\rm gas}$ scaling relation from Figure 3.3, with blue for undermassive and red for overmassive BHs. 2D bins with at least ten objects are colour-coded according to the mean BH mass offset, and otherwise we plot the individual objects colour-coded by their respective BH mass offsets. Galaxies with overmassive BHs have increased outflow and inflow rates, leading to a bimodal distribution for the total mass flow rate. The outflows are faster and hotter in the overmassive regime. Overmassive BHs are also associated with reduced gas fractions and increased BH luminosities. Furthermore, the mass loading factor β is increased, whilst the sSFRs are suppressed.

wide range of gas masses for a given stellar mass. We will point out differences between the $M_{\rm gas}$-dependent and $M_{\rm stellar}$-dependent plots as we discuss the different quantities.

The first column of Figure 3.4 shows the mass outflow rates as well as the total mass flow rates. At both redshifts, overmassive BHs are associated with increased outflow as well as increased inflow rates. For the total mass flow rate this leads to a bimodal distribution with both extreme inflow and outflow rates correlated with overmassive BHs. This bimodality is to be expected as on the one hand large gas inflow rates will allow BHs to grow more quickly and become overmassive, and on the other hand these overmassive BHs are then able to drive more powerful outflows than their undermassive counterparts. Outflow rates are higher at $z = 1$ than at $z = 0$, and in both cases increase towards higher gas masses. At $z = 0$, overmassive BHs reach outflow rates up to $\sim 50\ \mathrm{M_\odot\,yr^{-1}}$, whilst at $z = 1$ these have outflow rates of up to $\sim 160\ \mathrm{M_\odot\,yr^{-1}}$. Note that we obtain the same trends at fixed stellar mass, however the overmassive BH population is not as clearly separated and the variations in BH masses at fixed $M_{\rm stellar}$ are smaller.

The second column shows the outflow velocity and temperature of the total gas at $R_{\rm vir}$. Outflows are on average faster and reach higher temperatures for overmassive BHs. Furthermore, the outflow velocities and temperatures are on average higher at $z = 1$ than at $z = 0$. This is particularly noteworthy considering that, at fixed halo mass, the average gas density within $R_{\rm vir}$ will be higher at higher redshifts.

We note that when we inspect the same outflow properties at $0.2R_{\rm vir}$, whilst the trends for the mass flow rates remain the same, the trends for $v_{\rm out}$ and $T_{\rm out}$ with BH mass offset are much more distinct. This suggests that the AGN mainly accelerates and heats the gas at a local level, while for the large-scale outflows the difference is somewhat less significant. This is especially true for the distribution at fixed $M_{\rm stellar}$ where there is not a strong link between outflow temperatures and BH mass offsets at $R_{\rm vir}$, however, there is a clear correlation at $0.2R_{\rm vir}$.

At $z = 0$, the mean outflow temperature stays relatively constant with increasing gas mass at $\sim 2 \times 10^5$ K. At $z = 1$, the outflow temperature increases with gas mass from $\sim 2 \times 10^5$ to $\sim 7 \times 10^5$ K. The outliers at both the low-temperature and the high-temperature end are dominated by undermassive BHs, suggesting that the link between BH mass and outflow temperature at $R_{\rm vir}$ is slightly weaker. We found that the high-temperature outliers at $0.2R_{\rm vir}$, on the other hand, are overmassive giving further support to the hypothesis that the AGN heating mainly affects the small-scale outflows.

For the $z = 0$ galaxies, the mean outflow velocity ranges from $\sim 10 - 40\ \mathrm{km\,s^{-1}}$ and for the $z = 1$ galaxies from $\sim 20 - 70\ \mathrm{km\,s^{-1}}$. Galaxies with overmassive BHs at both

redshifts reach typical outflow velocities of $\sim 100\,\mathrm{km\,s^{-1}}$, with the outliers reaching up to $\sim 200\,\mathrm{km\,s^{-1}}$.

Using the virial velocity $V_{\rm vir}$ as a proxy for the escape velocity (as in Section 3.3.1), we find that at $z = 0$, the mean escape velocity increases with gas mass from $\sim 80 - 140\,\mathrm{km\,s^{-1}}$, and at $z = 1$ from $\sim 100 - 220\,\mathrm{km\,s^{-1}}$. Therefore, at both redshifts, the fastest outflows should be able to escape the halo, whilst for the systems that lie on the mean relation, the outflow velocities are not high enough to escape the halo. Though note that, as discussed in Section 3.3.1, the outflows are multiphase and that even if the outflow velocity for the total gas, as considered here, is too slow to escape the halo, the hot and fast outflow phase may still be able to escape.

At $0.2R_{\rm vir}$, the outflow velocities are significantly higher with the mean outflow velocity ranging from $\sim 20 - 90\,\mathrm{km\,s^{-1}}$ at $z = 0$ and from $\sim 70 - 140\,\mathrm{km\,s^{-1}}$ at $z = 1$, implying that the outflows are decelerating. At both redshifts, typical outflow velocities for overmassive BHs are $\sim 200 - 300\,\mathrm{km\,s^{-1}}$. The properties of AGN-driven outflows in the low-mass regime are still relatively unconstrained by observations due to the high resolution requirements. Manzano-King et al. (2019) presented the first direct detection and measurements of AGN-driven outflows in dwarf galaxies. They find outflow velocities from $375 - 1090\,\mathrm{kms^{-1}}$ for galaxies with masses $\sim 4 \times 10^8 - 9 \times 10^9\,\mathrm{M_\odot}$. However, they measure these outflows in a relatively small region ($1.5 - 3.0$ kpc from the centre), whilst our outflow measurements at $0.2R_{\rm vir}$ correspond to length scales of ~ 10 kpc in the dwarf regime. As we find that the FABLE outflows are decelerating, velocities in the above range could be plausible for the total gas in the central region. Though we cannot test this due to the resolution of FABLE, as the gravitational softening length is ~ 3.5 kpc so the galaxies' central regions are not resolved in our simulation.

Next, we investigate the relation between overmassive BHs and gas fractions as well as BH luminosities in the third column of Figure 3.4. $f_{\rm gas}$ is reduced for large offsets from the mean BH mass, with overmassive BHs mostly found in galaxies with gas fractions $f_{\rm gas} \leq 1$. This is in agreement with the observed suppressed gas fractions of low-mass galaxies with AGN activity (Bradford et al., 2018; Ellison et al., 2019). Furthermore, the overmassive BHs are also correlated with high BH luminosities suggesting that these overmassive BHs are still actively accreting.

Finally, we investigate the properties related to star formation. The last column shows the mass loading factor at the virial radius $\beta(R_{\rm vir}) = \dot{M}_{\rm out}(R_{\rm vir})/\mathrm{SFR}(\leq R_{\rm vir})$ and the sSFR $=$ $\mathrm{SFR}/M_{\rm stellar}$ (the latter is evaluated within twice the stellar half-mass radius). Note that at $z = 0$, 0.5 per cent of objects have a sSFR below 10^{-11} (for 0.3 per cent of objects the sSFR is zero). These objects are also extremely gas-depleted and are not plotted here.

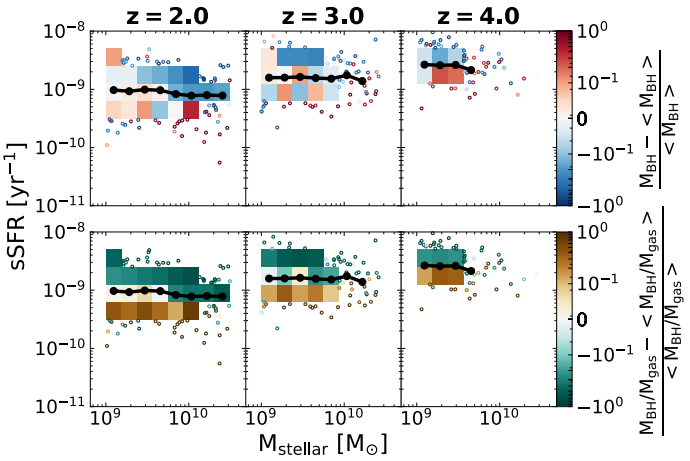

Fig. 3.5 High-redshift evolution of the sSFR against stellar mass. At each redshift, the binned mean relation is shown as a solid black curve with the filled black circles indicating the bin midpoints. In the upper panel, the colour coding indicates the offset from the mean $M_{\rm BH} - M_{\rm stellar}$ scaling relation from Figure 3.3, with red for overmassive BHs and blue for undermassive BHs. In the lower panel, the colour coding indicates the offset from the mean $M_{\rm BH}/M_{\rm gas}$ ratio of the respective stellar mass bin, with brown for above-average and green for below-average $M_{\rm BH}/M_{\rm gas}$ ratios. 2D bins with at least ten objects are colour-coded according to the bins' mean offsets, and otherwise we plot the individual objects. At high redshifts, overmassive BHs are correlated with suppressed sSFRs across the whole stellar mass range (contrary to the low-redshift case, see Figure 3.11). The correlation is even stronger when the $M_{\rm BH}/M_{\rm gas}$ ratio is considered, indicating that at high-redshift, the BHs are able to drive the gas out of dwarf galaxies and suppress star formation.

Overmassive BHs are associated with higher mass loading factors and suppressed sSFRs for the whole gas mass range. For overmassive BHs at $z = 0$, we obtain sSFRs in the range $\sim 10^{-11} - 2 \times 10^{-10}$ yr^{-1}. Whilst at $z = 1$, where the mean sSFR is significantly higher, the majority of overmassive BHs have sSFRs in the range $10^{-10} - 6 \times 10^{-10}$ yr^{-1}.

However, there are clear differences when we plot these two (star-formation related) quantities at fixed stellar mass instead (see Figure 3.11). For both β and the sSFR there is a turnover in the massive dwarf regime at $\sim 6 \times 10^9$ M$_\odot$ at $z = 0$ and $z = 1$. Below this mass, the trends from Figure 3.4 are either reversed or washed out. This suggests that star formation in FABLE dwarfs is not affected by AGN feedback at low redshifts ($z < 2$).

For $z \geq 2$, however, as the AGN reach higher luminosities (see Figure 3.2), there is a clear correlation between overmassive BHs and suppressed sSFRs across the whole stellar mass range. This is illustrated in Figure 3.5, where we plot the sSFR against stellar mass for $z = 2, 3$ and 4. We show the distribution of the sSFRs colour-coded by both the offset from the mean $M_{\rm BH} - M_{\rm stellar}$ relation (upper panel) as well as by the offset from the mean $M_{\rm BH}/M_{\rm gas}$ ratio for the respective stellar mass bin (lower panel). At high redshifts, overmassive BHs at fixed $M_{\rm stellar}$ are associated with suppressed sSFRs down to the dwarf regime – contrary to

the low-redshift case. The correlation is even stronger when considering the offset from the mean $M_{\rm BH}/M_{\rm gas}$ ratio. This implies that at $z \gtrsim 2$, the AGN feedback can drive the gas out of dwarf galaxies and help regulate star formation, whilst at low redshifts, stellar feedback is the dominant quenching process. However, we note that based on the undermassive FABLE BHs at $z = 0$ compared to the observed scaling relations (see Figure 3.3) and the lack of high-luminosity X-ray in FABLE (see Figure 3.10), this quenching transition at $z \sim 2$ could also be delayed to lower redshifts with more efficient BH growth at late times.

In observations, low-mass galaxies (with a typical stellar mass of $M_{\rm stellar} \sim 9 \times 10^9 {\rm M}_\odot$) with overmassive BHs (with respect to the $M_{\rm BH} - \sigma$ relation) have been found to also have reduced star formation – although this correlation is less significant than for massive galaxies (Martín-Navarro and Mezcua, 2018). This trend is also found in Illustris, across the whole galaxy mass range, whilst for IllustrisTNG the correlation is much weaker (Li et al., 2020). Furthermore, Sharma et al. (2020) find that isolated dwarf galaxies with overmassive BHs in ROMULUS25 experience star formation suppression starting at around $z = 2$.

Nevertheless, the enhancement of outflows by AGN is observed throughout cosmic time. We investigate the outflow properties more closely in Figure 3.6 where we plot the momentum and kinetic energy outflow rates for the total gas, as defined in Section 3.2.4, against gas mass. In the top row, we show these rates in units of the BH luminosity and in the bottom row in cgs units. We use the same colour-coding as in Figure 3.4 with red indicating overmassive BHs and blue indicating undermassive BHs with respect to the mean $M_{\rm BH} - M_{\rm gas}$ relation.

Overmassive BHs have both higher momentum and higher energy outflow rates. However, once we normalise these rates by the BH luminosity the trends become weaker, as overmassive BHs also have higher BH luminosities (see Figure 3.4). This is particularly true for $z = 1$ where the BHs reach significantly higher luminosities and the BH offsets are correlated with the luminosities across a wider gas mass range.

We also investigated the momentum and energy outflow rates plotted against stellar mass (see Figure 3.12 in Appendix 3.A). As with the previous plot, we recover similar trends at fixed stellar mass but the trends are weaker due to the variation in gas supply as well as the small scatter in BH masses at fixed $M_{\rm stellar}$. When we normalise the trends at fixed stellar mass by the BH luminosity, the correlation is reversed. This is because the correlation with BH luminosity at fixed stellar mass is much stronger (see Figure 3.11) and therefore able to invert the outflow trends.

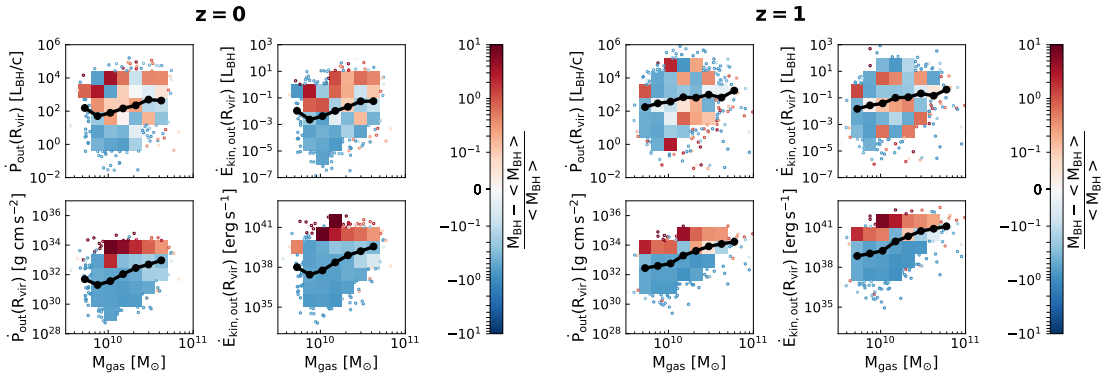

Fig. 3.6 Momentum and kinetic energy outflow rates of the total gas against total gas mass at $z = 0$ (left panel) and $z = 1$ (right panel) for the FABLE low-mass galaxy sample. The top row is normalised by the BH luminosity whilst the bottom row shows the outflow quantities in cgs units. The binned mean relations are shown as solid black curves, with the bin midpoints indicated by the filled black circles. Colour coding indicates the offset from the mean $M_{BH} - M_{gas}$ scaling relation from Figure 3.3, with blue for undermassive and red for overmassive BHs. Where there are fewer than ten objects per 2D bin, the individual objects are plotted. In cgs units, both momentum and energy outflow rates are clearly enhanced for overmassive BHs. However normalizing by the BH luminosity washes out this correlation at $z = 1$ due to strong coupling between BH masses and luminosities (see Figure 3.4).

3.3.4 Kinematic properties: mock MaNGA observations

In Section 3.3.3, we demonstrated that overmassive BHs drive more powerful outflows reaching higher velocities, temperatures, and mass loading factors. Next, we assess the potential impact of overmassive BHs on observations of low-mass galaxies.

Penny et al. (2018) find that dwarf galaxies (which they define as galaxies with $M_{stellar} \lesssim 5 \times 10^9$ $M_\odot$) with AGN signatures are more likely to have an ionized gas component with large kinematic offsets with respect to the stellar component (difference between global kinematic PAs is $30° \leq \Delta PA < 150°$). They interpret this as indirect evidence for AGN-driven outflows which may be responsible for the kinematically misaligned ionized gas.

In Chapter 2, we found that the AGN-boosted outflows can indeed lead to kinematic offsets between the ionized gas and stellar component using isolated dwarf simulations (see Section 2.4.4). Here we test this hypothesis in a cosmological context by producing mock MaNGA l.o.s. velocity maps for both the stars and the ionized gas following the procedure described in Section 3.2.5. To account for the cosmological nature and lower resolution of these simulations, we slightly adapt our procedure for creating the mock MaNGA maps from the previous chapter. The main adjustments for the cosmological simulations are checking for rotational support, adjusting for the systemic velocity and only projecting across the FoF group (rather than the whole simulation box) to avoid foreground effects. Furthermore, due to the much lower simulation resolution compared to the MaNGA resolution for local objects,

we also take the spatial extent of the resolution elements into account and smooth out both the stellar and gas distributions using the smoothing kernel of the stellar particles and gas cells, respectively.

We create the l.o.s. velocity maps at three different redshifts ($z = 0.0, 0.2, 0.4$) with a pixel size of 0.5 arcsec (size of the MaNGA square spaxels) and we convolve the maps with a Gaussian filter of 2.5 arcsec, matching the MaNGA PSF. Further, we only include stars and gas within a 2D aperture with radius $1.5r_{\rm eff}$, which corresponds to the spatial coverage of the primary MaNGA sample. Note that Henden et al. (2020) find that FABLE galaxies with $M_{\rm stellar} < 10^{11}$ M$_\odot$ have larger half-mass radii $r_{\rm eff}$ than observed galaxies (e.g. Baldry et al., 2012) by roughly a factor of two. This means that we can better resolve FABLE galaxies with the MaNGA PSF than may be the case for the observed galaxies (see figure A1 in Henden et al., 2020, for the median relationship between galaxy size and stellar mass for galaxies in the FABLE simulation compared to the sizes from other simulations as well as observed sizes).

To check for the effect of orientation, we create the l.o.s. velocity projections for each galaxy at two fixed orientations: edge-on (inclination angle $\theta = 0°$) and inclined by $\theta = 45°$. We rotate the galaxies automatically by aligning $\mathbf{J}_{\rm stellar}$ with the vertical axis. Note that we only include galaxies that are rotationally supported. See Section 3.2.5 for more details on the mock l.o.s. velocity maps.

To assess the impact of the AGN-boosted outflows in galaxies with overmassive BHs, we select the galaxies below the 20$^{\rm th}$ percentile (P$_{20}$) and above the 80$^{\rm th}$ percentile (P$_{80}$) of the $M_{\rm BH}/M_{\rm gas}$ distribution for each of the three stellar mass bins (dwarfs with $9.0 \leq \log(M_{\rm stellar}\ [{\rm M}_\odot]) < 9.5$, massive dwarfs with $9.5 \leq \log(M_{\rm stellar}\ [{\rm M}_\odot]) < 10.0$, and $\mathscr{M}^*$ galaxies with $10.0 \leq \log(M_{\rm stellar}\ [{\rm M}_\odot]) < 10.5$) at each redshift. Note that we only consider galaxies that are resolved by at least 50 star particles and 50 ionized gas cells within the $1.5r_{\rm eff}$ MaNGA aperture (see Section 3.2.5 for details). We then create mock MaNGA maps for these galaxies and determine the kinematic offsets between the ionized gas and the stars to assess whether heightened AGN activity produces a significantly higher percentage of kinematically misaligned galaxies.

Figure 3.7 shows example mock MaNGA maps for FABLE galaxies from each of the three stellar mass bins at $z = 0.0, 0.2, 0.4$, demonstrating some of the qualitative features of interest. Note that all of the projections shown here are at an inclination of $\theta = 0°$ (edge-on). All of the example galaxies have overmassive BHs and would be classified as kinematically misaligned. In addition to the mock MaNGA maps, we also show the l.o.s. velocity maps of the whole gas at the original resolution of the simulation (projection dimensions: $0.2R_{\rm vir} \times 0.2R_{\rm vir} \times 2R_{\rm vir}$). The $1.5r_{\rm eff}$ MaNGA aperture is indicated by a dashed black circle. Furthermore, we show

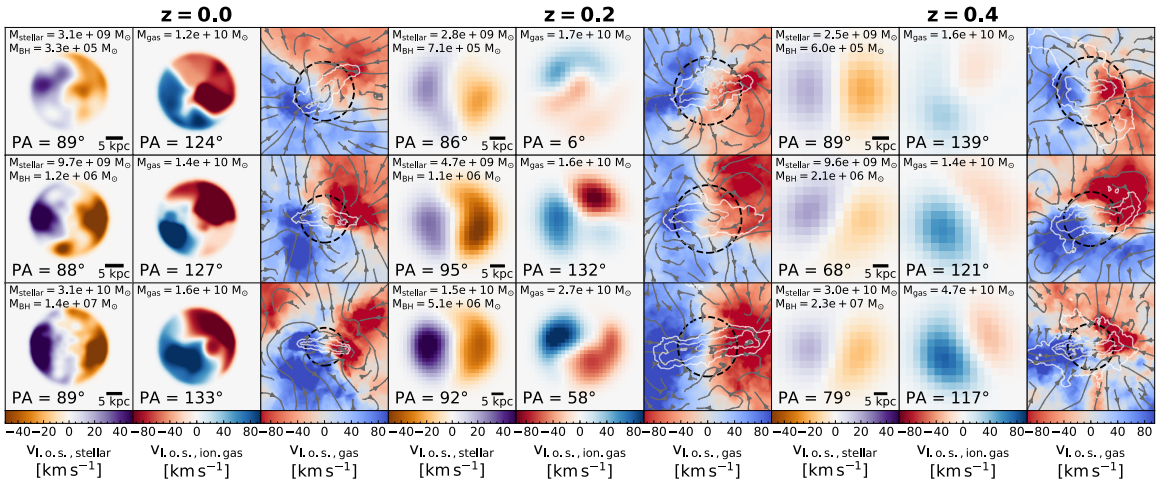

Fig. 3.7 Example mock MaNGA maps of nine different kinematically misaligned FABLE galaxies (difference in global kinematic PAs between the stellar and ionized gas component lies in the range $30° \leq \Delta\text{PA} < 150°$) at $z = 0.0$ (left panel), $z = 0.2$ (middle panel), and $z = 0.4$ (right panel). For each panel, the first and second columns show l.o.s. velocity maps for the stars and ionized gas, respectively, matching the MaNGA resolution and including all resolution elements of the FoF group within the $1.5r_{\text{eff}}$ 2D MaNGA aperture. The third column shows the l.o.s. velocity of the total gas at the original resolution of the simulation (projection dimensions: $0.2R_{\text{vir}} \times 0.2R_{\text{vir}} \times 2R_{\text{vir}}$). For reference, the $1.5r_{\text{eff}}$ 2D MaNGA aperture is shown as a dashed black circle, the velocity streamlines are shown in dark grey and the gas density contours are plotted in light grey. We show examples from all of the three stellar mass bins considered: dwarf galaxies ($9.0 \leq \log(M_{\text{stellar}}\ [\text{M}_\odot]) < 9.5$, first row), massive dwarf galaxies ($9.5 \leq \log(M_{\text{stellar}}\ [\text{M}_\odot]) < 10.0$, second row), and $\mathscr{M}^*$ galaxies ($10.0 \leq \log(M_{\text{stellar}}\ [\text{M}_\odot]) < 10.5$, third row). All of the example galaxies shown here have a $M_{\text{BH}}/M_{\text{gas}}$ ratio above the 80th percentile for their respective stellar mass bin and have been rotated to be viewed as edge-on. In some cases the kinematic misalignment is caused by fast outflows, however other factors, such as inflows or mergers, also play a role.

the gas density contours in light grey and the velocity streamlines in dark grey to highlight the inflowing and outflowing streams around the gas disc.

The kinematic PA is measured from the vertical axis and traces the position of the maximum change in velocity. We determine the kinematic PA from our mock MaNGA maps for both ionized gas and stars using the `fit_kinematic_pa` routine (see Krajnović et al., 2006). The stellar l.o.s. velocity maps are dominated by the rotational motion of the disc. Since we have aligned $\mathbf{J}_{\text{stellar}}$ with the vertical axis, we would therefore expect the kinematic PA of the stellar component to be PA $\sim 90°$.

For the example galaxies shown here, this is recovered within $\pm 22°$. For the ionized gas component, however, we obtain large kinematic offsets, with respect to the stellar component, from $\Delta\text{PA} = 34°$ to $\Delta\text{PA} = 80°$. This means that the method for determining kinematic PAs

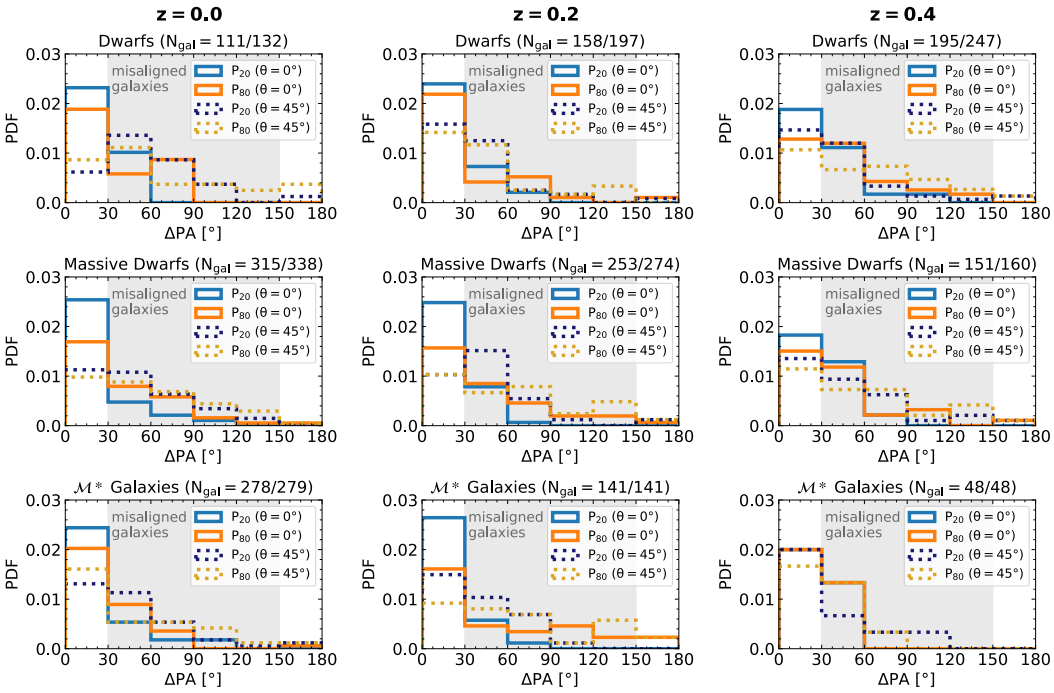

Fig. 3.8 PDFs of the difference between global kinematic PAs of stars and ionized gas, ΔPA, for $z = 0.0$ (left panel), $z = 0.2$ (middle panel), and $z = 0.4$ (right panel), separated into three mass bins of equal widths in log space: dwarf galaxies ($9.0 \leq \log(M_{\rm stellar}\ [{\rm M}_\odot]) < 9.5$, first row), massive dwarfs ($9.5 \leq \log(M_{\rm stellar}\ [{\rm M}_\odot]) < 10.0$, second row), and $\mathscr{M}^*$ galaxies ($10.0 \leq \log(M_{\rm stellar}\ [{\rm M}_\odot]) < 10.5$, third row). Within each mass bin, we select the galaxies that fall below the 20$^{\rm th}$ percentile or above the 80$^{\rm th}$ percentile of the $M_{\rm BH}/M_{\rm gas}$ ratio distribution. We show the PDFs of ΔPA for two fixed inclination angles: $\theta = 0°$ (edge-on) and $\theta = 45°$. The plot titles give the sizes of the samples of galaxies that are sufficiently resolved and sufficiently rotationally supported for projections at $\theta = 0°$ and $\theta = 45°$, respectively. Galaxies with overmassive BHs are more likely to be offset across mass bins and redshifts. This difference is even more pronounced for $\theta = 0°$, as rotational features are stronger and therefore only fast inflows or outflows can offset the rotational motion in projection.

is sufficiently robust and the large kinematic offsets between stars and ionized gas are real features.

The gas kinematics at the original resolution of the simulation (third column of each panel) reveal complex inflow-outflow structures. Fast outflows can cause kinematic misalignment, see e.g. the example $\mathscr{M}^*$ galaxy at $z = 0.0$ (Figure 3.7, left panel, third row). However, we identified a number of different physical processes other than outflows that can also result in kinematic misalignment. These include galactic fountains, as for the example dwarf galaxy at $z = 0.2$ (see Figure 3.7, middle panel, first row). Furthermore inflowing gas from mergers can also offset the rotational motion in projection, see e.g. the gas inflow from the lower left corner for the example $\mathscr{M}^*$ galaxy at $z = 0.4$ (Figure 3.7, right panel, third row). Similarly, cosmic gas inflows can also cause misalignment, as for the example massive dwarf galaxy at

$z = 0.0$ (Figure 3.7, left panel, second row). Finally, the entire gas disc can be misaligned so that misalignment stems from the rotational motion rather than gas inflows or outflows, as in the example dwarf galaxy at $z = 0.0$ (Figure 3.7, left panel, first row). This shows that kinematically misaligned ionized gas is not necessarily due to feedback activity alone, but misalignment still correlates with enhanced feedback (since inflows and mergers can also trigger feedback events).

To assess the relationship between overmassive BHs and kinematic misalignment more quantitatively, we systematically compare kinematic offsets for the undermassive ($M_{\rm BH}/M_{\rm gas}$ below $\rm P_{20}$) and the overmassive sample ($M_{\rm BH}/M_{\rm gas}$ above $\rm P_{80}$) in Figure 3.8. We plot the distributions of ΔPA for the edge-on, $\theta = 0°$ case (solid lines) and the $\theta = 45°$ case (dashed lines), with the shaded grey area indicating the misaligned regime. From left to right, the panels show the three different redshifts and from top to bottom, the panels show the three different stellar mass bins (as indicated by the plot titles). The plot titles also give the sizes of the samples of galaxies that are sufficiently resolved and sufficiently rotationally supported for projections at $\theta = 0°$ and $\theta = 45°$, respectively.

We note that the massive dwarfs and $\mathscr{M}^*$ galaxies sample sizes increase with decreasing redshift, whilst the size of the dwarf galaxies sample decreases. This is due to the above mentioned resolution criterion (at least 50 star particles and 50 ionized gas cells within $1.5r_{\rm eff}$) which forces us to discard an increasing number of dwarf galaxies as the amount of ionized gas decreases with redshift. Comparing the sample sizes for the two inclination angles, we can see that the $\theta = 45°$ sample size is greater than or equal to the $\theta = 0°$ sample size in all cases. Again this is caused by the above mentioned resolution issues. When the galaxy is inclined towards the observer, we are likely to have a higher amount of gas in the l.o.s. due to the presence of outflows, so a higher number of galaxies will fulfill the resolution criterion at higher inclination.

Focusing first on the $\theta = 0°$ projections, we can see that in all cases, the galaxies above $\rm P_{80}$ are either more likely (or for the $\mathscr{M}^*$ galaxies at $z = 0.4$ equally likely, though note the small sample size) to be categorised as kinematically misaligned. Furthermore, these galaxies are also more likely to have extreme misalignments ($60° \leq \Delta\rm PA < 120°$).

Moving on to the $\theta = 45°$ projections, we first note that in all cases these are more likely to be misaligned (or for the P_{20} $\mathscr{M}^*$ galaxies at $z = 0.4$ equally likely) compared to their $\theta = 0°$ counterparts, as it is easier for inflows or outflows to offset the projected gas kinematics when the galaxy is inclined towards the observer.

Comparing the P_{20} sample to the P_{80} sample at $\theta = 45°$ yields a more complex picture. In the majority of cases (six out of nine), the overmassive BHs are still more likely to be

misaligned. However, in the remaining three cases, the P_{20} galaxies are more or equally likely to be misaligned.

We interpret these distributions by noting that overmassive BHs are associated with both extreme mass inflow and outflow rates (see Figure 3.4) as well as higher outflow velocities. The higher outflow velocities make it easier to offset the rotational motion in projection leading to significant kinematic offsets. As we incline the galaxy disc towards the observer, the l.o.s. component of the rotational velocity decreases so outflows moving at slower velocities can also offset the rotational motion in projection, and the distinction between undermassive and overmassive BHs becomes less clear. We tested this hypothesis by inspecting the distribution of kinematic offsets split by $v_{\rm out}$ instead of $M_{\rm BH}/M_{\rm gas}$ and found that we obtain a similar distribution, demonstrating that outflow velocity is an important factor for shaping the ΔPA distribution – though outflows are not the only process generating kinematically misaligned gas (see Figure 3.7).

Furthermore, observed differences between the distributions of ΔPA for AGN and non-AGN galaxies are also influenced by the inclination angle. We estimated inclination angles of the MaNGA galaxies from Penny et al. (2018) using the b/a axial ratios at $r_{\rm eff}$ from the NASA-Sloan Atlas catalogue. We found that the median inclination angle (measured with respect the edge-on configuration) for the dwarfs without AGN signatures is $\theta \sim 46°$, whilst the median inclination angle for the dwarfs with AGN signatures is $\theta \sim 55°$, so this might slightly increase the difference in kinematic offsets between non-AGN and AGN dwarfs (though note that this difference in inclination angles is much smaller than the difference between the two angles we consider here). Also note that Penny et al. (2018) only considered quiescent dwarf galaxies. We do not impose a star formation based cut on our sample as this would leave us with too few objects, so this is a potential disparity as kinematic misalignment due to stellar feedback is likely more prominent in our sample.

The observed higher incidence of kinematically misaligned ionized gas for dwarf galaxies with AGN signatures could be caused by AGN-boosted outflow velocities (see also Duckworth et al., 2020), but also by other physical processes like cosmic inflows or mergers. Moreover, spectroscopic AGN signatures are easier to identify for galaxies which are inclined towards the observer, further increasing the likelihood of kinematic misalignment. To sum up, we find that kinematically misaligned gas is correlated with overmassive BHs but not always caused by AGN feedback itself.

3.3.5 Radiative properties: mock X-ray luminosities

As discussed in Section 1.4.3, there have been a number of systematic X-ray searches for AGN in dwarf galaxies. Mezcua et al. (2018) presented a sample of 40 AGN candidates in

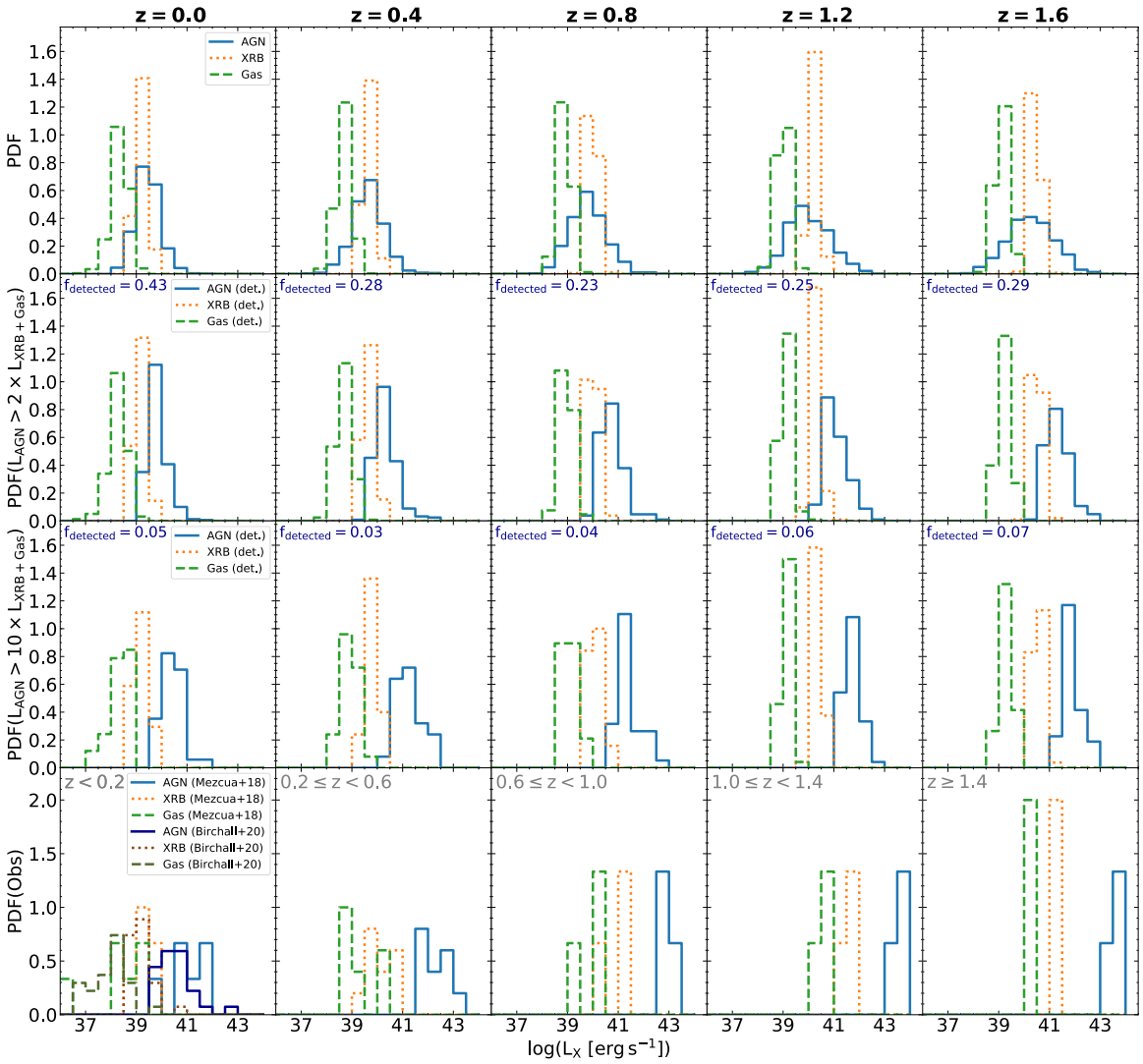

Fig. 3.9 Distribution of the X-ray luminosities of BHs, XRBs, and hot gas across different redshifts. The top row shows the X-ray luminosity distributions for all FABLE dwarf galaxies ($9.0 \leq \log(M_{\rm stellar}\ [{\rm M}_\odot]) < 9.5$). The second row only includes the FABLE dwarfs that fulfil the AGN selection criterion from Birchall et al. (2020): $L_{\rm AGN} > 2 \times L_{\rm XRB+Gas}$. We also examine the X-ray luminosity distributions using an even stricter criterion ($L_{\rm AGN} > 10 \times L_{\rm XRB+Gas}$) in the third row. In both cases, we give the fraction of FABLE dwarf galaxies with BHs that would get categorised as AGN using these criteria in the upper left hand corner. With the Birchall et al. (2020) criterion, a high fraction of BHs in dwarf galaxies are categorised as AGN, demonstrating that contamination from XRBs and hot gas should likely not pose a significant issue, even at the low-mass end. For comparison, we also show the X-ray distributions of the observed dwarf galaxies with AGN from Mezcua et al. (2018) and Birchall et al. (2020) in the bottom row. The local detections are in broad agreement with the FABLE distributions, though the observed AGN are shifted towards higher luminosities. From the FABLE luminosity distributions, we would expect many more AGN in dwarf galaxies to be detected by future X-ray surveys with higher sensitivities.

dwarfs at $z \lesssim 2.4$ drawn from the *Chandra* COSMOS Legacy Survey. Recently, Birchall et al. (2020) found 61 AGN candidates in local dwarf galaxies ($z \lesssim 0.25$) using the common footprint of the MPA-JHU catalogue and XMM DR7. Here we compare the X-ray properties of the FABLE dwarf galaxies to the these observations, focusing on the redshift evolution and the detectability of these BHs in dwarf galaxies using X-ray surveys.

Current X-ray studies searching for AGN in dwarf galaxies face two main challenges. Since BHs in dwarf galaxies have relatively low masses ($M_{\rm BH} \sim 10^5$ M$_\odot$), their luminosities are also correspondingly lower. This makes it difficult to identify AGN in dwarf galaxies, unless they have a high Eddington fraction. For example, Mezcua et al. (2018) estimate that 95 per cent of their AGN candidates have near to super Eddington accretion rates ($f_{\rm Edd} > 10^{-2}$). Contrast this with Section 3.3.1, where we found that only one to ten per cent of FABLE low-mass galaxies have BHs with $f_{\rm Edd} > 10^{-2}$ between $z = 0$ and $z = 1$, though due to the efficient SN feedback at the low-mass end in FABLE, this might be a lower limit.

Birchall et al. (2020), on the other hand, have a higher proportion of low-luminosity AGN in their sample, with a typical Eddington fraction of $f_{\rm Edd} \sim 10^{-3}$, as they focus on local galaxies. Furthermore, their technique for separating AGN from other X-ray sources might allow them to identify more AGN sources (see below).

The second main issue for X-ray surveys is contamination from XRBs as well as hot gas emission. Due to the lower AGN luminosities, there is an overlap between the luminosity distributions of the contaminants and the AGN. In observational studies, it is therefore necessary to estimate the contributions from XRBs and hot gas to check that the integrated luminosity is significantly higher than the expected contribution from non-AGN sources.

Birchall et al. (2020) use the relation from Lehmer et al. (2016) to estimate the XRB contribution based on $M_{\rm stellar}$ and the SFR. For the hot gas contribution, they use the relation from Mineo et al. (2012) which gives the X-ray luminosity of the gas based on the SFR. They require that the total X-ray luminosity has to be three times higher than the estimated luminosity of the non-AGN sources (i.e. the putative AGN luminosity, $L_{\rm AGN}$, has to be twice as high as the luminosity of the contaminants, $L_{\rm XRB+Gas}$). This leaves them with 61 AGN candidates out of the 86 X-ray active dwarf galaxies in their original sample. Note that in their sample, galaxies with significantly higher X-ray luminosities than expected from XRBs also exceed the expected contribution from hot gas, so the latter is less of an issue when identifying AGN.

The AGN candidates from Mezcua et al. (2018) are drawn from a parent sample of ~ 2300 X-ray-selected type-2 AGN out to $z \sim 3$ (see Suh et al., 2017). These sources were classified by their spectroscopic type when available, or the photometric type. Mezcua et al. (2018) also check the contamination from XRBs using the Lehmer et al. (2016) relation.

They find that the observed X-ray luminosities are more than $\sim 6\sigma$ larger than expected from XRBs, and using the Mineo et al. (2012) relation, they find that the X-ray luminosities of all their sources are more than $\sim 34\sigma$ above the luminosity expected from hot gas. So there is an extremely low chance of contamination – which is to be expected given the high Eddington fractions of the AGN candidates in this sample.

To study the redshift evolution of AGN and contaminant luminosities in FABLE, we plot the PDFs of the AGN, XRB, and hot gas X-ray luminosities in Figure 3.9. We use the bolometric corrections from Shen et al. (2020) to estimate the FABLE X-ray AGN luminosities in the $0.5-10$ keV band, matching the band used by Mezcua et al. (2018). In analogy to the observational studies, we estimate the XRB and hot gas contributions from the relations by Lehmer et al. (2016) and Mineo et al. (2012), respectively. See Section 3.2.6 for more details on the calculation of the different X-ray luminosities.

The top row of Figure 3.9 shows the luminosity distributions of all FABLE dwarfs. There is a significant overlap between the luminosity distributions of AGN and XRBs. For the local galaxies, the contamination from XRBs is less significant as the sSFR is significantly lower (see Figure 3.4). Note that for all redshifts, the hot gas and the AGN contribution are well separated, with the hot gas distribution shifted towards significantly lower luminosities than the XRB contribution. In agreement with the observational studies, we therefore conclude that the hot gas contribution should not pose a significant issue for the identification of AGN in dwarf galaxies.

In the second row, we show the distribution of the X-ray luminosities for all FABLE dwarf galaxies that fulfil the Birchall et al. (2020) criterion ($L_{\rm AGN} > 2 \times L_{\rm XRB+Gas}$). In the top left corner, we give the fraction of dwarf galaxies with BHs, $f_{\rm detected}$, that fulfil this criterion. As expected from the full distribution, the highest fraction of AGN in dwarf galaxies are recovered for $z = 0$ with $f_{\rm detected} = 0.43$. This then decreases with redshift to $f_{\rm detected} = 0.23$ at $z = 0.8$ and then increases again, as the mean AGN luminosities move towards higher values with higher redshift, to $f_{\rm detected} = 0.29$ at $z = 1.6$. Note that since Birchall et al. (2020) identified 61 out of 86 X-ray active dwarf galaxies as AGN, they obtained an even higher AGN fraction using this criterion. This difference is likely linked to the harder X-ray band used in their study ($2-12$ keV) as well as completeness limits. Note that their original sample is shifted towards higher X-ray luminosities compared to FABLE and that it only has a few dwarf galaxies with X-ray luminosities below 10^{39} erg s^{-1}.

In the third row, we show the distribution of the FABLE galaxies with an even stricter criterion of $L_{\rm AGN} > 10 \times L_{\rm XRB+Gas}$. Whilst this efficiently separates the distributions of the AGN and the contaminants, it only classifies between three and seven per cent of sources as AGN.

In the bottom row, we plot the observed distributions from Mezcua et al. (2018) and Birchall et al. (2020). We show the Mezcua et al. (2018) galaxies in five different redshift bins, approximately corresponding to the FABLE redshifts considered. The last bin also includes a few higher redshift objects, as there is only a small number of AGN candidates at $z \geq 1.4$. The Birchall et al. (2020) galaxies are plotted in the $z < 0.2$ panel, as all of their sources are at low redshifts. Again note that the X-ray luminosities from Birchall et al. (2020) are based on a harder X-ray band ($2-12$ keV), so these distributions are not directly comparable.

We only include observed dwarf galaxies with $M_{\rm stellar} \geq 10^9$ M$_\odot$ in this plot to match the FABLE dwarf sample. The Mezcua et al. (2018) stellar masses were calculated from galaxy model templates based on the Chabrier IMF so we do not adjust these stellar masses. The stellar masses from Birchall et al. (2020) are derived using the Kroupa IMF, so we subtract 0.05 dex to adjust these to a Chabrier IMF.

The Mezcua et al. (2018) AGN luminosities are clearly separated from the contaminant distributions and more akin to the FABLE distributions using the stricter separation criterion of $L_{\rm AGN} > 10 \times L_{\rm XRB+Gas}$. Though note that towards higher redshifts ($z \gtrsim 1.0$) the observed AGN luminosities have very high values ($L_{\rm AGN} \sim 10^{43}$ erg s^{-1}), demonstrating that the observations mainly pick up a few very bright objects. Interestingly, we have no FABLE objects with $L_{\rm AGN} \gtrsim 10^{43}$ erg s^{-1} at any of the redshifts considered here, indicating again that the observed dwarfs may be accreting more efficiently than in our sub-grid model. From our simulated X-ray luminosity distributions, we would expect many more candidates to be identified by future X-ray surveys with lower flux limits.

The local Birchall et al. (2020) AGN distribution is less clearly separated from the contaminants than the Mezcua et al. (2018) dwarfs. Though the AGN luminosity distribution is still shifted towards higher luminosities than the equivalent FABLE distribution. We also note that for both observational studies, there are no AGN sources with luminosities below 10^{39} erg s^{-1}. This again suggests that AGN accreting at low Eddington fractions are missed by these surveys.

We therefore conclude that sensitivity limits will be the main issue for further X-ray searches for AGN in dwarf galaxies. Whilst emission from XRBs and hot gas is less of an issue and a high fraction of BHs in dwarf galaxies should be identified despite contamination from these sources (between ~ 20 and ~ 40 per cent).

Though note that the relations used here to estimate the XRB and hot gas contribution are derived from massive galaxies. As dwarf galaxies tend to have sub-solar metallicities they might have an enhanced high-mass XRB population (see discussion in e.g. Mezcua et al., 2018; Birchall et al., 2020). Lehmer et al. (2019) observe this enhancement for four dwarf

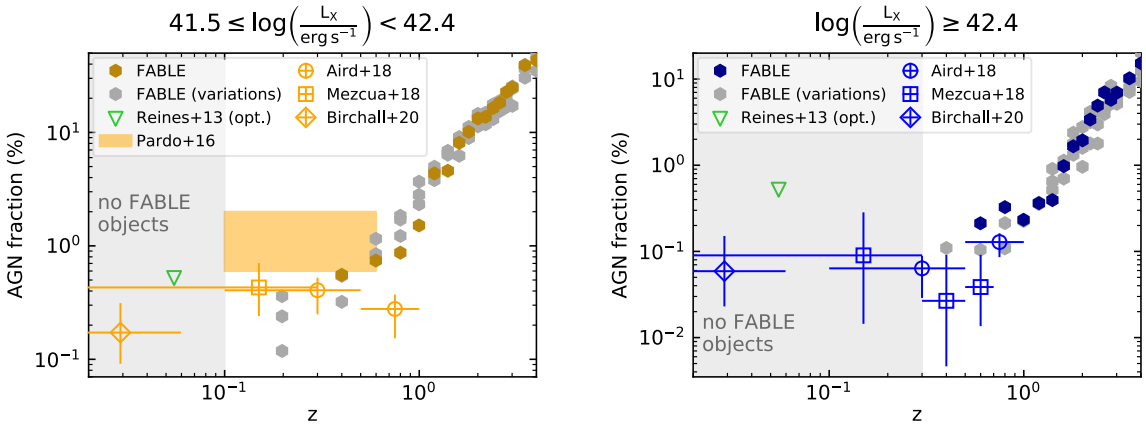

Fig. 3.10 AGN fraction in dwarf galaxies ($9.0 \leq \log(M_{\mathrm{stellar}}\ [\mathrm{M}_\odot]) < 9.5$) as a function of redshift for two X-ray luminosity bins: $3.7 \times 10^{41}\ \mathrm{erg\,s^{-1}} \leq L_X < 2.4 \times 10^{42}\ \mathrm{erg\,s^{-1}}$ (left panel) and $L_X \geq 2.4 \times 10^{42}\ \mathrm{erg\,s^{-1}}$ (right panel). The AGN fractions for the fiducial FABLE run are shown as dark orange and dark blue hexagons, respectively. Furthermore, we plot the AGN fractions of three of the FABLE calibration runs, which tested different variants of the AGN feedback model, as grey hexagons. Observational data are also shown for comparison, as indicated by the legend. At low redshifts there are no FABLE objects in either of the X-ray luminosity bins, suggesting that the FABLE feedback model might suppress the occurrence of these highly-accreting objects in the local Universe. At intermediate redshifts, FABLE is in agreement with observed X-ray AGN fractions. For $z > 1$, the simulation predicts that the AGN fraction should rapidly increase in both of the luminosity bins. Figure adapted from Mezcua et al. (2018) and Birchall et al. (2020).

galaxies, however, more data is needed to reliably estimate the XRB population in low-mass galaxies.

As X-ray searches are relatively unaffected by contamination from other sources, they can be used to establish an AGN fraction in different X-ray luminosity bins above the completeness limit of the respective survey. Next we compare these observed X-ray AGN fractions with AGN fractions from FABLE. In Figure 3.10, we show the AGN fraction against redshift in two different X-ray luminosity bins: $3.7 \times 10^{41}\ \mathrm{erg\,s^{-1}} \leq L_X < 2.4 \times 10^{42}\ \mathrm{erg\,s^{-1}}$ (left panel) and $L_X \geq 2.4 \times 10^{42}\ \mathrm{erg\,s^{-1}}$ (right panel).

For both of these luminosity bins, we plot the observed AGN fractions obtained by Aird et al. (2018), Mezcua et al. (2018), and Birchall et al. (2020). Though note again that the Birchall et al. (2020) luminosities were measured in a slightly different X-ray band (2 - 12 keV band) whilst the other two studies use the 0.5 - 10 keV band. As in the previous section, the FABLE luminosities are based on the 0.5 - 10 keV band.

In addition, we show the AGN fraction obtained by Pardo et al. (2016) in the upper panel. Though this AGN fraction should be taken as an upper limit due to the relatively small sample, with over half of the detected AGN having X-ray luminosities below $10^{41}\ \mathrm{erg\,s^{-1}}$.

We also show the AGN fraction from Reines et al. (2013). However, this fraction should also be taken as an upper limit as it was derived from optically-selected dwarf galaxies. We plot this fraction as a green down-pointing triangle for comparison in both panels.

We show the simulation data from the fiducial FABLE run for the two luminosity bins as dark orange and dark blue hexagons, respectively. Here the AGN fraction is defined as the number of dwarfs with an overall X-ray luminosity $L_{\rm X} = L_{\rm AGN} + L_{\rm XRB+Gas}$ in the respective luminosity bin normalised by the total number of dwarfs at the given redshift. We include the luminosity of the contaminants for consistency with the observations, though for these high-luminosity sources this makes little difference as the AGN is by far the dominant contribution (see Figure 3.9). Note that, as in the previous sections, we only consider central dwarf galaxies here so we might slightly overestimate the AGN fraction.

To get a sense of the uncertainty in the simulated AGN fractions, we also plot the AGN fractions obtained by three of the FABLE calibrations runs, where multiple variations of the AGN feedback parameters were tested, including variants without a duty cycle and weaker radio feedback (see appendix A of Henden et al., 2018, for details). The AGN fractions from the runs with the alternative AGN feedback models are shown as grey hexagons.

For the 3.7×10^{41} erg s$^{-1} \leq L_{\rm X} < 2.4 \times 10^{42}$ erg s^{-1} luminosity bin, there are no FABLE dwarfs at $z = 0.0$ for any of the AGN feedback variations. At $z = 0.2$, all of the three variant AGN feedback models produce AGN in this bin, with AGN fractions from ~ 0.1 to 0.4 per cent. Although note that in absolute numbers, this corresponds to one to three AGN in this luminosity bin, so these AGN fractions will be affected by small-number statistics. The fiducial FABLE run only has AGN in this luminosity bin from $z = 0.4$ on-wards. We shade the plot area corresponding to $z \leq 0.1$ grey to indicate that we have no FABLE objects in this redshift range.

The absence of these objects could be due the FABLE outputs not being frequent enough[6] as accretion rates are highly variable and AGN might only spend a short time in the high accretion state. Furthermore, it could be that we do not find any bright objects as the FABLE sub-grid models prevent the AGN from reaching these high luminosities.

For the redshifts where there are both simulated and observed data points, $0.2 \leq z \leq 1$, the AGN fractions from FABLE are in broad agreement with the observed fractions. Both the observed and the simulated data points are consistent with no significant evolution of the AGN fraction until $z \sim 1$. From $z = 1$ on-wards, where we have no observational constraints, the simulations predict a significant rise in the AGN fraction from ~ 1.5 per cent at $z = 1$ to ~ 43 per cent at $z = 4$.

[6]The FABLE simulation outputs are spaced in redshift by $\Delta z = 0.2$ for $z \leq 3$ and by $\Delta z = 0.5$ for $3 < z \leq 4$.

Next, we focus on the highest luminosity bin $L_X \geq 2.4 \times 10^{42}$ erg s^{-1} in the lower panel. Here there are no FABLE objects below $z = 0.4$. At $z = 0.4$, only one of the calibration runs has any AGN in this luminosity bins, with an AGN fraction of ~ 0.1 per cent, whilst the fiducial run only has AGN in this bin from $z = 0.6$. For $0.4 \leq z \leq 1.0$ where we have both observational and simulated data points, these are in good agreement and both consistent with no significant evolution in the AGN fraction until $z \sim 1$. Similar to the other luminosity bin, however, we see a significant increase in bright AGN at high redshifts, increasing from ~ 0.2 per cent at $z = 1$ to ~ 15 per cent at $z = 4$. We caution, however, that these AGN fractions are sensitive to the seeding model and the assumption that every DM halo above $5 \times 10^{10}\ h^{-1}\,\mathrm{M}_\odot$ should host a BH (see Section 3.2.2.2 for details on the FABLE seeding model).

The prediction that the high-luminosity AGN fraction in dwarf galaxies will significantly increase with redshift can be tested with upcoming X-ray missions. We estimate the X-ray luminosity limits across the redshift range using the flux limits for *Athena*[7], and *Lynx*[8]. For a given redshift, we calculate the luminosity limit as $L_X = 4\pi d_L^2 f_X$, where d_L is the luminosity distance and f_X is the flux limit. Both of the above instruments are more sensitive in the soft band (0.5 - 2 keV) than in the hard band (2 - 10 keV). Therefore, we use the soft and hard band flux limits to obtain lower and upper limits for detectable X-ray luminosities, respectively.

We find that *Athena* should be able to measure the AGN fraction for $L_X \geq 2.4 \times 10^{42}$ erg s^{-1} up to $z \sim 1.5 - 3.2$. The AGN fraction for 3.7×10^{41} erg s^{-1} $\leq L_X < 2.4 \times 10^{42}$ erg s^{-1} should be measurable up to $z \sim 0.7 - 1.5$. Therefore, *Athena* should be able to detect the upturn in the AGN fraction at $z \gtrsim 1.0$ for the high-luminosity AGN, and it might also provide further constraints for the other luminosity bin.

Lynx, however, will be able to constrain the AGN fraction across the whole redshift range ($0 \leq z \leq 4$) for both of the luminosity bins considered here. At $z = 4$, we find that the soft X-ray luminosity limit is $L_{X,soft} \sim 1.3 \times 10^{40}$ erg s^{-1} and the hard X-ray luminosity limit is $L_{X,hard} \sim 1.6 \times 10^{40}$ erg s^{-1}, so *Lynx* will be able to observe the evolution of the AGN fraction even for low-luminosity AGN.

[7] https://www.cosmos.esa.int/documents/400752/507693/Athena_SciRd_iss1v5.pdf
[8] https://wwwastro.msfc.nasa.gov/lynx/docs/LynxInterimReport.pdf

3.4 Discussion

3.4.1 Feedback processes in dwarf galaxies

Dwarf galaxies are an important testbed of galaxy formation and cosmology. Notwithstanding massive theoretical effort, it remains challenging to match the observed abundances and structural properties of dwarfs, requiring either to revisit our physical models or to even think outside of the standard ΛCDM framework. For example, the majority of large-scale galaxy formation simulations employ strong SN feedback to reproduce the low-mass end of the observed GSMF (see e.g. Bower et al., 2012; Dubois et al., 2014a; Vogelsberger et al., 2014b; Schaye et al., 2015; Pillepich et al., 2018). However, this approach is called into question by high-resolution (zoom-in) galaxy formation simulations (as well as small scale simulations of the ISM), which find it difficult to regulate star formation with SN feedback alone (e.g. Hopkins et al., 2014; Kim and Ostriker, 2015; Kimm et al., 2015; Hu et al., 2016, 2017; Marinacci et al., 2019; Smith et al., 2019) so that other sources of star formation regulation need to be invoked such as stellar winds, photo-heating, radiation pressure effects, cosmic rays and (MHD) turbulence.

Interestingly, when some of these additional physical processes are implemented alongside SN feedback, stellar feedback still struggles to regulate star formation in dwarf simulations (e.g. Kimm et al., 2018). To obtain efficient feedback in a cosmological setting, stellar feedback then needs to be enhanced, e.g. by boosting SN rates (Rosdahl et al., 2018) or via high star formation efficiencies (Hopkins et al., 2018a).

While strong stellar feedback seems required to match the observed dwarfs, it is likely to stunt AGN growth and feedback in these low-mass systems if a considerable gas reservoir is removed from the innermost regions (see e.g. Anglés-Alcázar et al., 2017b; Habouzit et al., 2017; Trebitsch et al., 2018; Habouzit et al., 2021). Moreover, it is worth noting that most galaxy formation simulations use the Bondi-Hoyle-Lyttleton rate to model BH accretion, which suppresses BH growth close to the seed mass due to its quadratic dependency on $M_{\rm BH}$. In cosmological simulations, seed masses of $\sim 10^5 - 10^6$ $\mathrm{M}_\odot$ are typically employed, so that the slow growth phase then by construction of these models corresponds to the dwarf regime.

3.4.2 Comparison with other works

The suppression of BH growth in dwarf galaxies (both by strong SN feedback and the Bondi-like accretion prescription) has meant that so far AGN feedback in dwarfs has largely been neglected by simulators. Novel observations of AGN in dwarf galaxies question these

assumptions, as contrary to the common theoretical models, there is a population of dwarf galaxies where AGN can accrete efficiently.

Recent theoretical works have started exploring BH activity in the dwarf regime using analytical tools (Silk, 2017; Dashyan et al., 2018), isolated simulations (Koudmani et al., 2019), cosmological zoom-in simulations (Trebitsch et al., 2018; Barai and De Gouveia Dal Pino, 2019; Bellovary et al., 2019) as well as cosmological boxes (Di Cintio et al., 2017; Habouzit et al., 2017; Sharma et al., 2020).

FABLE is a large-scale cosmological simulation with a ~ 60 Mpc box modelling a representative region of the Universe, including rare environments. This allows us to obtain a statistical sample of dwarf galaxies which can be compared to wide-field observational surveys: the FABLE box contains $\lesssim 10^3$ central dwarfs (i.e. not satellites) for simulation outputs between $z = 0$ and $z = 1$ and due to the efficient seeding, at least 98 per cent of these central dwarfs host a black hole. The sample size and range of environments are the main strength of this approach, enabling us to reproduce the rare bright AGN in dwarfs. However, due to the FABLE resolution, we cannot probe galaxies with stellar masses less than $M_{\rm stellar} = 10^9$ M$_\odot$, comparable in stellar mass to the Large Magellanic Cloud (LMC). Though note that most current observational investigations of AGN in dwarf galaxies are also (mainly) restricted to the LMC mass regime (Reines et al., 2013; Penny et al., 2018; Dickey et al., 2019; Liu et al., 2020) as Eddington-limited AGN in more massive dwarfs are brighter and therefore easier to detect. Furthermore, AGN identification methods which are based on samples of massive galaxies (such as the BPT diagram) still apply in the LMC mass range, whilst this is no longer the case for lower-mass dwarf galaxies (Cann et al., 2019, also see Section 1.4.3).

Other studies also analyse AGN feedback across a range of stellar masses down to the dwarf regime (e.g. Beckmann et al., 2017; Weinberger et al., 2018; Zinger et al., 2020), however, the focus of these studies is mostly on the high-mass regime as special care needs to be taken to distinguish the AGN trends in the low-mass regime due to the strong supernova feedback employed by the majority of large-scale cosmological simulations.

Sharma et al. (2020) present a similar study on AGN feedback in dwarfs based on the ROMULUS25 simulation, using a 25 cMpc box compared to the ~ 60 cMpc box used for FABLE, but with significantly higher resolution ($\gtrsim 100$ higher DM mass resolution). These simulations also model the BH dynamics due to dynamical friction (Tremmel et al., 2015). Note that the BHs in dwarf galaxies in ROMULUS25 are overmassive with respect to the observed scaling relations, whilst the BHs in the FABLE dwarfs are undermassive compared to observations, so the results from Sharma et al. (2020) likely provide an upper limit for the

impact of AGN feedback on dwarfs. Encouragingly, they find that dwarfs with increased BH growth have suppressed star formation rates, even at low redshifts.

3.4.3 Future prospects

3.4.3.1 Next-generation AGN models

The next step is now to develop novel subgrid models for BH physics to study AGN activity much more realistically in a cosmological context. AGN feedback in dwarf galaxies is an exciting possibility as it is still under-explored theoretically, but very promising energetically (see Dashyan et al., 2018).

Several BH seeding mechanisms should naturally predict BHs in dwarfs, for example remnants of Population III stars (e.g. Madau and Rees, 2001; Heger et al., 2003; Volonteri et al., 2003; Heger and Woosley, 2010; Whalen and Fryer, 2012; Karlsson et al., 2013) or dense nuclear star clusters (e.g. Begelman and Rees, 1978; Portegies Zwart and McMillan, 2002; Freitag et al., 2006; Omukai et al., 2008; Devecchi and Volonteri, 2009; Katz et al., 2015). Recent work has started exploring alternative seeding models in cosmological simulations, growing BHs from smaller seeds (see e.g. Habouzit et al., 2017; DeGraf and Sijacki, 2020). However, observations cannot yet clearly distinguish between different seeding models (e.g. see discussion in Volonteri et al., 2008; Mezcua, 2019; Greene et al., 2020) and the true occupation fraction of BHs in dwarf galaxies is still unknown (see Section 1.4.3).

To investigate AGN in dwarf galaxies, in addition to improved seeding models, it will be necessary to explore accretion mechanisms beyond the widely adopted (yet very simplistic) Bondi model, with several models considered, such as a supply-limited accretion scheme (Beckmann et al., 2018; Beckmann et al., 2019b), torque-driven BH growth (Anglés-Alcázar et al., 2015, 2017a) or accretion disc models (e.g. Power et al., 2011; Fiacconi et al., 2018; Bustamante and Springel, 2019).

The modelling of the different AGN feedback channels is equally important. Here, with FABLE, we only consider simple, isotropic feedback, however observations find evidence for bipolar outflows from AGN (e.g. Rupke and Veilleux, 2011; Maiolino et al., 2012). Note that AGN feedback in FABLE is modelled as mechanical feedback and a radiation field around the BH (see Section 3.2.2.3), but other processes that are not included here could also play an important role, such as outflows driven by radiation pressure (e.g. Bieri et al., 2017; Costa et al., 2018a,b) or jet-driven outflows. With a more realistic AGN feedback model, FABLE underestimating the BH luminosity would have an impact beyond just underestimating the mechanical AGN feedback and photoionization, since increasing the BH luminosity would also e.g. increase radiation pressure.

Even though FABLE under-predicts AGN activity in dwarf galaxies, as evidenced by the comparison with observed scaling relations and high-luminosity X-ray AGN fractions, there is still an effect by AGN feedback on dwarf galaxy properties in FABLE. This suggests that in reality the impact of AGN feedback on dwarfs could be even more significant (with the caveat that whilst the FABLE BH growth is inefficient, the seeding is very efficient, see e.g. DeGraf and Sijacki, 2020). Taking these results at face value, it is then inevitable to conclude that the effects of AGN feedback on the evolutionary history of dwarfs need to be explored, which may lead to re-evaluation of stellar feedback models as well.

To aid the development of theoretical models, it will be crucial to assess how many dwarfs harbour central BHs and how these BHs grow through cosmic time. Future observational facilities like *Lynx* or LISA will provide important observational constraints, as these instruments will probe the evolutionary history mapping both BH seeding and BH growth.

3.4.3.2 The 'cusp versus core' problem

AGN feedback in dwarf galaxies might also contribute to the resolution of an on-going debate about the so-called 'cusp versus core' problem. This controversy stems from the observed rotation curves of some dwarf galaxies, which seem to suggest cored DM density profiles rather than the cuspy profiles predicted by ΛCDM (Flores and Primack, 1994; Moore, 1994; Blok et al., 2001; Gentile et al., 2004; Walker and Parrubia, 2011). Currently there is no consensus about the origin of the diversity of inferred DM density profiles. Some suggest that the inferred cored profiles could be due to uncertainties in circular velocity measurements (e.g. Marasco et al., 2018; Oman et al., 2019). Others have questioned the validity of ΛCDM and come up with alternative DM models – such as warm DM (e.g. Lovell et al., 2012) or self-interacting DM (e.g. Vogelsberger et al., 2014a). Yet others have invoked baryonic processes transforming cusps to cores via strong feedback (see e.g. Navarro et al., 1996a; Governato et al., 2010; Di Cintio et al., 2013; Oñorbe et al., 2015; Fitts et al., 2016).

In FABLE, we find no significant differences in DM profiles for dwarf galaxies with overmassive BHs (not shown here), despite the clear impact on the baryonic component. This indicates that the FABLE AGN feedback is not strong enough to influence the DM component. Furthermore, this is likely also compounded with the resolution of the simulations. However, given that FABLE likely underestimates the luminosities of AGN in dwarf galaxies, AGN feedback may still play a role in transforming cusps into cores in dwarfs.

3.5 Conclusions

Recent observations have uncovered a population of dwarf galaxies hosting AGN, providing tantalizing hints that AGN feedback could also play a role in low-mass galaxies (see Section 1.4.3). We used the cosmological simulation suite FABLE to investigate the impact of AGN feedback on (central) low-mass galaxies ($10^{9.0}$ $M_\odot \leq M_{\rm stellar} < 10^{10.5}$ $M_\odot$), with a particular focus on dwarf galaxies ($10^{9.0}$ $M_\odot \leq M_{\rm stellar} < 10^{9.5}$ $M_\odot$). We examined the distribution of bolometric BH luminosities (Section 3.3.1) as well as the scaling relations (Section 3.3.2). Furthermore, we studied the correlations between overmassive BHs and host galaxy properties, in particular outflows, in Section 3.3.3. We also compared the FABLE low-mass galaxies to observational studies by creating mock MaNGA l.o.s. velocity maps (Section 3.3.4). Moreover, we estimated the X-ray luminosities for AGN, XRBs and hot gas to assess the detectability of AGN in dwarf galaxies with wide-field X-ray surveys (Section 3.3.5). Our most important findings are the following:

1. The majority of AGN in low-mass galaxies, and in particular in dwarf galaxies, are outshone by the stellar component. This renders these AGN difficult to detect. However, the high-redshift regime is more promising as more low-mass galaxies reach high Eddington fractions and luminosities.

2. The $M_{\rm BH} - M_{\rm stellar}$ scaling relation for FABLE low-mass galaxies is broadly in agreement with observed late-type scaling relations, though note that the FABLE relation is undermassive compared to most of the observed relations. This indicates that SN feedback may be too strong in the low-mass systems stunting BH growth.

3. Low-mass galaxies with large positive offsets from the $M_{\rm BH} - M_{\rm gas}$ or the $M_{\rm BH} - M_{\rm stellar}$ relation have increased mass outflow and inflow rates. These overmassive BHs cause higher outflow velocities and hotter (albeit multiphase) outflows. While warm outflows typically generate galactic fountains, the hot outflow component is able to escape the host haloes, leading to a reduced gas reservoir. Future MUSE observations should be able to test our predicted outflow properties.

4. We find that quenching of dwarfs proceeds via two channels. At lower redshifts ($z \lesssim 2$) where AGN accretion rates are low, SN feedback mainly regulates star formation in dwarf galaxies, whilst above $z \sim 2$, AGN feedback is strong enough to suppress star formation in dwarfs as well. We note that these conclusions are sensitive to the strong SN model adopted, with AGN quenching possibly more important at lower redshifts, too.

5. Galaxies with overmassive BHs are more likely to have an ionized gas component that is kinematically misaligned from the stellar component in mock MaNGA l.o.s. velocity maps in agreement with observations. While fast AGN-boosted outflows are partly responsible for this misalignment, we caution that other factors such as cosmic inflows or mergers are also important.

6. X-ray surveys are a promising tool for identifying AGN in dwarf galaxies. Even at the low-mass end, the AGN, XRB and hot gas X-ray luminosity distributions are sufficiently separated to identify a high fraction of AGN in dwarfs. Sensitivity remains the main issue, with the observed X-ray distributions shifted towards higher luminosities than FABLE. We predict that future X-ray surveys should uncover many more dwarf galaxies with AGN with lower Eddington fractions and at higher redshifts.

7. By comparing the occupation fraction of luminous AGN in dwarf galaxies in FABLE to observations, we find that luminous AGN are missing from FABLE at low redshifts, again indicating SN feedback-starved BH growth. Good agreement is, however, reached for intermediate redshifts. For high redshifts ($z > 1$), where there are currently no observational constraints, we predict that the fraction of luminous AGN in dwarf galaxies should rise rapidly.

Like the majority of galaxy formation simulations, FABLE has been designed such that SN feedback regulates the low-mass end of the galaxy mass function. Notwithstanding this, we find that AGN feedback in FABLE has a clear impact on the outflow properties of dwarf galaxies across cosmic time and contributes to quenching at high redshifts. Ongoing and upcoming state-of-the-art observations with e.g. *JWST*, MUSE, *Athena*, *Lynx*, ngVLA, and LISA will be able to probe the elusive AGN population in dwarfs to much lower luminosities and at higher redshifts. It is hence of paramount importance to develop next-generation galaxy formation models with more realistic seeding models and more efficient AGN accretion in low-mass objects to explore this currently unknown territory, with the ultimate goal of elucidating the role of AGN in dwarf galaxies.

3.A Overmassive black holes at fixed stellar mass

In Section 3.3.3, we illustrated how the offset from the $M_{\rm BH} - M_{\rm gas}$ relation is correlated with the properties of the host galaxy, in particular with the outflow properties. We found that low-mass galaxies with overmassive BHs are associated with more powerful outflows, lower sSFRs and gas fractions, as well as higher BH luminosities.

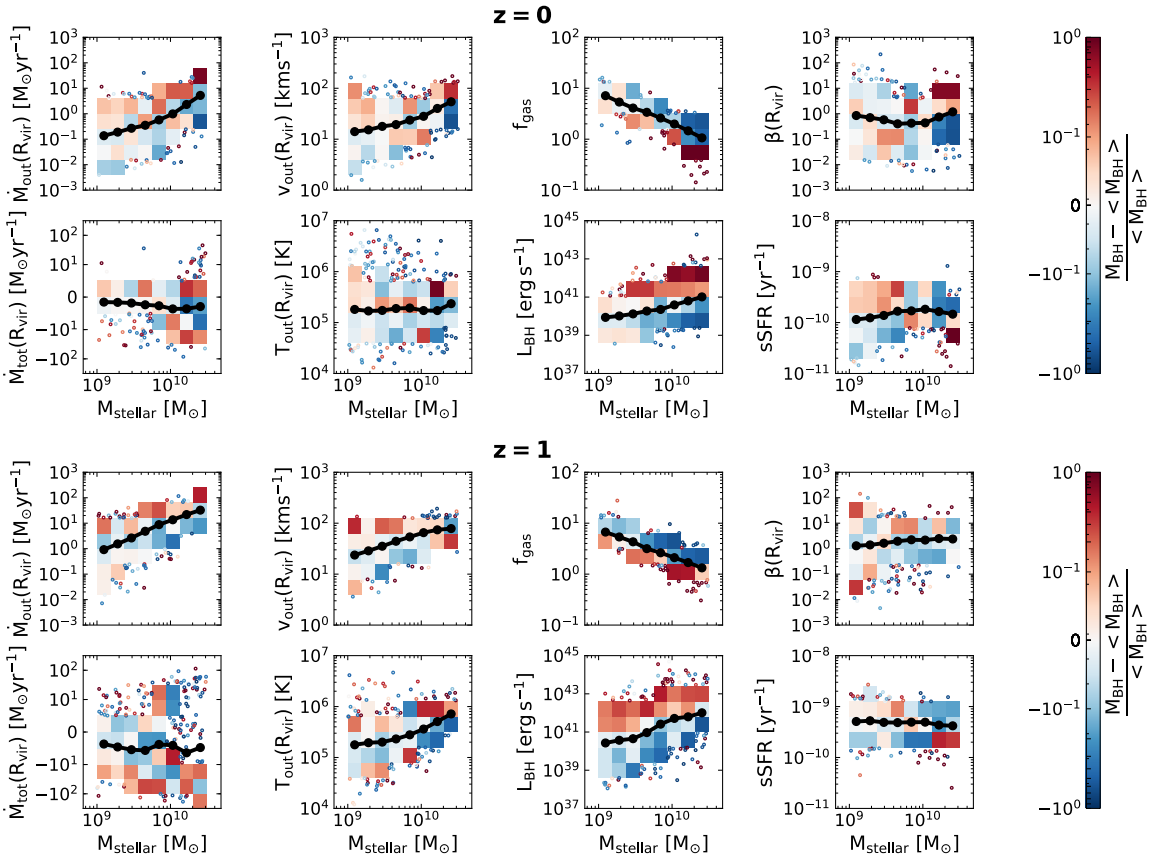

Fig. 3.11 Outflow characteristics and galaxy properties against total stellar mass at $z = 0$ (upper panel) and $z = 1$ (lower panel) for the FABLE low-mass galaxy sample. In each case the binned mean relation is shown as a solid black curve with the filled black circles indicating the bin midpoints. The colour coding of the distribution indicates the offset from the mean $M_{\rm BH} - M_{\rm stellar}$ scaling relation from Figure 3.3, with blue for undermassive and red for overmassive BHs. 2D bins with at least ten objects are colour-coded according to the mean BH mass offset, and otherwise we plot the individual objects colour-coded by their respective BH mass offsets. Galaxies with overmassive BHs have increased outflow and inflow rates, leading to a bimodal distribution for the total mass flow rate. The outflows are faster and hotter in the overmassive regime, similar to the fixed gas mass case. Overmassive BHs at fixed $M_{\rm stellar}$ are also associated with reduced gas fractions and increased BH luminosities. The trends for the star-formation related properties (mass loading factor and sSFR), however are either washed out or inverted below $M_{\rm stellar} \lesssim 6 \times 10^9$ M$_\odot$ compared to the fixed gas mass plots. See Figure 3.4 for corresponding plots at fixed gas mass.

We focused on the effect of varying BH mass at fixed gas mass, as gas abundance is the key driver for BH activity. On the one hand gas provides the fuel for the BH to grow through accretion, and on the other hand a certain amount of gas is needed to be able to drive outflows.

However note that overmassive BHs at fixed gas mass tend to also have larger stellar masses than their undermassive counterparts due to the tight relation between $M_{\rm BH}$ and $M_{\rm stellar}$ (see Figure 3.3). To ensure that the increased outflow activity is not just driven by stellar feedback, we present plots analogous to the ones in Section 3.3.3, but at fixed stellar mass.

Figure 3.11, in analogy to Figure 3.4, shows outflow quantities at $R_{\rm vir}$ (mass outflow rate $\dot{M}_{\rm out}$, total mass flow rate $\dot{M}_{\rm tot}$, outflow velocity $v_{\rm out}$, outflow temperature $T_{\rm out}$, mass loading factor β) as well as integrated galaxy properties (gas mass to stellar mass ratio $f_{\rm gas}$, BH luminosity $L_{\rm BH}$, sSFR) at $z = 0$ (top panel) and at $z = 1$ (bottom panel) plotted against stellar mass.

We plot the distribution of the whole low-mass galaxy population. The colour-coding indicates the offset from the $M_{\rm BH} - M_{\rm stellar}$ relation from Figure 3.3, with red for overmassive and blue for undermassive BHs. Where there are at least ten objects per 2D bin we show the mean BH mass offset of the respective bin, and otherwise we plot the individual objects. Note that the scatter in BH masses at fixed stellar mass is much smaller than at fixed gas mass (see Figure 3.3). We also plot the mean relation as a solid black curve, with the bin midpoints marked by filled black circles.

At fixed stellar mass, we recover the same outflow trends as at fixed gas mass, albeit with a weaker correlation due to the smaller scatter and differing gas reservoirs at fixed stellar mass. We find that overmassive BHs are correlated with both increased mass outflow rates and mass inflow rates, leading to a bimodal distribution for the total mass outflow rate (see Figure 3.11, first column).

Moving on to the second column, we find that overmassive BHs at fixed stellar mass tend to be associated with faster and hotter outflows, but the correlation is weaker than at fixed gas mass. We also inspected the outflow properties at smaller scales and found that there is a much stronger correlation between overmassive BHs and increased outflow velocities and temperatures at $0.2R_{\rm vir}$. Similarly, we found that at fixed gas mass, the strength of the correlation between overmassive BHs and $v_{\rm out}$ and $T_{\rm out}$ is stronger at $0.2R_{\rm vir}$. This suggests that the hot phase driven by the AGN is more dominant at smaller radii, indicating that some of the hot gas falls back as a galactic fountain.

The third column of Figure 3.11 shows that there is a clear correlation between overmassive BHs and suppressed gas fractions, in agreement with the results at fixed gas mass.

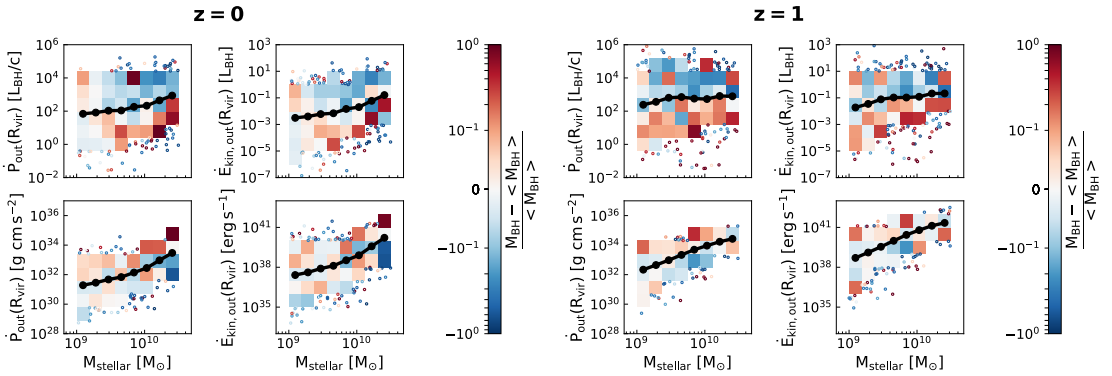

Fig. 3.12 Momentum and kinetic energy outflow rates against total stellar mass at $z = 0$ (left panel) and $z = 1$ (right panel) for the FABLE low-mass galaxy sample. The top row is normalised by the BH luminosity whilst the bottom row shows the outflow quantities in cgs units. The binned mean relations are shown as solid black curves, with the bin midpoints indicated by the filled black circles. Colour coding indicates the offset from the mean $M_{\rm BH} - M_{\rm stellar}$ scaling relation from Figure 3.3, with blue for undermassive and red for overmassive BHs. Where there are fewer than ten objects per 2D bin, the individual objects are plotted. In cgs units, both momentum and energy outflow rates are clearly enhanced for overmassive BHs. However normalizing by the BH luminosity washes out this correlation at both redshifts due to strong coupling between BH masses and luminosities (see Figure 3.11). See Figure 3.6 for corresponding plots at fixed gas mass.

Furthermore, overmassive BHs are generally associated with higher BH luminosities, though this trend is less significant for dwarf galaxies at $z = 0$.

The last column shows galaxy properties related to star formation: the mass loading factor β and the sSFR. Here we find the most significant difference between the trends at fixed gas mass and fixed stellar mass. Whilst at fixed gas mass, we found that overmassive BHs are associated with increased β and suppressed sSFRs for the whole galaxy gas mass range, the trends are less clear at fixed stellar mass. Below $M_{\rm stellar} \lesssim 6 \times 10^9$ M$_\odot$, the correlation is either washed out or inverted. This suggests that for dwarf galaxies in FABLE there is no strong connection between AGN activity and quenching at low redshifts. Though note that the sub-grid model might underestimate AGN luminosities in this mass range (see Figure 3.10 in Section 3.3.5).

Finally, we also consider the momentum and kinetic energy outflow rates at fixed stellar mass in Figure 3.12 (see Figure 3.6 for the equivalent figure at fixed gas mass). We show these outflow rates at $z = 0$ (left panel) and $z = 1$ (right panel). The top row shows the momentum and energy outflow rates in units of the BH luminosity, whilst the bottom row shows the same quantities in cgs units. Again, the colour-coding indicates the offset from the $M_{\rm BH}$ - $M_{\rm stellar}$ relation. We show the mean bin values where there are at least ten objects per

2D bin, and otherwise plot the individual objects. The mean outflow rates are shown as solid black curves, with the bin midpoints marked by filled black circles.

Focusing first on the bottom row, we find that galaxies with overmassive BHs have increased momentum and energy outflow rates, at both redshifts. The correlation is less strong than at fixed gas mass, which we attribute again to the range of gas reservoirs at fixed $M_{\rm stellar}$ and the small scatter in the $M_{\rm BH}$ - $M_{\rm stellar}$ relation.

However, when we normalise the momentum and energy outflow rates by the BH luminosity, the relationship is inverted (top row). This is because overmassive BHs are correlated with higher BH luminosities (see Figure 3.11), and this correlation is significantly stronger than the one for the outflow rates.

Overall, we find that the trends at fixed gas mass from Section 3.3.3 are still recovered at fixed stellar mass. An exception to this are the mass loading factor and the sSFR. At low redshifts, we only see a clear trend for the upper end of the massive dwarf regime ($M_{\rm stellar} \gtrsim 6 \times 10^9$ M$_\odot$) and the $\mathscr{M}^*$ galaxies. This difference is most likely due to the strong SN feedback in FABLE which clears the gas out of dwarf galaxies, preventing the AGN from accreting efficiently. However, at higher redshifts ($z \geq 2$), where accretion rates are higher and a significant fraction of BHs is in the quasar mode (see Figure 3.2), there is a clear correlation between overmassive BHs and suppressed sSFRs across the whole stellar mass range (see Figure 3.5). This indicates that if the AGN are able to accrete efficiently, they are able to regulate star formation in dwarf galaxies.

CHAPTER 4

AGN VERSUS SN FEEDBACK IN COSMOLOGICAL ZOOM-IN SIMULATIONS OF DWARFS

4.1 Background

The systematic analysis of optical large-scale surveys has revealed a population of highly-accreting active galactic nuclei (AGN) in dwarf galaxies (e.g. Greene and Ho, 2004, 2007; Reines et al., 2013; Chilingarian et al., 2018) and recent resolved studies have even found evidence for AGN-driven outflows in dwarfs (Penny et al., 2018; Manzano-King et al., 2019; Liu et al., 2020). See Section 1.4.3 for a detailed account of the observational evidence for AGN feedback in dwarf galaxies.

In Chapter 2, we assess the maximum impact of AGN feedback in an isolated dwarf galaxy simulation by employing constant high Eddington fractions. We find that AGN feedback enhances the outflow temperatures and velocities by up to two orders of magnitude, however, the impact on star formation rates (SFRs) is negligible since the hot outflows follow the 'path of least resistance' and simply escape perpendicularly to the galaxy disc. This then leaves open the possibility that AGN may still be able to regulate star formation in more realistic simulations, which include the cosmological environment, as the AGN-boosted outflows could hinder cosmic gas inflows.

In Chapter 3, we test this possibility using the cosmological simulation suite FABLE. We find that low-mass galaxies with black hole (BH) growth above the mean FABLE scaling relations have enhanced outflow temperatures and velocities. These overmassive BHs are also associated with increased gas outflow rates and, at high redshifts ($z \gtrsim 2$), with suppressed SFRs compared to the mean of the FABLE dwarf population. At lower redshifts, AGN luminosities in dwarf galaxies decrease dramatically and supernova (SN) feedback is the main regulator of star formation. However, we also find that FABLE underproduces high-luminosity

AGN in dwarfs at low redshifts compared to the constraints set by large-scale X-ray surveys. This suggests that the strong SN feedback and the Bondi accretion prescription employed by FABLE (and by the majority of large-scale cosmological simulations) may artificially suppress AGN accretion in the dwarf regime.

In this chapter, we now aim to combine 'the best of both approaches' and test AGN feedback in the high-accretion regime within a realistic cosmological environment. To this end, we run high-resolution cosmological zoom-in simulations of one low-mass dwarf galaxy reducing the strength of the SN feedback compared to FABLE and we carry out several numerical experiments including varying the boost factor of the Bondi prescription and employing constant high-Eddington accretion bursts.

The structure of this chapter is as follows. In Section 4.2, we outline the basic simulation properties as well as our modifications to the fiducial FABLE set-up and provide an overview of all the simulations runs. We then introduce our simulation suite with visualisations of the large-scale inflow – outflow structures in Section 4.3.1 before analysing the simulations based on the Bondi accretion model and employing high-Eddington accretion bursts in Sections 4.3.2 and 4.3.3, respectively. Finally, we discuss our results in Section 4.4 and present our conclusions in Section 4.5.

4.2 Methodology

We conduct an in-depth study of a dwarf galaxy in a relatively low-density environment using a series of zoom-in simulations. Note that this is the same system as 'Dwarf 1' in Smith et al. (2019) which focused on investigating the multi-phase interstellar medium (ISM) model from Smith et al. (2018) in a cosmological context. Here we use the same initial conditions but evolve the system based on the FABLE physics, varying the SN energetics and AGN feedback prescriptions.

4.2.1 Basic simulation properties

We carry out these simulations with the AREPO code (Springel, 2010), where the equations of hydrodynamics are solved on a moving unstructured mesh defined by the Voronoi tessellation of a set of discrete points which (approximately) move with the velocity of the local flow.

The initial conditions are generated with the MUSIC code (Hahn and Abel, 2011) at $z = 127$ and, as in FABLE, we use the cosmological parameters from Planck Collaboration XIII (2016) which are also listed in Table 1.1.

Table 4.1 Overview of the cosmological zoom-in simulation runs, where we list the wind energy fraction, $\varepsilon_{\mathrm{W,SN}}$, which determines the strength of the SN feedback (see Section 4.2.2.1 for details on this parameter), the BH accretion prescription, the BH seed mass, M_{seed}, the seeding redshift, z_{seed}, and the duration of AGN feedback activity, Δt_{AGN}.

Name	$\varepsilon_{\mathrm{W,SN}}$	BH accretion	M_{seed} $[\mathrm{M}_\odot]$	z_{seed}	Δt_{AGN}
Strong SN	1.5	–	–	–	–
SN	0.5	–	–	–	–
SN, Bondi (NoFeed)	0.5	$10^2 \times \dot{M}_{\mathrm{Bondi}}(M_{\mathrm{BH}})$	10^4	4.0	–
SN, Bondi	0.5	$10^2 \times \dot{M}_{\mathrm{Bondi}}(M_{\mathrm{BH}})$	10^4	4.0	as in FABLE[1]
SN, BondiBoost	0.5	$10^3 \times \dot{M}_{\mathrm{Bondi}}(M_{\mathrm{BH}})$	10^4	4.0	as in FABLE
SN, Bondi (NoFeed, L&ES)	0.5	$10^2 \times \dot{M}_{\mathrm{Bondi}}(M_{\mathrm{BH}})$	10^3	6.0	–
SN, Bondi (L&ES)	0.5	$10^2 \times \dot{M}_{\mathrm{Bondi}}(M_{\mathrm{BH}})$	10^3	6.0	as in FABLE
SN, BondiBoost (L&ES)	0.5	$10^3 \times \dot{M}_{\mathrm{Bondi}}(M_{\mathrm{BH}})$	10^3	6.0	as in FABLE
SN, BondiExtraBoost (L&ES)	0.5	$10^4 \times \dot{M}_{\mathrm{Bondi}}(M_{\mathrm{BH}})$	10^3	6.0	as in FABLE
SN, 100Edd, 100 Myr	0.5	$\dot{M}_{\mathrm{Edd}}(M_{\mathrm{seed}})$	10^4	4.0	100 Myr
SN, 50Edd, 100 Myr	0.5	$0.5 \times \dot{M}_{\mathrm{Edd}}(M_{\mathrm{seed}})$	10^4	4.0	100 Myr
SN, 100Edd, 2×10 Myr	0.5	$\dot{M}_{\mathrm{Edd}}(M_{\mathrm{seed}})$	10^4	4.0	2×10 Myr
SN, 100Edd, 25 Myr	0.5	$\dot{M}_{\mathrm{Edd}}(M_{\mathrm{seed}})$	10^4	4.0	25 Myr
SN, 50Edd, 25 Myr	0.5	$0.5 \times \dot{M}_{\mathrm{Edd}}(M_{\mathrm{seed}})$	10^4	4.0	25 Myr

The dwarf galaxy that we focus on for our investigations is selected at $z = 0$ from a 10 cMpch^{-1} box with 256^3 particles, i.e. the coarse resolution is 7.47×10^6 $\mathrm{M}_\odot$. In the coarse simulation, the virial mass is 1.04×10^{10} $\mathrm{M}_\odot$ and the virial radius is 62.0 kpc at $z = 0$. This halo is then re-simulated at higher resolution with the selection region at $z = 0$ set to a sphere of radius 736 kpc.

The resolution within this zoom-in region is increased by a factor of 16^3 so that the high-resolution dark matter mass is $m_{\mathrm{DM}} = 1536$ $\mathrm{M}_\odot$ and the high-resolution target gas mass is $m_{\mathrm{gas}} = 287$ $\mathrm{M}_\odot$. For the high-resolution dark matter particles, gas cells and star particles, we employ comoving softening lengths of 0.129 ckpc which are held constant from $z = 2$.

4.2.2 Feedback models and parameters

Our aim is to determine whether AGN feedback could be a viable alternative to the strong SN feedback that is being employed by the majority of the large-scale cosmological simulations. The FABLE galaxy formation model (Henden et al., 2018), which forms the basis for our

[1] In the FABLE model, the AGN is always accreting, however, the thermal AGN feedback is injected following a duty cycle with $\delta_{\mathrm{duty}} = 25$ Myr, see Section 4.2.2.4 for details.

investigations, has been described in detail in Chapter 3 and we only recap the most important details here and outline the modifications made to the FABLE set-up.

4.2.2.1 Stellar feedback

The stellar feedback model in FABLE is based on the Illustris model (Vogelsberger et al., 2013) with a few modifications to the parameters that govern the galactic winds. The wind energy fraction, $\varepsilon_{\rm W,SN}$, which is related to the amount of energy available from core collapse SNe, is set to $\varepsilon_{\rm W,SN} = 3.0$ in Illustris. This corresponds to a very strong energy normalisation, ~ 1.09 times the amount of energy available from core collapse SNe.

The coupling choice in Illustris is justified by the additional stellar feedback processes other than SNe (such as photoionization or stellar winds) which would also drive these galactic outflows but are not explicitly included in the modelling. However, it could also be reasoned that the value of this coupling should be chosen smaller than one given that there are further uncertainties when and how the feedback energy should be coupled to the ISM and the radiative losses associated with this.

In fact, as an extreme choice, the wind particles in Illustris (and in FABLE) are temporarily decoupled from hydrodynamic interactions until they have left the ISM (based on either a density threshold or a limit on the elapsed travel time), so that cooling losses are minimised. Hence the $\varepsilon_{\rm W,SN} = 3.0$ parametrization in Illustris likely represents an upper limit.

In FABLE the wind energetics are somewhat reduced with $\varepsilon_{\rm W,SN} = 1.5$. However, whilst the Illustris winds are purely kinetic, one third of the wind energy in FABLE is injected thermally which reduces overcooling and therefore compensates for the lower $\varepsilon_{\rm W,SN} = 1.5$ value, still resulting in very strong SN feedback.

With this parametrization the SN feedback is the dominant process regulating star formation at the low-mass end as we saw in Chapter 3. Furthermore, we found that with the fiducial FABLE set-up AGN activity in low-mass galaxies is artificially suppressed: the bright X-ray AGN in local-Universe dwarfs are not reproduced by the FABLE model and the BHs in the FABLE low-mass galaxies are undermassive compared to the observed relations.

Here we would like to assess whether AGN feedback in tandem with more realistic SN feedback parameters could be a plausible alternative to the strong SN feedback set-up. To this end, we significantly reduce the energy imparted to the SN-driven winds by a factor of a third for our dwarf AGN simulations: in addition to the fiducial FABLE set-up with $\varepsilon_{\rm W,SN} = 1.5$, the 'Strong SN' run, we also run a simulation with $\varepsilon_{\rm W,SN} = 0.5$, the 'SN' run, and then add various AGN feedback prescriptions to this set-up (see Table 4.1).

We do not explore other values of the wind energy parameter or vary alternative parameters related to the SN feedback efficiency as this would be beyond the scope of this work.

Here we focus on determining whether weaker SN feedback allows the AGN to be more efficient and whether the weaker SN feedback can be compensated for by AGN feedback in terms of overall star formation suppression.

In the future, we will aim to explore the interplay between SNe and AGN in dwarfs more self-consistently by employing a multiphase ISM model that injects energy and momentum in accordance with the stage of the SN remnant evolution resolved (e.g. Kimm et al., 2016; Hopkins et al., 2018a; Smith et al., 2018; Gutcke et al., 2021), significantly reducing the number of free parameters.

4.2.2.2 BH seeding

BH seeding mechanisms are still largely unconstrained (see Inayoshi et al., 2020, for a recent review of BH assembly mechanisms). Hence we just seed the BH particle 'by hand' in our simulations, inserting a collisionless sink particle at redshift $z_{\rm seed}$ with mass $M_{\rm seed}$ at the potential minimum of the subhalo moving with the peculiar velocity of the group (defined as centre-of-mass velocity of the FoF group).

We focus on intermediate-mass seeds with $M_{\rm seed} = 10^3$–10^4 M$_\odot$ here, which could result from gravitational runaway in nuclear star clusters, as massive BH seeds from direct gas collapse with $M_{\rm seed} \sim 10^5$ M$_\odot$ would be unrealistic for our low-mass systems, whilst low-mass seeds from Population III star remnants with $M_{\rm seed} \sim 100$ M$_\odot$ would be unresolved in our simulations.

The seeding redshifts are chosen in accordance with the stellar mass evolution in the 'SN' base run (see Figure 4.2) and the scaling relations by Reines and Volonteri (2015). We test two different seeding redshifts, $z_{\rm seed} = 6$ and $z_{\rm seed} = 4$, with two different seed masses, $M_{\rm seed} = 10^3$ M$_\odot$ and $M_{\rm seed} = 10^4$ M$_\odot$, respectively. The former lies at the upper end of the 2σ region of the extrapolated BH mass – stellar mass scaling relation by Reines and Volonteri (2015) whilst the latter is somewhat above it (see Figure 4.9).

We choose the massive and late seeding parameters as our fiducial seeding set-up, as we expect this model to be more impactful, and label the light and early seeding set-up, with $z_{\rm seed} = 6$ and $M_{\rm seed} = 10^3$ M$_\odot$, as 'L&ES', see Table 4.1.

The 'L&ES' set-up represents a conservative choice which allows us to explore the growth of light seeds, whilst our second scenario allows us to investigate the maximum AGN impact, employing heavier seeds which are seeded slightly above the 2σ region of the observed local scaling relations. Note that seeding the heavier seeds later would yield better agreement with the scaling relations, however, seeding at such a late point in the stellar mass assembly would make it difficult for the AGN to have a significant influence on the stellar

mass evolution. Given that the scaling relations are heavily extrapolated in this mass regime we therefore insert the heavy seeds at $z = 4$.

Note that whilst the value of the BH subgrid mass, which is used to calculate the BH accretion rates, is set to $M_{\rm seed}$, we set the initial dynamical mass, $M_{\rm dyn}$, which is used to calculate the gravitational potential, to $M_{\rm dyn} = 10^4$ M$_\odot$ for both set-ups. We found that this was necessary to ensure that the BH dynamics are properly resolved, avoiding two body scattering effects with the dark matter particles. For the $M_{\rm seed} = 10^3$ M$_\odot$ runs, we then only allow the dynamical BH mass to increase once the subgrid BH mass has caught up. This also allows us to dispense with the repositioning scheme that was used in FABLE to keep the BHs at the potential minimum of their host haloes.

4.2.2.3 BH accretion

In FABLE, the BHs accrete at a Bondi-Hoyle-Lyttleton-like rate (Hoyle and Lyttleton, 1939; Bondi and Hoyle, 1944; Bondi, 1952), $\dot{M}_{\rm Bondi}$, boosted by a factor of $\alpha = 100$ (and limited by the Eddington rate). The BH accretion rate, $\dot{M}_{\rm BH}$, is then given by:

$$\dot{M}_{\rm BH} = \alpha \dot{M}_{\rm Bondi} = \alpha \frac{4\pi {\rm G}^2 M_{\rm BH}^2 \rho}{c_{\rm s}^3}, \tag{4.1}$$

where G is the gravitational constant, $M_{\rm BH}$ is the BH mass, ρ is the density and $c_{\rm s}$ is the sound speed in the vicinity of the BH[2]. The boost factor α was introduced in the Bondi accretion prescription to account for the unresolved multi-phase nature of the ISM (e.g. Springel et al., 2005a; Booth and Schaye, 2009; Johansson et al., 2009; Sijacki et al., 2011). As in FABLE, we estimate the density and the sound speed in the vicinity of the BH based on the properties of the host cell. The host cell is then also used as the reservoir for the gas draining.

Firstly, we set up runs with the fiducial $\alpha = 100$ set-up from FABLE, labelled as 'Bondi' to test whether the reduction of the SN feedback strength is sufficient to allow for high-luminosity AGN in dwarfs. We also set up simulations with AGN accretion but without AGN feedback (labelled as 'NoFeed') to assess the impact of feedback self-regulation on the BH growth.

As noted in previous chapters, the strong dependency of the Bondi model on $M_{\rm BH}$ suppresses the growth of low-mass BHs so that it is difficult to explore efficient AGN accretion in dwarf galaxies within the constraints of this framework. Here, we take advantage

[2]The traditional Bondi-Hoyle-Lyttleton model also includes a relative velocity term in the denominator, though we neglect this here for simplicity (also note that our relative velocities may not always be accurate given the increased dynamical BH mass for some of our runs).

of the boost parameter α as a cheap way to explore higher accretion rates. We emphasise that these boost factors should then be thought of as numerical experiments rather than within the Bondi framework. We run simulations with $\alpha = 10^3$, labelled as 'BondiBoost', for both seed masses, see Table 4.1.

Again due to the significant cost of the simulation, we can only explore a limited number of set-ups and hence we simply increase this parameter by an order of magnitude to explore the high-accretion regime. For the light seeds, we also trial an even more extreme parameter choice with $\alpha = 10^4$, labelled as 'BondiExtraBoost', as the light seeds are even more severely affected by suppression from the Bondi model. We only run this additional set-up to $z = 1$. All other simulations are run to $z = 0.5$. Note that for all of these simulation runs, we still impose the Eddington limit as a cap on the accretion rates.

In addition to the boost factors, we also utilise constant-luminosity AGN bursts to explore the high-accretion regime. Here we let the BH accrete at a fixed fraction of the Eddington rate, $\dot{M}_{\rm Edd}$, which is given by:

$$\dot{M}_{\rm Edd} = \frac{4\pi {\rm G} M_{\rm BH} {\rm m_p}}{\varepsilon_{\rm r} \sigma_{\rm T} {\rm c}}, \tag{4.2}$$

where $\rm m_p$ is the proton mass, $\varepsilon_{\rm r}$ is the radiative efficiency, $\sigma_{\rm T}$ is the Thomson cross section and c is the speed of light. We trial bursts at both 100 per cent and 50 per cent of the $\dot{M}_{\rm Edd}$, labelled as '100Edd' and '50 Edd', see Table 4.1. Furthermore, we vary the length of the bursts, testing single bursts of duration $\Delta t_{\rm AGN} = 25$ Myr and $\Delta t_{\rm AGN} = 100$ Myr as well as two bursts of duration $\Delta t_{\rm AGN} = 10$ Myr (separated by 10 Myr of inactivity). The burst lengths are motivated by the gas binding energy in the central region (see Figure 4.8). Note that we use the Eddington rate based on the seed mass to calculate the accretion rates for the bursts, so that the we have a constant accretion rate (and luminosity) rather than exponential BH mass growth (to prevent runaway growth). All of these simulations are seeded at $z = 4$ with $M_{\rm seed} = 10^4$ $\rm M_\odot$ (focussing on the heavy-seed set-up to assess the maximum impact of AGN bursts) and run to redshift $z = 0.5$.

We note that for all of the AGN set-ups, the host gas cell is used as a reservoir for the gas draining procedure and since the AREPO code keeps the mass of the gas cells approximately constant (within a factor of two), there is always a fixed gas mass reservoir available even if the density of the central region is very low, with the central cell growing to large sizes. In the future, we will implement a more consistent approach where gas accretion is halted once the number of gas cells within the central resolved region (determined by the softening length) falls below a critical value.

4.2.2.4 BH feedback

The BH luminosity is obtained by multiplying the BH accretion rate with the radiative efficiency, which is here assumed to have the value $\varepsilon_{\rm r} = 0.1$, as in FABLE. For simplicity, we then always couple a fraction $\varepsilon_{\rm f} = 0.1$ of this luminosity as thermal feedback, rather than distinguishing between a quasar and a radio mode as in the original FABLE implementation or in Illustris (Sijacki et al., 2015).

For the runs based on the Bondi prescription, we inject this thermal energy following a duty cycle of $\delta_{\rm duty} = 25$ Myr, as in FABLE, to avoid overcooling (also see Booth and Schaye, 2009). For the AGN bursts, on the other hand, we inject the thermal energy continuously for the duration of the burst. In both cases, the feedback energy is distributed across the 32 nearest neighbours weighted according to the gas cell masses and the smoothing kernel.

We do not explore other AGN feedback set-ups here as this would be beyond the scope of this work, however, we note that AGN feedback assumptions may significantly impact our results. In particular, alternative injection geometries, such as the bipolar winds used in the isolated simulations in Chapter 2, could allow for more efficient BH growth. Exploring the impact of different AGN feedback models in dwarfs is left to future work (see Sections 6.2.1 and 6.2.2).

4.3 Results

4.3.1 Visualisations

In the previous chapters, we found that AGN feedback has a crucial impact on outflow properties, significantly enhancing both outflow temperatures and velocities. We therefore start our investigations by inspecting large-scale temperature maps of our zoom-in simulation runs.

Figure 4.1 shows $5R_{\rm vir} \times 5R_{\rm vir} \times 10$ kpc temperature projections at $z = 3.7, 3.0, 2.0$ for the 'Strong SN', 'SN, BondiExtraBoost (L&ES)', and 'SN, 100 Edd, 2×10 Myr' runs. The streamlines of the outflows are also plotted with the colour-coding according to the sign of the radial velocity (red streamlines for outflowing and blue streamlines for inflowing gas). Furthermore, we indicate the region enclosed by the virial radius as a white dashed circle.

The 'Strong SN' run (first row) experiences significant gas inflows, in particular at early times. By $z = 2.0$, large-scale SN-driven outflows have developed which are able to partially suppress the cosmic inflows. The temperature maps of the 'SN' run (not shown here) look very similar, however the outflows are slightly weaker due to the lower SN energetics and hence the inflow suppression at late times is also a little bit weaker.

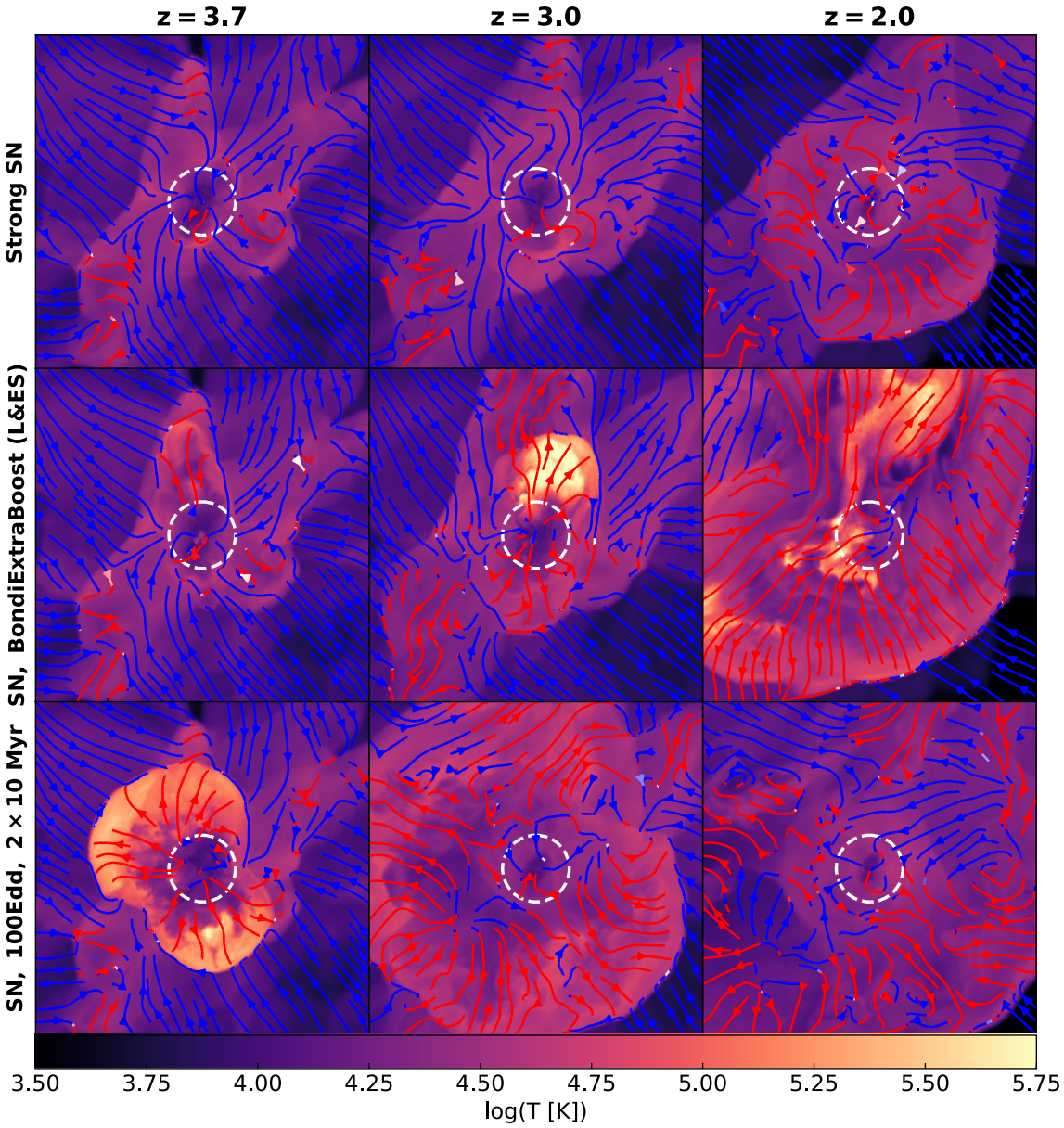

Fig. 4.1 Large-scale gas temperature projections and streamlines of dwarf zoom-in simulations. The projection dimensions are $5R_{\rm vir} \times 5R_{\rm vir} \times 10$ kpc. The colour-coding of the streamlines indicates the sign of the gas radial velocity with red streamlines for outflowing gas and blue streamlines for inflowing gas. The region enclosed by the virial radius is shown as a white dashed circle. The AGN feedback configurations shown here drive hotter and more powerful outflows than the 'Strong SN' run. This allows the AGN to efficiently regulate star formation via the suppression of cosmic inflows.

The 'SN, BondiExtraBoost (L&ES)' run (second row) drives powerful outflows which build up to higher temperatures and larger scales across the range of redshifts shown. At $z = 2$, inflows are virtually completely suppressed by the AGN – significantly more so than in the 'Strong SN' run.

In the last row, we show the temperature projections of the 'SN, 100Edd, 2×10 Myr' run. Note that with this run, the AGN is only active between $z = 4.01$ and $z = 3.97$, with two 10 Myr burst at the Eddington limit separated by 10 Myr of inactivity. This hot outflow efficiently suppresses cosmic inflows until $z \sim 3$. Afterwards cosmic inflows are able reach the inner regions again as the hot bubble has propagated to even larger radii and significantly cooled down. Though there is still some degree of additional inflow suppression compared to the 'Strong SN' run.

In the following sections, we explore the impact of different AGN feedback configurations on star formation and outflow properties more systematically.

4.3.2 Simulation runs based on Bondi accretion model

4.3.2.1 Star formation properties

Firstly, we analyse the simulation runs based on the Bondi accretion model. Figure 4.2 shows the SFRs (left panel) as well as the stellar and gas masses (right panel) of the simulated dwarf galaxies as a function of time. The SN-only runs are shown in blue, the heavy-seed runs ($z_{\rm seed} = 4$) in purple and the light-seed runs ($z_{\rm seed} = 6$) in green.

Focusing on the SN-only runs, we can see that the 'Strong SN' set-up significantly suppresses star formation compared to the fiducial 'SN' run, with the final stellar masses at $z = 0.5$ differing by a factor of ~ 5. However, note that the difference in gas masses is negligible, suggesting that the increased SN energetics lead to additional gas heating rather than increased ejection of gas.

For the heavy-seed runs, with $M_{\rm seed} = 10^4$ M$_\odot$ and $z_{\rm seed} = 4$, there are no significant differences compared to the base 'SN' run when the BH is accreting at the Bondi rate without AGN feedback ('SN, Bondi (NoFeed)') or with AGN feedback ('SN, Bondi').

However, if the boost parameter α in the Bondi rate is enhanced by a further factor of ten, the AGN has a crucial effect on the evolution of the dwarf. From $z \sim 2$ to $z \sim 1.5$, the gas mass decreases by three orders of magnitude from $M_{\rm gas} \sim 10^8$ M$_\odot$ to $M_{\rm gas} \sim 10^5$ M$_\odot$ before gas inflows increase the gas mass again to $M_{\rm gas} \lesssim 10^6$ M$_\odot$. This set-up results in a similar final stellar mass as the 'Strong SN' run albeit with the feedback mainly operating in an ejective manner. Also note that the stellar mass of this run slightly decreases once the galaxy has been quenched. This is due to our definition of the stellar mass which we measure

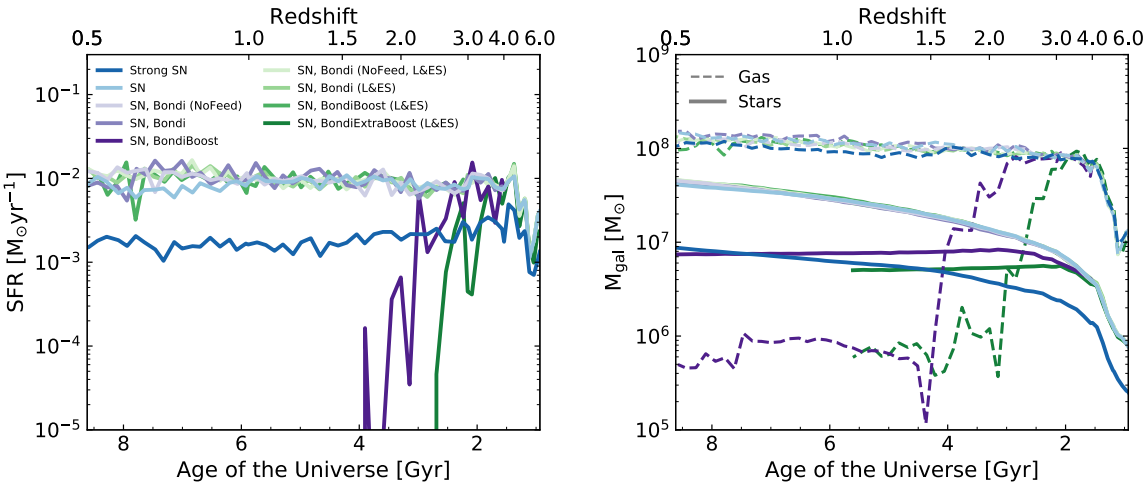

Fig. 4.2 Star formation properties of the zoom-in simulations runs based on the Bondi prescription. The runs with $M_{\rm seed} = 10^4$ M$_\odot$ and $z_{\rm seed} = 4$ are shown in purple and the runs with $M_{\rm seed} = 10^3$ M$_\odot$ and $z_{\rm seed} = 6$ are shown in green. For reference the base 'SN' run and the 'Strong SN' run with the parameters from FABLE are also plotted in light blue and dark blue, respectively. *Left panel*: SFRs within twice the stellar half-mass radius as a function of cosmic time. The Bondi prescription needs to be boosted by $\alpha = 10^3$ and $\alpha = 10^4$ for heavy and light seeds, respectively, so that AGN feedback can suppress star formation compared to the base 'SN' run. Otherwise the growth of low-mass seeds is suppressed by the Bondi model and the AGN feedback is inefficient by construction. *Right panel:* Stellar masses (solid lines) and gas masses (dashed lines) within twice the stellar half-mass radius as a function of cosmic time. The efficient AGN runs are able to drive the gas out of the galaxy, significantly decreasing the gas mass.

within twice the stellar half mass radius. As the stellar distribution slightly contracts the stellar mass is then nominally reduced.

For the light-seed runs, with $M_{\rm seed} = 10^3$ M$_\odot$ and $z_{\rm seed} = 6$, the BH does not have an impact on star formation, even with the $\alpha = 10^3$ boost parameter. The growth of the light seeds is suppressed by the quadratic dependency on $M_{\rm BH}$ in the Bondi prescription so that the impact of the AGN feedback is only minimal, i.e. the limitations of the Bondi model are so severe that one cannot explore high accretion onto low-mass seeds using this model. To test this explicitly, we also set up another run as an experiment where we boosted the Bondi rate by a further factor of a 100, i.e. $\alpha = 10^4$, and ran this additional simulation to $z = 1$. This run, 'SN, BondiExtraBoost (L&ES)', produces a notable suppression in the SFR and gas mass. Whilst the gas depletion levels are similar to the 'SN, BondiBoost' run, the stellar mass decrease compared to the SN-only runs is even more severe as the galaxy gets quenched earlier.

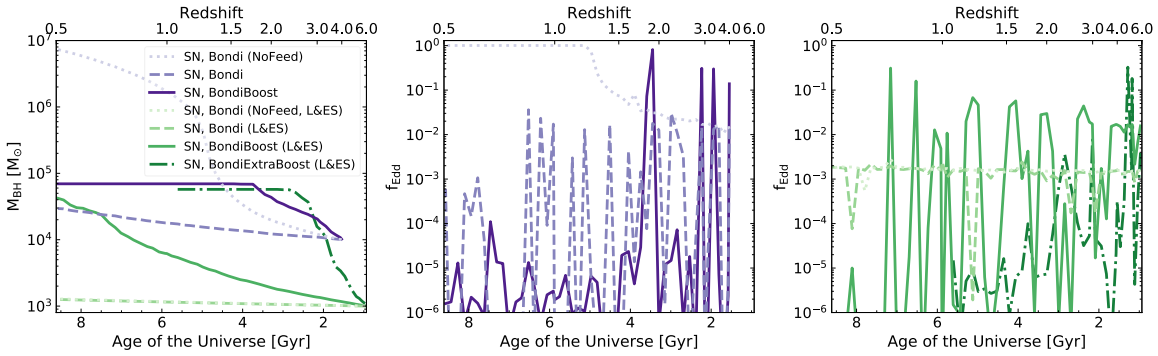

Fig. 4.3 BH growth as a function of cosmic time for the zoom-in simulations runs based on the Bondi prescription. Again the heavy-seed runs ($M_{\rm seed} = 10^4$ M$_\odot$, $z_{\rm seed} = 4$) are indicated by the purple lines and the light-seed runs ($M_{\rm seed} = 10^3$ M$_\odot$, $z_{\rm seed} = 6$) are indicated by the green lines. *Left panel:* BH masses as a function of cosmic time. *Middle and right panels:* Eddington fractions as a function of cosmic time for the heavy-seed and light-seed runs, respectively.

This demonstrates that there is principally enough gas available in these dwarf galaxies for efficient AGN accretion and feedback, though this efficient AGN feedback can only be obtained when departing from the Bondi model by modifying the boost parameter.

4.3.2.2 Accretion properties

We investigate the BH growth more closely in Figure 4.3, which shows BH masses (left panel) and Eddington fractions (middle and right panels) as a function of cosmic time for the simulations runs based on the Bondi accretion model.

The 'SN, Bondi (NoFeed)' run experiences dramatic BH growth from $z \sim 2$, accreting at the Eddington limit from $z \sim 1.2$. The final BH mass is $M_{\rm BH} \sim 8 \times 10^6$ M$_\odot$, much higher than what would be expected for such a low-mass system (also see Section 4.4.3). This extreme growth can happen since, as in FABLE and Illustris, we gradually drain the parent gas cell of its mass and as AREPO keeps the mass of the gas cells approximately constant (within a factor of two) there is a fixed mass to accrete from. Therefore the temperature of the central region needs to be significantly increased to suppress the accretion rates. SN feedback typically does not achieve this so that AGN feedback is required to prevent run-away BH growth once the BH mass is high enough.

Indeed, when thermal AGN feedback is activated with otherwise the same set-up, the BH growth is significantly slowed down in the 'SN, Bondi' simulation run. The thermal feedback leads to bursty BH accretion rates, which are limited by the Bondi rate which is still quite low near the seed mass ($f_{\rm Edd} \sim 0.02$). Therefore these bursts only achieve minimal growth and do not have a significant impact on the host galaxy (see Section 4.3.2.1).

This is all changed for the 'SN, BondiBoost' run, where the boost parameter in the Bondi formula has been increased by a further factor of ten (so that $\alpha = 10^3$). This enables the accretion bursts to reach much higher Eddington fractions and drive efficient BH growth as well as feedback. This run has four high-Eddington bursts with $f_{\rm Edd} > 0.1$ between $z = 4$ and $z = 1.9$, with the final burst reaching the Eddington limit. The subsequent BH growth is almost negligible as the gas reservoir has been exhausted (see Figure 4.2, right panel) and the final BH mass is $M_{\rm BH} \sim 7 \times 10^4$ M$_\odot$.

The light-seed runs experience barely any BH growth under the fiducial Bondi prescription, even without AGN feedback. The Eddington fraction stays at a constant value of about $f_{\rm Edd} \sim 2 \times 10^{-3}$ for the duration of the simulation, with low-level feedback regulation occasionally suppressing the accretion rates of the 'SN, Bondi (L&ES)' run.

Interestingly, when comparing the no-feedback Bondi runs for the two different seed masses at $z = 4$, we can see that the Eddington fraction of the light-seed run is almost exactly one order of magnitude lower than the Eddington fraction of the heavy-seed run, which can be entirely explained by the scalings of $\dot{M}_{\rm Bondi} \propto M_{\rm BH}^2$ and $\dot{M}_{\rm Edd} \propto M_{\rm BH}$ so that $f_{\rm Edd} = \dot{M}_{\rm Bondi}/\dot{M}_{\rm Edd} \propto M_{\rm BH}$, i.e. the ratio between the Eddington fractions corresponds to the ratio of the BH masses. The BH growth is therefore strongly dependent on the seed mass when using the Bondi model.

With the enhanced boost parameter, $\alpha = 10^3$, in 'SN, BondiBoost (L&ES)', the BH is able to grow by over an order of magnitude to $M_{\rm BH} \sim 4 \times 10^4$ M$_\odot$ by the end of the simulation – slightly overtaking the 'SN, Bondi' run. Indeed, the time evolution of the Eddington fraction for these two runs is very similar with bursty accretion rates, due to the thermal feedback, which however tend to stay below 10 per cent of the Eddington limit. Though note that towards the end of the simulation, when the 'SN, BondiBoost (L&ES)' and 'SN, Bondi' runs have reached similar masses, the former is able to reach much higher Eddington fractions due to the enhanced boost factor. Overall, neither of these two runs achieves star formation regulation via AGN feedback since, as we will see in subsequent sections, early efficient feedback is crucial.

With the additional boost factor applied in the 'SN, BondiExtraBoost (L&ES)' run, so that $\alpha = 10^4$, the BH growth is rapid, overtaking all of the heavy seed runs by redshift $z \sim 3$, which is achieved with two high-Eddington accretion bursts. From then onwards this AGN has the most profound impact on its host galaxy out of all of our set-ups as it has reached a similar BH mass to the heavy-seed runs but has a significantly higher boost parameter. Alongside with the earlier injection of feedback due to the early seeding this then leads to earlier gas depletion as well as star formation suppression (see Figure 4.2). From $z \sim 2.5$,

however, when the gas reservoir has been depleted, the BH growth ceases in this run with a final BH mass very similar to the 'SN, BondiBoost' run.

4.3.2.3 Outflow properties

We turn to investigating the impact of the AGN feedback on our dwarf system more closely by inspecting the outflow properties at the virial radius. Figure 4.4 shows the mass outflow rate, $\dot{M}_{\rm out}$, mass inflow rate, $\dot{M}_{\rm in}$, outflow temperature, $T_{\rm out}$, and outflow velocity, $v_{\rm out}$ as a function of redshift. All of the quantities are calculated based on spherical shells at the virial radius of width $\Delta r = 2$ kpc, centred on the potential minimum of the halo and with the kinematics of the centre of mass taken into account and the Hubble flow subtracted. For reasons of clarity, we focus on comparing the SN-only and heavy-seed runs here and only include 'SN, BondiExtraBoost (L&ES)' from the light-seed run series for comparison, as the AGN feedback is inefficient for all other runs starting from a light seed.

Overall, the outflow properties of the two SN-only runs are fairly similar. The mass outflow rates and outflow velocities are somewhat enhanced for the 'Strong SN' run compared to the 'SN' run, in particular at $z \sim 2.6$ and $z \sim 1.2$. Both of these outflow episodes are also followed by a suppression in inflow rates. This outflow enhancement would be expected due to the more energetic winds, though only moderate differences are obtained for these two runs since the decreased wind energetics are compensated for by the higher SFRs in the 'SN' run.

For both runs, the outflow temperatures steadily increase across cosmic time whilst the inflow rates steadily decrease. This can be interpreted by the build-up of an SN-driven hot outflow which becomes increasingly successful at suppressing cosmic inflows (also see Figure 4.1). At least in this set-up, AGN feedback can then be particularly important at early times, regulating cosmic inflows before SN feedback becomes efficient.

As expected from the negligible impact on SFRs and gas content, the 'SN, Bondi (NoFeed)' and 'SN, Bondi' runs have very similar outflow properties to the 'SN' run.

For the 'SN, BondiBoost' run, however, the outflows are significantly enhanced, with higher mass outflow rates, outflow temperatures and outflow velocities. This is particularly notable from $z \sim 2$, when the high-Eddington accretion burst drives a high-velocity, hot bubble, which also leads to an almost complete suppression of inflows at $z \sim 1.5$. This is in agreement with our findings from Chapters 2 and 3, where we also found that AGN feedback in dwarfs drives hotter and faster outflows which may suppress inflows in a cosmological setting.

The outflows of the 'SN, BondiExtraBoost (L&ES)' run are similarly enhanced by the AGN, though the effect sets in more quickly and is more pronounced due to the early feedback

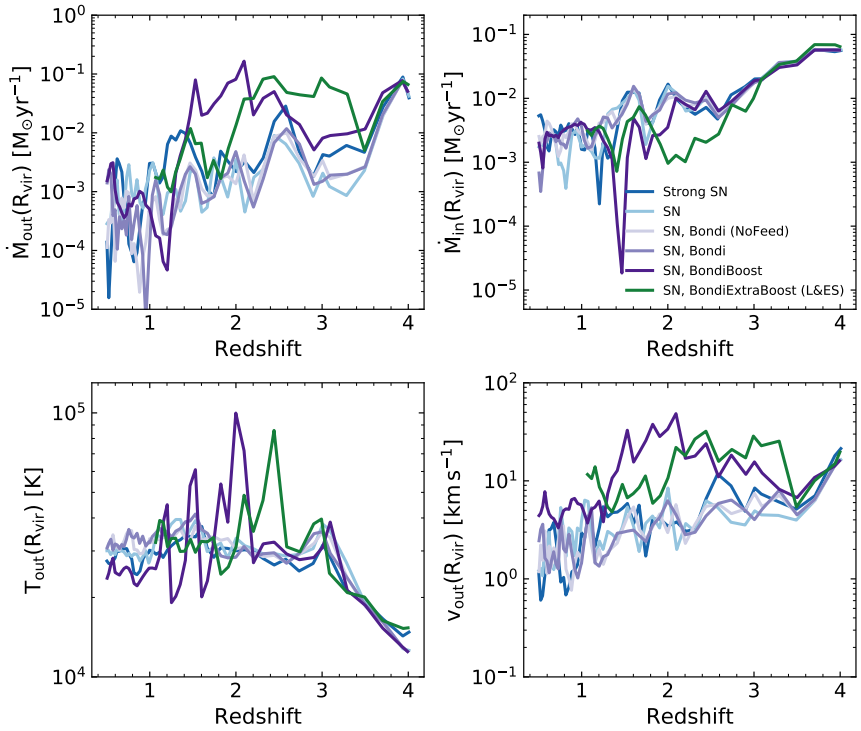

Fig. 4.4 Outflow properties of the zoom-in simulations runs based on the Bondi prescription. The mass outflow rate, mass inflow rate, outflow temperature and outflow velocity are shown as a function of redshift. All outflow quantities are measured at the virial radius. The heavy-seed runs are plotted in purple and for reasons of clarity, we only show the 'SN, BondiExtraBoost (L&ES)' run from the light-seed run series (all other light-seed runs have inefficient AGN feedback and are therefore similar to the 'SN' base run). The outflow properties of the 'Strong SN' and 'SN' runs are plotted, for reference, in blue. Efficient AGN feedback is associated with enhanced outflow rates, suppressed inflow rates as well as increased outflow temperatures and velocities.

episodes and higher accretion rates. In particular, this leads to significant and persistent suppression of cosmic inflows at early times.

4.3.3 The impact of high-Eddington accretion bursts

The results from Section 4.3.2 suggest that high-Eddington accretion bursts can efficiently drive outflows and regulate star formation in dwarfs via ejective as well as preventative feedback, in particular at early times. Though the fiducial Bondi model generally prevents the AGN from entering this regime as the quadratic dependency on $M_{\rm BH}$ strongly suppresses accretion, forcing us to use unrealistic boost factors to explore the high-accretion regime.

To investigate the impact of AGN on dwarfs more systematically, we therefore dispense with the Bondi prescription in this section and let the AGN accrete at a fixed fraction of the Eddington rate, akin to our simulations in Chapter 2. We test different Eddington fractions

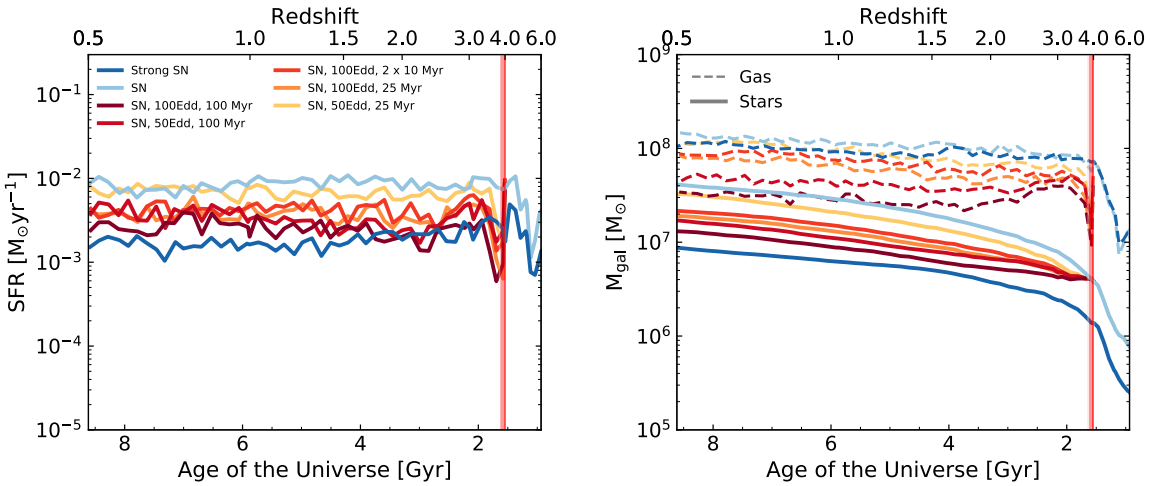

Fig. 4.5 Star formation properties of the high-Eddington accretion burst runs. The AGN runs are plotted as red and orange lines and the SN-only runs are shown as blue lines for reference, as listed in the legend. We also indicate the duration of the 25 Myr and 100 Myr bursts as red and light red shaded regions, respectively. *Left panel*: SFRs within twice the stellar half-mass radius as a function of cosmic time. The strength of the AGN bursts dictates the severity of the star formation suppression. *Right panel:* Stellar masses (solid lines) and gas masses (dashed lines) within twice the stellar half-mass radius as a function of cosmic time. All AGN bursts lead to gas depletion of varying levels, with more severe depletion for longer and higher-luminosity bursts.

and burst durations as detailed in Table 4.1. For all of these runs, the BH is seeded at $z_{\rm seed} = 4$ with $M_{\rm seed} = 10^4$ M$_\odot$ and we run all of these simulations to $z = 0.5$.

4.3.3.1 Star formation properties

Figure 4.5 shows the SFRs (left panel) as well as stellar and gas masses (right panel) of the fixed-$f_{\rm Edd}$ runs (red and orange lines). For reference, the two SN-only runs are also shown (blue lines).

To guide the eye, we have indicated the duration of the 100 Myr burst as a light red shaded region and the duration of the 25 Myr burst as a red shaded region. Note that the 'SN, 100Edd, 2×10 Myr' run has two bursts of duration 10 Myr separated by a 10 Myr break, i.e. the AGN is switched off permanently after 30 Myr. We do not indicate the burst durations of this run separately as these would be difficult to tell apart from the $\Delta t_{\rm AGN} = 25$ Myr run.

The AGN bursts lead to a significant depletion of the gas mass by up to an order of magnitude which is closely followed by a suppression of the SFRs. After the AGN has shut off, the gas masses somewhat recover though they generally remain below the gas mass of the 'SN' run and, apart from the 'SN, 50Edd, 25 Myr', all AGN runs also consistently have

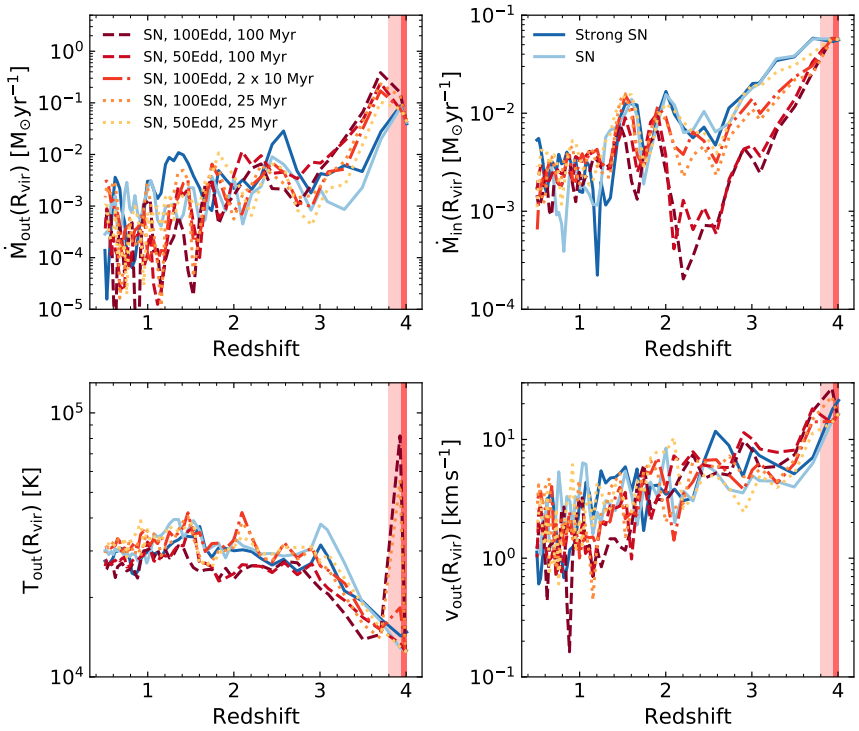

Fig. 4.6 Outflow properties of the high-Eddington accretion burst runs. The mass outflow rate, mass inflow rate, outflow temperature and outflow velocity are shown as a function of redshift. The AGN runs are plotted as red and orange lines and the 'Strong SN' and 'SN' runs as blue lines. We also indicate the duration of the 25 Myr and 100 Myr bursts as red and light red shaded regions, respectively. The AGN bursts increase the mass outflow rates as well as enhance outflow velocities and temperatures. However, the most long-term impact is on the inflow rates which are suppressed up to $z \sim 2$.

gas masses below the 'Strong SN' run. This demonstrates that gas depletion is a long-term effect (rather than the bursts just driving a galactic fountain).

The gas depletion leads to a sustained suppression of star formation compared to the 'SN' run for all AGN burst luminosities and durations considered. The range of AGN energetics spanned by our simulations leads to a continuous transition between the 'Strong SN' and 'SN' runs in terms of severity of star formation suppression, with the 'SN, 100Edd, 100 Myr' run having SFRs just slightly higher than the 'Strong SN' run and the 'SN, 50 Edd, 25 Myr' run having SFRs only slightly lower than the 'SN' base run.

Consequently, the final stellar masses of the AGN runs also form a continuous spectrum in between the edge values given by the 'SN' and 'Strong SN' runs.

4.3.3.2 Outflow properties

Next we assess the outflow properties of the high-Eddington accretion burst runs. In particular, we aim to investigate what mechanism prevents further cosmic gas inflows and ensures the permanent gas depletion long after the AGN has shut down.

Figure 4.6 shows $\dot{M}_{\rm out}$, $\dot{M}_{\rm in}$, $T_{\rm out}$, and $v_{\rm out}$ as a function of redshift. The outflow properties are calculated at the virial radius based on a spherical shell of thickness 2 kpc as in Section 4.3.2.3. The durations of the 25 Myr and 100 Myr bursts are indicated in the plot by the red and light red shaded regions, respectively.

The mass outflow rates are significantly enhanced by the AGN bursts and remain above the outflow rates of the 'SN' run until $z \sim 3$. Again the magnitude of this enhancement depends on the AGN energetics, with the 100 Myr burst runs having the most significant impact. Outflow rates are similar for the AGN and SN-only runs between $z = 3 - 2$. From $z \sim 2$ onwards, the AGN runs have somewhat lower outflow rates as both star formation activity and the gas reservoir have been suppressed by the AGN bursts.

The impact of the AGN bursts on the mass inflow rates is even more dramatic, with significant inflow suppression compared to the SN-only runs until $z \sim 3$ for short bursts ($\Delta t_{\rm AGN} = 25$ Myr or two bursts of duration 10 Myr) and until $z \sim 2$ for the $\Delta t_{\rm AGN} = 100$ Myr runs. For the latter, the inflow suppression compared to the SN-only runs is of an order of magnitude so that the gas abundances remain at very low levels for the $\Delta t_{\rm AGN} = 100$ Myr burst runs.

The outflow velocities are only slightly enhanced by the AGN bursts and this offset fades away quickly, only lasting until $z \sim 3.4$. From then onwards the outflow velocities are fairly similar to the ones of the SN-only runs. If anything, there is a slight suppression of the outflow velocities of the AGN runs at late times, coincidental with the decline in mass outflow rates. Again, the decrease in outflow activity can be attributed to the decline in both star formation and gas availability. These results suggests more sustained AGN activity would be required for driving faster outflows.

Finally, we turn to the outflow temperatures. The AGN bursts drive a hot bubble so that the outflow temperatures at the virial radius are enhanced momentarily. Once the AGN has been shut down, the hot bubble propagates to larger radii and there is no significant differences between the temperatures at the virial radius for the AGN and SN-only runs at late times.

This is illustrated in Figure 4.7, which shows the temperature profiles at $z = 4.01$ (just before the AGN switches on), $z = 3.99$ (just after the AGN has switched on), $z = 3.93$ (just after $\Delta t_{\rm AGN} = 25$ Myr), $z = 3.7$ (just after $\Delta t_{\rm AGN} = 100$ Myr), $z = 3.01$ and $z = 2.0$.

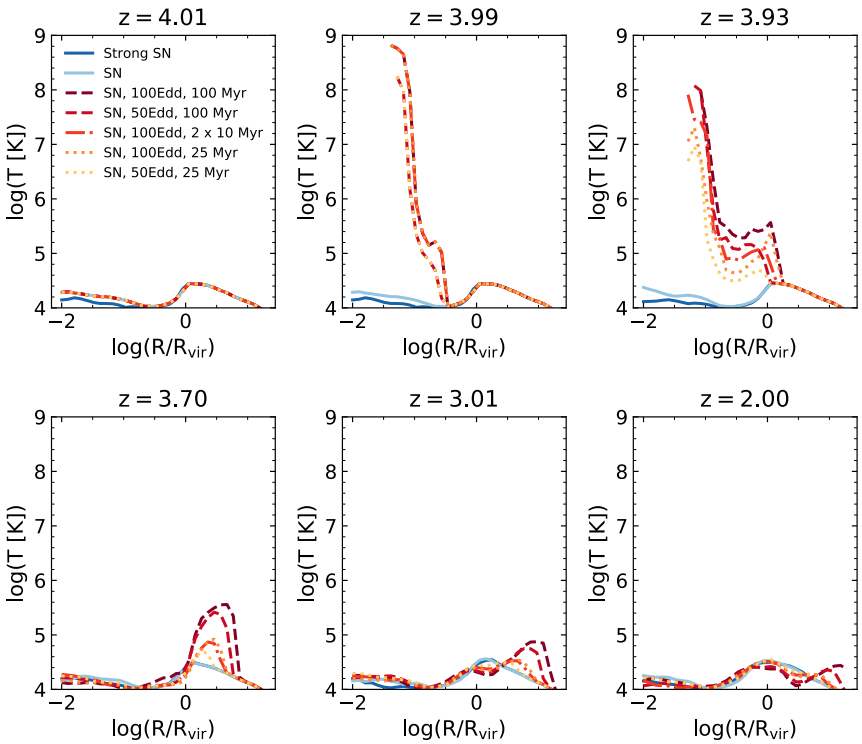

Fig. 4.7 Temperature profiles of the high-Eddington accretion burst runs at $z = 4.01$ (just before the AGN switches on), $z = 3.99$ (just after the AGN has switched on), $z = 3.93$ (just after $\Delta t_{\rm AGN} = 25$ Myr), $z = 3.7$ (just after $\Delta t_{\rm AGN} = 100$ Myr), $z = 3.01$ and $z = 2.0$. The AGN runs are plotted as orange and red lines, the SN-only runs are also shown in blue, for reference. The AGN bursts drive a hot bubble which survives at large radii until $z \sim 3$ for short-duration bursts and until $z \sim 2$ for long-duration bursts, coincidental with the suppression of inflows.

At $z = 3.99$ we have an extremely hot bubble with temperatures $\sim 10^8$ K for the $f_{\rm Edd} = 0.5$ runs and temperatures of $\lesssim 10^9$ K for the $f_{\rm Edd} = 1.0$ runs. By $z = 3.93$, the outer layers of this bubble have managed to propagate to the virial radius, cooling to $\sim 10^5$ K in the process. By $z = 3.7$, the inner regions of the galaxy have cooled down again completely whilst the hot bubble with $T \sim 10^5$ K is still present at large radii with $R_{\rm vir} < r < 10R_{\rm vir}$ (also see Figure 4.1). This heating effect at large radii persists until $z \sim 3$ for the short-duration bursts and until $z \sim 2$ for the long-duration bursts in line with the time frame of the inflow suppression from Figure 4.6.

We also carried out two additional zoom-in runs with $f_{\rm Edd} = 0.5$ and $f_{\rm Edd} = 1.0$ and a single burst of duration $\Delta t_{\rm AGN} = 10$ Myr (not shown here). These very short AGN bursts do not have any significant impact on the star formation and outflow properties of the host galaxy.

This can be interpreted by comparing the injected AGN energy with the binding energy of the gas. Figure 4.8 shows the energy released during a burst with a luminosity of 50 per

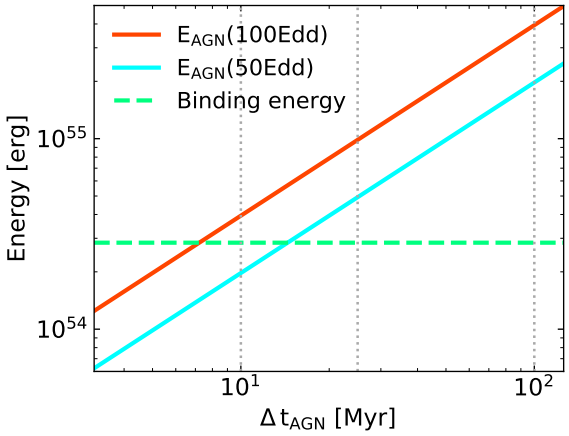

Fig. 4.8 Comparison between the binding energy of the gas and injected AGN energy for fixed-luminosity AGN bursts. The binding energy of the gas (green dashed line) is calculated within the stellar half-mass radius at $z_{\rm seed} = 4$. The injected AGN energy is calculated as a function of burst duration, $\Delta t_{\rm AGN}$, for fixed luminosities $0.5 L_{\rm Edd}(M_{\rm BH} = 10^4$ M$_\odot)$, blue solid line, and $L_{\rm Edd}(M_{\rm BH} = 10^4$ M$_\odot)$, red solid line. The grey dotted lines indicate $\Delta t_{\rm AGN} = 10, 25, 100$ Myr, for reference.

cent (blue solid line) or 100 per cent (red solid line) of the Eddington limit for a seed mass $M_{\rm seed} = 10^4$ M$_\odot$ as function of burst duration, $\Delta t_{\rm AGN}$. We emphasise that the Eddington luminosity in the fixed AGN burst runs is always calculated based on the seed mass, i.e. the bursts have a constant luminosity throughout so that we do not get a runaway effect caused by exponential growth at the Eddington limit. We also show the binding energy of the gas within the stellar half-mass radius at $z_{\rm seed} = 4$ as a green dashed line. Furthermore, we indicate $\Delta t_{\rm AGN} = 10, 25, 100$ Myr as grey dotted lines, for reference.

For $\Delta t_{\rm AGN} = 10$ Myr, the energy released by a 50 per cent Eddington burst is still below the binding energy so that this set-up is not sufficient to drive an outflow. A 100 per cent Eddington burst of the same duration reaches just above the binding energy, however, due to cooling losses this energy injection then still does not have a significant impact. Though interestingly we found that the run with two $\Delta t_{\rm AGN} = 10$ Myr bursts (separated by 10 Myr of no AGN activity) drives large-scale outflows and suppresses star formation, suggesting that bursts of this duration can still have an impact as long as there is more than one feedback episode.

The $\Delta t_{\rm AGN} = 25$ Myr run with $f_{\rm Edd} = 1.0$ comfortably ($\sim$ factor of four) exceeds the binding energy and can therefore efficiently drive outflows, whilst the $f_{\rm Edd} = 0.5$ set-up only injects $\sim$ a factor of two higher energy than the binding energy limit so that the impact on the host galaxy is small, in agreement with the minor impact on star formation and outflow properties with this set-up.

Finally, for $\Delta t_{\rm AGN} = 100$ Myr run, the injected energy is much higher than the binding energy for both Eddington fractions (around an order of magnitude higher) and the SFRs as well as outflow properties are therefore significantly changed with this set-up.

4.4 Discussion

We have demonstrated that high-Eddington accretion episodes can efficiently suppress star formation in dwarf galaxies in lieu of strong SN feedback, provided that the injected AGN energy exceeds the binding energy of the gas. However, these high-Eddington accretion bursts are difficult to obtain with the Bondi prescription as low-mass BHs grow slowly by construction due the quadratic dependency on $M_{\rm BH}$. We therefore freely varied the boost parameter in the Bondi formula to allow for higher (but still self-regulated) accretion rates (see Section 4.3.2). Furthermore, we tested the impact of accretion bursts with a fixed Eddington fraction (see Section 4.3.3).

4.4.1 Possible extensions and caveats

For this investigation, we only focused on one system. However, the cosmic environment and merger history may play an important role in the efficiency of AGN accretion and the effectiveness of AGN feedback. Therefore, it would be crucial to also simulate dwarfs in other environments (e.g. high-density regions) in a follow-up study.

Furthermore, one could take advantage of the super-Lagrangian refinement technique, as in Chapter 2, to increase the resolution in the immediate vicinity of the BH and test more sophisticated AGN energy injection mechanisms such as bipolar feedback. This could have a positive impact on the BH accretion rates as we find that the isotropic thermal feedback significantly suppresses accretion and injecting the AGN energy into a bipolar cone may allow for a cold gas reservoir to survive at the centre. Increasing the resolution around the BH would also allow us to consistently resolve the Bondi radius and thereby obtain a more reliable estimate of the Bondi accretion rate.

Finally, it would also be interesting to run these simulations with a more realistic multi-phase ISM model. Smith et al. (2019) simulated the same system (albeit only to to $z = 4$) using metal-line cooling to 10 K and a mechanical SN feedback model, which delivers the correct amount of momentum corresponding to the stage of the SN remnant evolution resolved. They found that SNe were insufficient to regulate star formation in this dwarf galaxy (as well as in most other low-mass systems they investigated) due to the early build-up

of dense gas and suggested that other mechanisms would have to be invoked to prevent this, e.g. other stellar feedback channels and/or currently unresolved turbulent support.

We found that energetically less powerful SNe can be supported in suppressing star formation by high-Eddington accretion bursts and it would be worthwhile to investigate whether AGN feedback could also work in tandem with more physical SN feedback models in dwarf galaxies.

4.4.2 Observational context

We continued the SN-only simulation runs to $z = 0$ and found that the final stellar mass of our dwarf system is 1.2×10^7 $M_\odot$ for the 'Strong SN' run and 6.9×10^7 $M_\odot$ for the 'SN' run, i.e. in the lowest mass range of observed dwarf galaxies with AGN activity. In particular, this is the mass range where the BPT (Baldwin et al., 1981) diagram may become unreliable for AGN identification (Cann et al., 2019). Therefore the AGN occupation fraction in this mass range is still very unconstrained, though X-ray observations suggest it may be just under three per cent (for a cut-off X-ray luminosity of 10^{39} ergs^{-1}) in the local Universe (Birchall et al., 2020).

In our simulations, AGN feedback in dwarfs mainly regulates star formation by ejecting gas or by preventing gas accretion – rather than just heating or dispersing the gas locally like the strong SN feedback. Observationally, this would then manifest itself as a difference in gas mass fractions. Interestingly, observations have found that (local) dwarf galaxies with AGN activity are HI poor at fixed stellar mass[3] – even when the control sample is additionally matched in SFR (Bradford et al., 2018; Ellison et al., 2019). Note that this effect was also found in other simulations for a range of redshifts (e.g. Sharma et al., 2020; Koudmani et al., 2021). This then suggests that AGN feedback could indeed be responsible for the gas depletion in these low-mass systems.

In addition to the gas mass fractions, there are various other observables that may guide the evaluation of the success of a particular prescription for BH growth and feedback, such as the quenched fraction of isolated dwarf galaxies or the stellar mass function. Note that for zoom-in simulations, we are mostly restricted to comparing with mean observed quantities, as we do not have a statistically significant sample of simulated galaxies. These comparisons are particularly useful with regards to observed correlations that only have a relatively small amount of scatter, e.g. the stellar mass to halo mass ratio.

[3]Note that these results are only for more massive dwarfs with $M_{\rm stellar} \gtrsim 10^9$ $M_\odot$, however, the samples are either limited to this stellar mass and/or the AGN activity is identified via the BPT diagram, which precludes the identification of AGN in lower-mass dwarfs.

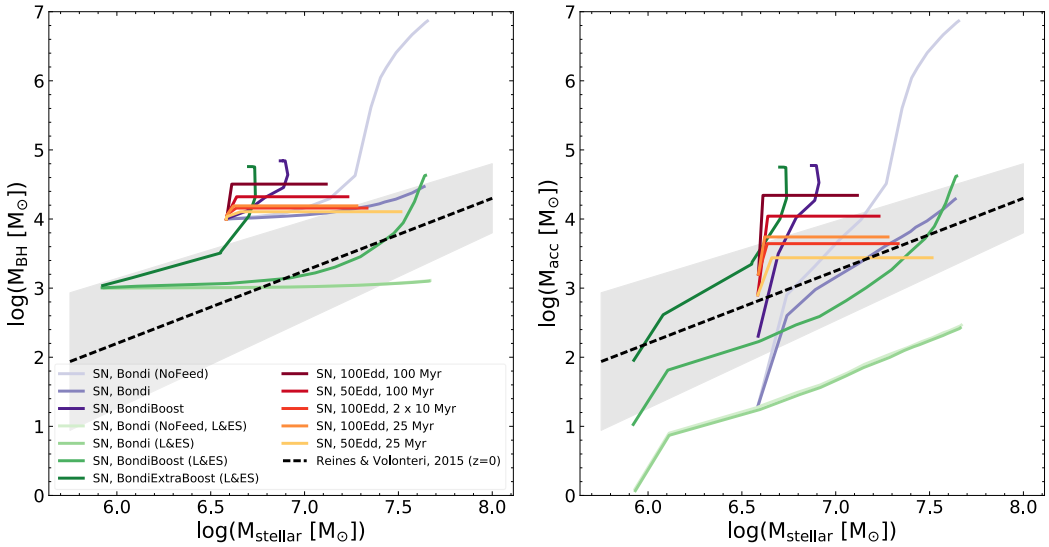

Fig. 4.9 BH mass – stellar mass scaling relations for the cosmological zoom-in simulation runs. For comparison, we also show the mean BH mass – stellar mass scaling relation (black dashed line) and 2σ region (grey shaded area) for observed local AGN from Reines and Volonteri (2015). *Left panel:* The evolution of all of the AGN runs in $M_{\rm stellar} - M_{\rm BH}$ space. The efficient AGN runs based on the Bondi prescription ('SN, BondiBoost' and 'SN, BondiExtraBoost (L&ES)') end up significantly above the observed local relation and are therefore most likely unrealistic. The short AGN bursts, however, are consistent with the observations. *Right panel:* Same as left panel but here we plot the accreted BH mass, $M_{\rm acc}$, rather than total BH mass as the BH seed mass is largely unconstrained so that $M_{\rm acc}$ may provide a cleaner measure. This shows that the BH growth associated with longer bursts is also principally plausible, however the efficient AGN runs based on the Bondi prescription remain firmly excluded.

FABLE is in good agreement with the observed stellar mass to halo mass ratio for massive haloes (see Henden et al., 2018, 2020) and we find that our zoom-in run with the fiducial FABLE model (the 'Strong SN' run) matches the expected stellar masses from abundance matching as in Behroozi et al. (2013). We therefore require that 'successful' AGN models yield total stellar masses similar to the 'Strong SN' run. This is achieved by the Bondi-based runs with suitably increased boost factors, 'SN, BondiBoost' and 'SN, BondiExtraBoost (L&ES)', as well as the long-duration high-Eddington burst run, 'SN, 100Edd, 100 Myr'. However, note that the AGN activity would likely not be restricted to a single burst event in the dwarf's history and in the future we will explore the impact of a series of bursts dependent on the gas supply in the central region.

4.4.3 BH growth

Another useful observational constraint is provided by the scaling relations which allow us to assess whether the BH growth that is required for efficient AGN feedback in our simulations is realistic.

Figure 4.9 shows the evolution of the different simulation runs in $M_{\rm stellar} - M_{\rm BH}$ space. The left-hand panel shows the BH (subgrid) mass whilst the right-hand panel shows the accreted BH mass. For comparison, we also plot the mean $M_{\rm BH} - M_{\rm stellar}$ scaling relation from the sample of local AGN (including dwarf AGN) by Reines and Volonteri (2015) as a black dashed line with the 2σ region indicated by a grey shaded area. Note that this relation is for $z = 0$ galaxies, whilst we only ran our simulations to $z = 0.5$ ($z = 1$ for the 'SN, BondiExtraBoost (L&ES)' run). Furthermore, this relation has been heavily extrapolated, indeed the lowest-mass galaxy in the Reines and Volonteri (2015) sample is Pox 52 with $\log(M_{\rm stellar}) = 8.63$. Depending on the BH seeding mechanism, we may expect the relation to significantly flatten off in the stellar mass regime that we consider here (e.g. Greene et al., 2020).

Keeping these caveats in mind, we find that the short AGN burst runs ($\Delta t_{\rm AGN} = 25$ Myr and the two bursts with $\Delta t_{\rm AGN} = 10$ Myr) are in agreement with the relation from Reines and Volonteri (2015) within 2σ, though note that they all lie above the mean relation.

The boosted Bondi runs which lead to efficient quenching ('SN, BondiBoost' and 'SN, BondiExtraBoost (L&ES)') lie significantly above the 2σ region and therefore the BH growth associated with these models is most likely unrealistic.

The 'SN, BondiBoost (L&ES)' run also lies above the 2σ region, whilst the 'SN, Bondi' run is still in agreement with the observational constraints by the end of the simulation at $z = 0.5$.

Also interestingly, whilst the extreme BH growth of the 'SN, Bondi (NoFeed)' run exceeds the limits set by the observed scaling relation, the equivalent run with a light seed, 'SN, Bondi (NoFeed, L&ES)' ends up significantly (~ 1 order of magnitude) below the mean relation, with the final BH mass even outside the limits set by the 2σ region. Similarly, the 'SN, Bondi (L&ES)' run only experiences minimal growth. This again demonstrates the strong dependency of the Bondi prescription on the BH seed mass.

In addition, it is worthwhile to consider the accreted BH mass which provides a cleaner measure than the total BH mass since the BH seed mass is essentially a free parameter. The accreted BH mass can then tell us how much gas accretion is required to power efficient feedback and whether this required BH growth is still in line with the limits set by the observed scaling relations.

Considering the evolution of the accreted mass, we find much better agreement for the AGN runs, with the 'SN, 50 Edd, 100 Myr' run also within the observational constraints. However, even with the accreted BH mass as a measure, the boosted Bondi runs still lie above the observational constraints.

Overall, we therefore find that self-regulated models based on the Bondi prescription require unrealistic BH growth for efficient AGN feedback. This is due to the very limited framework of the Bondi prescription which suppresses the growth of low-mass seeds.

On the other hand, an accretion model that produces high-Eddington bursts at high redshift efficiently suppresses star formation and would still be within the observational constraints. The development of next-generation AGN accretion models will be crucial for properly investigating AGN physics in the dwarf regime and we explore this in Chapter 5.

4.5 Conclusions

We have systematically investigated the impact of AGN feedback on dwarf galaxies using cosmological zoom-in simulations, varying the SN feedback energetics, AGN feedback prescriptions as well as well as BH seeding redshifts and masses. Our main findings are summarised below:

- The commonly employed Bondi prescription does not allow for significant AGN feedback in dwarf galaxies due to its strong dependency on $M_{\rm BH}$. Hence we need to apply unrealistic boost factors to obtain efficient AGN feedback – these should be considered more of a numerical experiment than BH growth modelling within the Bondi framework. However, note that these boosted Bondi runs are still Eddington-limited and indeed, even with the boost factors applied, the Eddington limit is rarely reached due to self-regulation by thermal AGN feedback.

- The boost factors result in several high-Eddington accretion episodes which quench the dwarf by expelling vast quantities of gas in hot outflows which then also prevent further gas accretion from the cosmic web.

- However, even with this AGN feedback parametrization, the BH growth required for efficient AGN feedback is likely too high as the resulting BH masses and stellar masses do not match the (extrapolated) observed $M_{\rm BH} - M_{\rm stellar}$ scaling relation from Reines and Volonteri (2015).

- We also trial fixed-luminosity AGN bursts (at 50 or 100 per cent of the Eddington rate of the BH seed mass) and find that these can efficiently quench the dwarf galaxy,

provided that the injected AGN energy exceeds the binding energy of the gas at the seeding redshift.

- These bursts drive a hot bubble which propagates to the circumgalactic medium and prevents cosmic inflows from reaching the galaxy long after the AGN has switched off.
- The observed $M_{\rm BH} - M_{\rm stellar}$ scaling relation provides an upper limit on plausible burst durations with single bursts of duration 25 Myr or two bursts of duration 10 Myr both within the observational constraints, whilst still having a significant impact on star formation.

We therefore conclude that AGN feedback in tandem with a more realistic SN feedback prescription could be a viable alternative to strong SN feedback in dwarf galaxies. However, we found that AGN feedback in dwarfs cannot be explored in the high-accretion regime with the traditional Bondi model as this model prevents significant BH growth for low-mass BHs. Upcoming state-of-the-art observations with e.g. SKA, *JWST*, *RST*, *Athena*, *Lynx*, and LISA will be able to constrain these theoretical possibilities and, in particular, will extend the BH – galaxy scaling relations to much lower BH masses (e.g. Greene et al., 2020). Next-generation galaxy formation simulations with updated feedback models will be key for guiding the interpretation of these surveys and for modelling the impact of massive BHs on galaxies across the whole stellar mass range.

CHAPTER 5

MASS AND SPIN EVOLUTION OF AGN WITH A NEW UNIFIED ACCRETION DISC MODEL

5.1 Background

Feedback from active galactic nuclei (AGN) has been found to play a crucial role in galaxy formation simulations. The modelling of the gas accretion onto the AGN is essential for obtaining realistic AGN feedback as the AGN luminosity is directly tied to the accretion rate. However, the widely adopted 'Bondi-Hoyle-Lyttleton' model for black hole (BH) accretion is very simplistic, assuming radial symmetry and neglecting angular momentum transfer. Furthermore, this model is strongly dependent on the BH mass, artificially suppressing accretion onto lower mass BHs.

As the resolution of hydrodynamical simulations improves, novel AGN accretion disc prescriptions have also been explored (e.g. Power et al., 2011; Dubois et al., 2014b; Fiacconi et al., 2018; Yuan et al., 2018; Beckmann et al., 2019a; Bustamante and Springel, 2019; Cenci et al., 2021), which can follow the BH spin evolution self-consistently. See also other methods that have been developed to take the gas angular momentum into account in hydrodynamical simulations, e.g. Rosas-Guevara et al. (2015) or Curtis and Sijacki (2016). Furthermore, there is a rich body of work which has focused on developing AGN accretion disc prescriptions for semi-analytical models of galaxy formation (e.g. Volonteri et al., 2005; Berti and Volonteri, 2008; Lagos et al., 2009; Fanidakis et al., 2011; Barausse, 2012; Volonteri et al., 2013; Sesana et al., 2014; Gaspari and Sądowski, 2017).

However, these accretion disc models mostly focus on the thin disc (TD) case (the high-Eddington-ratio regime) for the steady state as this regime can be described analytically with the Shakura-Sunyaev disc model (Shakura and Sunyaev, 1973), whilst there is no equivalent

global analytical disc model for the low-Eddington-ratio regime (though see Fanidakis et al., 2011; Yuan et al., 2018).

Observations of black hole binaries (BHBs) and AGN indicate that at low Eddington ratios ($f_{\rm Edd} \lesssim 0.01$) accretion occurs via a different mode than the standard TD, e.g. observations show hard X-ray spectra instead of soft blackbody-like spectra and low radiative efficiencies. The ADAF (Advection Dominated Accretion Flow) solution has been shown to have the properties required to provide a physical description of the observations (e.g. Narayan and McClintock, 2008).

Most BHBs in the hard and quiescent state are deduced to accrete via so-called truncated discs with an outer TD and an inner ADAF component (e.g. Yuan and Narayan, 2014). There is also some observational evidence that this phenomenon could transfer over to AGN (e.g. Trump et al., 2011; Yu et al., 2011; Nemmen et al., 2014).

Theoretical arguments suggest that ADAFs should produce strong winds and this outflow behaviour can be modelled with the general adiabatic inflow – outflow solution (ADIOS) for radiatively inefficient accretion flows (Blandford and Begelman, 1999).

Building on these observations and theoretical frameworks, as well as results from GR(-R-)MHD simulations, we have developed a hybrid accretion disc subgrid model that proceeds via the TD model from Fiacconi et al. (2018) at high Eddington ratios and via the ADIOS flow model at low Eddington ratios. For intermediate Eddington ratios, we smoothly model the transition between these two modes via a truncated disc (see Figure 5.1). A hybrid model for accretion through a truncated TD and inner ADIOS flow does not currently exist for cosmological simulations, so our new method is an important advancement for modelling accretion onto AGN in general.

A closed set of equations has been formulated and the model is currently being tested on a set of simulations in post-processing. Note that this model has not yet been employed in any simulations on-the-fly, this is the plan for future work.

The structure of this chapter is as follows. In Section 5.2, we outline the theoretical background and equations governing the new unified accretion disc model. We then present the results from validation tests carried out in post-processing and provide an outlook on applications of the model in Section 5.3. Finally, we conclude and summarise our findings in Section 5.4.

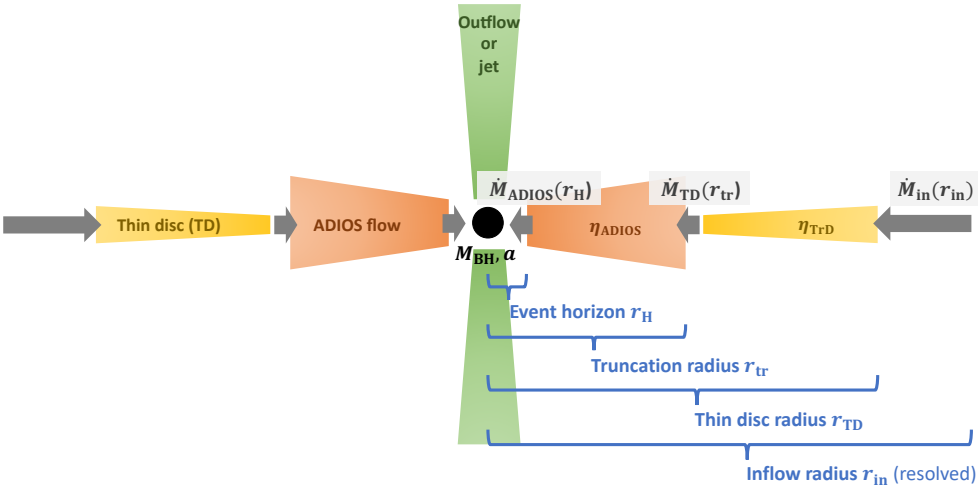

Fig. 5.1 Schematic of the unified accretion disc model: an inner ADIOS flow, an outer truncated TD and an outflow or jet.

5.2 Methodology

5.2.1 Notation conventions

In this chapter, we adopt the convention whereby lower-case r is a radius expressed in units of the Schwarzschild radius $R_{\rm S} = \frac{2GM_\bullet}{c^2}$, where G is Newton's gravitational constant, $M_\bullet$ is the BH mass, and c is the speed of light.

5.2.2 Constants

5.2.2.1 α-viscosity

It is now widely accepted that angular momentum transport in ionized accretion flows occurs via the magnetorotational instability (Balbus and Hawley, 1991, 1998). MHD simulations (e.g. McKinney et al., 2012; Tchekhovskoy et al., 2012; Sadowski et al., 2013; Ryan et al., 2017; Liska et al., 2019) model this self-consistently but for our hydro-only simulations we need to work with an α-like prescription for the viscous stress. For a fully ionized accretion disc, we would expect relatively high viscosities (cf. e.g. Martin et al., 2019). Here we need to work with an effective viscosity prescription and we set α to the canonical value of $\alpha = 0.1$. Note that this value is also used in the radiative efficiency modelling by Xie and Yuan (2012), which we employ to model the radiative efficiency of the accretion flow

(see Appendix 5.A). Also the α-viscosity values obtained from the GRMHD simulations by McKinney et al. (2012) are $\mathcal{O}(0.1)$.

5.2.2.2 Disc scale height

In the thick disc regime, the disc scale height obeys $H/R > \alpha$. As the disc is unresolved in our simulations, we fix this to a value which matches the high-resolution simulations that we use as inputs for our subgrid model, setting $H/R = 0.3$ (see Tchekhovskoy et al., 2012).

In the TD regime we have $H/R < \alpha$, and again, we fix the disc scale height to a constant value $H/R = 0.006$ motivated by calibrating the viscous timescale of the disc to match the timescales obtained from the accretion model by Fiacconi et al. (2018), also see Section 5.2.5.2.

5.2.2.3 Magnetic flux parameter

We parametrize the magnetic field strength using the dimensionless magnetic flux parameter $\phi_{\rm H}$ as given in Gaussian-cgs units by Tchekhovskoy et al. (2011)

$$\phi_{\rm H} = \frac{\Phi_{\rm H}}{(\dot{M} R_{\rm g} c)^{1/2}}, \tag{5.1}$$

where $\dot{M}$ is the accretion rate and $R_{\rm g} = GM_\bullet/c^2$ is the gravitational radius of the BH and $\Phi_{\rm H} = 1/2 \int_\theta \int_\varphi |B^r| {\rm d}A_{\theta\varphi}$ is the magnetic flux threading one hemisphere of the BH horizon.

As our simulations do not include magnetic fields, we assume the 'MAD' (magnetically arrested disc) state corresponding to a maximally saturated magnetic field. Interestingly, Sadowski et al. (2013) find that even simulations initialised with weak magnetic fields (the 'SANE' set-up), provided that they have non-zero spin, approach the MAD state towards the end of the simulation, indicating that the accretion flow has a tendency to be pushed towards that limit. See Yuan and Narayan (2014) for a detailed discussion of the MAD and SANE states.

We then calculate the magnetic flux parameter $\phi_{\rm H}$ as a function of BH spin, a, using the fitting function obtained by Tchekhovskoy et al. (2012) for MAD simulations ($\phi_{\rm H}(a) \sim 50$). The values given are also in good agreement with the simulations from Sadowski et al. (2013).

5.2.3 Inflow quantities

The resolved inflow quantities are calculated in analogy to Fiacconi et al. (2018). These fluxes are obtained from the hydro solver and connect our subgrid model with the hydrodynamical

simulation. In brief, the inflow radius, $r_{\rm in}$, is defined as the kernel-weighted average size of the gas cell neighbours of the BH within the smoothing length. The mass inflow rate, $\dot{M}_{\rm in}$, is defined as the mass flux on to the BH particle, which is calculated via a kernel-weighted average of the mass flux provided by the neighbours within the smoothing length. Similarly $\mathbf{L}_{\rm in}$ is the kernel-weighted average specific angular momentum.

For a given timestep Δt, the disc mass $M_{\rm d}$ and disc angular momentum $\mathbf{J}_{\rm d}$ then get updated as:

$$M_{\rm d} \rightarrow M_{\rm d} + \dot{M}_{\rm in}\Delta t, \tag{5.2}$$

$$\mathbf{J}_{\rm d} \rightarrow \mathbf{J}_{\rm d} + \dot{M}_{\rm in}\mathbf{L}_{\rm in}\Delta t. \tag{5.3}$$

5.2.4 Disc mode

There are three disc modes: TD, truncated disc (TrD) consisting of an inner ADIOS flow and outer TD, and a pure ADIOS flow.

Initially, one has to make an educated guess with regards to which state the system should be in. To make this guess effectively, we calculate an auxiliary Eddington fraction, $f_{\rm Edd,aux}$, based on $\dot{M}_{\rm in}$:

$$f_{\rm Edd,aux} = \frac{\dot{M}_{\rm in}}{\dot{M}_{\rm Edd}}, \tag{5.4}$$

where $\dot{M}_{\rm Edd}$ is the Eddington rate. We then use $f_{\rm Edd,aux}$ to determine the characteristic radii of the disc system (see Section 5.2.4.2).

We note that the definition of the Eddington rate depends on the assumed radiative efficiency η. A common reference value is $\eta = 0.1$, however, others employ a variable η to calculate the Eddington rate. In particular, in Fiacconi et al. (2018), $\dot{M}_{\rm Edd}$ is a function of the radiative efficiency (and the BH mass). Here we follow the convention where $\dot{M}_{\rm Edd}$ is calculated under the assumption that $\eta = 0.1$, for simplicity.

5.2.4.1 Disc truncation

At intermediate Eddington ratios, the outer TD is expected to be truncated at a characteristic radius $r_{\rm tr}$, transitioning into a hot accretion flow. The physical reason for this transition is not fully understood and there are several possible mechanisms such as the disc evaporation model, the turbulent diffusion model and the large viscosity model – all of which predict that the truncation radius $r_{\rm tr}$ should decrease as $f_{\rm Edd}$ increases in agreement with observations of BHBs and low-luminosity AGN (see Yuan and Narayan, 2014, and references therein). Also

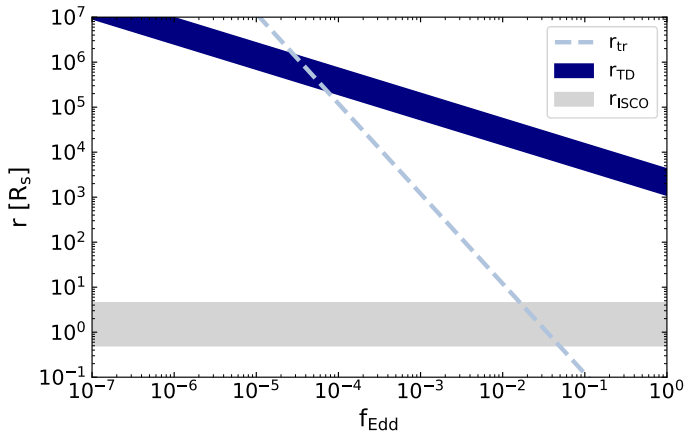

Fig. 5.2 Disc radii as a function of Eddington fraction. The outer TD radius ($r_{\rm TD}$) is calculated for BH mass $M_\bullet = 10^7$ M$_\odot$ and disc mass $M_{\rm d} = 10^4$ M$_\odot$. The shaded regions indicate the parameter space covered by the possible BH spin values.

see Liu and Taam (2009) for a discussion on the application of disc evaporation models to AGN.

5.2.4.2 Characteristic radii

To determine the accretion mode of the disc system, we compare the radius of the innermost stable circular orbit (ISCO) of the TD, $r_{\rm ISCO}$, the truncation radius, $r_{\rm tr}$, and the radius of the TD, $r_{\rm TD}$.

Firstly, we estimate the radius that the TD would have in the absence of evaporation using the expression from Fiacconi et al. (2018):

$$r_{\rm TD} = 40 \left(\frac{M_{\rm d}}{\rm M_\odot}\right)^{4/5} \left(\frac{\alpha}{0.1}\right)^{16/25} \left(\frac{M_\bullet}{10^6\ \rm M_\odot}\right)^{-44/25} f_{\rm Edd,aux}^{-14/25} \tag{5.5}$$

And following Yuan et al. (2018), we estimate the truncation radius as:

$$r_{\rm tr} = 3 \left(\frac{2\times10^{-2}}{f_{\rm Edd,aux}}\right)^2. \tag{5.6}$$

Finally, $r_{\rm ISCO}$ is given by

$$r_{\rm ISCO} = \frac{\Lambda(a)}{2}, \tag{5.7}$$

where $\Lambda(a)$ is a function of the BH spin a (see e.g. Fiacconi et al., 2018, for an expression for $\Lambda(a)$).

These characteristic radii are shown as a function of Eddington fraction in Figure 5.2. If $r_{\rm tr} \leq r_{\rm ISCO}$, then the ADIOS flow component is within the ISCO of the TD, so we proceed with the standard TD model from Fiacconi et al. (2018). If $r_{\rm tr} \geq r_{\rm TD}$ (i.e. the size of the ADIOS flow is larger than the size of the TD) or the gas does not have sufficient angular momentum to circularise at the truncation radius ($\sqrt{GM_\bullet R_{\rm tr}} > J_{\rm d}/M_{\rm d}$), then we proceed with the pure ADIOS flow model.

If $r_{\rm ISCO} < r_{\rm tr} < r_{\rm TD}$ and $\sqrt{GM_\bullet R_{\rm tr}} \leq J_{\rm d}/M_{\rm d}$, we evolve the disc system as a truncated disc.

Having developed a mechanism for determining the state of the accretion disc system, we are now ready to calculate the mass transfer, luminosity and angular momentum transfer for each of the accretion disc configurations. For the TD case, we simply follow the equations from Fiacconi et al. (2018) to calculate the mass and spin evolution as well as BH luminosities.

In Sections 5.2.5 and 5.2.6, we outline the equations governing the mass transfer and angular momentum transfer if we have a pure ADIOS flow or a truncated disc with an inner ADIOS flow.

5.2.5 Mass transfer

In the ADIOS model (Blandford and Begelman, 1999) the accretion rate depends on the radius due to the winds. Therefore the definition of the Eddington fraction becomes more subtle. Here we follow Xie and Yuan (2012) and define the Eddington fraction of the ADIOS flows with respect to the mass accretion rate at the (outer) event horizon, $r_{\rm H}(a) = \frac{1+\sqrt{1-a^2}}{2}$, which represents the rest mass flux onto the BH, $\dot{M}_{\rm BH,0}$. The Eddington fraction is then given by:

$$f_{\rm Edd,ADIOS} = \frac{\dot{M}_{\rm BH,0}}{\dot{M}_{\rm Edd}}. \tag{5.8}$$

Once the state of the disc has been decided, we can then drop $f_{\rm Edd,aux}$ and use the actual Eddington fraction of the ADIOS flow to estimate the radiative efficiency $\eta_{\rm ADIOS}$ together with the BH spin and the magnetic flux parameter (see Appendix 5.A). Note that since we estimate the magnetic flux parameter using a fitting function $\phi_{\rm H}(a)$ for the MAD state, the radiative efficiency is just a function of the Eddington fraction and the BH spin in our case. Figure 5.3 shows $\eta_{\rm ADIOS}$ as a function of BH spin with the different coloured lines corresponding to different Eddington fractions. This shows how the radiative efficiency increases for higher Eddington fractions and higher spin magnitudes (with prograde configurations achieving higher efficiencies than retrograde set-ups).

We can calculate the luminosity of the ADIOS flow as

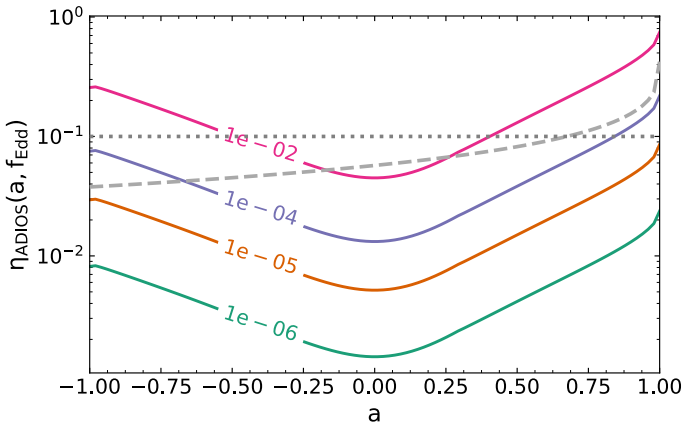

Fig. 5.3 Radiative efficiency, η_{ADIOS}, as a function of BH spin, a. The solid lines show η_{ADIOS} in the MAD regime for different Eddington fractions, as indicated by the line labels. The dashed grey line shows the radiative efficiency of the TD and the dotted grey line indicates the constant $\eta = 0.1$ radiative efficiency typically employed by large-scale simulations, for comparison.

$$\dot{E}_{\mathrm{ADIOS}} = \eta_{\mathrm{ADIOS}}(a, f_{\mathrm{Edd}})\dot{M}_{\mathrm{BH},0}\mathrm{c}^2, \tag{5.9}$$

and the BH growth rate as:

$$\dot{M}_\bullet = (1 - \eta_{\mathrm{ADIOS}})\dot{M}_{\mathrm{BH},0}. \tag{5.10}$$

The rest mass flux onto the BH, $\dot{M}_{\mathrm{BH},0}$, will depend on the disc model. In particular, we obtain different rest mass fluxes for the pure ADIOS flow and the inner ADIOS flow of the truncated disc model. This is mainly due to different accretion rates at the outer edge of the ADIOS flow (in the truncated disc case this is set by the TD rate) and different wind losses (in the truncated disc case these tend to be lower due to the smaller size of the ADIOS flow). In Sections 5.2.5.1 and 5.2.5.2, we outline how $\dot{M}_{\mathrm{BH},0}$ is calculated for the pure ADIOS flow model and the truncated disc model, respectively.

5.2.5.1 Pure ADIOS flow model

For the moment we have chosen that the ADIOS flow always falls below the resolution limit of the simulation, but we plan to validate, and possibly relax, this limit in the future as this decision will have to be re-evaluated for different resolutions. For now, we limit the size of the accretion flow, r_{ADIOS}, to r_{in}:

$$r_{\mathrm{ADIOS}} = \min(r_{\mathrm{tr}}, r_{\mathrm{in}}). \tag{5.11}$$

We then estimate the mass accretion rate at $r_{\rm ADIOS}$ as

$$\dot{M}(r_{\rm ADIOS}) = M_{\rm d}/\tau_{\rm visc,ADIOS}, \tag{5.12}$$

where $\tau_{\rm visc,ADIOS}$ is the viscous timescale of the ADIOS flow. Since the disc mass $M_{\rm d}$ is updated as $M_{\rm d} \rightarrow M_{\rm d} + \dot{M}_{\rm in}\Delta t$, this mass accretion rate at $r_{\rm ADIOS}$ is simply the inflow rate rescaled by the viscous timescale and corrected for disc draining.

Following Esin et al. (1997), the viscous timescale is given by:

$$\tau_{\rm visc,ADIOS} = \frac{R_{\rm ADIOS}}{v_{\rm r}} \sim 0.025 \left(\frac{M_\bullet}{10\ {\rm M}_\odot}\right)\left(\frac{0.25}{\alpha}\right)\left(\frac{r_{\rm ADIOS}}{10}\right)^{3/2}\ {\rm s}, \tag{5.13}$$

where $v_{\rm r}$ is the radial velocity of the accretion flow. Note that their estimate is based on the self-similar ADAF solution by Narayan and Yi (1995) rather than the ADIOS model, however, as $v_{\rm r}$ is not density-related, this estimate stays the same for the ADIOS model (Yuan et al., 2012).

Following Blandford and Begelman (1999), we can then use the accretion rate at $r_{\rm ADIOS}$ to calculate the mass accretion rate at the event horizon ($r_{\rm H}$):

$$\dot{M}_{\rm BH,0} = \dot{M}(r_{\rm ADIOS})\left(\frac{r_{\rm H}}{r_{\rm ADIOS}}\right)^s = \frac{M_{\rm d}}{\tau_{\rm visc,ADIOS}}\left(\frac{r_{\rm H}}{r_{\rm ADIOS}}\right)^s, \tag{5.14}$$

where s characterises the importance of the outflow. This parameter cannot exceed $s = 1$ for energetic reasons and $s = 0$ corresponds to no outflow. Here we set $s = 0.4$ for consistency with Xie and Yuan (2012) who assume this value in their numerical determination of the radiative efficiency of the outflow. Note that in the theoretical ADIOS model by Blandford and Begelman (1999) the accretion rate is a smoothly varying function of radius. Here, we assume that the accretion rate is constant throughout the disc until the event horizon where the outflow is released (also see Section 5.2.7).

Using the ADIOS luminosity from equation 5.9, we carry out a final sanity check on the ADIOS size, ensuring that the ADIOS flow does not grow beyond the size expected for the torus, the sublimation radius $R_{\rm sublimation}$, which can be estimated as (see e.g. Granato et al., 1997):

$$\left(\frac{R_{\rm sublimation}}{\rm pc}\right) = 0.2\left(\frac{\dot{E}_{\rm ADIOS}}{10^{46}\ {\rm erg\,s^{-1}}}\right)^{1/2}. \tag{5.15}$$

5.2.5.2 Truncated disc model

The derivation of the TD mass accretion rate in Fiacconi et al. (2018) relies on the inner disc radius being much smaller than the outer disc radius. This is generally true when the inner radius is at the ISCO, however, this assumption may no longer be valid for the truncated disc model when the truncation radius can reach a significant fraction of the the TD radius. For this reason, we only use the formula for $\dot{M}_{\rm TD}$ from Fiacconi et al. (2018) if $r_{\rm tr}/r_{\rm TD} < 10^{-2}$. In this case, the TD accretion rate is given by:

$$\dot{M}(r_{\rm tr}) = \dot{M}_{\rm TD} = 0.76 \left(\frac{M_{\rm d}}{10^4\ {\rm M}_\odot}\right)^5 \left(\frac{M_\bullet}{10^6\ {\rm M}_\odot}\right)^{-47/7} \left(\frac{aJ_{\rm d}/J_\bullet}{3}\right)^{-25/7} \dot{M}_{\rm Edd}. \tag{5.16}$$

If $r_{\rm tr}/r_{\rm TD} \geq 10^{-2}$, we estimate the TD accretion rate via the viscous timescale $\tau_{\rm visc}$:

$$\dot{M}(r_{\rm tr}) = \frac{M_{\rm TD}}{\tau_{\rm visc}}, \tag{5.17}$$

Here we assume that the viscous timescale for the truncated disc case is given by the standard expression assuming a thin α-disc (e.g. Pringle, 1981), adjusted for the truncation radius:

$$\tau_{\rm visc} = \frac{(R_{\rm TD} - R_{\rm tr})^2}{\nu} = \frac{(1 - R_{\rm tr}/R_{\rm TD})^2}{\alpha\sqrt{{\rm G}M_\bullet}} R_{\rm TD}^{3/2} (H/R)^{-2}, \tag{5.18}$$

where $\nu = \alpha c_{\rm s} H$ is the kinematic viscosity and $M_\bullet$ is the BH mass. The TD mass $M_{\rm TD}$, adjusted for the truncation radius, is given by (see Fiacconi et al., 2018):

$$M_{\rm TD} = 10^{-2} \left(\frac{\alpha}{0.1}\right)^{-4/5} \left(\frac{M_\bullet}{10^6\ {\rm M}_\odot}\right)^{11/5} f_{\rm Edd}^{7/10} (r_{\rm TD}^{5/4} - r_{\rm tr}^{5/4})\ {\rm M}_\odot. \tag{5.19}$$

$\dot{M}(r_{\rm tr})$ and $M_{\rm TD}$ are then determined via an iterative process. Note that since the unresolved disc scale height H/R is essentially a free parameter in our model (as long as $H/R < \alpha$), we choose this value so that $\frac{M_{\rm TD}}{\tau_{\rm visc}}$ matches $\dot{M}_{\rm TD}$ for small truncation radii. This yields a value of $H/R \sim 0.006$.

To calculate the feeding rate at the truncation radius, the radiative losses in the TD need to be estimated. Note that for the 'pure' TD model the radiative efficiency is given by

$$\eta_{\rm TD}(a) = 1 - \sqrt{1 - \frac{1}{3r_{\rm ISCO}(a)}}, \tag{5.20}$$

as $r_{\rm ISCO}$ defines an effective surface for the maximum feasible energy extraction from infalling particles. In the TrD case, we can only extract energy from the TD component up to $r_{\rm tr}$, so the expression for $\eta_{\rm TrD}$ then becomes

$$\eta_{\rm TrD} = 1 - \sqrt{1 - \frac{1}{3r_{\rm tr}}}. \tag{5.21}$$

The ADIOS flow feeding rate at the truncation radius is therefore set by the TD mass accretion rate $\dot{M}_{\rm TD}$ and the radiative efficiency $\eta_{\rm TrD}$. In analogy to the previous section, we can then use this feeding rate to estimate the accretion rate at the event horizon (ADIOS model):

$$\dot{M}_{\rm BH,0} = \dot{M}(r_{\rm tr})(1-\eta_{\rm TrD})\left(\frac{r_{\rm H}}{r_{\rm tr}}\right)^{s}, \tag{5.22}$$

where, as for the pure ADIOS model, we assume $s = 0.4$.

5.2.6 Angular momentum transfer

In this section, we describe how to model the angular momentum transfer for each disc state both due to accretion (see Section 5.2.6.1) and due to Lense-Thirring precession (see Section 5.2.6.2). Note that the BH angular momentum, $\mathbf{J}_\bullet$, is defined as

$$\mathbf{J}_\bullet = \frac{{\rm G}M_\bullet^2 a}{\rm c}\mathbf{j}_\bullet, \tag{5.23}$$

where $\mathbf{j}_\bullet$ is the normalised BH angular momentum vector.

If we are in the TD regime, we evolve the angular momenta of the disc and the BH according to the equations from Fiacconi et al. (2018), as for the mass transfer. Below we outline our scheme for the pure ADIOS flow and truncated disc cases.

5.2.6.1 Accretion

For both the pure ADIOS flow and the truncated disc model with an inner ADIOS flow, we model the evolution of the BH angular momentum due to accretion as

$$\left.\frac{{\rm d}\mathbf{J}_\bullet}{{\rm d}t}\right|_{\rm acc} = \dot{M}_{\rm BH,0} L_{\rm ISCO,ADIOS}\ {\rm sign}(\mathbf{j}_\bullet \cdot \mathbf{j}_{\rm d})\,\mathbf{j}_\bullet, \tag{5.24}$$

where $\mathbf{j}_{\rm d}$ is the normalised (total) angular momentum of the disc and $L_{\rm ISCO,ADIOS}$ is the specific angular momentum of the ADIOS flow at the event horizon. The latter is evaluated at the event horizon because for thick discs the stress is non-zero down to the horizon (see

e.g. Sadowski et al., 2016). To evaluate this expression, we need to know the value of $L_{\rm ISCO,ADIOS}$, which we would expect to be sub-Keplerian, i.e. lower than the TD value, due to additional (gas and magnetic) pressure support. We estimate $L_{\rm ISCO,ADIOS}(a)$ using the spin-up function[1] $\mathscr{S}(a)$ from the GRMHD simulations of an ADIOS flow in the MAD state by Tchekhovskoy et al. (2012):

$$\lambda_{\rm ISCO,ADIOS}(a) = \mathscr{S}(a) - 2a\varepsilon_{\rm ADIOS}(a), \tag{5.25}$$

where $\lambda_{\rm ISCO,ADIOS}$ is the dimensionless specific angular momentum of the ADIOS flow at the event horizon, i.e. $\lambda_{\rm ISCO,ADIOS} = \frac{\rm c}{GM_\bullet} L_{\rm ISCO,ADIOS}$, and $\varepsilon_{\rm ADIOS}$ is the dimensionless specific energy at the event horizon, i.e. $\varepsilon_{\rm ADIOS}(a) = 1 - \eta_{\rm tot,ADIOS}(a)$. Here $\eta_{\rm tot,ADIOS}$ is the total radiative efficiency including the jet contribution, which arises naturally in the GRMHD simulations. We estimate $\eta_{\rm tot,ADIOS}$ using the corresponding fitting functions from Tchekhovskoy et al. (2012) for consistency.

5.2.6.2 Lense-Thirring precession

Next, we focus on the angular momentum transfer between the BH and the disc due to the Lense-Thirring effect (Lense and Thirring, 1918). Lense-Thirring precession is a frame-dragging effect which manifests itself as nodal precession of orbits whose angular momentum is misaligned with the BH spin. In the weak-field limit, the precession frequency, $\omega_{\rm LT}$, is given by

$$\omega_{\rm LT} \approx \pm \frac{\rm c}{R_{\rm g}} \frac{2a}{(R/R_{\rm g})^3}. \tag{5.26}$$

Accretion discs are warped by the differential nature of the Lense-Thirring precession frequency. How these warps propagate depends on the type of accretion disc.

In the diffusive regime ($\alpha > H/R$, TD case), the warps are communicated by viscosity resulting into the so-called Bardeen-Petterson configuration (Bardeen and Petterson, 1975), where the disc is aligned with the BH equatorial plane at small radii ($r < r_{\rm warp}$) and retains its initial tilt at large radii ($r > r_{\rm warp}$) with a smooth warp in between at $r_{\rm warp}$ which is given by (see Fiacconi et al., 2018, for derivation):

$$r_{\rm warp} = 476\,\xi^{-4/7} \left(\frac{\alpha}{0.1}\right)^{24/35} \left(\frac{M_\bullet}{10^6\,{\rm M}_\odot}\right)^{4/35} f_{\rm Edd}^{-6/35} a^{4/7}, \tag{5.27}$$

[1] The spin-up function is given by $\mathscr{S}(a) = \frac{{\rm d}a}{{\rm d}t} \frac{M_\bullet}{M_{\rm BH,0}}$.

where ξ is a parameter $\mathcal{O}(1)$ which is related to the ratio of the radial viscosity ν_1 and vertical viscosity ν_2 as $\nu_1/\nu_2 = \xi/(2\alpha^2)$ and can be determined numerically (Papaloizou and Pringle, 1983; Lodato and Pringle, 2007).

In the wave-like regime ($\alpha < H/R$, ADIOS case), warps are communicated by pressure waves. These so-called bending waves result in a smooth warp far from BH, whilst radial tilt oscillations are obtained close to the BH.

For our pure ADIOS flow model, the whole system is in the wave-like regime. The whole flow, which is strongly coupled by the pressure waves (the local sound crossing timescale is much shorter than the precession timescale), then remains misaligned and precesses as a solid body (see Ingram et al., 2009; Ingram and Done, 2011; Ingram and Motta, 2019).

For our TrD model, the extent of the truncation radius determines whether we are in the diffusive or the wave-like regime.

If $r_{\rm tr} < r_{\rm warp}$, the TD feeds the ADIOS flow component aligned material thereby twisting the ADIOS flow into alignment. Also see Liska et al. (2019) who find in their numerical simulations that the angular momentum of the inner hot flow is negligible so that the TD can easily affect its alignment.

If $r_{\rm tr} \geq r_{\rm warp}$, the TD feeds misaligned material to the inner flow, so there is no alignment in the inner region and the inner ADIOS flow precesses as a solid body just as in the pure ADIOS flow case.

Following Ingram and Motta (2019), we can calculate the angular frequency of solid body precession, $\omega_{\rm prec}$, as:

$$\omega_{\rm prec} = \frac{\int_{R_{\rm in}}^{R_{\rm out}} \omega_{\rm LT}(R)\mathscr{L}(R)R{\rm d}R}{\int_{R_{\rm in}}^{R_{\rm out}} \mathscr{L}(R)R{\rm d}R}, \tag{5.28}$$

where $\mathscr{L}(R) = \Sigma R^2 \Omega_\phi$ is the angular momentum per unit area. Note that since the $\mathscr{L}(R)$ term appears in both the numerator and the denominator, we only need to know how this term scales with R, but not the absolute value. Using the scaling relations for the ADIOS model from Yuan and Narayan (2014), we have that the angular frequency scales as $\Omega_\phi \sim R^{3/2}$ and the volume density scales as $\rho \sim R^{-3/2+s}$. Under the assumption of a constant H/R ratio, the surface density then scales as $\Sigma \sim R^{-1/2+s}$. Using the weak-field formula for $\omega_{\rm LT}$ (equation 5.26), the integrals in equation 5.28 can then be evaluated analytically (Fragile et al., 2007; Ingram et al., 2009). Alternatively, a more precise description can be obtained by using a polynomial approximation (De Falco and Motta, 2018) and we adopt this polynomial approximation to compute $\omega_{\rm prec}$ in our model.

Note that with $s = 0.4$, the surface density Σ is nearly constant. However, GRMHD simulations predict that for misaligned discs, the density should sharply drop off in the region

dominated by radial tilt oscillations. We therefore set the inner radius to be the bending wave radius $r_{\rm bw} = 2.5(H/R)^{-4/5}a^{2/5}$ and the outer radius is set to equal to the extent of the ADIOS flow.

The torque due to Lense-Thirring precession is then given by

$$\left.\frac{\mathrm{d}\mathbf{J}_\bullet}{\mathrm{d}t}\right|_{\rm LT} = \mathbf{J}_{\rm d,ADIOS} \times (\omega_{\rm prec}\mathbf{j}_\bullet), \tag{5.29}$$

where in the pure ADIOS flow model, we simply have $\mathbf{J}_{\rm d,ADIOS} = \mathbf{J}_{\rm d}$. In the truncated disc case, we assume that the $\Sigma \sim R^{-3/4}$ scaling still holds for the TD component, so that we can evaluate the TD angular momentum as:

$$\mathbf{J}_{\rm d,TD} = \frac{8\dot{M}\sqrt{GM_\bullet}}{21C}(R_{\rm TD}^{7/4} - R_{\rm tr}^{7/4}), \tag{5.30}$$

with

$$C = 9\times10^6\left(\frac{\alpha}{0.1}\right)^{4/5}\left(\frac{M_\bullet}{10^6\,\mathrm{M}_\odot}\right)^{1/20}\left(\frac{f_{\rm Edd}}{\eta_{0.1}}\right)^{3/10}\mathrm{cm}^{5/4}\,\mathrm{s}^{-1}, \tag{5.31}$$

and then $\mathbf{J}_{\rm d,ADIOS} = \mathbf{J}_{\rm d} - \mathbf{J}_{\rm d,TD}$.

Finally, we note that in the MAD regime, jets can force the inner part of the ADIOS flow to align rapidly with the BH spin in GRMHD simulations (e.g. McKinney et al., 2013). However, Liska et al. (2018) investigated a range of initial conditions for GRMHD simulations of tilted BH discs and found that the importance of this effect crucially depends on the magnetic field configuration in the initial conditions. As we model neither the magnetic field nor the jet component, we do not include electromagnetic alignment due to jets here. However, we will consider this effect in future work when coupling our accretion disc model with an AGN jet subgrid prescription (see Section 5.3.2).

5.2.7 Winds

The mass outflow rate from winds, which naturally arise from the ADIOS model, can be estimated as:

$$\dot{M}_{\rm wind} = \dot{M}(r_{\rm ADIOS})\left[1 - \left(\frac{r_{\rm H}}{r_{\rm ADIOS}}\right)^s\right]. \tag{5.32}$$

These wind outflow rates can inform the injection of mass for AGN feedback subgrid models (in addition to the injection of energy according to the radiative efficiency) both for the pure ADIOS model and the inner ADIOS component of the truncated disc.

In addition to mass, the winds also carry angular momentum. Here we associate the wind angular momentum with the specific angular momentum at the ISCO which represents a

lower limit and assumes that the wind originates from the inner region. Note in the original ADIOS model, the wind mass flow rate is a smoothly varying function of radius. Here, we have instead chosen to model the wind as being released from the centre with the outer regions of the disc experiencing no wind loss.

Currently, we only model disc winds for the ADIOS component. The TD component is also expected to have winds, in particular at high Eddington fractions, and including these winds would be an important extension for future work.

5.2.8 Summary of the model

Here, we summarise the relevant equations for the mass and spin evolution of the BH particle – disc system. Firstly, the BH mass evolves as:

$$\frac{\mathrm{d}M_\bullet}{\mathrm{d}t} = (1-\eta)\dot{M}_{\mathrm{BH},0}, \tag{5.33}$$

where $\dot{M}_{\mathrm{BH},0}$ is the rest mass flux onto the BH and η is the radiative efficiency. The disc mass evolution is described by:

$$\frac{\mathrm{d}M_\mathrm{d}}{\mathrm{d}t} = -\dot{M} + \dot{M}_\mathrm{in}, \tag{5.34}$$

where $\dot{M}$ is the steady state rest mass flux through the disc. Note that if there is no mass loss via a jet or a wind then $\dot{M} = \dot{M}_{\mathrm{BH},0}$. Here we distinguish between these two quantities because we model mass loss through a wind if there is an ADIOS component present.

The angular momentum of the BH evolves both due to accretion and due to Lense-Thirring precession:

$$\frac{\mathrm{d}\mathbf{J}_\bullet}{\mathrm{d}t} = \dot{M}_{\mathrm{BH},0} L_\mathrm{ISCO}\ \mathrm{sign}(\mathbf{j}_\bullet \cdot \mathbf{j}_\mathrm{d})\ \mathbf{j}_\bullet + \left.\frac{\mathrm{d}\mathbf{J}_\bullet}{\mathrm{d}t}\right|_\mathrm{LT}, \tag{5.35}$$

where L_ISCO is the (spin-dependent) specific angular momentum at the ISCO. The angular momentum of the disc then evolves as:

$$\frac{\mathrm{d}\mathbf{J}_\mathrm{d}}{\mathrm{d}t} = -\dot{M} L_\mathrm{ISCO}\ \mathrm{sign}(\mathbf{j}_\bullet \cdot \mathbf{j}_\mathrm{d})\ \mathbf{j}_\bullet - \left.\frac{\mathrm{d}\mathbf{J}_\bullet}{\mathrm{d}t}\right|_\mathrm{LT} + \dot{\mathbf{J}}_\mathrm{in}. \tag{5.36}$$

Here we assume that the outflows are happening in the inner region so that the winds carry away the specific angular momentum associated with the ISCO, which represents a lower limit for the angular momentum loss. Also we note that in the case of misalignment between the inner ADIOS flow and the outer TD, there would be an additional torque between these

two components, which we have not included in our model as it would be beyond the scope of this work.

With the equations above, the evolution of the BH – disc particle system can be fully specified given η, $\dot{M}_{\rm BH,0}$, $\dot{M}$, $L_{\rm ISCO}$ and $\left.\frac{\mathrm{d}\mathbf{J}_\bullet}{\mathrm{d}t}\right|_{\rm LT}$. These quantities are listed for each state of the disc system in Table 5.1. We also list the relevant references for all of the equations.

Note that the derivations of the TD equations can be found in Fiacconi et al. (2018), in particular the derivation of the Bardeen-Petterson torque for Lense-Thirring precession in the TD regime as listed in Table 5.1 (here $J_\bullet$ is the magnitude of the BH angular momentum and $\tau_{\rm align}$ is the time-scale for the torque to modify the BH angular momentum). Note that if the warp radius exceeds the TD radius, instantaneous alignment of BH and disc angular momenta is assumed for the TD case, as listed in Table 5.1.

5.3 Testing and outlook

The unified accretion disc model has not yet been explored in any simulations on-the-fly. This is the plan for future work and depending on these validation tests the details of the implementation above may need to be changed.

We have started testing this model in post-processing and below we discuss some of the first results from these tests in Section 5.3.1. Furthermore, we give an outlook on potential applications and extensions of our model in Section 5.3.2.

5.3.1 Post-processing

5.3.1.1 Simulation details

To test our system of equations, we post-process a set of high-resolution simulations of supermassive BH (SMBH) binaries from Fiacconi et al. (in prep). Before presenting some first results from our analysis, we briefly summarise the salient details of the simulation set-up.

Here, we focus on an equal-mass SMBH binary system with initial BH mass $M_\bullet = 10^6$ M$_\odot$. The binary is initially on a Keplerian orbit with eccentricity $e = 0$ and the initial semi-major axis is $a = 2$ pc, corresponding to a period of 0.187 Myr. The binary is surrounded by a gaseous circumbinary disc and, for the set-up considered here, the binary and the circumbinary disc are coplanar. The target gas mass for this simulation is $m_{\rm g} = 0.2$ M$_\odot$ and the softening length is set to 0.005 pc.

These initial conditions are relaxed for 50 binary orbits: the binary perturbs the inner region of the circumbinary disc which creates a low-density cavity. The resolution in the

Table 5.1 Overview of the unified accretion disc model.

Disc state	Relevant equations and quantities
Thin Disc	$\eta = \eta_{\rm TD}(a)$ [Bardeen et al. 1972]
	$\dot{M} = \dot{M}_{\rm BH,0} = \dot{M}_{\rm TD} = 0.76 \left(\frac{M_{\rm d}}{10^4\ {\rm M}_\odot}\right)^5 \left(\frac{M_\bullet}{10^6\ {\rm M}_\odot}\right)^{-47/7} \left(\frac{aJ_{\rm d}/J_\bullet}{3}\right)^{-25/7} \dot{M}_{\rm Edd}$ [assuming no outflows, Fiacconi et al. 2018]
	$L_{\rm ISCO} = L_{\rm ISCO,TD}(a)$ [Bardeen et al. 1972]
	$\left.\frac{{\rm d}\mathbf{J}_\bullet}{{\rm d}t}\right\vert_{\rm LT} = \begin{cases} -J_\bullet \left\{ \frac{\sin(\pi/7)}{\tau_{\rm align}} [\mathbf{j}_\bullet \times \mathbf{j}_{\rm d}] + \frac{\cos(\pi/7)}{\tau_{\rm align}} [\mathbf{j}_\bullet \times (\mathbf{j}_\bullet \times \mathbf{j}_{\rm d})] \right\} & \text{if } r_{\rm warp} < r_{\rm TD} \\ \text{[instantaneous alignment, King et al. 2005]} & \text{if } r_{\rm warp} \geq r_{\rm TD} \end{cases}$ [Martin et al. 2007; Perego et al. 2009; Dotti et al. 2013; Fiacconi et al. 2018]
Pure ADIOS	$\eta = \eta_{\rm ADIOS}(a, f_{\rm Edd})$ [Xie and Yuan 2012; Sadowski et al. 2013; Inayoshi et al. 2019]
	$\dot{M} = \frac{M_{\rm d}}{\tau_{\rm visc,ADIOS}}$ [Narayan and Yi 1995; Esin et al. 1997]
	$\dot{M}_{\rm BH,0} = \frac{M_{\rm d}}{\tau_{\rm visc,ADIOS}} \left(\frac{r_{\rm H}}{r_{\rm ADIOS}}\right)^s$ [Blandford and Begelman 1999]
	$L_{\rm ISCO} = L_{\rm ISCO,ADIOS}(a)$ [Tchekhovskoy et al. 2012]
	$\left.\frac{{\rm d}\mathbf{J}_\bullet}{{\rm d}t}\right\vert_{\rm LT} = \mathbf{J}_{\rm d} \times (\omega_{\rm prec} \mathbf{j}_\bullet)$ [Ingram and Motta 2019]
Truncated Disc	$\eta = \eta_{\rm ADIOS}(a, f_{\rm Edd})$ [Xie and Yuan 2012; Sadowski et al. 2013; Inayoshi et al. 2019]
	$\dot{M} = \dot{M}(r_{\rm tr})$
	$\dot{M}(r_{\rm tr}) = \begin{cases} \dot{M}_{\rm TD} \text{ [Fiacconi et al. 2018]} & \text{if } r_{\rm tr}/r_{\rm TD} < 10^{-2} \\ M_{\rm TD}/\tau_{\rm visc} \text{ [Pringle 1981; Fiacconi et al. 2018]} & \text{if } r_{\rm tr}/r_{\rm TD} \geq 10^{-2} \end{cases}$
	$\dot{M}_{\rm BH,0} = (1 - \eta_{\rm TrD}) \dot{M}(r_{\rm tr}) \left(\frac{r_{\rm H}}{r_{\rm tr}}\right)^s$ [Blandford and Begelman 1999]
	$L_{\rm ISCO} = L_{\rm ISCO,ADIOS}(a)$ [Tchekhovskoy et al. 2012]
	$\left.\frac{{\rm d}\mathbf{J}_\bullet}{{\rm d}t}\right\vert_{\rm LT} = \begin{cases} \text{[as thin disc case, Fiacconi et al. 2018]} & \text{if } r_{\rm tr} < r_{\rm warp} \\ \mathbf{J}_{\rm TrADIOS} \times (\omega_{\rm prec} \mathbf{j}_\bullet) \text{ [Ingram and Motta 2019]} & \text{if } r_{\rm tr} \geq r_{\rm warp} \end{cases}$

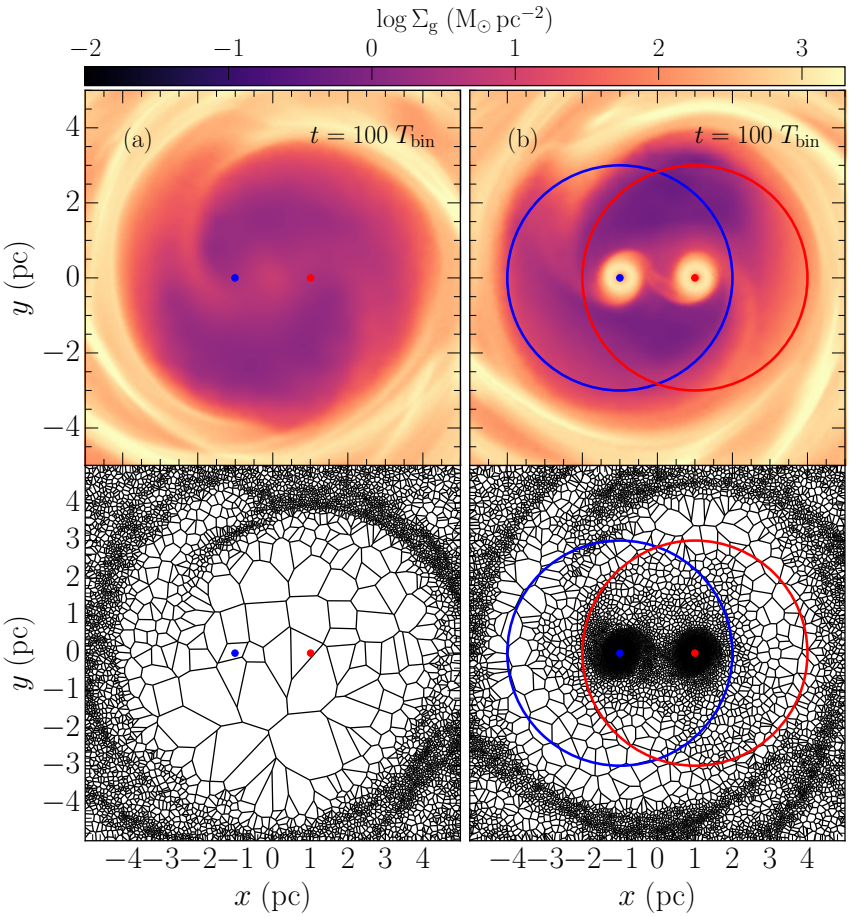

Fig. 5.4 Visualisation of the SMBH binary simulation set-up used for post-processing. The left panels and right panels compare the surface density of the gas (top row) and mesh structure (bottom row) after 100 binary orbits without and with super-Lagrangian refinement. This figure is reproduced from Fiacconi et al. (in prep).

inner region therefore needs to be significantly increased to still reliably resolve gas inflow rates at the scale of the accretion disc.

The super-Lagrangian refinement scheme is therefore employed in these simulations to ensure sufficient resolution in the inner regions. To this end, the refinement region radius is set to 3 pc (which is just larger than the size of the cavity) and the target spatial resolution at the outer edge of the refinement region is set to 0.2 pc, whilst the central target spatial resolution is set to 0.01 pc. Furthermore, a lower mass limit of $10^{-5} m_{\rm g}$ is imposed to avoid excessive mass refinement of cells.

Figure 5.4 shows the profound effect of the super-Lagrangian refinement on the cavity. The top row shows the surface density of the gas, whilst the bottom row show the mesh structure after 100 binary orbits. The left-hand panels have no super-Lagrangian refinement, whilst the right-hand panels have had super-Lagrangian refinement activated for the last 50

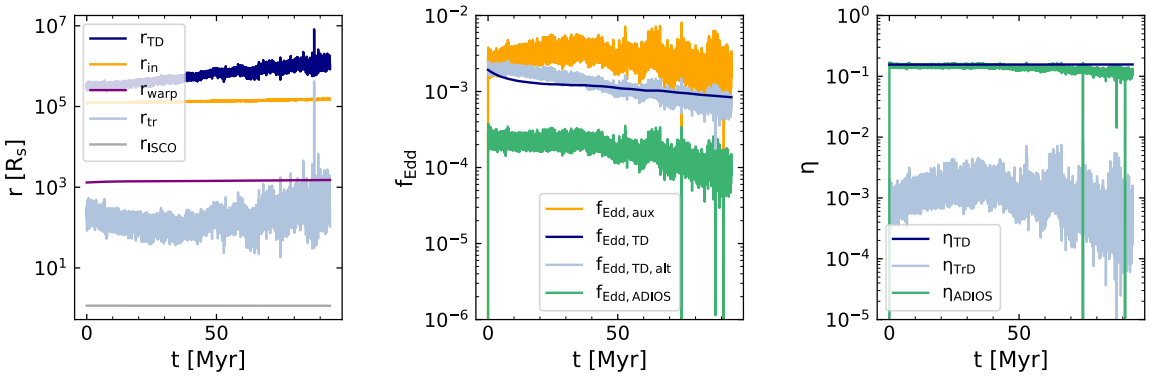

Fig. 5.5 Time evolution of key physical quantities in the unified accretion disc model calculated in post-processing. Characteristic radii (*left panel*), Eddington fractions (*middle panel*), and radiative efficiencies (*right panel*) are plotted for the different disc components with dark blue showing the TD quantities from the original simulation. The truncated disc quantities are shown in light blue and the ADIOS quantities in green. For reference, the inflow radius, $r_{\rm in}$, and the auxiliary Eddington fraction associated with the mass inflow rate, $f_{\rm Edd,aux}$, are shown in orange.

orbits. With super-Lagrangian refinement, the streams are much better resolved and are able to bring material close to the central region, forming gaseous puffed-up mini discs around the BHs.

Having been relaxed for 50 orbits without super-Lagrangian refinement and 50 orbits with super-Lagrangian refinement, the system is then evolved with the TD model from Fiacconi et al. (2018). It is assumed that both BHs are highly spinning, with the initial BH spin set to $a = 0.9$. The initial accretion disc mass is assumed to be $M_{\rm d} = 10^{-3} M_\bullet$ and the initial accretion rate is chosen close to the mass inflow rate from the mini discs. The initial disc angular momentum is assumed to be aligned with the respective mini disc, whilst the BH spins are given random and arbitrary initial directions.

5.3.1.2 First results

We use the inflow and accretion disc particle data from one of the BHs in the binary to test some of the key quantities and equations in our unified accretion disc model. Figure 5.5 shows the characteristic radii (left panel), Eddington fractions (middle panel), and radiative efficiencies (right panel) associated with the different disc components.

Firstly, we focus on the characteristic radii in the left panel. The super-Lagrangian refinement ensures that the inflows at the disc scale are well-resolved as $r_{\rm in} < r_{\rm TD}$ for the duration of the simulation. Based on the inflow rates, we have $r_{\rm ISCO} < r_{\rm tr} < r_{\rm TD}$ for the duration of the simulation, i.e. this system would be in the truncated disc state according to our unified accretion disc model.

Furthermore, comparing $r_{\rm warp}$ and $r_{\rm tr}$ shows that initially the truncation radius is smaller than the warp radius so that the outer TD would feed aligned gas to the inner ADIOS. At late times ($t \gtrsim 80$ Myr), however, the truncation radius increases (as inflow rates decrease) and exceeds the warp radius so that we would enter the regime where the inner ADIOS flow precesses as a solid body. Though we note that by $t = 80$ Myr, the efficient Bardeen Petterson torques have already largely aligned the BH and the disc with $\mathbf{j}_{\rm d} \cdot \mathbf{j}_{\bullet} \sim 0.8$, so torques due to the solid-body precession would be small.

Next, we inspect the Eddington fractions in the middle panel. The Eddington fraction associated with the steady-state mass accretion rate through the TD, $f_{\rm Edd,TD}$, is always somewhat lower than the Eddington fraction associated with the mass inflow rate, $f_{\rm Edd,aux}$ due to the longer accretion timescales. For comparison, we also show the Eddington fraction that would be obtained for the TD with the $\dot{M} = M_{\rm TD}/\tau_{\rm visc}$ prescription, $f_{\rm Edd,TD,alt}$. We can see that this yields a modulated version of the inflow rate with reduced noise and added disc draining. The two estimates of the TD Eddington fraction are in good agreement, though we note that this is partly by construction as we have calibrated the value of H/R to achieve this (see Section 5.2.5.2). The Eddington fraction of the inner ADIOS flow, $f_{\rm Edd,ADIOS}$, is significantly suppressed compared to the feeding rate from the outer TD. This is due to the strong ADIOS wind with the suppression of the feeding rate scaling as $(r_{\rm H}/r_{\rm tr})^{0.4}$.

Finally, we compare the radiative efficiencies of the different disc components and configurations in the right panel. Interestingly, the radiative efficiency based on the TD-only configuration, $\eta_{\rm TD}$, is very similar to the radiative efficiency of the inner ADIOS flow. Note that $f_{\rm Edd,ADIOS} \sim 10^{-4}$ for the duration of the simulation. We also checked the time evolution of the BH spin (not shown here) and found that $a \gtrsim 0.9$ throughout the simulation. From Figure 5.3, we can then see that we are in the regime where $\eta_{\rm TD} \sim \eta_{\rm ADIOS}$ as the radiative efficiency of the MAD flow is significantly increased for high spin values (and in particular for prograde configurations which can trap the magnetic flux more efficiently).

However, the resulting luminosity of the inner ADIOS flow would still be much lower than the luminosity of the TD-only configuration as the radiative efficiency is calculated with respect to the accretion rate at the ISCO (i.e. at the event horizon for the ADIOS flow), which is significantly lower than the TD accretion rate at the ISCO due to the suppression from the ADIOS winds (as shown in the middle panel).

We also show the radiative efficiency of the outer truncated TD, $\eta_{\rm TrD}$, which is significantly suppressed compared to the TD-only configuration as energy can only be extracted up to the truncation radius rather than the ISCO. Due to the efficient energy extraction with the high-spin MAD set-up, the inner ADIOS flow would therefore reach higher luminosities than the outer TD.

Our results show that predictions for multimessenger signatures of massive BH mergers are going to be hugely sensitive to the assumed disc state. We find that the predicted luminosities can differ by an order of magnitude between the TD and truncated disc models. This demonstrates that next-generation AGN accretion prescriptions will be crucial for robust modelling of electromagnetic (EM) counterparts of gravitational wave events which will be detectable by pulsar timing arrays and LISA. In particular, these models will provide important input to monitoring efforts which aim to identify EM counterparts even prior to merging.

5.3.2 Outlook

After the validation tests in post-processing have been completed, the next step will be to couple the accretion disc model with AGN feedback mechanisms and test the AGN evolution self-consistently in a dedicated suite of isolated simulations, starting from simulations like the ones presented here and then moving to isolated galaxy merger simulations.

The unified accretion disc model self-consistently yields the mass outflow rates associated with the ADIOS winds and the radiative efficiencies of the ADIOS flow, which could be employed to inform the mass and energy injection of a resolved outflow, e.g. using the bipolar outflow model from Chapter 2. Furthermore, it would be straightforward to combine the unified accretion disc model with the Blandford-Znajek (BZ, Blandford and Znajek, 1977) jet implementation from Talbot et al. (2021).

Note that the TD should also have disc winds but we have not included this in our AGN subgrid scheme yet. However in the future, it would also be important to model winds in the quasar mode. Furthermore, we have not yet considered super-Eddington accretion in our model. This would also be an interesting path to explore in the future, in particular with regards to investigating the rapid growth of BH seeds at high redshifts.

5.4 Conclusions

We have introduced a novel unified accretion disc model for AGN accretion in galaxy formation simulations. This model is built both on analytical descriptions of the ADAF (Narayan and Yi, 1995) and ADIOS (Blandford and Begelman, 1999) models as well as GR(-R-)MHD simulations of radiatively inefficient accretion flows (e.g. McKinney et al., 2012; Tchekhovskoy et al., 2012; Sadowski et al., 2013; Inayoshi et al., 2019). We have presented some first validation tests of the model by post-processing high-resolution simulations of gas accretion onto a BH binary embedded in a circumbinary disc. We found that the unified

accretion disc model may substantially modify the evolution of this system which would be in a truncated disc state (rather than a pure TD) in our model. This would lead to strong winds from the inner ADIOS flow throughout the simulation and solid-body precession of the inner ADIOS flow, rather than Bardeen Petterson alignment, at late times.

The unified accretion disc model would lend itself to several astrophysical applications. We plan to couple the accretion disc model self-consistently with AGN feedback implementations for bipolar outflows (based on the ADIOS winds) and BZ jets. After investigating the outflow rates and jet power evolution in isolated simulations, this model could then be used to run full cosmological simulations where all radiative regimes can be explored together.

5.A ADIOS radiative efficiency

We model the radiative efficiency $\eta_{\rm ADIOS}$ dependent on the Eddington fraction $f_{\rm Edd}$, the BH spin a, and the magnetic flux parameter $\phi_{\rm H}$. For the Eddington fraction dependence, we use the analytical fitting function obtained by numerically solving the dynamical equations of a two-temperature plasma from Xie and Yuan (2012) corrected by the GR-R-MHD simulation results from Ryan et al. (2017) (see Inayoshi et al., 2019), which we denote here by $\eta_{\rm ADIOS}(f_{\rm Edd})$.

Note that Xie and Yuan (2012) did not take the possible effects of magnetic fields and/or BH spin into account and the Ryan et al. (2017) simulations only have a moderate (constant) BH spin $a = 0.5$ and weak magnetic fields. However, we would also like to model the effects of BH spin and magnetic fields on the radiative efficiency, as these may be important factors in the production of jets.

To model magnetic and BH spin effects, we employ the results from GRMHD simulations of magnetized non-radiative geometrically thick accretion discs by Sadowski et al. (2013). They give empirical formulae for the energy outflow rates which are divided into a jet component signifying the energy extraction from the BH spin via the BZ mechanism (Blandford and Znajek, 1977) and the wind component which represents the energy outflow rate due to the accretion process itself. The outflow rates are normalized by the mass accretion onto the BH, so we can take the wind energy outflow rate as a proxy for the radiative efficiency of the ADIOS flow. Sadowski et al. (2013) give their fitting function in terms of the magnetic flux threading the BH horizon, $\phi_{\rm H}$, and the BH horizon angular frequency, $\Omega_{\rm H}$, which solely depends on the BH spin:

$$\Omega_{\rm H} = \frac{a}{4r_{\rm H}}, \quad r_{\rm H} = \frac{1+\sqrt{1-a^2}}{2}, \tag{5.37}$$

where $r_{\rm H}$ is the radius of the outer event horizon (in units of the Schwarzschild radius). The radiative efficiency of the accretion process can the be written as:

$$\eta_{\rm ADIOS}(\phi_{\rm H}, a) \sim 0.005[1 + 3\tilde{\phi}_{\rm H}^2 \tilde{\Omega}_{\rm H}(a)^2], \tag{5.38}$$

where $\tilde{\phi}_{\rm H} = \phi_{\rm H}/50$ is the magnetic flux threading the horizon normalized by the characteristic value for the MAD state, and $\tilde{\Omega}_{\rm H} = \Omega_{\rm H}/0.2$ is the horizon angular frequency normalised by the angular frequency for a spin $a = 0.7$. Note that the energy loss in the wind is dominated by the inner-most regions so this fitting function given should be reasonably converged. The efficiency, to first order, scales with a^2 in agreement with efficiency scalings given by Tchekhovskoy (2015). Note that Tchekhovskoy and McKinney (2012) find that prograde BH spins are associated with higher efficiencies. This asymmetry is introduced because more magnetic flux can be trapped with the prograde set-up. We model this implicitly with our variable $\phi_{\rm H}$.

As pure GRMHD simulations are scale-free the dimensionless code units can be scaled for arbitrary BH masses and accretion rates, so that these simulations do not correspond to a specific Eddington ratio (see Appendix 5.B). However, running the non-radiative limit loses its validity beyond a certain maximum Eddington ratio, as radiative effects become important. The neglect of radiative cooling is reasonable for systems accreting at $< 10^{-5}$ of the Eddington rate, $\dot{M}_{\rm Edd}$, so that the synchrotron cooling time is much longer than the accretion time (cf. Mahadevan and Quataert, 1997; Ressler et al., 2015). The zero spin and zero magnetic field value fits in reasonably well with the picture from Inayoshi et al. (2019), as it corresponds to an accretion rate of approximately $10^{-5}\dot{M}_{\rm Edd}$. However, note that the exact transition value is still debated. Dibi et al. (2012) find that radiative cooling becomes important above 10^{-7} of the Eddington rate, whilst Sadowski et al. (2013) emphasise that this cut-off depends on assumptions regarding the electron temperature in the two-temperature plasma, and more conservatively one might expect radiative effects to become important above 10^{-4} of the Eddington rate. Overall, the Sadowski et al. (2013) and Inayoshi et al. (2019) schemes seem to be in agreement with each other if radiation physics is assumed to be negligible up to at least $10^{-5}\dot{M}_{\rm Edd}$. We can then write our full equation for the radiative efficiency as

$$\eta_{\rm ADIOS}(f_{\rm Edd}, a, \phi_{\rm H}) = \eta_{\rm ADIOS}(f_{\rm Edd})[1 + 3\tilde{\phi}_{\rm H}^2 \tilde{\Omega}_{\rm H}(a)^2] \tag{5.39}$$

Note this assumes that the radiative and spin/magnetic effects are completely decoupled.

5.B Geometrical units

The results from many GRMHD studies are reported in dimensionless code units, where $GM_\bullet = c = 1$ (geometrical units). This sets the scale of length ($R_\mathrm{g} = \frac{GM_\bullet}{c^2}$) and the scale of time ($t_\mathrm{g} = \frac{GM_\bullet}{c^3}$). Note that since the mass of the accreting fluid does not contribute to the dynamics, the density is essentially scale-free. The mass scale is determined by setting the observed mass accretion rate $\dot{M}$ equal to the accretion rate through the BH horizon at r_H as measured in the simulation, so we have $\rho_{0,\mathrm{disc}} = \dot{M}(R_\mathrm{H})t_\mathrm{g}/R_\mathrm{g}^3$ and the mass scale is given by $m = \rho_{0,\mathrm{disc}}R_\mathrm{g}^3 = \dot{M}(R_\mathrm{H})t_\mathrm{g}$ (McKinney and Narayan, 2007). Attaching physical units to the results then demands choosing two parameters. A particular choice of BH mass, $M_\bullet$, to determine the units of length and time and a particular value of the accretion rate $\dot{M}$ to determine the unit of mass in the fluid (cf. Noble et al., 2011). Note that once we enter the radiative regime, the introduction of a radiative scale via the electron scattering Thomson cross section, σ_T, and radiation constant, a_rad, forces $\dot{M}$ and $M_\bullet$ to be specific values.

CHAPTER 6

CONCLUSIONS AND OUTLOOK

6.1 Conclusions

Contrary to what has become standard lore, there is increasing observational evidence for active galactic nuclei (AGN) feedback at the low-mass end of the galaxy population (e.g. Greene and Ho, 2004, 2007; Reines et al., 2013; Penny et al., 2018; Dickey et al., 2019; Manzano-King et al., 2019). However, modern cosmological simulations, such as EAGLE (Schaye et al., 2015), Horizon-AGN (Dubois et al., 2014a) or Illustris (Vogelsberger et al., 2014b; Sijacki et al., 2015), which have made huge progress in modelling the co-evolution of massive galaxies and their central black holes (BHs), assume very weak AGN feedback in low-mass galaxies by construction. The recent observational discoveries of highly-accreting AGN in dwarf galaxies have prompted a re-evaluation of these feedback models, which could lead to a paradigm shift in galaxy formation theory.

In this thesis, I have investigated the role of AGN feedback in dwarf galaxies employing isolated simulations, cosmological boxes, and cosmological zoom-in simulations. I found that AGN feedback has a crucial impact on the outflow properties of dwarfs and can suppress star formation by hindering cosmic gas inflows. However, the Bondi prescription and the (artificially) strong supernova (SN) feedback, which are employed by most cosmological simulations, generally prevent low-mass AGN from entering the high-Eddington accretion regime. Therefore next-generation AGN models are needed to explore the high-accretion regime self-consistently in dwarfs. Motivated by these issues, I have developed a new accretion disc subgrid model for the radiatively inefficient regime based on the adiabatic inflow-outflow solution (ADIOS, Blandford and Begelman, 1999), which combines the advection-dominated accretion flow (ADAF, Narayan and Yi, 1995) with a disc wind. This model is fully coupled with a standard thin disc (Shakura and Sunyaev, 1973), covering all radiative regimes, and self-consistently taking into account not just mass accretion but also

gas angular momentum transport. This model could therefore be a promising replacement for the simplistic Bondi prescription.

Before outlining some possible future projects building on this work in Section 6.2, I briefly summarise the main results of each thesis chapter below:

- In Chapter 2, I carried out a series of high-resolution isolated simulations of dwarf galaxies with the moving-mesh code AREPO and investigated different AGN models ranging from simple energy-driven spherical winds to collimated, mass-loaded, bipolar outflows. For these simulations, the accretion rates were set to a constant fraction of the Eddington luminosity to avoid the tight constraints set by the Bondi model. I found that the outflows are significantly enhanced by the AGN to much higher temperatures and velocities in agreement with kinematic signatures from the MaNGA survey (Penny et al., 2018). The AGN also has a small but significant suppression effect on the central star formation rates (SFRs). The global SFRs, on the other hand, are only marginally affected by the AGN activity as the majority of the AGN energy escapes perpendicularly to the galaxy disc in a hot outflow. In view of the significant impact of the AGN on the outflow properties, I concluded that AGN feedback might still be able to indirectly regulate star formation in dwarfs by hindering cosmic gas inflows – providing strong motivation to investigate AGN feedback within a cosmological context.

- In Chapter 3, I used the cosmological simulation suite FABLE (Henden et al., 2018) to explore AGN feedback in dwarf galaxies within a realistic cosmological environment. Similarly to the isolated simulations, dwarfs with efficient BH growth reach higher outflow velocities and temperatures in FABLE. These AGN-boosted outflows can also appear as a kinematically misaligned ionized gas component in mock MaNGA velocity maps, though cosmic inflows and mergers contribute to misalignments as well. In the local Universe, the majority of AGN in dwarfs are much dimmer than the stellar component, but for $z \geq 2$ there is a significant population of AGN that outshine their hosts. These high-redshift overmassive BHs contribute to the quenching of dwarfs, whereas at late cosmic times SN feedback is more efficient. The FABLE AGN luminosity distributions are overall consistent with local observations and FABLE predicts that future observations may uncover many more AGN in dwarfs with lower luminosities and at higher redshifts. However, the lack of high-luminosity X-ray AGN in FABLE's dwarfs at low redshifts highlights an interesting possibility that the AGN accretion rates could be artificially suppressed in FABLE by the constraints of the strong SN feedback and the Bondi prescription.

- In Chapter 4, I performed a series of high-resolution cosmological zoom-in simulations with the moving-mesh code AREPO. Here I focused on simulating one low-mass system and carried out several 'numerical experiments', varying the SN energetics and AGN accretion prescription, to assess whether efficient AGN feedback in tandem with more realistic SN feedback could be a viable alternative to the commonly employed strong SN feedback. To model the high-accretion regime, I used two approaches: increasing the boost factor in the Bondi rate to obtain more efficient (albeit still self-regulated) AGN accretion as well as high-Eddington accretion bursts with a fixed luminosity and duration. I found that brief, Eddington-limited accretion episodes can have a profound impact on the dwarf galaxy. The AGN feedback drives a hot bubble which lingers in the circumgalactic medium long after the AGN has switched off, preventing cosmic gas inflows from reaching the galaxy and thereby regulating star formation with maintenance mode type feedback.

- In Chapter 5, I introduced a new unified AGN accretion disc model for galaxy formation simulations. I combined the ADIOS model with the truncated disc model (e.g. Liu et al., 1999) and fitting functions from general relativistic (radiation) magnetohydrodynamical (GRMHD, GRRMHD) simulations (e.g. McKinney et al., 2012; Tchekhovskoy et al., 2012; Sadowski et al., 2013; Inayoshi et al., 2019) to derive how the different accretion disc properties (such as radiative efficiency or truncation radius) depend on the different variables (such as Eddington fraction or BH spin). I presented a closed set of equations for the mass and spin evolution of the BH and also showed some first results of tests that have been carried out in post-processing. These tests demonstrate that robust accretion disc modelling will be crucial for the prediction of multimessenger signatures of supermassive BH binaries.

6.2 Outlook

The unified accretion disc model has only been presented as a proof of concept here, however, there are several applications as well as possible extensions to this scheme. In particular, it would be a worthwhile endeavour to supplement the AGN accretion disc model with complementary AGN feedback prescriptions (in the form of disc winds, jets, and radiation fields) and BH formation models. This comprehensive new BH model could then be used to run next-generation galaxy formation simulations and make predictions for future facilities including *JWST*, *RST*, *Athena*, *Lynx*, SKA, and LISA.

Whilst these novel AGN schemes could be applied to several astrophysical questions, they are particularly important for modelling AGN feedback in dwarfs which is difficult to

explore with the constraints of the current AGN prescriptions. Below I outline some of the possible future projects that could follow on from the work presented in this thesis.

6.2.1 Unified accretion disc model in cosmological simulations

It is clear from the results presented in this thesis that the overly simplistic Bondi model is unsuitable for studying efficient AGN accretion in dwarf galaxies. I have presented a new unified accretion disc model for AGN accretion in high-resolution simulations, which addresses several of the shortcomings of the Bondi prescription. Therefore a natural next step would be to run a series of zoom-in simulations of dwarf galaxies to test the new accretion disc model in a cosmological context, for the first time self-consistently tracking gas angular momentum and mass flow from the cosmological environment down to the (truncated) accretion disc.

As discussed in Chapter 5, this accretion disc model already self-consistently includes ADIOS winds and could straightforwardly be combined with the Blandford-Znajek (BZ, Blandford and Znajek, 1977) jet prescription from Talbot et al. (2021). The BZ jets and ADIOS winds could then be used as the fiducial AGN feedback mechanisms for a first set of cosmological zoom-in simulations with the novel accretion disc model, focusing on the AGN accretion rates. Though note that since BH feedback regulates BH growth, it would also be crucial to break this degeneracy and model the AGN feedback itself in more detail (see Section 6.2.2).

A brand-new set of zoom-in simulations covering different environments and epochs would be very timely as these simulations could be used to predict the radio power evolution of AGN in dwarfs, which future SKA observations will be able to probe, and also for comparisons with observations of powerful high-redshift radio jets in dwarfs (Mezcua et al., 2019).

In addition, high-resolution simulations covering all radiative regimes would be very important for the interpretation of integral-field unit (IFU) observations, which are starting to uncover the low-luminosity AGN population in dwarfs (e.g. Penny et al., 2018; Mezcua and Domínguez Sánchez, 2020). These zoom-ins could also be used to make predictions for outflow properties (e.g. outflow rates, mass loading factors, kinetic power, momentum rates) which can be measured by IFU observations, e.g. with MUSE, GMOS, or KCWI (Liu et al., 2020) and, in the future, with *JWST* NIRSpec.

6.2.2 The role of radiative feedback

Another promising avenue for future research would be improving the models for AGN feedback, which is crucial for regulating further BH growth and star formation. Previous simulations have typically adopted very simple models, injecting thermal energy isotropically around the BH. What is more, due to the prohibitively high costs of full radiative transfer, radiative AGN feedback has mostly been neglected in cosmological simulations. Hence it would be very worthwhile to build on the unified ADIOS flow scheme and develop a model for radiative AGN feedback depending on the disc state.

It would be most straightforward to start with modelling the X-ray radiation, which has two main advantages: the majority of the AGN power is emitted in X-rays and the interstellar medium (ISM) is optically thin to hard X-rays. Therefore the propagation can be modelled as an inverse square law taking advantage of the gravity tree (building on the AREPO implementation of the interstellar FUV radiation field in Smith et al., 2020).

The X-ray radiative feedback could be calculated using a variable bolometric conversion term based on the spectral energy distributions (SEDs) of the ADIOS and thin-disc components. This would allow for the inclusion of both the non-thermal emission due to the hot optically thin matter and the thermal emission due to the cold optically thick matter (see Giustini and Proga, 2019). The interaction of the X-ray photons with the ISM could then be modelled in three ways: photoionization, heating, and radiation pressure (also see Hambrick et al., 2011; Kim et al., 2011).

This new model could then be explored with additional zoom-in simulations of dwarf galaxies and be used to make predictions for future X-ray missions, such *Athena* and *Lynx*. Furthermore, the detailed modelling of the SEDs would allow for direct comparisons with local *Chandra* and *XMM-Newton* observations of AGN in dwarfs, in particular contrasting the simulated and observed hardness ratios (e.g. Birchall et al., 2020) would provide a further useful test for the unified accretion disc model.

6.2.3 Black hole seeds and high-resolution cosmological boxes

Finally, as discussed in Chapter 4, there are still significant uncertainties around BH formation with the seed masses largely unconstrained. The three most popular ‘seeding mechanisms’ for the formation of the first central BHs are Population III stars, dense nuclear star clusters (both resulting in light seeds) and the direct collapse of massive gas clouds (resulting in heavy seeds). Note that cosmological simulations typically employ heavy seeds which are inserted based on a halo mass threshold rather than following criteria from possible seeding

models, severely limiting their predictive power for the early phase of BH growth (also see Chapter 3).

Hence another interesting route of investigation would be to implement the three main seeding mechanisms and tie these together with the new methods for BH growth in feedback described in Sections 6.2.1 and 6.2.2.

All of the above seeding models favour low-metallicity environments in the early Universe, so the seeding criterion could be based on the star formation criterion combined with metallicity and divergence criteria (e.g. Bellovary et al., 2011; Habouzit et al., 2017). The seed masses could then be obtained for the given BH formation channel, taking advantage of theoretical predictions for the Pop III initial mass function, the relationship between nuclear star cluster mass and resultant BH mass (Katz et al., 2015), and the direct collapse model by Lodato and Natarajan (2006) (also see Volonteri et al., 2008; Ricarte and Natarajan, 2018; DeGraf and Sijacki, 2020).

This comprehensive new BH model could then be used to run high-resolution cosmological boxes and make predictions for key observables such as the BH luminosity function, Eddington ratio distribution and scaling relations, which will be extended by *JWST* and *RST* to much lower BH luminosities and to higher redshifts. In particular *JWST* will deliver important constraints on the active BH fraction in dwarfs as infrared coronal lines will allow for the identification of AGN that are otherwise outshone by the stellar component (e.g. Satyapal et al., 2021).

Note that seeding mechanisms will be hard to distinguish using local observations alone because varied accretion and feedback histories can blur the early differences in these models (see e.g. Greene et al., 2020). Hence it is crucial to make predictions for seeding pathways incorporating as realistic AGN accretion and feedback models as possible. Furthermore, these degeneracies may be broken by comparing the simulations with the observed redshift evolution of AGN. *JWST* will push constraints on AGN activity to much higher redshifts (including faint sources) with local observations providing an anchor point. The synergy with *Athena* and SKA will allow for the inclusion of even fainter objects as well as radio sources so that the whole diversity of the AGN population can be captured up to high redshifts. This will provide extremely valuable data for comparison with the simulations, in particular with regards to the multi-wavelength luminosity function.

Depending on the resolution requirements, it may be necessary to adjust the accretion and feedback recipes for these simulations using a subgrid prescription that reproduces the coarse-grained properties arising from the higher resolution zoom-in simulations from the first two studies. Furthermore, probing low-mass seeds in cosmological simulations will also require developing a prescription for the unresolved dynamical friction experienced by

the BH. This could be included via analytical BH dynamics models (e.g. Chatterjee et al., 2002a,b; Tremmel et al., 2017; Pfister et al., 2019; Chen et al., 2021). Modelling the BH dynamics is particularly important since offset AGN have been observed in dwarf galaxies (e.g. Mezcua and Domínguez Sánchez, 2020; Reines et al., 2020), and the position of the BH could dictate the efficiency of AGN accretion and feedback in dwarfs.

6.2.4 Final remarks

Future deep electromagnetic surveys (for example with *JWST*, *RST*, *Athena*, *Lynx*, SKA) will be able to constrain the BH growth via accretion, whilst gravitational-wave observatories (such as AION, LISA and PTA) will provide complementary constraints on BH merger rates. The synergy between these upcoming electromagnetic and gravitational wave observatories will revolutionise our view of BHs in galaxy formation and is bound to bring new discoveries.

In this thesis, I have investigated the hitherto unexplored impact of AGN feedback on dwarf galaxies and presented a new AGN accretion model which will make it possible to model all radiative AGN regimes self-consistently. The new AGN model lends itself to several extensions, in particular with regards to combining the accretion prescription with new schemes for AGN feedback and BH seeding. These next-generation theoretical AGN models will allow us to make detailed predictions for the multimessenger signatures of BHs and to constrain different theoretical possibilities, with the ultimate aim of determining what shapes the build-up of galaxies and their central BHs.

REFERENCES

Agertz, O., R. Teyssier, and B. Moore (2011). "The formation of disc galaxies in a ΛCDM universe". *MNRAS* 410, 1391.

Agertz, O. et al. (2007). "Fundamental differences between SPH and grid methods". *MNRAS* 380, 963.

Agertz, O. et al. (2020). "EDGE: the mass-metallicity relation as a critical test of galaxy formation physics". *MNRAS* 491, 1656.

Aird, J., A. L. Coil, and A. Georgakakis (2018). "X-rays across the galaxy population - II. The distribution of AGN accretion rates as a function of stellar mass and redshift". *MNRAS* 474, 1225.

Anglés-Alcázar, D., R. Davé, C. A. Faucher-Giguère, F. Özel, and P. F. Hopkins (2017a). "Gravitational torque-driven black hole growth and feedback in cosmological simulations". *MNRAS* 464, 2840.

Anglés-Alcázar, D., C. A. Faucher-Giguère, E. Quataert, P. F. Hopkins, R. Feldmann, P. Torrey, A. Wetzel, and D. Kereš (2017b). "Black holes on FIRE: Stellar feedback limits early feeding of galactic nuclei". *MNRAS* 472, L109.

Anglés-Alcázar, D., F. Özel, R. Davé, N. Katz, J. A. Kollmeier, and B. D. Oppenheimer (2015). "Torque-limited growth of massive black holes in galaxies across cosmic time". *ApJ* 800, 127.

Angulo, R. E., V. Springel, S. D. M. White, A. Jenkins, C. M. Baugh, and C. S. Frenk (2012). "Scaling relations for galaxy clusters in the Millennium-XXL simulation". *MNRAS* 426, 2046.

Bahé, Y. M. et al. (2017). "The Hydrangea simulations: galaxy formation in and around massive clusters". *MNRAS* 470, 4186.

Balbus, S. A. and J. F. Hawley (1991). "A powerful local shear instability in weakly magnetized disks. I - Linear analysis. II - Nonlinear evolution". *ApJ* 376, 214.

Balbus, S. A. and J. F. Hawley (1998). "Instability, turbulence, and enhanced transport in accretion disks". *Rev. Mod. Phys.* 70, 1.

Baldassare, V. F., A. E. Reines, E. Gallo, and J. E. Greene (2015). "A $\sim 50,000$ $M_\odot$ black hole in the nucleus of RGG 118". *ApJ* 809, L14.

Baldassare, V. F., M. Geha, and J. Greene (2020). "A Search for Optical AGN Variability in 35,000 Low-mass Galaxies with the Palomar Transient Factory". *ApJ* 896, 10.

Baldassare, V. F., A. E. Reines, E. Gallo, and J. E. Greene (2017). "X-Ray and Ultraviolet Properties of AGNs in Nearby Dwarf Galaxies". *ApJ* 836, 20.

Baldry, I. K. et al. (2012). "Galaxy And Mass Assembly (GAMA): the galaxy stellar mass function at $z < 0.06$". *MNRAS* 421, 621.

Baldwin, A., M. M. Phillips, and R. Terlevich (1981). "Classification Parameters for the Emission-Line Spectra of Extragalactic Objects". *PASP* 93, 817.

Balogh, M. L., F. R. Pearce, R. G. Bower, and S. T. Kay (2001). "Revisiting the cosmic cooling crisis". *MNRAS* 326, 1228.

Barai, P. and E. M. De Gouveia Dal Pino (2019). "Intermediate-mass black hole growth and feedback in dwarf galaxies at high redshifts". *MNRAS* 487, 5549.

Barausse, E. (2012). "The evolution of massive black holes and their spins in their galactic hosts". *MNRAS* 423, 2533.

Bardeen, J. M. and J. A. Petterson (1975). "The Lense-Thirring Effect and Accretion Disks around Kerr Black Holes". *ApJ* 195, L65.

Bardeen, J. M., W. H. Press, and S. A. Teukolsky (1972). "Rotating Black Holes: Locally Nonrotating Frames, Energy Extraction, and Scalar Synchrotron Radiation". *ApJ* 178, 347.

Barnes, D. J. et al. (2017). "The Cluster-EAGLE project: global properties of simulated clusters with resolved galaxies". *MNRAS* 471, 1088.

Barnes, J. and P. Hut (1986). "A hierarchical O(N log N) force-calculation algorithm". *Nature* 324, 446.

Barth, A. J., L. E. Strigari, M. C. Bentz, J. E. Greene, and L. C. Ho (2009). "Dynamical constraints on the masses of the nuclear star cluster and black hole in the late-type spiral galaxy NGC 3621". *ApJ* 690, 1031.

Bauer, A. and V. Springel (2012). "Subsonic turbulence in smoothed particle hydrodynamics and moving-mesh simulations". *MNRAS* 423, 2558.

Beckmann, R. S., A. Slyz, and J. Devriendt (2018). "Bondi or not Bondi: The impact of resolution on accretion and drag force modelling for supermassive black holes". *MNRAS* 478, 995.

Beckmann, R. S. et al. (2017). "Cosmic evolution of stellar quenching by AGN feedback: clues from the Horizon-AGN simulation". *MNRAS* 472, 949.

Beckmann, R. S. et al. (2019a). "Dense gas formation and destruction in a simulated Perseus-like galaxy cluster with spin-driven black hole feedback". *A&A* 631, A60, A60.

Beckmann, R. S., J. Devriendt, and A. Slyz (2019b). "Zooming in on supermassive black holes: How resolving their gas cloud host renders their accretion episodic". *MNRAS* 483, 3488.

Begelman, M. C. and M. J. Rees (1978). "The fate of dense stellar systems". *MNRAS* 185, 847.

Behroozi, P. S., C. Conroy, and R. H. Wechsler (2010). "A Comprehensive Analysis of Uncertainties Affecting the Stellar Mass-Halo Mass Relation for $0 < z < 4$". *ApJ* 717, 379.

Behroozi, P. S., R. H. Wechsler, and C. Conroy (2013). "The Average Star Formation Histories of Galaxies in Dark Matter Halos from z = 0-8". *ApJ* 770, 57, 57.

Bell, E. F., D. H. McIntosh, N. Katz, and M. D. Weinberg (2003). "The Optical and Near-Infrared Properties of Galaxies. I. Luminosity and Stellar Mass Functions". *ApJS* 149, 289.

Bellovary, J., M. Volonteri, F. Governato, S. Shen, T. Quinn, and J. Wadsley (2011). "The first massive black hole seeds and their hosts". *ApJ* 742, 13.

Bellovary, J. M., C. E. Cleary, F. Munshi, M. Tremmel, C. R. Christensen, A. Brooks, and T. R. Quinn (2019). "Multimessenger signatures of massive black holes in dwarf galaxies". *MNRAS* 482, 2913.

Bennett, C. L. et al. (2003). "First-Year Wilkinson Microwave Anisotropy Probe (WMAP) Observations: Preliminary Maps and Basic Results". *ApJS* 148, 1.

Benson, A. J., S. Cole, C. S. Frenk, C. M. Baugh, and C. G. Lacey (2000). "The nature of galaxy bias and clustering". *MNRAS* 311, 793.
Berlind, A. A. and D. H. Weinberg (2002). "The Halo Occupation Distribution: Toward an Empirical Determination of the Relation between Galaxies and Mass". *ApJ* 575, 587.
Berti, E. and M. Volonteri (2008). "Cosmological Black Hole Spin Evolution by Mergers and Accretion". *ApJ* 684, 822.
Bieri, R., Y. Dubois, J. Rosdahl, A. Wagner, J. Silk, and G. A. Mamon (2017). "Outflows driven by quasars in high-redshift galaxies with radiation hydrodynamics". *MNRAS* 464, 1854.
Binney, J. and G. Tabor (1995). "Evolving cooling flows". *MNRAS* 276, 663.
Birchall, K. L., M. G. Watson, and J. Aird (2020). "X-ray detected AGN in SDSS dwarf galaxies". *MNRAS* 492, 2268.
Blandford, R. D. and R. L. Znajek (1977). "Electromagnetic extraction of energy from Kerr black holes". *MNRAS* 179, 433.
Blandford, R. D. and M. C. Begelman (1999). "On the fate of gas accreting at a low rate on to a black hole". *MNRAS* 303, L1.
Blanton, M. R. et al. (2017). "Sloan Digital Sky Survey IV: Mapping the Milky Way, Nearby Galaxies, and the Distant Universe". *AJ* 154, 28.
Blok, W. J. G. de, S. S. McGaugh, A. Bosma, and V. C. Rubin (2001). "Mass Density Profiles of Low Surface Brightness Galaxies". *ApJ* 552, L23.
Blondin, J. M., E. B. Wright, K. J. Borkowski, and S. P. Reynolds (1998). "Transition to the Radiative Phase in Supernova Remnants". *ApJ* 500, 342.
Blumenthal, G. R., H. Pagels, and J. R. Primack (1982). "Galaxy formation by dissipationless particles heavier than neutrinos". *Nature* 299, 37.
Bond, J. R., G. Efstathiou, and J. Silk (1980). "Massive Neutrinos and the Large-Scale Structure of the Universe". *PRL* 45, 1980.
Bondi, H. (1952). "On spherically symmetrical accretion". *MNRAS* 112, 195.
Bondi, H. and F. Hoyle (1944). "On the Mechanism of Accretion by Stars". *MNRAS* 104, 273.
Bongiorno, A. et al. (2014). "The MBH-M* relation for X-ray-obscured, red QSOs at $1.2 < z < 2.6$". *MNRAS* 443, 2077.
Bonnor, W. B. (1957). "Jeans' formula for gravitational instability". *MNRAS* 117, 104.
Booth, C. M., O. Agertz, A. V. Kravtsov, and N. Y. Gnedin (2013). "Simulations of Disk Galaxies with Cosmic Ray Driven Galactic Winds". *ApJ* 777, L16, L16.
Booth, C. M. and J. Schaye (2009). "Cosmological simulations of the growth of supermassive black holes and feedback from active galactic nuclei: Method and tests". *MNRAS* 398, 53.
Bose, S., W. A. Hellwing, C. S. Frenk, A. Jenkins, M. R. Lovell, J. C. Helly, and B. Li (2016). "The Copernicus Complexio: statistical properties of warm dark matter haloes". *MNRAS* 455, 318.
Bourne, M. A., S. Nayakshin, and A. Hobbs (2014). "Black hole feedback in a multiphase interstellar medium". *MNRAS* 441, 3055.
Bower, R. G., A. J. Benson, and R. A. Crain (2012). "What shapes the galaxy mass function? Exploring the roles of supernova-driven winds and active galactic nuclei". *MNRAS* 422, 2816.
Bower, R. G., A. J. Benson, R. Malbon, J. C. Helly, C. S. Frenk, C. M. Baugh, S. Cole, and C. G. Lacey (2006). "Breaking the hierarchy of galaxy formation". *MNRAS* 370, 645.

Bower, R. G., I. Vernon, M. Goldstein, A. J. Benson, C. G. Lacey, C. M. Baugh, S. Cole, and C. S. Frenk (2010). "The parameter space of galaxy formation". *MNRAS* 407, 2017.

Boylan-Kolchin, M., J. S. Bullock, and M. Kaplinghat (2011). "Too big to fail? The puzzling darkness of massive Milky Way subhaloes". *MNRAS* 415, L40.

Boylan-Kolchin, M., V. Springel, S. D. M. White, A. Jenkins, and G. Lemson (2009). "Resolving cosmic structure formation with the Millennium-II Simulation". *MNRAS* 398, 1150.

Bradford, J. D., M. C. Geha, J. E. Greene, A. E. Reines, and C. M. Dickey (2018). "The Effect of AGNs on the Global H i Content of Isolated Low-mass Galaxies". *ApJ* 861, 50.

Bromm, V. (2013). "Formation of the first stars". *Reports on Progress in Physics* 76, 112901, 112901.

Brooks, A. M. (2019). "Understanding Dwarf Galaxies in Order to Understand Dark Matter". *Illuminating Dark Matter*. Ed. by R. Essig, J. Feng, and K. Zurek. Vol. 56, 19.

Bruzual, G. and S. Charlot (2003). "Stellar population synthesis at the resolution of 2003". *MNRAS* 344, 1000.

Bryan, G. L. and M. L. Norman (1998). "Statistical Properties of X-Ray Clusters: Analytic and Numerical Comparisons". *ApJ* 495, 80.

Bullock, J. S., T. S. Kolatt, Y. Sigad, R. S. Somerville, A. V. Kravtsov, A. A. Klypin, J. R. Primack, and A. Dekel (2001). "Profiles of dark haloes: evolution, scatter and environment". *MNRAS* 321, 559.

Bullock, J. S. and M. Boylan-Kolchin (2017). "Small-Scale Challenges to the ΛCDM Paradigm". *ARA&A* 55, 343.

Bullock, J. S., R. H. Wechsler, and R. S. Somerville (2002). "Galaxy halo occupation at high redshift". *MNRAS* 329, 246.

Bundy, K. et al. (2014). "Overview of the SDSS-IV MaNGA Survey: Mapping nearby Galaxies at Apache Point Observatory". *ApJ* 798, 7.

Bustamante, S. and V. Springel (2019). "Spin evolution and feedback of supermassive black holes in cosmological simulations". *MNRAS* 490, 4133.

Cann, J. M., S. Satyapal, N. P. Abel, C. Ricci, N. J. Secrest, L. Blecha, and M. Gliozzi (2018). "The Hunt for Intermediate-mass Black Holes in the JWST Era". *ApJ* 861, 142.

Cann, J. M., S. Satyapal, N. P. Abel, L. Blecha, R. F. Mushotzky, C. S. Reynolds, and N. J. Secrest (2019). "The Limitations of Optical Spectroscopic Diagnostics in Identifying Active Galactic Nuclei in the Low-mass Regime". *ApJ* 870, L2.

Cenci, E., L. Sala, A. Lupi, P. R. Capelo, and M. Dotti (2021). "Black hole spin evolution in warped accretion discs". *MNRAS* 500, 3719.

Chabrier, G. (2003). "Galactic Stellar and Substellar Initial Mass Function". *PASP* 115, 763.

Chandrasekhar, S. (1931). "The Maximum Mass of Ideal White Dwarfs". *ApJ* 74, 81.

Chatterjee, P., L. Hernquist, and A. Loeb (2002a). "Brownian Motion in Gravitationally Interacting Systems". *PhRvL* 88, 121103, 121103.

Chatterjee, P., L. Hernquist, and A. Loeb (2002b). "Dynamics of a Massive Black Hole at the Center of a Dense Stellar System". *ApJ* 572, 371.

Chen, N., Y. Ni, M. Tremmel, T. Di Matteo, S. Bird, C. DeGraf, and Y. Feng (2021). "Dynamical Friction Modeling of Massive Black Holes in Cosmological Simulations and Effects on Merger Rate Predictions". *ArXiv e-prints*, arXiv:2104.00021.

Cheng, S., H.-R. Yu, D. Inman, Q. Liao, Q. Wu, and J. Lin (2020). "CUBE – Towards an Optimal Scaling of Cosmological N-body Simulations". *2020 20th IEEE/ACM International Symposium on Cluster, Cloud and Internet Computing (CCGRID)*, 685.

Chilingarian, I. V., I. Y. Katkov, I. Y. Zolotukhin, K. A. Grishin, Y. Beletsky, K. Boutsia, and D. J. Osip (2018). "A Population of Bona Fide Intermediate Mass Black Holes Identified as Low Luminosity Active Galactic Nuclei". *ApJ* 863, 1.

Choi, E., J. P. Ostriker, T. Naab, and P. H. Johansson (2012). "Radiative and momentum-based mechanical active galactic nucleus feedback in a three-dimensional galaxy evolution code". *ApJ* 754, 125.

Civano, F. et al. (2019). "Cosmic evolution of supermassive black holes: A view into the next two decades". *ArXiv e-prints*, arXiv:1903.11091.

Cole, S. (1991). "Modeling galaxy formation in evolving dark matter halos". *ApJ* 367, 45.

Cole, S., C. G. Lacey, C. M. Baugh, and C. S. Frenk (2000). "Hierarchical galaxy formation". *MNRAS* 319, 168.

Cole, S. et al. (2005). "The 2dF Galaxy Redshift Survey: power-spectrum analysis of the final data set and cosmological implications". *MNRAS* 362, 505.

Colín, P., A. A. Klypin, A. V. Kravtsov, and A. M. Khokhlov (1999). "Evolution of Bias in Different Cosmological Models". *ApJ* 523, 32.

Colless, M. et al. (2001). "The 2dF Galaxy Redshift Survey: spectra and redshifts". *MNRAS* 328, 1039.

Conroy, C., R. H. Wechsler, and A. V. Kravtsov (2006). "Modeling Luminosity-dependent Galaxy Clustering through Cosmic Time". *ApJ* 647, 201.

Costa, T., J. Rosdahl, D. Sijacki, and M. G. Haehnelt (2018a). "Quenching star formation with quasar outflows launched by trapped IR radiation". *MNRAS* 479, 2079.

Costa, T., J. Rosdahl, D. Sijacki, and M. G. Haehnelt (2018b). "Driving gas shells with radiation pressure on dust in radiation-hydrodynamic simulations". *MNRAS* 473, 4197.

Costa, T., D. Sijacki, and M. G. Haehnelt (2014). "Feedback from active galactic nuclei: energy- versus momentum-driving". *MNRAS* 444, 2355.

Couchman, H. M. P. (1991). "Mesh-refined P 3M: A Fast Adaptive N-Body Algorithm". *ApJ* 368, L23.

Crain, R. A. et al. (2009). "Galaxies-intergalactic medium interaction calculation - I. Galaxy formation as a function of large-scale environment". *MNRAS* 399, 1773.

Croton, D. J. (2006). "Evolution in the black hole mass-bulge mass relation: A theoretical perspective". *MNRAS* 369, 1808.

Curtis, M. and D. Sijacki (2015). "Resolving flows around black holes: Numerical technique and applications". *MNRAS* 454, 3445.

Curtis, M. and D. Sijacki (2016). "Resolving flows around black holes: the impact of gas angular momentum". *MNRAS* 463, 63.

Dalla Vecchia, C. and J. Schaye (2012). "Simulating galactic outflows with thermal supernova feedback". *MNRAS* 426, 140.

Dashyan, G. and Y. Dubois (2020). "Cosmic ray feedback from supernovae in dwarf galaxies". *A&A* 638, A123, A123.

Dashyan, G., J. Silk, G. A. Mamon, Y. Dubois, and T. Hartwig (2018). "AGN feedback in dwarf galaxies?" *MNRAS* 473, 5698.

Davis, B. L., A. W. Graham, and E. Cameron (2018). "Black Hole Mass Scaling Relations for Spiral Galaxies. II. M_{BH}-$M_{*,tot}$ and M_{BH}-$M_{*,disk}$". *ApJ* 869, 113.

Davis, B. L., A. W. Graham, and E. Cameron (2019). "Black Hole Mass Scaling Relations for Spiral Galaxies. I. M_{BH}-$M_{*,sph}$". *ApJ* 873, 85.

Davis, M., G. Efstathiou, C. S. Frenk, and S. D. M. White (1985). "The evolution of large-scale structure in a universe dominated by cold dark matter". *ApJ* 292, 371.

Dawson, K. S. et al. (2013). "The Baryon Oscillation Spectroscopic Survey of SDSS-III". *AJ* 145, 10, 10.

De Falco, V. and S. Motta (2018). "Polynomial approximation of the Lense-Thirring rigid precession frequency". *MNRAS* 476, 2040.

De Lorenzi, F., M. Hartmann, V. P. Debattista, A. C. Seth, and O. Gerhard (2013). "Three-integral multicomponent dynamical models and simulations of the nuclear star cluster in NGC 4244". *MNRAS* 429, 2974.

DeGraf, C. and D. Sijacki (2020). "Cosmological simulations of massive black hole seeds: predictions for next-generation electromagnetic and gravitational wave observations". *MNRAS* 491, 4973.

Dekel, A. and J. Silk (1986). "The origin of dwarf galaxies, cold dark matter, and biased galaxy formation". *ApJ* 303, 39.

Den Brok, M. et al. (2015). "Measuring the Mass of the Central Black Hole in the Bulgeless Galaxy NGC 4395 from Gas Dynamical Modeling". *ApJ* 809, 101.

Devecchi, B. and M. Volonteri (2009). "Formation of the first nuclear clusters and massive black holes at high redshift". *ApJ* 694, 302.

Di Cintio, A., C. B. Brook, A. V. Macciò, G. S. Stinson, A. Knebe, A. A. Dutton, and J. Wadsley (2013). "The dependence of dark matter profiles on the stellar-to-halo mass ratio: A prediction for cusps versus cores". *MNRAS* 437, 415.

Di Cintio, A., M. Tremmel, F. Governato, A. Pontzen, J. Zavala, A. B. Fry, A. Brooks, and M. Vogelsberger (2017). "A rumble in the dark: Signatures of self-interacting dark matter in supermassive black hole dynamics and galaxy density profiles". *MNRAS* 469, 2845.

Di Matteo, T., J. Colberg, V. Springel, L. Hernquist, and D. Sijacki (2008). "Direct Cosmological Simulations of the Growth of Black Holes and Galaxies". *ApJ* 676, 33.

Di Matteo, T., R. A. C. Croft, V. Springel, and L. Hernquist (2003). "Black Hole Growth and Activity in a Λ Cold Dark Matter Universe". *ApJ* 593, 56.

Di Matteo, T., R. A. C. Croft, V. Springel, and L. Hernquist (2004). "The Cosmological Evolution of Metal Enrichment in Quasar Host Galaxies". *ApJ* 610, 80.

Di Matteo, T., V. Springel, and L. Hernquist (2005). "Energy input from quasars regulates the growth and activity of black holes and their host galaxies". *Nature* 433, 604.

Dibi, S., S. Drappeau, P. C. Fragile, S. Markoff, and J. Dexter (2012). "General relativistic magnetohydrodynamic simulations of accretion on to Sgr A*: how important are radiative losses?" *MNRAS* 426, 1928.

Dickey, C. M., M. Geha, A. Wetzel, and K. El-Badry (2019). "AGN All the Way Down? AGN-like Line Ratios Are Common in the Lowest-mass Isolated Quiescent Galaxies". *ApJ* 884, 180.

Ding, X. et al. (2020). "The Mass Relations between Supermassive Black Holes and Their Host Galaxies at $1 < z < 2$ with HST -WFC3". *ApJ* 888, 37.

Dobbs, C. L. et al. (2014). "Formation of Molecular Clouds and Global Conditions for Star Formation". *Protostars and Planets VI*. Ed. by H. Beuther, R. S. Klessen, C. P. Dullemond, and T. Henning, 3.

Dolag, K., S. Borgani, G. Murante, and V. Springel (2009). "Substructures in hydrodynamical cluster simulations". *MNRAS* 399, 497.

Dotti, M., M. Colpi, S. Pallini, A. Perego, and M. Volonteri (2013). "On the Orientation and Magnitude of the Black Hole Spin in Galactic Nuclei". *ApJ* 762, 68, 68.

Dubois, Y. et al. (2014a). "Dancing in the dark: Galactic properties trace spin swings along the cosmic web". *MNRAS* 444, 1453.

Dubois, Y., M. Volonteri, J. Silk, J. Devriendt, and A. Slyz (2014b). "Black hole evolution - II. Spinning black holes in a supernova-driven turbulent interstellar medium". *MNRAS* 440, 2333.

Dubois, Y., M. Volonteri, J. Silk, J. Devriendt, A. Slyz, and R. Teyssier (2015). "Black hole evolution - I. Supernova-regulated black hole growth". *MNRAS* 452, 1502.

Dubois, Y. et al. (2020). "Introducing the NewHorizon simulation: galaxy properties with resolved internal dynamics across cosmic time". *ArXiv e-prints*, arXiv:2009.10578.

Duckworth, C., T. K. Starkenburg, S. Genel, T. A. Davis, M. Habouzit, K. Kraljic, and R. Tojeiro (2020). "Decoupling the rotation of stars and gas – II. The link between black hole activity and simulated IFU kinematics in IllustrisTNG". *MNRAS* 495, 4542.

Eckart, A. and R. Genzel (1997). "Stellar proper motions in the central 0.1 PC of the Galaxy". *MNRAS* 284, 576.

Efstathiou, G. (1992). "Suppressing the formation of dwarf galaxies via photoionization". *MNRAS* 256, 43P.

Efstathiou, G., M. Davis, S. D. M. White, and C. S. Frenk (1985). "Numerical techniques for large cosmological N-body simulations". *ApJS* 57, 241.

Einasto, J., E. Saar, A. Kaasik, and A. D. Chernin (1974). "Missing mass around galaxies - Morphological evidence". *Nature* 252, 111.

Einstein, A. (1915). "Zur allgemeinen Relativitätstheorie". *Sitzungsberichte der Königlich Preußischen Akademie der Wissenschaften (Berlin)*, 778.

Eisenstein, D. J. et al. (2005). "Detection of the Baryon Acoustic Peak in the Large-Scale Correlation Function of SDSS Luminous Red Galaxies". *ApJ* 633, 560.

Eke, V. R., J. F. Navarro, and M. Steinmetz (2001). "The Power Spectrum Dependence of Dark Matter Halo Concentrations". *ApJ* 554, 114.

Ellison, S. L., T. Brown, B. Catinella, and L. Cortese (2019). "Atomic gas fractions in active galactic nucleus host galaxies". *MNRAS* 482, 5694.

Emerick, A., G. L. Bryan, and M.-M. Mac Low (2018). "Stellar Radiation is Critical for Regulating Star Formation and Driving Outflows in Low Mass Dwarf Galaxies". *ApJ* 865, L22.

Emerick, A., G. L. Bryan, and M.-M. Mac Low (2019). "Simulating an isolated dwarf galaxy with multichannel feedback and chemical yields from individual stars". *MNRAS* 482, 1304.

Emerick, A., G. L. Bryan, and M.-M. Mac Low (2020). "The Role of Stellar Feedback in the Chemical Evolution of a Low Mass Dwarf Galaxy". *arXiv e-prints*, arXiv:2007.03702.

Esin, A. A., J. E. McClintock, and R. Narayan (1997). "Advection-Dominated Accretion and the Spectral States of Black Hole X-Ray Binaries: Application to Nova Muscae 1991". *ApJ* 489, 865.

Fall, S. M. and G. Efstathiou (1980). "Formation and rotation of disc galaxies with haloes". *MNRAS* 193, 189.

Fanidakis, N., C. M. Baugh, A. J. Benson, R. G. Bower, S. Cole, C. Done, and C. S. Frenk (2011). "Grand unification of AGN activity in the ΛCDM cosmology". *MNRAS* 410, 53.

Farber, R., M. Ruszkowski, H. .-Y. K. Yang, and E. G. Zweibel (2018). "Impact of Cosmic-Ray Transport on Galactic Winds". *ApJ* 856, 112, 112.

Faucher-Giguère, C.-A. (2020). "A cosmic UV/X-ray background model update". *MNRAS* 493, 1614.

Faucher-Giguère, C.-A., A. Lidz, M. Zaldarriaga, and L. Hernquist (2009). "A New Calculation of the Ionizing Background Spectrum and the Effects of He II Reionization". *ApJ* 703, 1416.

Ferrarese, L. and D. Merritt (2000). "A Fundamental Relation between Supermassive Black Holes and Their Host Galaxies". *ApJ* 539, L9.
Fiacconi, D., D. Sijacki, and J. E. Pringle (2018). "Galactic nuclei evolution with spinning black holes: Method and implementation". *MNRAS* 477, 3807.
Filippenko, A. V. and W. L. W. Sargent (1989). "Discovery of an Extremely Low Luminosity Seyfert 1 Nucleus in the Dwarf Galaxy NGC 4395". *ApJ* 342, L11.
Fitts, A. et al. (2016). "FIRE in the Field: Simulating the Threshold of Galaxy Formation". *MNRAS* 471, 3547.
Flores, R. A. and J. R. Primack (1994). "Observational and theoretical constraints on singular dark matter halos". *ApJ* 427, L1.
Fragile, P. C., O. M. Blaes, P. Anninos, and J. D. Salmonson (2007). "Global General Relativistic Magnetohydrodynamic Simulation of a Tilted Black Hole Accretion Disk". *ApJ* 668, 417.
Freitag, M., M. Atakan Gürkan, and F. A. Rasio (2006). "Runaway collisions in young star clusters - II. Numerical results". *MNRAS* 368, 141.
Frenk, C. S., S. D. M. White, G. Efstathiou, and M. Davis (1985). "Cold dark matter, the structure of galactic haloes and the origin of the Hubble sequence". *Nature* 317, 595.
Frenk, C. S. et al. (1999). "The Santa Barbara Cluster Comparison Project: A Comparison of Cosmological Hydrodynamics Solutions". *ApJ* 525, 554.
Frenk, C. S., S. D. M. White, M. Davis, and G. Efstathiou (1988). "The Formation of Dark Halos in a Universe Dominated by Cold Dark Matter". *ApJ* 327, 507.
Friedmann, A. (1922). "Über die Krümmung des Raumes". *Zeitschrift fur Physik* 10, 377.
Gabor, J. M. and F. Bournaud (2014). "Active galactic nuclei-driven outflows without immediate quenching in simulations of high-redshift disc galaxies". *MNRAS* 441, 1615.
Gallazzi, A., J. Brinchmann, S. Charlot, and S. D. White (2008). "A census of metals and baryons in stars in the local Universe". *MNRAS* 383, 1439.
Gaspari, M. and A. Sądowski (2017). "Unifying the Micro and Macro Properties of AGN Feeding and Feedback". *ApJ* 837, 149, 149.
Gebhardt, K. et al. (2000). "A Relationship between Nuclear Black Hole Mass and Galaxy Velocity Dispersion". *ApJ* 539, L13.
Geen, S., J. Rosdahl, J. Blaizot, J. Devriendt, and A. Slyz (2015). "A detailed study of feedback from a massive star". *MNRAS* 448, 3248.
Geha, M., M. R. Blanton, R. Yan, and J. L. Tinker (2012). "A stellar mass threshold for quenching of field galaxies". *ApJ* 757, 85.
Genel, S. et al. (2014). "Introducing the Illustris project: The evolution of galaxy populations across cosmic time". *MNRAS* 445, 175.
Gentile, G., P. Salucci, U. Klein, D. Vergani, and P. Kalberla (2004). "The cored distribution of dark matter in spiral galaxies". *MNRAS* 351, 903.
Ghez, A. M., B. L. Klein, M. Morris, and E. E. Becklin (1998). "High Proper-Motion Stars in the Vicinity of Sagittarius A*: Evidence for a Supermassive Black Hole at the Center of Our Galaxy". *ApJ* 509, 678.
Ghigna, S., B. Moore, F. Governato, G. Lake, T. Quinn, and J. Stadel (1998). "Dark matter haloes within clusters". *MNRAS* 300, 146.
Gingold, R. A. and J. J. Monaghan (1977). "Smoothed particle hydrodynamics: theory and application to non-spherical stars." *MNRAS* 181, 375.
Giustini, M. and D. Proga (2019). "A global view of the inner accretion and ejection flow around super massive black holes: Radiation-driven accretion disk winds in a physical context". *A&A* 630, A94.

Governato, F. et al. (2010). "Bulgeless dwarf galaxies and dark matter cores from supernova-driven outflows". *Nature* 463, 203.
Graham, A. W., R. Soria, and B. L. Davis (2019). "Expected intermediate-mass black holes in the Virgo cluster - II. Late-type galaxies". *MNRAS* 484, 814.
Granato, G. L., L. Danese, and A. Franceschini (1997). "Thick Tori around Active Galactic Nuclei: The Case for Extended Tori and Consequences for Their X-Ray and Infrared Emission". *ApJ* 486, 147.
Grand, R. J. J. et al. (2017). "The Auriga Project: the properties and formation mechanisms of disc galaxies across cosmic time". *MNRAS* 467, 179.
Green, A. M., S. Hofmann, and D. J. Schwarz (2004). "The power spectrum of SUSY-CDM on subgalactic scales". *MNRAS* 353, L23.
Greene, J. E. and L. C. Ho (2004). "Active Galactic Nuclei with Candidate Intermediate-Mass Black Holes". *ApJ* 610, 13.
Greene, J. E. and L. C. Ho (2007). "The Mass Function of Active Black Holes in the Local Universe". *ApJ* 667, 19.
Greene, J. E., L. C. Ho, and J. S. Ulvestad (2006). "The Radio Quiescence of Active Galaxies with High Accretion Rates". *ApJ* 636, 56.
Greene, J. E., J. Strader, and L. C. Ho (2020). "Intermediate-Mass Black Holes". *ARA&A* 58, 257.
Greene, J. E. et al. (2010). "Precise black hole masses from megamaser disks: Black hole-bulge relations at low mass". *ApJ* 721, 26.
Greene, J. E. et al. (2016). "Megamaser Disks Reveal a Broad Distribution of Black Hole Mass in Spiral Galaxies". *ApJL* 826, L32.
Greengard, L. and V. Rokhlin (1987). "A Fast Algorithm for Particle Simulations". *Journal of Computational Physics* 73, 325.
Guedes, J., S. Callegari, P. Madau, and L. Mayer (2011). "Forming Realistic Late-type Spirals in a ΛCDM Universe: The Eris Simulation". *ApJ* 742, 76, 76.
Gültekin, K. et al. (2009). "The M-σ and M-L Relations in Galactic Bulges, and Determinations of Their Intrinsic Scatter". *ApJ* 698, 198.
Gunn, J. E. and I. Gott J. Richard (1972). "On the Infall of Matter Into Clusters of Galaxies and Some Effects on Their Evolution". *ApJ* 176, 1.
Guo, Q., S. White, R. E. Angulo, B. Henriques, G. Lemson, M. Boylan-Kolchin, P. Thomas, and C. Short (2013). "Galaxy formation in WMAP1 and WMAP7 cosmologies". *MNRAS* 428, 1351.
Gutcke, T. A., R. Pakmor, T. Naab, and V. Springel (2021). "LYRA - I. Simulating the multiphase ISM of a dwarf galaxy with variable energy supernovae from individual stars". *MNRAS* 501, 5597.
Haardt, F. and P. Madau (2012). "Radiative Transfer in a Clumpy Universe. IV. New Synthesis Models of the Cosmic UV/X-Ray Background". *ApJ* 746, 125, 125.
Habouzit, M., M. Volonteri, and Y. Dubois (2017). "Blossoms from black hole seeds: properties and early growth regulated by supernova feedback". *MNRAS* 468, 3935.
Habouzit, M. et al. (2021). "Supermassive black holes in cosmological simulations I: M_{BH} - $M_\star$ relation and black hole mass function". *MNRAS* 503, 1940.
Haehnelt, M. G. and G. Kauffmann (2000). "The correlation between black hole mass and bulge velocity dispersion in hierarchical galaxy formation models". *MNRAS* 318, L35.
Hahn, O. and T. Abel (2011). "Multi-scale initial conditions for cosmological simulations". *MNRAS* 415, 2101.

Haiman, Z. et al. (2019). "Electromagnetic Window into the Dawn of Black Holes". *ArXiv e-prints*, arXiv:1903.08579.

Hambrick, D. C., J. P. Ostriker, T. Naab, and P. H. Johansson (2011). "The effects of X-ray feedback from active galactic nuclei on host galaxy evolution". *ApJ* 738.

Hanasz, M., H. Lesch, T. Naab, A. Gawryszczak, K. Kowalik, and D. Wóltański (2013). "Cosmic Rays Can Drive Strong Outflows from Gas-rich High-redshift Disk Galaxies". *ApJ* 777, L38, L38.

Häring, N. and H.-W. Rix (2004). "On the Black Hole Mass-Bulge Mass Relation". *ApJ* 604, L89.

Hawkins, E. et al. (2003). "The 2dF Galaxy Redshift Survey: correlation functions, peculiar velocities and the matter density of the Universe". *MNRAS* 346, 78.

Heger, A., C. L. Fryer, S. E. Woosley, N. Langer, and D. H. Hartmann (2003). "How Massive Single Stars End Their Life". *ApJ* 591, 288.

Heger, A. and S. E. Woosley (2010). "Nucleosynthesis and evolution of massive metal-free stars". *ApJ* 724, 341.

Heitmann, K. et al. (2008). "The cosmic code comparison project". *Computational Science and Discovery* 1, 015003.

Henden, N. A., E. Puchwein, S. Shen, and D. Sijacki (2018). "The FABLE simulations: A feedback model for galaxies, groups, and clusters". *MNRAS* 479, 5385.

Henden, N. A., E. Puchwein, and D. Sijacki (2019). "The redshift evolution of X-ray and Sunyaev-Zel'dovich scaling relations in the FABLE simulations". *MNRAS* 489, 2439.

Henden, N. A., E. Puchwein, and D. Sijacki (2020). "The baryon content of groups and clusters of galaxies in the FABLE simulations". *MNRAS* 498, 2114.

Henriques, B. M. B., P. A. Thomas, S. Oliver, and I. Roseboom (2009). "Monte Carlo Markov Chain parameter estimation in semi-analytic models of galaxy formation". *MNRAS* 396, 535.

Holguin, F., M. Ruszkowski, A. Lazarian, R. Farber, and H. .-Y. K. Yang (2019). "Role of cosmic-ray streaming and turbulent damping in driving galactic winds". *MNRAS* 490, 1271.

Hopkins, P. F., G. T. Richards, and L. Hernquist (2007). "An Observational Determination of the Bolometric Quasar Luminosity Function". *ApJ* 654, 731.

Hopkins, P. F. et al. (2018a). "FIRE-2 simulations: Physics versus numerics in galaxy formation". *MNRAS* 480, 800.

Hopkins, P. F. (2013). "A general class of Lagrangian smoothed particle hydrodynamics methods and implications for fluid mixing problems". *MNRAS* 428, 2840.

Hopkins, P. F. (2015). "A new class of accurate, mesh-free hydrodynamic simulation methods". *MNRAS* 450, 53.

Hopkins, P. F., T. K. Chan, J. Squire, E. Quataert, S. Ji, D. Kereš, and C.-A. Faucher-Giguère (2021). "Effects of different cosmic ray transport models on galaxy formation". *MNRAS* 501, 3663.

Hopkins, P. F., D. Kereš, J. Oñorbe, C. A. Faucher-Giguère, E. Quataert, N. Murray, and J. S. Bullock (2014). "Galaxies on FIRE (Feedback In Realistic Environments): Stellar feedback explains cosmologically inefficient star formation". *MNRAS* 445, 581.

Hopkins, P. F. et al. (2018b). "How to model supernovae in simulations of star and galaxy formation". *MNRAS* 477, 1578.

Hoyle, F. (1949). "The Origin of the Rotations of the Galaxies". *Problems of Cosmical Aerodynamics*, 195.

Hoyle, F. and W. A. Fowler (1963). "On the nature of strong radio sources". *MNRAS* 125, 169.
Hoyle, F. and R. A. Lyttleton (1939). "The effect of interstellar matter on climatic variation". *Math. Proc. Cambridge Philos. Soc.* 35, 405.
Hu, C. Y., T. Naab, S. C. Glover, S. Walch, and P. C. Clark (2017). "Variable interstellar radiation fields in simulated dwarf galaxies: Supernovae versus photoelectric heating". *MNRAS* 471, 2151.
Hu, C. Y., T. Naab, S. Walch, S. C. Glover, and P. C. Clark (2016). "Star formation and molecular hydrogen in dwarf galaxies: A non-equilibrium view". *MNRAS* 458, 3528.
Hu, C.-Y. (2019). "Supernova-driven winds in simulated dwarf galaxies". *MNRAS* 483, 3363.
Hu, W., R. Barkana, and A. Gruzinov (2000). "Fuzzy Cold Dark Matter: The Wave Properties of Ultralight Particles". *PRL* 85, 1158.
Hubble, E. P. (1925). "NGC 6822, a remote stellar system." *ApJ* 62, 409.
Hubble, E. P. (1926). "A spiral nebula as a stellar system: Messier 33." *ApJ* 63, 236.
Hubble, E. P. (1929a). "A Relation between Distance and Radial Velocity among Extra-Galactic Nebulae". *Proceedings of the National Academy of Science* 15, 168.
Hubble, E. P. (1929b). "No. 376. A spiral nebula as a stellar system. Messier 31." *Contributions from the Mount Wilson Observatory / Carnegie Institution of Washington* 376, 1.
Hui, L., J. P. Ostriker, S. Tremaine, and E. Witten (2017). "Ultralight scalars as cosmological dark matter". *PRD* 95, 043541.
Hut, P. and S. D. M. White (1984). "Can a neutrino-dominated Universe be rejected?" *Nature* 310, 637.
Icke, V. (1973). "Formation of Galaxies inside Clusters". *A&A* 27, 1.
Inayoshi, K., K. Ichikawa, J. P. Ostriker, and R. Kuiper (2019). "Transition of BH feeding from the quiescent regime into star-forming cold disc regime". *MNRAS* 486, 5377.
Inayoshi, K., E. Visbal, and Z. Haiman (2020). "The Assembly of the First Massive Black Holes". *ARA&A* 58, 27.
Ingram, A. and C. Done (2011). "A physical model for the continuum variability and quasi-periodic oscillation in accreting black holes". *MNRAS* 415, 2323.
Ingram, A., C. Done, and P. C. Fragile (2009). "Low-frequency quasi-periodic oscillations spectra and Lense-Thirring precession". *MNRAS* 397, L101.
Ingram, A. R. and S. E. Motta (2019). "A review of quasi-periodic oscillations from black hole X-ray binaries: Observation and theory". *NewAR* 85, 101524.
Iršič, V. et al. (2017). "New constraints on the free-streaming of warm dark matter from intermediate and small scale Lyman-α forest data". *PRD* 96, 023522.
Jeans, J. H. (1902). "The Stability of a Spherical Nebula". *Philosophical Transactions of the Royal Society of London Series A* 199, 1.
Johansson, P. H., A. Burkert, and T. Naab (2009). "The Evolution of Black Hole Scaling Relations in Galaxy Mergers". *ApJ* 707, L184.
Kannan, R. et al. (2014a). "Galaxy formation with local photoionization feedback - I. Methods". *MNRAS* 437, 2882.
Kannan, R., F. Marinacci, M. Vogelsberger, L. V. Sales, P. Torrey, V. Springel, and L. Hernquist (2020). "Simulating the interstellar medium of galaxies with radiative transfer, non-equilibrium thermochemistry, and dust". *MNRAS* 499, 5732.
Kannan, R., G. S. Stinson, A. V. Macciò, C. Brook, S. M. Weinmann, J. Wadsley, and H. M. P. Couchman (2014b). "The MaGICC volume: reproducing statistical properties of high-redshift galaxies". *MNRAS* 437, 3529.

Kant, I. (1755). *Allgemeine Naturgeschichte und Theorie des Himmels*.
Karlsson, T., V. Bromm, and J. Bland-Hawthorn (2013). "Pregalactic metal enrichment: The chemical signatures of the first stars". *Rev. Mod. Phys.* 85, 809.
Katz, H., D. Sijacki, and M. G. Haehnelt (2015). "Seeding high-redshift QSOs by collisional runaway in primordial star clusters". *MNRAS* 451, 2352.
Katz, H. et al. (2020). "How to quench a dwarf galaxy: The impact of inhomogeneous reionization on dwarf galaxies and cosmic filaments". *MNRAS* 494, 2200.
Katz, N., D. H. Weinberg, and L. Hernquist (1996). "Cosmological Simulations with TreeSPH". *ApJS* 105, 19.
Katz, N. and S. D. M. White (1993). "Hierarchical Galaxy Formation: Overmerging and the Formation of an X-Ray Cluster". *ApJ* 412, 455.
Kauffmann, G., S. D. M. White, and B. Guiderdoni (1993). "The formation and evolution of galaxies within merging dark matter haloes". *MNRAS* 264, 201.
Kauffmann, G. and M. Haehnelt (2000). "A unified model for the evolution of galaxies and quasars". *MNRAS* 311, 576.
Kaviraj, S., G. Martin, and J. Silk (2019). "AGN in dwarf galaxies: frequency, triggering processes and the plausibility of AGN feedback". *MNRAS* 489, L12.
Kereš, D., M. Vogelsberger, D. Sijacki, V. Springel, and L. Hernquist (2012). "Moving-mesh cosmology: Characteristics of galaxies and haloes". *MNRAS* 425, 2027.
Kerr, R. P. (1963). "Gravitational Field of a Spinning Mass as an Example of Algebraically Special Metrics". *PRL* 11, 237.
Khandai, N., T. Di Matteo, R. Croft, S. Wilkins, Y. Feng, E. Tucker, C. DeGraf, and M. S. Liu (2015). "The MassiveBlack-II simulation: The evolution of haloes and galaxies to z $\sim$ 0". *MNRAS* 450, 1349.
Kim, C. G. and E. C. Ostriker (2015). "Momentum injection by supernovae in the interstellar medium". *ApJ* 802, 99.
Kim, J. H., J. H. Wise, M. A. Alvarez, and T. Abel (2011). "Galaxy formation with self-consistently modeled stars and massive black holes. I. Feedback-regulated star formation and black hole growth". *ApJ* 738, 54.
Kimm, T., R. Cen, J. Devriendt, Y. Dubois, and A. Slyz (2015). "Towards simulating star formation in turbulent high-z galaxies with mechanical supernova feedback". *MNRAS* 451, 2900.
Kimm, T., M. Haehnelt, J. Blaizot, H. Katz, L. Michel-Dansac, T. Garel, J. Rosdahl, and R. Teyssier (2018). "Impact of Lyman alpha pressure on metal-poor dwarf galaxies". *MNRAS* 475, 4617.
Kimm, T., H. Katz, M. Haehnelt, J. Rosdahl, J. Devriendt, and A. Slyz (2016). "Feedback-regulated star formation and escape of LyC photons from mini-haloes during reionisation". *MNRAS* 466, stx052.
King, A. R., S. H. Lubow, G. I. Ogilvie, and J. E. Pringle (2005). "Aligning spinning black holes and accretion discs". *MNRAS* 363, 49.
King, A. (2003). "Black Holes, Galaxy Formation, and the M_{BH}-σ Relation". *ApJ* 596, L27.
Klypin, A. A. and S. F. Shandarin (1983). "Three-dimensional numerical model of the formation of large-scale structure in the Universe." *MNRAS* 204, 891.
Klypin, A. A., A. V. Kravtsov, O. Valenzuela, and F. Prada (1999). "Where are the missing galactic satellites?" *ApJ* 522, 82.
Komossa, S. (2012). "Recoiling Black Holes: Electromagnetic Signatures, Candidates, and Astrophysical Implications". *Adv. Astron.* 2012, 364973, 364973.

Kormendy, J. and L. C. Ho (2013). "Coevolution (Or Not) of Supermassive Black Holes and Host Galaxies". *ARA&A* 51, 511.
Kormendy, J. and D. Richstone (1995). "Inward Bound—The Search For Supermassive Black Holes In Galactic Nuclei". *ARA&A* 33, 581.
Koudmani, S., N. A. Henden, and D. Sijacki (2021). "A little FABLE: exploring AGN feedback in dwarf galaxies with cosmological simulations". *MNRAS* 503, 3568.
Koudmani, S., D. Sijacki, M. A. Bourne, and M. C. Smith (2019). "Fast and energetic AGN-driven outflows in simulated dwarf galaxies". *MNRAS* 484, 2047.
Krajnović, D., M. Cappellari, P. T. De Zeeuw, and Y. Copin (2006). "Kinemetry: A generalization of photometry to the higher moments of the line-of-sight velocity distribution". *MNRAS* 366, 787.
Krajnović, D. et al. (2018). "A quartet of black holes and a missing duo: Probing the low end of the MBH-σ relation with the adaptive optics assisted integral-field spectroscopy". *MNRAS* 477, 3030.
Kravtsov, A. V. and A. A. Klypin (1999). "The Origin and Evolution of Halo Bias in Linear and Nonlinear Regimes". *ApJ* 520, 437.
Kristensen, M. T., K. Pimbblet, and S. Penny (2020). "Environments of dwarf galaxies with optical AGN characteristics". *MNRAS* 496, 2577.
Kroupa, P. (2002). "The Initial Mass Function of Stars: Evidence for Uniformity in Variable Systems". *Science* 295, 82.
Krumholz, M. R. and J. C. Tan (2007). "Slow Star Formation in Dense Gas: Evidence and Implications". *ApJ* 654, 304.
Kunth, D., W. L. W. Sargent, and G. D. Bothun (1987). "A Dwarf Galaxy with Seyfert Characteristics". *AJ* 93, 29.
Lacey, C. and S. Cole (1993). "Merger rates in hierarchical models of galaxy formation". *MNRAS* 262, 627.
Lagos, C. D. P., N. D. Padilla, and S. A. Cora (2009). "Black hole spin and radio loudness in a Λ cold dark matter universe". *MNRAS* 395, 625.
Laplace, P. S. (1796). *Exposition du systeme du monde [microform] / par Pierre-Simon Laplace*. De l'Imprimerie du Cercle-Social Paris, 2 v.
Larson, R. B. (1974). "Effects of supernovae on the early evolution of galaxies". *MNRAS* 169, 229.
Läsker, R., J. E. Greene, A. Seth, G. van de Ven, J. A. Braatz, C. Henkel, and K. Y. Lo (2016). "The Black Hole-Bulge Mass Relation in Megamaser Host Galaxies". *ApJ* 825, 3.
Leavitt, H. S. and E. C. Pickering (1912). "Periods of 25 Variable Stars in the Small Magellanic Cloud." *Harvard College Observatory Circular* 173, 1.
Lehmer, B. D. et al. (2016). "The Evolution of Normal Galaxy X-Ray Emission through Cosmic History: Constraints from the 6 MS Chandra Deep Field-South". *ApJ* 825, 7.
Lehmer, B. D. et al. (2019). "X-Ray Binary Luminosity Function Scaling Relations for Local Galaxies Based on Subgalactic Modeling". *ApJS* 243, 3.
Leitherer, C. et al. (1999). "Starburst99: Synthesis Models for Galaxies with Active Star Formation". *ApJS* 123, 3.
Lemaître, G. (1927). "Un Univers homogène de masse constante et de rayon croissant rendant compte de la vitesse radiale des nébuleuses extra-galactiques". *Annales de la Société Scientifique de Bruxelles* 47, 49.
Lemons, S. M., A. E. Reines, R. M. Plotkin, E. Gallo, and J. E. Greene (2015). "An X-ray-selected sample of candidate black holes in dwarf galaxies". *ApJ* 805, 12.

Lense, J. and H. Thirring (1918). "Über den Einfluß der Eigenrotation der Zentralkörper auf die Bewegung der Planeten und Monde nach der Einsteinschen Gravitationstheorie". *Physikalische Zeitschrift* 19, 156.

Li, Y. et al. (2020). "Correlations between Black Holes and Host Galaxies in the Illustris and IllustrisTNG Simulations". *ApJ* 895, 102.

Lifshitz, E. (1946). "On the gravitational stability of the expanding universe". *J. Phys. (Moscow)* 10, 116.

Liska, M., C. Hesp, A. Tchekhovskoy, A. Ingram, M. van der Klis, and S. Markoff (2018). "Formation of precessing jets by tilted black hole discs in 3D general relativistic MHD simulations". *MNRAS* 474, L81.

Liska, M., A. Tchekhovskoy, A. Ingram, and M. van der Klis (2019). "Bardeen-Petterson alignment, jets, and magnetic truncation in GRMHD simulations of tilted thin accretion discs". *MNRAS* 487, 550.

Liu, B. F. and R. E. Taam (2009). "Application of the disk evaporation model to active galactic nuclei". *ApJ* 707, 233.

Liu, B. F., W. Yuan, F. Meyer, E. Meyer-Hofmeister, and G. Z. Xie (1999). "Evaporation of Accretion Disks around Black Holes: The Disk-Corona Transition and the Connection to the Advection-dominated Accretion Flow". *ApJ* 527, L17.

Liu, W., S. Veilleux, G. Canalizo, D. S. N. Rupke, C. M. Manzano-King, T. Bohn, and V. U (2020). "Integral Field Spectroscopy of Fast Outflows in Dwarf Galaxies with AGNs". *ApJ* 905, 166.

Lodato, G. and P. Natarajan (2006). "Supermassive black hole formation during the assembly of pre-galactic discs". *MNRAS* 371, 1813.

Lodato, G. and J. E. Pringle (2007). "Warp diffusion in accretion discs: a numerical investigation". *MNRAS* 381, 1287.

Lovell, M. R., C. S. Frenk, V. R. Eke, A. Jenkins, L. Gao, and T. Theuns (2014). "The properties of warm dark matter haloes". *MNRAS* 439, 300.

Lovell, M. R. et al. (2012). "The haloes of bright satellite galaxies in a warm dark matter universe". *MNRAS* 420, 2318.

Lu, Y., H. J. Mo, M. D. Weinberg, and N. Katz (2011). "A Bayesian approach to the semi-analytic model of galaxy formation: methodology". *MNRAS* 416, 1949.

Lucy, L. B. (1977). "A numerical approach to the testing of the fission hypothesis." *AJ* 82, 1013.

Lupi, A., T. Sbarrato, and S. Carniani (2020). "Difficulties in mid-infrared selection of AGNs in dwarf galaxies". *MNRAS* 492, 2528.

Lynden-Bell, D. (1969). "Galactic Nuclei as Collapsed Old Quasars". *Nature* 223, 690.

Lynden-Bell, D. and M. J. Rees (1971). "On quasars, dust and the galactic centre". *MNRAS* 152, 461.

MacArthur, L. A., S. Courteau, and J. A. Holtzman (2003). "Structure of Disk-dominated Galaxies. I. Bulge/Disk Parameters, Simulations, and Secular Evolution". *ApJ* 582, 689.

Macciò, A. V., A. A. Dutton, and F. C. van den Bosch (2008). "Concentration, spin and shape of dark matter haloes as a function of the cosmological model: WMAP1, WMAP3 and WMAP5 results". *MNRAS* 391, 1940.

Madau, P. and M. J. Rees (2001). "Massive Black Holes as Population III Remnants". *ApJ* 551, L27.

Magorrian, J. et al. (1998). "The Demography of Massive Dark Objects in Galaxy Centers". *AJ* 115, 2285.

Mahadevan, R. and E. Quataert (1997). "Are Particles in Advection-dominated Accretion Flows Thermal?" *ApJ* 490, 605.
Maiolino, R. et al. (2012). "Evidence of strong quasar feedback in the early Universe". *MNRAS* 425, L66.
Manzano-King, C. M., G. Canalizo, and L. V. Sales (2019). "AGN-Driven Outflows in Dwarf Galaxies". *ApJ* 884, 54.
Marasco, A., K. A. Oman, J. F. Navarro, C. S. Frenk, and T. Oosterloo (2018). "Bars in dark-matter-dominated dwarf galaxy discs". *MNRAS* 476, 2168.
Marconi, A. and L. K. Hunt (2003). "The Relation between Black Hole Mass, Bulge Mass, and Near-Infrared Luminosity". *ApJ* 589, L21.
Marinacci, F., R. Pakmor, and V. Springel (2014). "The formation of disc galaxies in high-resolution moving-mesh cosmological simulations". *MNRAS* 437, 1750.
Marinacci, F., L. V. Sales, M. Vogelsberger, P. Torrey, and V. Springel (2019). "Simulating the interstellar medium and stellar feedback on a moving mesh: Implementation and isolated galaxies". *MNRAS* 489, 4233.
Marleau, F. R., D. Clancy, R. Habas, and M. Bianconi (2017). "Infrared signature of active massive black holes in nearby dwarf galaxies". *A&A* 602, A28.
Marsh, D. J. E. and J. Silk (2014). "A model for halo formation with axion mixed dark matter". *MNRAS* 437, 2652.
Martin, R. G., C. J. Nixon, J. E. Pringle, and M. Livio (2019). "On the physical nature of accretion disc viscosity". *New Astron.* 70, 7.
Martin, R. G., J. E. Pringle, and C. A. Tout (2007). "Alignment and precession of a black hole with a warped accretion disc". *MNRAS* 381, 1617.
Martín-Navarro, I. and M. Mezcua (2018). "Exploring the Limits of AGN Feedback: Black Holes and the Star Formation Histories of Low-mass Galaxies". *ApJ* 855, L20.
Martizzi, D., C.-A. Faucher-Giguère, and E. Quataert (2015). "Supernova feedback in an inhomogeneous interstellar medium". *MNRAS* 450, 504.
McKee, C. F. and J. P. Ostriker (1977). "A theory of the interstellar medium: three components regulated by supernova explosions in an inhomogeneous substrate." *ApJ* 218, 148.
McKinney, J. C. and R. Narayan (2007). "Disc-jet coupling in black hole accretion systems - I. General relativistic magnetohydrodynamical models". *MNRAS* 375, 513.
McKinney, J. C., A. Tchekhovskoy, and R. D. Blandford (2012). "General relativistic magnetohydrodynamic simulations of magnetically choked accretion flows around black holes". *MNRAS* 423, 3083.
McKinney, J. C., A. Tchekhovskoy, and R. D. Blandford (2013). "Alignment of Magnetized Accretion Disks and Relativistic Jets with Spinning Black Holes". *Science* 339, 49.
McLure, R. J. and J. S. Dunlop (2002). "On the black hole-bulge mass relation in active and inactive galaxies". *MNRAS* 331, 795.
Meneghetti, M., N. Yoshida, M. Bartelmann, L. Moscardini, V. Springel, G. Tormen, and S. D. M. White (2001). "Giant cluster arcs as a constraint on the scattering cross-section of dark matter". *MNRAS* 325, 435.
Mezcua, M., F. Civano, G. Fabbiano, T. Miyaji, and S. Marchesi (2016). "A Population of Intermediate-mass Black Holes in Dwarf Starburst Galaxies Up to Redshift=1.5". *ApJ* 817, 20.
Mezcua, M., F. Civano, S. Marchesi, H. Suh, G. Fabbiano, and M. Volonteri (2018). "Intermediate-mass black holes in dwarf galaxies out to redshift $\sim$2.4 in the Chandra COSMOS-Legacy Survey". *MNRAS* 478, 2576.

Mezcua, M., H. Suh, and F. Civano (2019). "Radio jets from AGNs in dwarf galaxies in the COSMOS survey: mechanical feedback out to redshift ∼3.4". *MNRAS* 488, 685.

Mezcua, M. (2019). "Dwarf galaxies might not be the birth sites of supermassive black holes". *Nature Astronomy* 3, 6.

Mezcua, M. and H. Domínguez Sánchez (2020). "Hidden AGNs in Dwarf Galaxies Revealed by MaNGA: Light Echoes, Off-nuclear Wanderers, and a New Broad-line AGN". *ApJ* 898, L30.

Michell, J. (1784). "On the Means of Discovering the Distance, Magnitude, &c. of the Fixed Stars, in Consequence of the Diminution of the Velocity of Their Light, in Case Such a Diminution Should be Found to Take Place in any of Them, and Such Other Data Should be Procured from Observations, as Would be Farther Necessary for That Purpose. By the Rev. John Michell, B. D. F. R. S. In a Letter to Henry Cavendish, Esq. F. R. S. and A. S." *Philosophical Transactions of the Royal Society of London Series I* 74, 35.

Miller, B. P., E. Gallo, J. E. Greene, B. C. Kelly, T. Treu, J. H. Woo, and V. Baldassare (2015). "X-ray constraints on the local supermassive black hole occupation fraction". *ApJ* 799, 98.

Mineo, S., M. Gilfanov, and R. Sunyaev (2012). "X-ray emission from star-forming galaxies - II. Hot interstellar medium". *MNRAS* 426, 1870.

Miralda-Escudé, J. (2002). "A Test of the Collisional Dark Matter Hypothesis from Cluster Lensing". *ApJ* 564, 60.

Mitchell, N. L., I. G. McCarthy, R. G. Bower, T. Theuns, and R. A. Crain (2009). "On the origin of cores in simulated galaxy clusters". *MNRAS* 395, 180.

Mo, H., F. C. van den Bosch, and S. White (2010). *Galaxy Formation and Evolution*.

Moore, B. (1994). "Evidence against dissipation-less dark matter from observations of galaxy haloes". *Nature* 370, 629.

Moore, B., S. Ghigna, F. Governato, G. Lake, T. Quinn, J. Stadel, and P. Tozzi (1999). "Dark Matter Substructure in Galactic Halos". *ApJ* 524, L19.

Mori, M., A. Ferrara, and P. Madau (2002). "Early Metal Enrichment by Pregalactic Outflows. II. Three-dimensional Simulations of Blow-Away". *ApJ* 571, 40.

Moster, B. P., T. Naab, and S. D. M. White (2018). "EMERGE - an empirical model for the formation of galaxies since z ∼ 10". *MNRAS* 477, 1822.

Moster, B. P., R. S. Somerville, C. Maulbetsch, F. C. van den Bosch, A. V. Macciò, T. Naab, and L. Oser (2010). "Constraints on the Relationship between Stellar Mass and Halo Mass at Low and High Redshift". *ApJ* 710, 903.

Muzzin, A. et al. (2013). "The evolution of the stellar mass functions of star-forming and quiescent galaxies to z = 4 from the COSMOS/ultraVISTA survey". *ApJ* 777, 18.

Naab, T. and J. P. Ostriker (2017). "Theoretical Challenges in Galaxy Formation". *ARA&A* 55, 59.

Nambu, Y. and M. Sasaki (1990). "Quantum treatment of cosmological axion perturbations". *PRD* 42, 3918.

Narayan, R. and J. E. McClintock (2008). "Advection-dominated accretion and the black hole event horizon". *New Astron. Rev.* 51, 733.

Narayan, R. and I. Yi (1995). "Advection-dominated Accretion: Underfed Black Holes and Neutron Stars". *ApJ* 452, 710.

Navarro, J. F., V. R. Eke, and C. S. Frenk (1996a). "The cores of dwarf galaxy haloes". *MNRAS* 283, L72.

Navarro, J. F., C. S. Frenk, and S. D. M. White (1996b). "The Structure of Cold Dark Matter Halos". *ApJ* 462, 563.

Navarro, J. F., C. S. Frenk, and S. D. M. White (1997). "A Universal Density Profile from Hierarchical Clustering". *ApJ* 490, 493.
Nelson, D. et al. (2019). "First results from the TNG50 simulation: galactic outflows driven by supernovae and black hole feedback". *MNRAS* 490, 3234.
Nemmen, R. S., T. Storchi-Bergmann, and M. Eracleous (2014). "Spectral models for low-luminosity active galactic nuclei in LINERs: The role of advection-dominated accretion and jets". *MNRAS* 438, 2804.
Neto, A. F. et al. (2007). "The statistics of Λ CDM halo concentrations". *MNRAS* 381, 1450.
Neumayer, N. and C. J. Walcher (2012). "Are nuclear star clusters the precursors of massive black holes?" *Adv. Astron.* 2012.
Newton, I. (1687). *Philosophiae Naturalis Principia Mathematica. Auctore Js. Newton*.
Newton, O., M. Cautun, A. Jenkins, C. S. Frenk, and J. C. Helly (2018). "The total satellite population of the Milky Way". *MNRAS* 479, 2853.
Nguyen, D. D. et al. (2018). "Nearby Early-type Galactic Nuclei at High Resolution: Dynamical Black Hole and Nuclear Star Cluster Mass Measurements". *ApJ* 858, 118.
Nguyen, D. D. et al. (2019). "Improved Dynamical Constraints on the Masses of the Central Black Holes in Nearby Low-mass Early-type Galactic Nuclei and the First Black Hole Determination for NGC 205". *ApJ* 872, 104.
Niemeyer, J. C. (2020). "Small-scale structure of fuzzy and axion-like dark matter". *Progress in Particle and Nuclear Physics* 113, 103787.
Noble, S. C., J. H. Krolik, J. D. Schnittman, and J. F. Hawley (2011). "Radiative efficiency and thermal spectrum of accretion onto schwarzschild black holes". *ApJ* 743, 115.
Norman, M. L. and G. L. Bryan (1999). "Cosmological Adaptive Mesh Refinement". *Numerical Astrophysics*. Ed. by S. M. Miyama, K. Tomisaka, and T. Hanawa. Vol. 240, 19.
Nyland, K. and K. Alatalo (2018). "Science with an ngVLA: Accreting Supermassive Black Holes in Nearby Low-mass Galaxies". *ArXiv e-prints*, arXiv:1810.06564.
Nyland, K., J. Marvil, J. M. Wrobel, L. M. Young, and B. A. Zauderer (2012). "The intermediate-mass black hole candidate in the center of NGC404: New evidence from radio continuum observations". *ApJ* 753, 103.
Nyland, K. et al. (2017). "A Multi-wavelength Study of the Turbulent Central Engine of the Low-mass AGN Hosted by NGC 404". *ApJ* 845, 50.
O'Shea, B. W., G. Bryan, J. Bordner, M. L. Norman, T. Abel, R. Harkness, and A. Kritsuk (2004). "Introducing Enzo, an AMR Cosmology Application". *ArXiv e-prints*, astro-ph/0403044.
O'Shea, B. W., K. Nagamine, V. Springel, L. Hernquist, and M. L. Norman (2005). "Comparing AMR and SPH Cosmological Simulations. I. Dark Matter and Adiabatic Simulations". *ApJS* 160, 1.
Okamoto, T., L. Gao, and T. Theuns (2008). "Mass loss of galaxies due to an ultraviolet background". *MNRAS* 390, 920.
Oman, K. A., A. Marasco, J. F. Navarro, C. S. Frenk, J. Schaye, and A. Benítez-Llambay (2019). "Non-circular motions and the diversity of dwarf galaxy rotation curves". *MNRAS* 482, 821.
Oman, K. A. et al. (2015). "The unexpected diversity of dwarf galaxy rotation curves". *MNRAS* 452, 3650.
Omukai, K., R. Schneider, and Z. Haiman (2008). "Can Supermassive Black Holes Form in Metal-enriched High-Redshift Protogalaxies?" *ApJ* 686, 801.

Oñorbe, J., M. Boylan-Kolchin, J. S. Bullock, P. F. Hopkins, D. Kereš, C. A. Faucher-Giguère, E. Quataert, and N. Murray (2015). "Forged in FIRE: Cusps, cores and baryons in low-mass dwarf galaxies". *MNRAS* 454, 2092.

Oppenheimer, J. R. and H. Snyder (1939). "On Continued Gravitational Contraction". *Physical Review* 56, 455.

Ostriker, J. P., P. J. E. Peebles, and A. Yahil (1974). "The Size and Mass of Galaxies, and the Mass of the Universe". *ApJ* 193, L1.

Pakmor, R., C. Pfrommer, C. M. Simpson, and V. Springel (2016). "Galactic Winds Driven by Isotropic and Anisotropic Cosmic-Ray Diffusion in Disk Galaxies". *ApJ* 824, L30, L30.

Papaloizou, J. C. B. and J. E. Pringle (1983). "The time-dependence of non-planar accretion discs". *MNRAS* 202, 1181.

Pardo, K. et al. (2016). "X-Ray Detected Active Galactic Nuclei in Dwarf Galaxies at $0 < z < 1$". *ApJ* 831, 203.

Park, D., J.-H. Woo, V. N. Bennert, T. Treu, M. W. Auger, and M. A. Malkan (2015). "Cosmic Evolution of Black Holes and Spheroids. V. The Relation between Black Hole Mass and Host Galaxy Luminosity for a Sample of 79 Active Galaxies". *ApJ* 799, 164.

Peebles, P. J. E. (1968). "Recombination of the Primeval Plasma". *ApJ* 153, 1.

Peebles, P. J. E. (1980). *The large-scale structure of the universe*.

Peebles, P. J. E. (2000). "Fluid Dark Matter". *ApJ* 534, L127.

Peng, Y.-j. et al. (2010). "Mass and Environment as Drivers of Galaxy Evolution in SDSS and zCOSMOS and the Origin of the Schechter Function". *ApJ* 721, 193.

Penny, S. J. et al. (2018). "SDSS-IV MaNGA: evidence of the importance of AGN feedback in low-mass galaxies". *MNRAS* 476, 979.

Penrose, R. (1965). "Gravitational Collapse and Space-Time Singularities". *PRL* 14, 57.

Penzias, A. A. and R. W. Wilson (1965). "A Measurement of Excess Antenna Temperature at 4080 Mc/s." *ApJ* 142, 419.

Perego, A., M. Dotti, M. Colpi, and M. Volonteri (2009). "Mass and spin co-evolution during the alignment of a black hole in a warped accretion disc". *MNRAS* 399, 2249.

Pfister, H., M. Volonteri, Y. Dubois, M. Dotti, and M. Colpi (2019). "The erratic dynamical life of black hole seeds in high-redshift galaxies". *MNRAS* 486, 101.

Pillepich, A. et al. (2018). "Simulating galaxy formation with the IllustrisTNG model". *MNRAS* 473, 4077.

Pillepich, A. et al. (2019). "First results from the TNG50 simulation: the evolution of stellar and gaseous discs across cosmic time". *MNRAS* 490, 3196.

Planck Collaboration XIII (2016). "Planck 2015 results: XIII. Cosmological parameters". *Astron. Astrophys.* 594.

Plotkin, R. M. and A. E. Reines (2018). "Science with an ngVLA: Local Constraints on Supermassive Black Hole Seeds". *ArXiv e-prints*, arXiv:1810.06814.

Polisensky, E. and M. Ricotti (2011). "Constraints on the dark matter particle mass from the number of Milky Way satellites". *PRD* 83, 043506.

Pontzen, A. and F. Governato (2014). "Cold dark matter heats up". *Nature* 506, 171.

Porciani, C., A. Dekel, and Y. Hoffman (2002). "Testing tidal-torque theory - I. Spin amplitude and direction". *MNRAS* 332, 325.

Portegies Zwart, S. F. and S. L. W. McMillan (2002). "The Runaway Growth of Intermediate-Mass Black Holes in Dense Star Clusters". *ApJ* 576, 899.

Potter, D., J. Stadel, and R. Teyssier (2017). "PKDGRAV3: beyond trillion particle cosmological simulations for the next era of galaxy surveys". *Computational Astrophysics and Cosmology* 4, 2, 2.

Power, C., J. F. Navarro, A. Jenkins, C. S. Frenk, S. D. M. White, V. Springel, J. Stadel, and T. Quinn (2003). "The inner structure of ΛCDM haloes - I. A numerical convergence study". *MNRAS* 338, 14.

Power, C., S. Nayakshin, and A. King (2011). "The accretion disc particle method for simulations of black hole feeding and feedback". *MNRAS* 412, 269.

Press, W. H. and P. Schechter (1974). "Formation of Galaxies and Clusters of Galaxies by Self-Similar Gravitational Condensation". *ApJ* 187, 425.

Pringle, J. E. (1981). "Accretion discs in astrophysics". *ARA&A* 19, 137.

Puchwein, E., F. Haardt, M. G. Haehnelt, and P. Madau (2019). "Consistent modelling of the meta-galactic UV background and the thermal/ionization history of the intergalactic medium". *MNRAS* 485, 47.

Puchwein, E. and V. Springel (2012). "Shaping the galaxy stellar mass function with supernova- and AGN-driven winds". *MNRAS* 428, 2966.

Randall, S. W., M. Markevitch, D. Clowe, A. H. Gonzalez, and M. Bradač (2008). "Constraints on the Self-Interaction Cross Section of Dark Matter from Numerical Simulations of the Merging Galaxy Cluster 1E 0657-56". *ApJ* 679, 1173.

Rantala, A., P. Pihajoki, P. H. Johansson, T. Naab, N. Lahén, and T. Sawala (2017). "Post-Newtonian Dynamical Modeling of Supermassive Black Holes in Galactic-scale Simulations". *ApJ* 840, 53, 53.

Read, J. I., T. Hayfield, and O. Agertz (2010). "Resolving mixing in smoothed particle hydrodynamics". *MNRAS* 405, 1513.

Reines, A. E. and A. T. Deller (2012). "Parsec-scale radio emission from the low-luminosity active galactic nucleus in the dwarf starburst galaxy Henize 2-10". *ApJ* 750, L24.

Reines, A. E., J. J. Condon, J. Darling, and J. E. Greene (2020). "A New Sample of (Wandering) Massive Black Holes in Dwarf Galaxies from High-resolution Radio Observations". *ApJ* 888, 36.

Reines, A. E., J. E. Greene, and M. Geha (2013). "Dwarf galaxies with optical signatures of active massive black holes". *ApJ* 775, 116.

Reines, A. E., R. M. Plotkin, T. D. Russell, M. Mezcua, J. J. Condon, G. R. Sivakoff, and K. E. Johnson (2014). "A candidate massive black hole in the low-metallicity dwarf galaxy pair Mrk 709". *ApJ* 787, 30.

Reines, A. E. and M. Volonteri (2015). "Relations between central black hole mass and total galaxy stellar mass in the local Universe". *ApJ* 813, 82.

Ressler, S. M., A. Tchekhovskoy, E. Quataert, M. Chandra, and C. F. Gammie (2015). "Electron thermodynamics in GRMHD simulations of low-luminosity black hole accretion". *MNRAS* 454, 1848.

Ricarte, A. and P. Natarajan (2018). "Exploring SMBH assembly with semi-analytic modelling". *MNRAS* 474, 1995.

Roberts, M. S. and A. H. Rots (1973). "Comparison of Rotation Curves of Different Galaxy Types". *A&A* 26, 483.

Rogstad, D. H. and G. S. Shostak (1972). "Gross Properties of Five Scd Galaxies as Determined from 21-CENTIMETER Observations". *ApJ* 176, 315.

Rosas-Guevara, Y. M. et al. (2015). "The impact of angular momentum on black hole accretion rates in simulations of galaxy formation". *MNRAS* 454, 1038.

Rosdahl, J. and R. Teyssier (2015). "A scheme for radiation pressure and photon diffusion with the M1 closure in RAMSES-RT". *MNRAS* 449, 4380.
Rosdahl, J. et al. (2018). "The SPHINX cosmological simulations of the first billion years: The impact of binary stars on reionization". *MNRAS* 479, 994.
Rose, M., C. Tadhunter, C. Ramos Almeida, J. Rodrıguez Zaurın, F. Santoro, and R. Spence (2018). "Quantifying the AGN-driven outflows in ULIRGs (QUADROS) - I: VLT/Xshooter observations of nine nearby objects". *MNRAS* 474, 128.
Rubin, V. C., J. Ford W. K., and N. Thonnard (1978). "Extended rotation curves of high-luminosity spiral galaxies. IV. Systematic dynamical properties, Sa -> Sc." *ApJ* 225, L107.
Rubin, V. C., J. Ford W. K., and N. Thonnard (1980). "Rotational properties of 21 SC galaxies with a large range of luminosities and radii, from NGC 4605 (R=4kpc) to UGC 2885 (R=122kpc)." *ApJ* 238, 471.
Rubin, V. C. and J. Ford W. Kent (1970). "Rotation of the Andromeda Nebula from a Spectroscopic Survey of Emission Regions". *ApJ* 159, 379.
Rupke, D. S. N., K. Gültekin, and S. Veilleux (2017). "Quasar-mode Feedback in Nearby Type 1 Quasars: Ubiquitous Kiloparsec-scale Outflows and Correlations with Black Hole Properties". *ApJ* 850, 40, 40.
Rupke, D. S. and S. Veilleux (2011). "Integral field spectroscopy of massive, kiloparsec-scale outflows in the infrared-luminous QSO Mrk 231". *ApJ* 729, 27.
Ryan, B. R., S. M. Ressler, J. C. Dolence, A. Tchekhovskoy, C. F. Gammie, and E. Quataert (2017). "The Radiative Efficiency and Spectra of Slowly Accreting Black Holes from Two-Temperature GRRMHD Simulations". *ApJ* 844, L24.
Sadowski, A., J. P. Lasota, M. A. Abramowicz, and R. Narayan (2016). "Energy flows in thick accretion discs and their consequences for black hole feedback". *MNRAS* 456, 3915.
Sadowski, A., R. Narayan, R. Penna, and Y. Zhu (2013). "Energy, momentum and mass outflows and feedback from thick accretion discs around rotating black holes". *MNRAS* 436, 3856.
Saglia, R. P. et al. (2016). "The SINFONI Black Hole Survey: The Black Hole Fundamental Plane Revisited and the Paths of (Co)evolution of Supermassive Black Holes and Bulges". *ApJ* 818, 47.
Saitoh, T. R. and J. Makino (2013). "A Density-independent Formulation of Smoothed Particle Hydrodynamics". *ApJ* 768, 44, 44.
Salem, M. and G. L. Bryan (2014). "Cosmic ray driven outflows in global galaxy disc models". *MNRAS* 437, 3312.
Salpeter, E. E. (1964). "Accretion of Interstellar Matter by Massive Objects." *ApJ* 140, 796.
Santos-Santos, I. M. E. et al. (2020). "Baryonic clues to the puzzling diversity of dwarf galaxy rotation curves". *MNRAS* 495, 58.
Sartori, L. F., K. Schawinski, E. Treister, B. Trakhtenbrot, M. Koss, M. Shirazi, and K. Oh (2015). "The search for active black holes in nearby low-mass galaxies using optical and mid-IR data". *MNRAS* 454, 3722.
Satyapal, S., N. J. Secrest, W. McAlpine, S. L. Ellison, J. Fischer, and J. L. Rosenberg (2014). "Discovery of a population of bulgeless galaxies with extremely red MID-IR colors: Obscured AGN activity in the low-mass regime?" *ApJ* 784, 113.
Satyapal, S., L. Kamal, J. M. Cann, N. J. Secrest, and N. P. Abel (2021). "The Diagnostic Potential of JWST in Characterizing Elusive AGNs". *ApJ* 906, 35, 35.
Sawala, T. et al. (2016). "The APOSTLE simulations: Solutions to the Local Group's cosmic puzzles". *MNRAS* 457, 1931.

Scannapieco, C. et al. (2012). "The Aquila comparison project: the effects of feedback and numerical methods on simulations of galaxy formation". *MNRAS* 423, 1726.
Schaye, J. et al. (2010). "The physics driving the cosmic star formation history". *MNRAS* 402, 1536.
Schaye, J. et al. (2015). "The EAGLE project: Simulating the evolution and assembly of galaxies and their environments". *MNRAS* 446, 521.
Schirra, A. P. et al. (2020). "Bringing faint Active Galactic Nuclei (AGN) to light". *ArXiv e-prints*, arXiv:2011.02501.
Schmidt, M. (1963). "3C 273 : A Star-Like Object with Large Red-Shift". *Nature* 197, 1040.
Schmidt, M. (1959). "The Rate of Star Formation." *ApJ* 129, 243.
Schramm, M. and J. D. Silverman (2013). "The Black Hole-Bulge Mass Relation of Active Galactic Nuclei in the Extended Chandra Deep Field-South Survey". *ApJ* 767, 13.
Schutte, Z., A. E. Reines, and J. E. Greene (2019). "The Black Hole–Bulge Mass Relation Including Dwarf Galaxies Hosting Active Galactic Nuclei". *ApJ* 887, 245.
Schwarzschild, K. (1916). "Über das Gravitationsfeld eines Massenpunktes nach der Einsteinschen Theorie". *Sitzungsberichte der Königlich Preußischen Akademie der Wissenschaften (Berlin)*, 189.
Sesana, A., E. Barausse, M. Dotti, and E. M. Rossi (2014). "Linking the Spin Evolution of Massive Black Holes to Galaxy Kinematics". *ApJ* 794, 104, 104.
Shakura, N. I. and R. A. Sunyaev (1973). "Black Holes in Binary Systems. Observational Experience". *A&A* 24, 337.
Shao, S., L. Gao, T. Theuns, and C. S. Frenk (2013). "The phase-space density of fermionic dark matter haloes". *MNRAS* 430, 2346.
Shapley, H. (1918). "Globular Clusters and the Structure of the Galactic System". *PASP* 30, 42.
Sharma, R. S., A. M. Brooks, R. S. Somerville, M. Tremmel, J. Bellovary, A. C. Wright, and T. R. Quinn (2020). "Black Hole Growth and Feedback in Isolated ROMULUS25 Dwarf Galaxies". *ApJ* 897, 103.
Shen, X., P. F. Hopkins, C.-A. Faucher-Giguère, D. M. Alexander, G. T. Richards, N. P. Ross, and R. C. Hickox (2020). "The bolometric quasar luminosity function at z = 0-7". *MNRAS* 495, 3252.
Shen, Y., H.-C. Hwang, N. Zakamska, and X. Liu (2019). "Varstrometry for Off-nucleus and Dual Sub-Kpc AGN (VODKA): How Well Centered Are Low-z AGN?" *ApJL* 885, L4.
Sheth, R. K., H. J. Mo, and G. Tormen (2001). "Ellipsoidal collapse and an improved model for the number and spatial distribution of dark matter haloes". *MNRAS* 323, 1.
Sijacki, D., V. Springel, T. Di Matteo, and L. Hernquist (2007). "A unified model for AGN feedback in cosmological simulations of structure formation". *MNRAS* 380, 877.
Sijacki, D., V. Springel, and M. G. Haehnelt (2011). "Gravitational recoils of supermassive black holes in hydrodynamical simulations of gas-rich galaxies". *MNRAS* 414, 3656.
Sijacki, D., M. Vogelsberger, S. Genel, V. Springel, P. Torrey, G. F. Snyder, D. Nelson, and L. Hernquist (2015). "The Illustris simulation: The evolving population of black holes across cosmic time". *MNRAS* 452, 575.
Sijacki, D., M. Vogelsberger, D. Kereš, V. Springel, and L. Hernquist (2012). "Moving mesh cosmology: the hydrodynamics of galaxy formation". *MNRAS* 424, 2999.
Silk, J. (1968). "Cosmic Black-Body Radiation and Galaxy Formation". *ApJ* 151, 459.
Silk, J. (2017). "Feedback by Massive Black Holes in Dwarf Galaxies". *ApJ* 839, 13.
Silk, J. and M. J. Rees (1998). "Quasars and galaxy formation". *A&A* 331, L1.
Simon, J. D. (2019). "The Faintest Dwarf Galaxies". *ARA&A* 57, 375.

Smith, B. D. et al. (2017). "GRACKLE: a chemistry and cooling library for astrophysics". *MNRAS* 466, 2217.
Smith, H. J. and D. Hoffleit (1963). "Light Variability and Nature of 3C273." *AJ* 68, 292.
Smith, M. C., D. Sijacki, and S. Shen (2018). "Supernova feedback in numerical simulations of galaxy formation: separating physics from numerics". *MNRAS* 478, 302.
Smith, M. C. (2021). "The sensitivity of stellar feedback to IMF averaging versus IMF sampling in galaxy formation simulations". *MNRAS* 502, 5417.
Smith, M. C., G. L. Bryan, R. S. Somerville, C.-Y. Hu, R. Teyssier, B. Burkhart, and L. Hernquist (2020). "Efficient early stellar feedback can suppress galactic outflows by reducing supernova clustering". *ArXiv e-prints*, arXiv:2009.11309.
Smith, M. C., D. Sijacki, and S. Shen (2019). "Cosmological simulations of dwarfs: the need for ISM physics beyond SN feedback alone". *MNRAS* 485, 3317.
Smith, R. J., J. R. Lucey, J. Price, M. J. Hudson, and S. Phillipps (2012). "Environmental quenching and hierarchical cluster assembly: evidence from spectroscopic ages of red-sequence galaxies in Coma". *MNRAS* 419, 3167.
Smoot, G. F. et al. (1992). "Structure in the COBE Differential Microwave Radiometer First-Year Maps". *ApJ* 396, L1.
Somerville, R. S. and R. Davé (2015). "Physical Models of Galaxy Formation in a Cosmological Framework". *ARA&A* 53, 51.
Somerville, R. S., P. F. Hopkins, T. J. Cox, B. E. Robertson, and L. Hernquist (2008). "A semi-analytic model for the co-evolution of galaxies, black holes and active galactic nuclei". *MNRAS* 391, 481.
Somerville, R. S. and J. R. Primack (1999). "Semi-analytic modelling of galaxy formation: the local Universe". *MNRAS* 310, 1087.
Spergel, D. N. et al. (2003). "First Year Wilkinson Microwave Anisotropy Probe (WMAP) Observations: Determination of Cosmological Parameters". *ApJS* 148, 175.
Spergel, D. N. and P. J. Steinhardt (2000). "Observational Evidence for Self-Interacting Cold Dark Matter". *PRL* 84, 3760.
Springel, V. and L. Hernquist (2003). "Cosmological smoothed particle hydrodynamics simulations: a hybrid multiphase model for star formation". *MNRAS* 339, 289.
Springel, V. et al. (2008). "The Aquarius Project: the subhaloes of galactic haloes". *MNRAS* 391, 1685.
Springel, V. (2010). "E pur si muove: Galilean-invariant cosmological hydrodynamical simulations on a moving mesh". *MNRAS* 401, 791.
Springel, V., T. Di Matteo, and L. Hernquist (2005a). "Modelling feedback from stars and black holes in galaxy mergers". *MNRAS* 361, 776.
Springel, V., S. D. White, G. Tormen, and G. Kauffmann (2001a). "Populating a cluster of galaxies - I. Results at z = 0". *MNRAS* 328, 726.
Springel, V., N. Yoshida, and S. D. M. White (2001b). "GADGET: a code for collisionless and gasdynamical cosmological simulations". *NA* 6, 79.
Springel, V. et al. (2005b). "Simulations of the formation, evolution and clustering of galaxies and quasars". *Nature* 435, 629.
Stinson, G., A. Seth, N. Katz, J. Wadsley, F. Governato, and T. Quinn (2006). "Star formation and feedback in smoothed particle hydrodynamic simulations - I. Isolated galaxies". *MNRAS* 373, 1074.
Suh, H., F. Civano, B. Trakhtenbrot, F. Shankar, G. Hasinger, D. B. Sanders, and V. Allevato (2020). "No Significant Evolution of Relations between Black Hole Mass and Galaxy Total Stellar Mass Up to $z \sim 2.5$". *ApJ* 889, 32.

Suh, H. et al. (2017). "Type 2 AGN Host Galaxies in the Chandra -COSMOS Legacy Survey: No Evidence of AGN-driven Quenching". *ApJ* 841, 102.
Sun, M. et al. (2015). "Evolution in the black hole-galaxy scaling relations and the duty cycle of nuclear activity in star-forming galaxies". *ApJ* 802, 14.
Sutherland, R. S. and M. A. Dopita (1993). "Cooling Functions for Low-Density Astrophysical Plasmas". *ApJS* 88, 253.
Talbot, R. Y., M. A. Bourne, and D. Sijacki (2021). "Blandford-Znajek jets in galaxy formation simulations: method and implementation". *MNRAS* 504, 3619.
Tasitsiomi, A., A. V. Kravtsov, R. H. Wechsler, and J. R. Primack (2004). "Modeling Galaxy-Mass Correlations in Dissipationless Simulations". *ApJ* 614, 533.
Tchekhovskoy, A. (2015). "Launching of Active Galactic Nuclei Jets". *The Formation and Disruption of Black Hole Jets*. Ed. by I. Contopoulos, D. Gabuzda, and N. Kylafis. Vol. 414, 45.
Tchekhovskoy, A., J. C. McKinney, and R. Narayan (2012). "General Relativistic Modeling of Magnetized Jets from Accreting Black Holes". *J. Phys. Conf. Ser.* 372, 012040.
Tchekhovskoy, A. and J. C. McKinney (2012). "Prograde and retrograde black holes: Whose jet is more powerful?" *MNRAS* 423, L55.
Tchekhovskoy, A., R. Narayan, and J. C. McKinney (2011). "Efficient generation of jets from magnetically arrested accretion on a rapidly spinning black hole". *MNRAS* 418, L79.
Tegmark, M. et al. (2004). "The Three-Dimensional Power Spectrum of Galaxies from the Sloan Digital Sky Survey". *ApJ* 606, 702.
Teyssier, R. (2002). "Cosmological hydrodynamics with adaptive mesh refinement. A new high resolution code called RAMSES". *A&A* 385, 337.
Thater, S., D. Krajnović, M. Cappellari, T. A. Davis, P. T. de Zeeuw, R. M. McDermid, and M. Sarzi (2019). "Six new supermassive black hole mass determinations from adaptive-optics assisted SINFONI observations". *A&A* 625, A62.
Thornton, K., M. Gaudlitz, H.-T. Janka, and M. Steinmetz (1998). "Energy Input and Mass Redistribution by Supernovae in the Interstellar Medium". *ApJ* 500, 95.
Tollerud, E. J., J. S. Bullock, L. E. Strigari, and B. Willman (2008). "Hundreds of Milky Way Satellites? Luminosity Bias in the Satellite Luminosity Function". *ApJ* 688, 277.
Torrey, P., M. Vogelsberger, S. Genel, D. Sijacki, V. Springel, and L. Hernquist (2014). "A model for cosmological simulations of galaxy formation physics: Multi-epoch validation". *MNRAS* 438, 1985.
Torrey, P., M. Vogelsberger, D. Sijacki, V. Springel, and L. Hernquist (2012). "Moving-mesh cosmology: Properties of gas discs". *MNRAS* 427, 2224.
Trebitsch, M., M. Volonteri, Y. Dubois, and P. Madau (2018). "Escape of ionizing radiation from high-redshift dwarf galaxies: role of AGN feedback". *MNRAS* 478, 5607.
Tremaine, S. et al. (2002). "The Slope of the Black Hole Mass versus Velocity Dispersion Correlation". *ApJ* 574, 740.
Tremmel, M., M. Karcher, F. Governato, M. Volonteri, T. R. Quinn, A. Pontzen, L. Anderson, and J. Bellovary (2017). "The Romulus cosmological simulations: a physical approach to the formation, dynamics and accretion models of SMBHs". *MNRAS* 470, 1121.
Tremmel, M. et al. (2019). "Introducing ROMULUSC: a cosmological simulation of a galaxy cluster with an unprecedented resolution". *MNRAS* 483, 3336.
Tremmel, M., F. Governato, M. Volonteri, A. Pontzen, and T. R. Quinn (2018). "Wandering Supermassive Black Holes in Milky-Way-mass Halos". *ApJ* 857, L22.

Tremmel, M., F. Governato, M. Volonteri, and T. R. Quinn (2015). "Off the beaten path: A new approach to realistically model the orbital decay of supermassive black holes in galaxy formation simulations". *MNRAS* 451, 1868.
Trump, J. R. et al. (2011). "Accretion rate and the physical nature of unobscured active galaxies". *ApJ* 733, 60.
Tseliakhovich, D. and C. Hirata (2010). "Relative velocity of dark matter and baryonic fluids and the formation of the first structures". *PRD* 82, 083520.
Tulin, S. and H.-B. Yu (2018). "Dark matter self-interactions and small scale structure". *Phys. Rep.* 730, 1.
Uhlig, M., C. Pfrommer, M. Sharma, B. B. Nath, T. A. Enßlin, and V. Springel (2012). "Galactic winds driven by cosmic ray streaming". *MNRAS* 423, 2374.
Uson, J. M. and D. T. Wilkinson (1984). "Improved limits on small-scale anisotropy in cosmic microwave background". *Nature* 312, 427.
van den Bosch, F. C. et al. (2007). "Towards a concordant model of halo occupation statistics". *MNRAS* 376, 841.
Vasudevan, R. V. and A. C. Fabian (2007). "Piecing together the X-ray background: Bolometric corrections for active galactic nuclei". *MNRAS* 381, 1235.
Vogelsberger, M., S. Genel, D. Sijacki, P. Torrey, V. Springel, and L. Hernquist (2013). "A model for cosmological simulations of galaxy formation physics". *MNRAS* 436, 3031.
Vogelsberger, M., D. Sijacki, D. Kereš, V. Springel, and L. Hernquist (2012a). "Moving mesh cosmology: Numerical techniques and global statistics". *MNRAS* 425, 3024.
Vogelsberger, M., J. Zavala, and A. Loeb (2012b). "Subhaloes in self-interacting galactic dark matter haloes". *MNRAS* 423, 3740.
Vogelsberger, M., J. Zavala, C. Simpson, and A. Jenkins (2014a). "Dwarf galaxies in CDM and SIDM with baryons: Observational probes of the nature of dark matter". *MNRAS* 444, 3684.
Vogelsberger, M. et al. (2014b). "Introducing the Illustris project: Simulating the coevolution of dark and visible matter in the universe". *MNRAS* 444, 1518.
Volonteri, M., M. Sikora, J. .-P. Lasota, and A. Merloni (2013). "The Evolution of Active Galactic Nuclei and their Spins". *ApJ* 775, 94, 94.
Volonteri, M., F. Haardt, and P. Madau (2003). "The Assembly and Merging History of Supermassive Black Holes in Hierarchical Models of Galaxy Formation". *ApJ* 582, 559.
Volonteri, M., G. Lodato, and P. Natarajan (2008). "The evolution of massive black hole seeds". *MNRAS* 383, 1079.
Volonteri, M., P. Madau, E. Quataert, and M. J. Rees (2005). "The Distribution and Cosmic Evolution of Massive Black Hole Spins". *ApJ* 620, 69.
Volonteri, M. et al. (2020). "Black hole mergers from dwarf to massive galaxies with the NewHorizon and Horizon-AGN simulations". *MNRAS* 498, 2219.
Wadepuhl, M. and V. Springel (2011). "Satellite galaxies in hydrodynamical simulations of Milky Way sized galaxies". *MNRAS* 410, 1975.
Wadsley, J. W., J. Stadel, and T. Quinn (2004). "Gasoline: a flexible, parallel implementation of TreeSPH". *NA* 9, 137.
Wagner, A. Y., M. Umemura, and G. V. Bicknell (2013). "Ultrafast outflows: Galaxy-scale active galactic nucleus feedback". *ApJ* 763, L18.
Walker, M. G. and J. Parrubia (2011). "A method for measuring (slopes of) the mass profiles of dwarf spheroidal galaxies". *ApJ* 742, 20.

Wang, L., R. Spurzem, S. Aarseth, K. Nitadori, P. Berczik, M. B. N. Kouwenhoven, and T. Naab (2015). "NBODY6++GPU: ready for the gravitational million-body problem". *MNRAS* 450, 4070.
Wechsler, R. H. and J. L. Tinker (2018). "The Connection Between Galaxies and Their Dark Matter Halos". *ARA&A* 56, 435.
Weinberger, R. et al. (2017). "Simulating galaxy formation with black hole driven thermal and kinetic feedback". *MNRAS* 465, 3291.
Weinberger, R. et al. (2018). "Supermassive black holes and their feedback effects in the IllustrisTNG simulation". *MNRAS* 479, 4056.
Wetzel, A. R., J. L. Tinker, C. Conroy, and F. C. van den Bosch (2013). "Galaxy evolution in groups and clusters: satellite star formation histories and quenching time-scales in a hierarchical Universe". *MNRAS* 432, 336.
Whalen, D. J. and C. L. Fryer (2012). "The formation of supermassive black holes from low-mass pop III seeds". *ApJ* 756, L19.
Wheeler, C. et al. (2019). "Be it therefore resolved: cosmological simulations of dwarf galaxies with 30 solar mass resolution". *MNRAS* 490, 4447.
White, S. D. M., M. Davis, and C. S. Frenk (1984). "The size of clusters in a neutrino-dominated universe". *MNRAS* 209, 27P.
White, S. D. M., C. S. Frenk, and M. Davis (1983). "Clustering in a neutrino-dominated universe". *ApJ* 274, L1.
White, S. D. M. and M. J. Rees (1978). "Core condensation in heavy halos: a two-stage theory for galaxy formation and clustering". *MNRAS* 183, 341.
White, S. D. M. and J. Silk (1979). "The growth of aspherical structure in the universe: Is the Local Supercluster an unusual system?" *ApJ* 231, 1.
White, S. D. M. and C. S. Frenk (1991). "Galaxy formation through hierarchical clustering". *ApJ* 379, 52.
Wiersma, R. P., J. Schaye, and B. D. Smith (2009a). "The effect of photoionization on the cooling rates of enriched, astrophysical plasmas". *MNRAS* 393, 99.
Wiersma, R. P., J. Schaye, T. Theuns, C. Dalla Vecchia, and L. Tornatore (2009b). "Chemical enrichment in cosmological, smoothed particle hydrodynamics simulations". *MNRAS* 399, 574.
Wright, T. (1750). *An original theory or new hypothesis of the universe*.
Wrobel, J. M., J. E. Greene, L. C. Ho, and J. S. Ulvestad (2008). "Steep-Spectrum Radio Emission from the Low-Mass Active Galactic Nucleus GH 10". *ApJ* 686, 838.
Wrobel, J. M. and L. C. Ho (2006). "Radio Emission on Subparsec Scales from the Intermediate-Mass Black Hole in NGC 4395". *ApJ* 646, L95.
Wyithe, J. S. B. and A. Loeb (2003). "Self-regulated Growth of Supermassive Black Holes in Galaxies as the Origin of the Optical and X-Ray Luminosity Functions of Quasars". *ApJ* 595, 614.
Xie, F. G. and F. Yuan (2012). "Radiative efficiency of hot accretion flows". *MNRAS* 427, 1580.
Yang, G. et al. (2018). "Linking black hole growth with host galaxies: The accretion-stellar mass relation and its cosmic evolution". *MNRAS* 475, 1887.
Yang, X., H. J. Mo, and F. C. van den Bosch (2003). "Constraining galaxy formation and cosmology with the conditional luminosity function of galaxies". *MNRAS* 339, 1057.
Yu, Z., F. Yuan, and L. C. Ho (2011). "On the origin of ultraviolet emission and the accretion model of low-luminosity active galactic nuclei". *ApJ* 726, 87.

Yuan, F. and R. Narayan (2014). "Hot Accretion Flows Around Black Holes". *ARA&A* 52, 529.

Yuan, F., M. Wu, and D. Bu (2012). "Numerical Simulation of Hot Accretion Flows. I. A Large Radial Dynamical Range and the Density Profile of Accretion Flow". *ApJ* 761, 129, 129.

Yuan, F., D. Yoon, Y.-P. Li, Z.-M. Gan, L. C. Ho, and F. Guo (2018). "Active Galactic Nucleus Feedback in an Elliptical Galaxy with the Most Updated AGN Physics. I. Low Angular Momentum Case". *ApJ* 857, 121, 121.

Zehavi, I. et al. (2002). "Galaxy Clustering in Early Sloan Digital Sky Survey Redshift Data". *ApJ* 571, 172.

Zel'dovich, Y. B. (1970). "Gravitational instability: an approximate theory for large density perturbations." *A&A* 5, 84.

Zel'dovich, Y. B. (1964). "The Fate of a Star and the Evolution of Gravitational Energy Upon Accretion". *Soviet Physics Doklady* 9, 195.

Zel'dovich, Y. B., V. G. Kurt, and R. A. Syunyaev (1969). "Recombination of Hydrogen in the Hot Model of the Universe". *Soviet Journal of Experimental and Theoretical Physics* 28, 146.

Zhao, D. H., Y. P. Jing, H. J. Mo, and G. Börner (2009). "Accurate Universal Models for the Mass Accretion Histories and Concentrations of Dark Matter Halos". *ApJ* 707, 354.

Zibetti, S., S. Charlot, and H. W. Rix (2009). "Resolved stellar mass maps of galaxies - I. Method and implications for global mass estimates". *MNRAS* 400, 1181.

Zinger, E. et al. (2020). "Ejective and preventative: the IllustrisTNG black hole feedback and its effects on the thermodynamics of the gas within and around galaxies". *MNRAS* 499, 768.

Zwicky, F. (1933). "Die Rotverschiebung von extragalaktischen Nebeln". *Helvetica Physica Acta* 6, 110.